Doctoral Dissertations   Dissertations and Theses

Fall 2014

Measurement of the Parity Violating Asymmetry in Elastic Electron Scattering off 208Pb

Jonathan W. Wexler
University of Massachusetts - Amherst

Measurement of the Parity Violating Asymmetry in Elastic Electron Scattering off ^{208}Pb

A Dissertation Presented

by

Jonathan William Wexler, Jr.

Submitted to the Graduate School of the
University of Massachusetts Amherst in partial fulfillment
of the requirements for the degree of

Doctor of Philosophy

September 2014

Physics Program

Measurement of the Parity Violating Asymmetry in Elastic Electron Scattering off ^{208}Pb

A Dissertation Presented

by

Jonathan William Wexler, Jr.

Approved as to style and content by:

_____

Krishna Kumar, chair

_____

Andrea Pocar, member

_____

John Dubach, member

_____

Grant Wilson, member

_____

Rory Miskimen, Department Chair

Physics

ABSTRACT

MEASUREMENT OF THE PARITY VIOLATING ASYMMETRY IN ELASTIC ELECTRON SCATTERING OFF ^{208}Pb

SEPTEMBER 2014

JONATHAN WILLIAM WEXLER, JR., B.A., HAMILTON COLLEGE

M.S., UNIVERSITY OF MASSACHUSETTS AMHERST

PH.D., UNIVERSITY OF MASSACHUSETTS AMHERST

Directed by Krishna Kumar

The Lead Radius Experiment (PREX) was carried out in order to provide a model-independent measurement of the RMS radius $\sqrt{\langle r_n^2 \rangle}$ of the neutron distribution in the ^{208}Pb nucleus. The parity-violating scattering asymmetry for longitudinally polarized 1.06 GeV electrons from an unpolarized ^{208}Pb target was measured at Q^2 = 0.00880 GeV^2. This measurement was performed by the PREX collaboration in Hall A at Jefferson Laboratory in Newport News, VA, between March and June, 2010. The electron detectors used in this measurement were designed and fabricated by University of Massachusetts-Amherst and Smith College. The resulting parity-violating asymmetry was measured as $A_{PV} =$ 656 ± 60(stat.) ± 14(sys.) ppb. This asymmetry extrapolates to a difference in radii between the nuclear neutron and proton distributions of $\sqrt{\langle r_n^2 \rangle}$ - $\sqrt{\langle r_p^2 \rangle} = 0.33^{+0.16}_{-0.18}$ fm.

CONTENTS

APPENDICES

LIST OF TABLES

LIST OF FIGURES

xvii

CHAPTER 1

INTRODUCTION

Most matter is composed of three constituents: electrons, protons and neutrons. The electron, discovered by J. J. Thomson in 1897 using cathode ray tubes, is a light, negatively charged particle. The proton, discovered by Ernest Rutherford in 1911, is a heavier, positively charged particle that groups together with other protons in a dense volume known as the atomic nucleus. As proposed by Niels Bohr in 1913, the electrons form a diffuse cloud around this nucleus, in numbers such that the total atom is uncharged. This nucleus also contains neutrons, a particle with no electric charge found by James Chadwick in 1932. The neutron answered the ongoing question regarding how the mass of highly charged nuclei was substantially larger than just the mass of the protons.

Beyond the discovery of the constituent particles, the understanding of the nucleus continued to evolve. Rutherford's scattering of electrons from protons allowed for measurements of the charge radius of the proton, which led to experiments in the 1960's and 1970's measuring electrons scattering from the nucleus to map the size of the proton distribution in the nucleus for various atoms including ^{40}Ca and ^{48}Ca[1], ^{58}Ni[2], and ^{208}Pb[3]. The Stern-Gerlach experiment, in 1925, discovered the electron interacted with a magnetic field differently based on some intrinsic property, later identified to be spin angular momentum. The spin of electrons, protons and neutrons was defined to be $\pm\frac{1}{2}$ in the model proposed by Wolfgang Pauli. The Pauli exclusion principle dictates that spin $\frac{1}{2}$ particles, known as fermions, cannot exist in identical states, meaning that the energy and spin states of any two particles in the same atom are excluded from being identical. The Pauli exclusion principle, combined with Niels Bohr's model for the atom, led to what is known as the nuclear shell model, describing the energetic arrangement of nucleons. Further research, such as the Bethe-Weizsäcker semi-empirical mass formula and electron-nucleus scattering experiments,

expands the understanding beyond the simple composition of atoms to include information such as atomic mass and size. This formula, from measurements of lighter nuclei, has shown to be a good description of the mass of light nuclei. However, while the semi-empirical mass formula predicts there is a dependence on the relative number of neutrons and protons, this dependence has not been experimentally measured.

From electron scattering experiments, the proton has been shown to have a non-zero radius, with a measurable root-mean square radius for the density of protons in a nucleus $\sqrt{\langle r_p^2 \rangle}$. Measurements have similarly been done to measure the r.m.s. radii of various nuclei, including ^{208}Pb. However, this approach cannot probe the uncharged neutrons. This results in uncertainties about the r.m.s. radius of the neutrons in a nucleus, $\sqrt{\langle r_n^2 \rangle}$ and how, if at all, the r.m.s. radius differs from that of the protons. Models suggest that, for heavier nuclei, with large differences in the number of constituent protons and neutrons, the neutron radius may extend significantly beyond that of the protons. However, these models do not agree on the extent to which the neutron distribution extends past the proton distribution, and as such a measurement of the neutron r.m.s. radius can be used as a constraint on models of dense nuclear matter, ranging from models of heavy nuclei to those of neutron stars.

Of the many possible avenues to measure the r.m.s. neutron radius $\sqrt{\langle r_n^2 \rangle}$, Donnelly, Dubach and Sick showed that a measurement of parity violating electron scattering from heavy nuclei allows for measurement of the weak charge density[4], directly related to the neutron density. The Lead (Pb) Radius Experiment, PREX, extracted the weak charge distribution of ^{208}Pb by measuring the parity violating electron scattering of longitudinally polarized electrons off a ^{208}Pb target. Parity violation is inherent in weak interactions between particles. Via exchange of a short range boson, either the charged $W^{\pm}$ or the uncharged Z^0, the weak interaction between the electrons and the weak charge associated with the neutron allows electrons to be used as a probe of the neutron distribution in the nucleus. As predicted by Yang and Lee [5] and experimentally measured by C. S. Wu et. al. [6], the weak force violates parity, and therefore, unlike the electromagnetic interaction, the weak interaction depends on the spin of the particles. Since only the weak interaction is spin dependent, parity-violating scattering experiments measure the scattering dependence on spin state to extract information on the weak interaction, in this case measuring the dominant weak interaction between the electron beam and the neutron distribution of ^{208}Pb.

The PREX experiment ran at the Thomas Jefferson National Laboratory in 2010 using a longitudinally polarized electron beam. The facilities at Jefferson Laboratory are capable of

providing a 190 μA beam of electrons, with energies up to 6 GeV, with longitudinal electron polarization between 85% and 90%. The Jefferson Lab electron source is able to flip the electron spin at a rate on the order of 10's of Hz. With the capability to quickly change the spin of the electron, the Jefferson Lab facility can emulate a parity transformation, essential to measuring parity violating electron scattering. In lieu of performing a parity transformation, which changes the spatial orientation while leaving this spin unchanged, the Jefferson Lab apparatus performs an effective parity transformation, changing the electron spin while leaving the spatial orientation fixed. Data on the flux of electrons scattering elastically from the target for each electron spin state was collected using detectors assembled at the University of Massachusetts-Amherst in collaboration with Smith College.

CHAPTER 2

THEORY AND MOTIVATIONS

2.1   Electron-Nucleus Scattering via Photon Exchange

2.1.1   Electron Scattering Formalism

One of the traditional methods of probing the nature of the nucleus is scattering electrons from the target material and mapping the distribution of scattered particles. The likelihood of the electron interacting with a particle in the nucleus is defined by the cross section σ. This cross section is dependent on kinematics, defined by the desired initial and final state, and the nature of the interaction described in terms of a scattering matrix element $\mathcal{M}$. The dominant interaction measured by electrons scattering from a nucleus is the electromagnetic scattering of electrons from the nuclear charge distribution via photon exchange. A free Dirac particle is defined in terms of momentum p and spinor $u\,(p)$ as

$$\psi = u(p)\mathrm{e}^{-\mathrm{ip\cdot x}} \tag{2.1}$$

For an electromagnetic interaction between two Dirac particles, with particles 1 and 2 each having initial and final spinors u_i and u_f, the matrix element $\mathcal{M}$ is

$$\mathcal{M} = (-ie\bar{u}_{f,2}\gamma^{\mu}u_{i,2})\,\frac{-ig_{\mu\nu}}{q^2}\,(-ie\bar{u}_{f,1}\gamma^{\nu}u_{i,1}) \tag{2.2}$$

The two particles interact via a photon with internal propagator $\frac{-ig_{\mu\nu}}{q^2}$. The four-momentum transfer q^2 is the change in momentum between the initial and final states, which in the case of elastic scattering is a function of the energy and scattering angle. Therefore, we can define q^2 as

$$q^2 = -Q^2 = (p_f - p_i)^2 = 2E^2 - 2\,(\vec{p_f}\cdot\vec{p_i}) = 2E^2(1 - cos\theta) \tag{2.3}$$

4

Each particle in an interaction has an associated current j_μ describing the changes the particle undergoes in the interaction. The current for each particle, with a initial particle spinor u_i transitioning to final spinor u_f, is given by

$$j_\mu^{fi} = -e\bar{\psi}_f\gamma^\mu\psi_i = -e\bar{u}\left(p_f\right)\gamma^\mu u\left(p_i\right)\mathrm{e}^{\mathrm{i}(\mathrm{p_f}-\mathrm{p_i})\cdot\mathrm{x}} \tag{2.4}$$

The matrix element describes the physical process in the cross section, which is defined as

$$d\sigma = \frac{\left|\mathcal{M}\right|^2}{F}dQ \tag{2.5}$$

for incident flux F and integration factor dQ, which contains a δ function and differential momentum volumes. The inclusion of dQ indicates the differential cross section includes some subset of the possible final particle momenta while obeying energy conservation. The probability of a given interaction occurring is dependent on the interaction's matrix element, normalized by the flux F of incident particles, and requires that energy be conserved. For a discussion of PREX, we will focus on the Mott cross section, which describes a massless electron scattering off a spin-0, point-like particle with a total charge Ze. This equation, for fine structure constant $\alpha = \frac{e^2}{4\pi} \simeq \frac{1}{137}$, scattering angle θ, and scattered electron energy E′, is

$$\left(\frac{d\sigma}{d\Omega}\right)_{\mathrm{Mott}} = \frac{4\alpha^2\mathrm{Z}^2(\mathrm{hc})^2\mathrm{E'}^2}{|\mathrm{qc}|^4}\cos^2\frac{\theta}{2} \tag{2.6}$$

Our choice of target nuclei allows for the simplicity of using the Mott cross section. The full, spin dependent electromagnetic cross section includes an additional $\sin^2\theta$ term, which we can neglect by selecting a spinless target particle. In the case of PREX, the experimental design results in measuring the scattering of electrons from the nucleus of a ^{208}Pb atom, which has closed shells for both the neutrons and protons (a feature known as "doubly magic") and therefore has a total spin of 0. From this discussion, we have a mathematical rubric for scattering an electron from a point-like distribution. However, for discussions of scattering from nuclei, we must introduce the second component of such a cross section, the form factor.

2.1.2   Form Factors

While the Mott cross section is a complete description of a spinless, point-like charged particle's photon exchange with a massless spin-$\frac{1}{2}$ particle, we must include an additional

term in our cross section to account for the finite size of a nucleus. The proton form factor $F_p(Q^2)$, which we can use interchangeably with the form factor for electric charge, provides a description of the extended distribution of electric charge contained in the nucleus. For values of Q^2 of ≈ 0.009 GeV^2, the order of Q^2 for the PREX measurement, the wavelength of the virtual photon is approximately 10^{-5} nm, on the order of a nucleus's radius. This allows a particle scattering at the given Q^2 to probe the size of the nuclear charge distribution. With the form factor to describe the nuclear charge distribution, the cross section for an electron scattering elastically from a spin-0 nucleus is given by

$$\frac{d\sigma}{d\Omega} = \left(\frac{d\sigma}{d\Omega}\right)_{\text{Mott}} \left|F_p\left(Q^2\right)\right|^2 \tag{2.7}$$

The elastic form factor does not include features relating to each constituent quark in the nucleus, instead simply describing the density of electric charge. For a static charge distribution (such as a stationary nucleus), we can show by via substitution of $A^\mu = (\phi, \vec{0})$ that the form factor for an electron scattering elastically is the Fourier transform of the charge distribution,

$$F_p(Q^2) = \int Z\rho\left(x\right) e^{-i q \cdot x} d^3 x \tag{2.8}$$

for the proton density $\rho(r)$ and total nuclear charge Z. This density ρ is defined as the probability for the existence of a proton at a given radius, and is normalized to 1

$$1 = \int \rho\left(x\right) d^3 x \tag{2.9}$$

At low values of $|q|$ we can expand Eq. 2.8 for q as

$$F_p(q) = \int \left(1 + iq \cdot x - \frac{(q \cdot x)^2}{2} + ...\right) \rho(x) d^3 x \tag{2.10}$$

From this expansion at low q, we see that the average radius of the density $\langle r^2 \rangle$ is given by

$$\langle r^2 \rangle = -6\hbar^2 \left. \frac{dF_p\left(Q^2\right)}{dQ^2} \right|_{Q^2=0} \tag{2.11}$$

This provides a link between the radius of a charge distribution for a nucleus and the scattering cross section. Measurements of the charge density of ^{208}Pb have been performed with the scattering of an electron via photon exchange, finding that the protons in the nucleus

have a form factor as predicted by a Fourier transform of a diffuse sphere[3], as shown in Fig. 2.1. However, the scattering of electrons is dominated by the photon exchange between charged particles, and is therefore sensitive to only protons and not neutrons.

2.2   Electron-Nucleus Scattering via Z^0 Exchange

In addition to the electromagnetic interaction between charged particles there is a contribution to elastic scattering from the weak force. The weak force was first predicted by Yang and Lee[5] as a solution to the τ^+-Θ^+ puzzle, with the solution being an interaction between particles that violates parity. This weak interaction was measured by C.S. Wu et. al. in decays of ^{60}Co, showing the existence of a parity-violating interaction[6].

Parity-violation is defined as an interaction that is not symmetric under the parity transformation. The parity transformation is a spatial inversion, with the transformation (x,y,z)→(-x,-y,-z). This transformation alters the overall signs of pseudoscalars and vectors, such as momentum, while leaving scalars and axial vectors, like spin, unchanged. While the electromagnetic interaction conserves parity (such that an interaction and it's spatially-inverted equivalent are the same) it has been shown the weak interaction does not.

Studies beyond the evidence of C.S. Wu describe the weak force as mediated by the charged $W^\pm$ or uncharged Z^0 bosons. This force is weaker than the electromagnetic force (as characterized by weak constant $G_F \simeq 1.1 \times 10^{-5} \ll \alpha$) but occurs between all particles. The uncharged weak boson Z^0 and the uncharged photon arise from a mixing of the electromagnetic and weak forces, with the contribution of each force to the resulting mediator quantified by the weak mixing angle θ_W, which has been measured as $\sin^2\theta_W \approx 0.23$. The Z^0 allows electrons to interact with neutrons in our fixed target, providing some handle on the neutron content. This force also allows Z^0 exchange between the electron and proton, but the weak charge of the proton, $1 - 4\sin^2(\theta_W) \simeq 0.08$ is smaller than the weak charge of the neutron, with the neutron's weak charge of -1, and as such is not the dominant weak interaction.

As a relevant aside, it is important to note that in the Dirac equation, angular momentum is not a conserved quantity. Instead, we recognize that an operator that commutes with both our Hamiltonian and momentum operators is the operator $\sum \cdot \hat{p}$, defined as

$$\frac{\sum \cdot p}{|p|} = \begin{pmatrix} \sigma \cdot p & 0 \\ 0 & \sigma \cdot p \end{pmatrix} \tag{2.12}$$
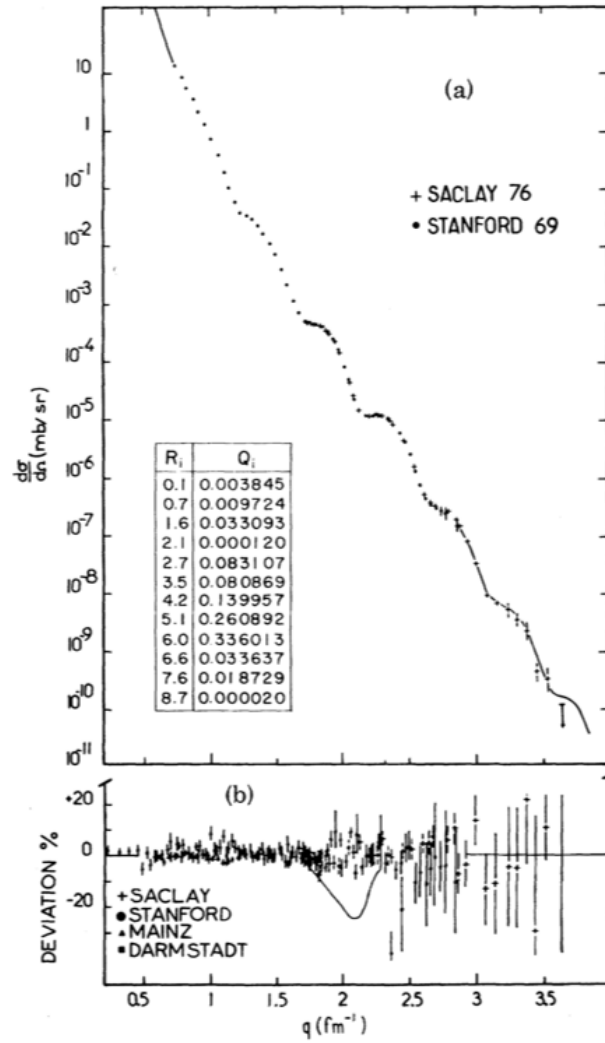
Figure 2.1: From Frois et. al.[3], a plot of the scattering of 502 MeV electrons from a ^{208}Pb target from data taken at the Stanford Linear Accelerator (SLAC) and at Saclay. This shows that the cross section, as a function of four-momentum transfer, follows the behavior predicted by the charge form factor with respect to Q^2.

This operator defines the helicity, or the projection of spin along momentum. This projection can be either positive or negative, with the positive quantity describing a left-handed particle (such as a neutrino) where a negative value describes a right-handed particle (such as the anti-neutrino). As it commutes with H and the momentum operator $P = -i\nabla$, it is also measurable and conserved.

For a purely weak interaction, such as those between neutrinos or involving the change of charge, the weak current is given by

$$j^\mu (f \rightarrow f') = \bar{u} (f') \gamma^\mu \frac{1}{2} (1 - \gamma^5) u (f) \tag{2.13}$$

for $\gamma^5 = \gamma^0 \gamma^1 \gamma^2 \gamma^3$. The weak bosons couple only to left handed particles, which is reflected by the additional term $(1 - \gamma^5)$ in Eq. 2.13 when compared to Eq. 2.4, the comparable purely EM current. The $\frac{1}{2} (1 - \gamma^5)$ composes the left-handed parity operator P_L (where $\frac{1}{2} (1 + \gamma^5)$ is the right-handed parity operator P_R). The eigenvalues of these operators are ± 1, for when the handedness of the parity operator and helicity match, or zero, such that

$$\frac{1}{2} (1 - \gamma^5) u_L = u_L; \frac{1}{2} (1 + \gamma^5) u_L = 0 \tag{2.14}$$

for left-handed spinors u_L, with this working similarly for right handed spinors u_R. As previously stated, in the case of the neutral current, there will be a coupling to the Z^0 and the photon. These couplings can be written as a vector coupling term, g_V, which is associated with the vector electromagnetic component, and a separate, helicity dependent axial coupling g_A. In this case, the neutral current is

$$j^\mu (f) = \bar{u} (f) \left[-ig\gamma^\mu \frac{1}{2} \left(c_V^f - \gamma^5 c_A^f \right) \right] u (f) \tag{2.15}$$

From this, we can construct a scattering matrix element $\mathcal{M}$ (which defines the transition amplitude) by

$$\mathcal{M} = \frac{G_F}{2} j_{n,p}^\mu \frac{g^{\mu\nu}}{M_Z^2 + q^2} j_{\nu e^-} \tag{2.16}$$

for nucleon current $j_{n,p}^\mu$ and electron current $j_{\nu e^-}$, with the weak propagator as the inverse of the sum of Z^0 mass squared and four momentum transfer q^2. From the inclusion of the γ^5 in the current, an electron scattering from a nucleon will see a helicity-dependent scattering potential associated with the axial coupling. Using this matrix element $\mathcal{M}$, we can construct a cross section analogous to the approach given for electromagnetic scattering, but in this

9

case the cross section has a helicity dependence. In the case of PREX, the axial potential is dependent on only the spin of the electrons, as the target is unpolarized and therefore we must average over the effects of the spin of the nucleon in the ^{208}Pb nucleus.

Following similar arguments from Sec. 2.1.2, we include a weak form factor in our scattering to model the effects of the nonzero radius of the nucleus. For the weak form factor we can, similar to the description of the charge density $\rho(r)$ in Eq. 2.9, define the weak charge Q_W, analogous to the electric charge $+Ze$ for Z protons but composed of the weak charges of both neutrons and protons, and weak charge density $\rho_W(r)$, which has been normalized to 1, as

$$Q_W = \int Q_W \rho_W(x) \, d^3x = \int \left(1 - 4\sin^2(\theta_W)\right) Z\rho_p(x) - N\rho_n(x) \, d^3x \qquad (2.17)$$

where the total weak charge and density are functions of the proton and neutron densities ρ_p and ρ_N, the number of each nucleon (Z,N) and the weak charge of those nucleons. We can then use this weak density to construct a weak form factor

$$F_W\left(Q^2\right) = \int e^{-iq\cdot x}\rho_W(x) \, d^3x = \int e^{-iq\cdot x}\left[\left(1 - 4\sin^2(\theta_W)\right)\rho_p(x) - \rho_n(x)\right] d^3x \qquad (2.18)$$

Note that the proton's contribution to the weak form factor has the same structure as it's contribution to the electromagnetic form factor from Eq. 2.8, as the Fourier transform of its density multiplied by the proton's weak charge of $(1 - 4\sin^2\theta_W)$. Using this weak form factor, we can calculate the cross section.

2.3   Parity Violating Asymmetry

The dependence of the cross section on spin relates to the parity violation of the weak force. As such, we can measure the difference in cross sections between a scattering and the parity-transformed scattering to isolate the contribution from the weak force. By measuring the difference in cross sections between spin states, we can measure an effective parity transform, with momenta fixed but spins inverted. This is equivalent to a parity transformation, where the vectors for particle momenta would be inverted and the axial vector spin would be fixed, such that the effective parity transformation measures the same parity-violating correlation between momenta and spin. With this information, for a left- or right-handed electron scattering with cross section σ_L and σ_R respectively, we can write the cross section as a

function of the four momentum transfer Q, particle flux F, and the electromagnetic and weak cross sections

$$\frac{d\sigma^{L,R}}{d\Omega} = \frac{dQ}{F} \left| \mathcal{M}_Z^{L,R} + \mathcal{M}_\gamma \right|^2,$$ (2.19)

a modification of Eq. 2.5 that combines the effects of γ exchange matrix element $\mathcal{M}_\gamma$ and Z^0 matrix elements for left- and right-handed electrons $\mathcal{M}_Z^L$ and $\mathcal{M}_Z^R$, respectively. The γ^5 matrix in the current results in $\mathcal{M}_Z^L = -\mathcal{M}_Z^R$, separating the spin dependent elements from the photon exchange element $\mathcal{M}_\gamma$. As the photon exchange matrix element is larger than that of the Z^0 by a factor of $\frac{\alpha}{G_F}$, the ratio of coupling constants, the photon's matrix element dominates the cross section. To see the effect of the Z^0 scattering, we can take the asymmetry between these cross sections

$$A_{PV} = \frac{\frac{d\sigma_L}{d\Omega} - \frac{d\sigma_R}{d\Omega}}{\frac{d\sigma_L}{d\Omega} + \frac{d\sigma_R}{d\Omega}}$$ (2.20)

or, after substituting the cross sections from Eq. 2.19,

$$A_{PV} \approx \frac{\left[\mathcal{M}_\gamma^2 + 2\mathcal{M}_Z\mathcal{M}_\gamma + \mathcal{M}_Z^2\right] - \left[\mathcal{M}_\gamma^2 - 2\mathcal{M}_Z\mathcal{M}_\gamma + \mathcal{M}_Z^2\right]}{\left[\mathcal{M}_\gamma^2 + 2\mathcal{M}_Z\mathcal{M}_\gamma + \mathcal{M}_Z^2\right] + \left[\mathcal{M}_\gamma^2 - 2\mathcal{M}_Z\mathcal{M}_\gamma + \mathcal{M}_Z^2\right]} = \frac{2\mathcal{M}_Z\mathcal{M}_\gamma}{\mathcal{M}_\gamma^2}$$ (2.21)

The scattering from the vector potential is not helicity dependent, and thus taking the difference between $\frac{d\sigma_L}{d\Omega}$ and $\frac{d\sigma_R}{d\Omega}$ will cancel that electromagnetic component, leaving the helicity-dependent $\gamma - Z^0$ interference term as the dominant element. In the Born approximation, this gives the result

$$A_{PV} = \frac{-G_F Q^2}{4\pi\alpha\sqrt{2}} \frac{F_W(Q^2)}{F_p(Q^2)}$$ (2.22)

for proton form factor F_p as the electromagnetic form factor in Eq. 2.8 and weak form factor F_W from Eq. 2.18. Separating the weak form factors of the neutron and proton (and recognizing that the form factor for the protons is identical to the electric charge form factor), we can rewrite Eq. 2.22 like

$$A_{PV} = \frac{G_F Q^2}{4\pi\alpha\sqrt{2}} \left[4\sin^2(\theta_W) - 1 + \frac{F_n(Q^2)}{F_p(Q^2)} \right]$$ (2.23)

This result directly connects a measurable quantity, the scattering asymmetry between left- and right-handed electrons, and the neutron form factor $F_n(Q^2)$, with all other factors,

11

G_F, Q^2, α and electric charge form factor F_p determined or measured. From a parity violating asymmetry measurement, the extraction of F_n allows us to calculate the neutron root mean square radius $\sqrt{\langle r_n^2 \rangle} = \frac{5}{3}$ R_n as shown in Eq. 2.11.

2.3.1 Kinematic Optimization

As the parity-violating asymmetry A_PV, from Eq. 2.23, depends on the four momentum transfer Q^2 a measurement such as PREX needs be designed for a given Q^2 in order to optimize the measured results. This optimization finds a Q^2 which can measure the neutron r.m.s. radius R_n to within 1% in the minimal amount of time given the mechanical constraints of the Jefferson Laboratory equipment as designed. We optimize this by maximizing the figure of merit (FOM), which is defined as

$$FOM = A^2 \sigma \varepsilon^2 \tag{2.24}$$

for sensitivity ε. The cross section σ decreases at larger four momentum transfer q, reflecting the decreased probability of a scattering occurring. However, the magnitude of the asymmetry increases at higher angles. These inverse dependencies on four momentum transfer q require selecting a q such that the scattering rate for electrons, proportional to the cross section, is large enough to accrue the statistics required and that the size of the asymmetry between helicity states, given by the asymmetry, is measurably large. The additional factor is the sensitivity ε, which quantifies the ability to resolve the mean neutron radius to 1% for a given asymmetry measurement. The sensitivity ε is defined as $\frac{dA}{A}$, where dA is the difference between the asymmetry for a given mean radius R_n and the asymmetry for a 1% increase in R_n[7]. The cross section, asymmetry, and ε are plotted in Fig. 2.2.

Fig. 2.2 shows that for low Q^2 the cross section and asymmetry are somewhat linear, though near $q \approx 0.4$ fm^{-1} the slope of the asymmetry decreases while cross section does not, suggesting that a Q^2 for $q < 0.6$ fm^{-1} is preferable. The bottom right plot of Fig. 2.2 shows the figure of merit as a function of electron energy E and scattering angle θ, the components of Q^2. For the Jefferson Laboratory apparatus, addressed in detail in Chapter 3, the electrons reaching the detectors scatter at a minimum θ of 6° with incident energy E of 0.8 GeV, providing additional constraints on Q^2. This minimum scattering angle of $\theta = 6°$ appears as the lower bound of the lower right plot in Fig. 2.2, where we note that while the figure of merit will increase below 6° we are limited by our apparatus in our ability to measure at
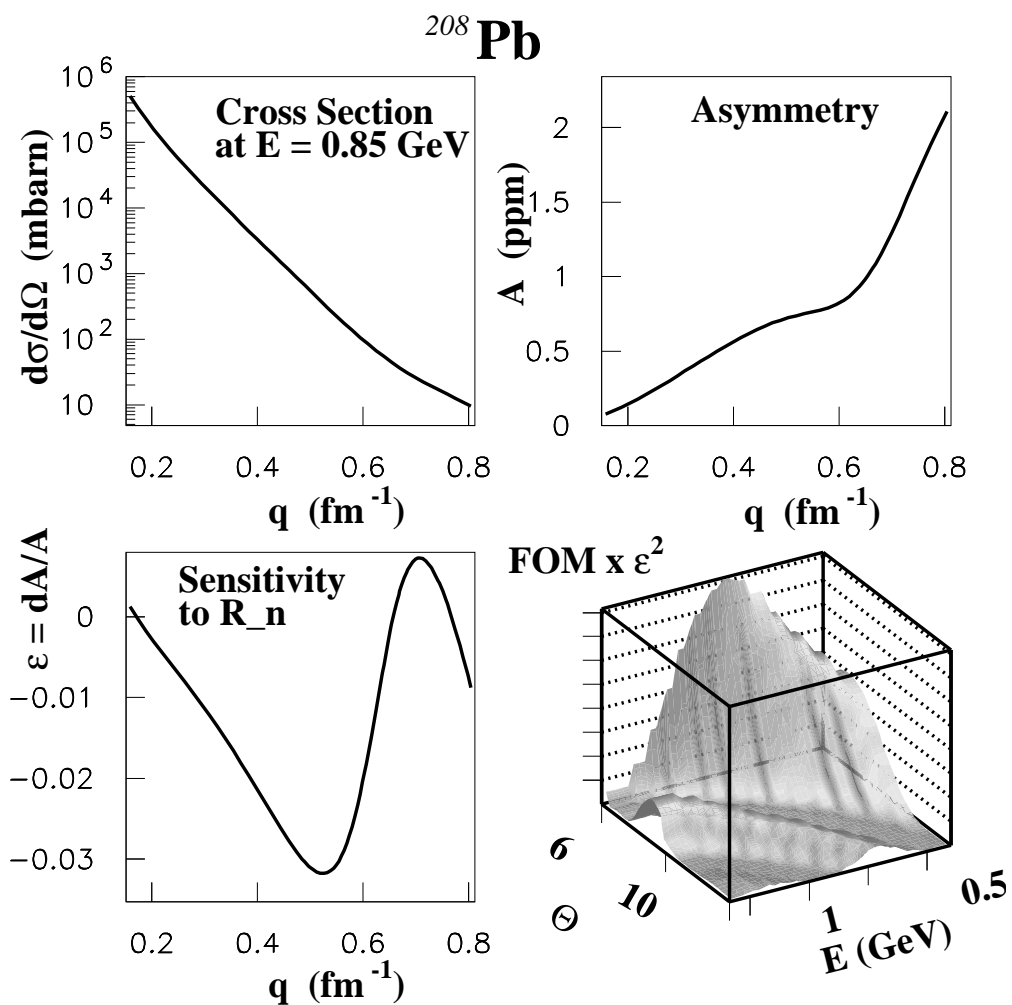
Figure 2.2: From C. Horowitz et. al.[7], plots of the asymmetry (upper left), cross section (upper right), and sensitivity ε (lower left) to R_n as a function of q for a 0.85 GeV beam. The bottom right shows the figure of merit as a function of scattering angle and electron energy.

13

that angle.

2.4   Applications of R_n

Models of the ^{208}Pb nucleus predict the neutron distribution will have a larger radius than that of the protons, with the purely neutron matter around the mixed proton-neutron core referred to as the 'neutron skin'. From a measurement of the neutron radius $\sqrt{\langle r_n^2 \rangle}$ we can calculate the thickness of this neutron skin R_{np} as $R_{np} = \sqrt{\langle r_n^2 \rangle} - \sqrt{\langle r_p^2 \rangle}$. The measurement of the skin thickness of a neutron-rich nucleus like ^{208}Pb provides constraints on our understanding of the behavior of dense baryonic matter. There are as-of-yet no facilities that are able to create exotic, neutron rich matter in a stable manner, which would allow in-situ studies of matter similar to that in neutron stars. However, as studied by B. A. Brown[8], we can use models to approximate the behavior of neutron stars using experimental inputs from measurements of dense nuclei like ^{208}Pb. The uncertainties in these models are associated with the symmetry energy, an effect associated with different numbers of protons and neutrons present.

2.4.1   Symmetry Energy

Baryonic matter self-assembles into a state that minimizes energy. The binding energy, the difference between the energy of the nucleus and the energy of an equivalent number of free nucleons, is in general dependent on the number of nucleons present, A. However, the symmetry energy is dependent on the number of neutrons relative to the number of protons, not the number of nucleons present. This symmetry energy describes the energy cost of having unequal numbers of protons and neutrons, quantifying the cost of having dissimilar numbers and balancing the forces applied. This energy increases with the difference in the number of neutrons N and protons Z. This energy exists in competition with the Coulomb energy (associated with the charge of the protons) and the Fermi energy (increasing for filled nucleon shells), representing the changes in energy associated with having different collections of protons and neutrons that still sum to total nucleon number A. It can be shown that, in the case of nuclei with more neutrons than protons, the existence of a neutron skin, with thickness R_{np}, provides a viable handle to address this energy difference. To describe the binding energy of the ^{208}Pb nucleus, we can write the energy for N neutrons and Z protons, with atomic number $A = N + Z$ using the Bethe-Weizsäcker semi-empirical mass formula

(SEMF), or Liquid Drop Formula (and improved upon by Myers and Swiatecki in their Droplet Model[9]). This gives the binding energy B of any nucleus as

$$B(A, Z, N) = a_v A - a_s A^{2/3} - a_C \frac{Z^2}{A^{1/3}} + a_p \frac{\delta}{A^{1/2}} + a_a \frac{(N-Z)^2}{A} \qquad (2.25)$$

in terms of atomic number A, with Z protons and N neutrons. This equation features a volume term with coefficient a_v and a surface term with a_s, as expected for the discussion of a nucleus with volume and surface. To account for the charge of the protons in the nucleus, we add a Coulomb energy term dependent on the number of protons and coefficient a_C. The pairing energy, with coefficient a_p, depends on the pairing of protons or neutrons, with $2\delta = (-1)^N + (-1)^Z$.

The last term, dependent on coefficient a_a, describes the symmetry energy relative to the asymmetry in neutrons and protons. We are concerned about the energy per nucleon, ε, which for a generalized baryon ensemble would be described by the density ρ. As only one term in the binding energy depends on the $N - Z$ asymmetry, we can write the energy density as

$$\varepsilon(\rho) = \frac{B(\rho, \eta)}{A} = \frac{B(\rho, \eta = 0)}{A} + S(\rho)\eta^2 \qquad (2.26)$$

with binding energy B expressed as a function of density ρ and nucleon asymmetry $\eta = \frac{N-Z}{A}$. This form separates the terms in the binding energy dependent only on the number of nucleons A to isolate the asymmetry energy per nucleon, given by asymmetry η^2 and symmetry energy coefficient $S(\rho)$, which depends on the density of nucleons.

This coefficient S(ρ), from calculations by Myers and Swiatecki[9], is maximized at the saturation density $\rho_0 = 0.016$ fm^{-3}, the density of a proton as calculated from it's mass and the empirically determined mass-radius constant $r_0 \approx 1.2 \frac{fm}{nucleons}$. Expanding S around saturation density ρ_0 gives

$$S(\rho) = S_0 + \frac{L}{3} \frac{\rho - \rho_0}{\rho_0} + \frac{K}{18} \left(\frac{\rho - \rho_0}{\rho_0} \right)^2 \qquad (2.27)$$

for symmetry energy slope L and curvature K. The constant S_0, via calculations and measurements, is fit from various known atomic masses at 32.5 MeV [9] by the Droplet Model, though the slopes L and K are not. Information about the symmetry energy slope L can be found from measurements of the symmetry energy, via

$$L = \frac{3}{\rho} \left. \frac{\partial S}{\partial \rho} \right|_{\rho_0} \tag{2.28}$$

Knowledge of L is an important component of building models of other baryonic matter.

2.4.2 Constraining Models

Parameters from the neutron distribution in ^{208}Pb, such as neutron skin thickness and the slope of the symmetry energy L, are important inputs to models of baryonic matter. Models such as relativistic mean field theory and the Skyrme model each try to define the behavior of nucleons in a nucleus. From these models, the relativistic mean field theory predicts the neutron skin thickness $R_{np} \approx 0.3$ fm, while the Skyrme model predicts a skin of 0.1 fm, with the discrepancies coming from the weak constraints on the symmetry energy S and its slope L[7].

The Skyrme and Gogny models rely on describing the baryonic behavior in terms of two nucleon (NN) and three nucleon (3N) zero-range forces. To approximate zero-range forces, these models use density to describe the locations of the nucleons. The Skyrme model, defined by T. H. Skyrme [10] and refined by Vautherin and Brink[11], describes NN interactions as central and non-local interactions by isospin exchange operators. To parametrize the 3N interactions, it claims the three body interaction can be described as a density-dependent two-body force. While this works well for low-density matter, the parameters governing the contributions of this 3N force are poorly constrained by the atomic information that constrains the rest of the model. Constraints to the Skyrme model can be applied in many ways to try to narrow the range of valid parameters, including pinning down the neutron equation of state, dependent on the neutron skin of ^{208}Pb[8]. This dependence on the neutron skin, here defined as "S(208Pb)", is shown in Fig. 2.3 as a function of the slope of the neutron equation of state for various Skyrme parametrizations.

Alternatively, one can use mean field theories to try to approximate nucleon behavior. Mean field theories attempt to build a complete Hamiltonian for baryon and light meson interactions that may affect any individual particle, then model the behavior from that Hamiltonian. In this case, the baryon and scalar densities are treated as the wave functions of these Hamiltonians, which are then fit to minimize the energy associated with that baryonic bound state, as well as inputs for source terms[12]. For mean field models, as well as the Skyrme case, constraints on the nuclear density from ^{208}Pb will constrain the possible
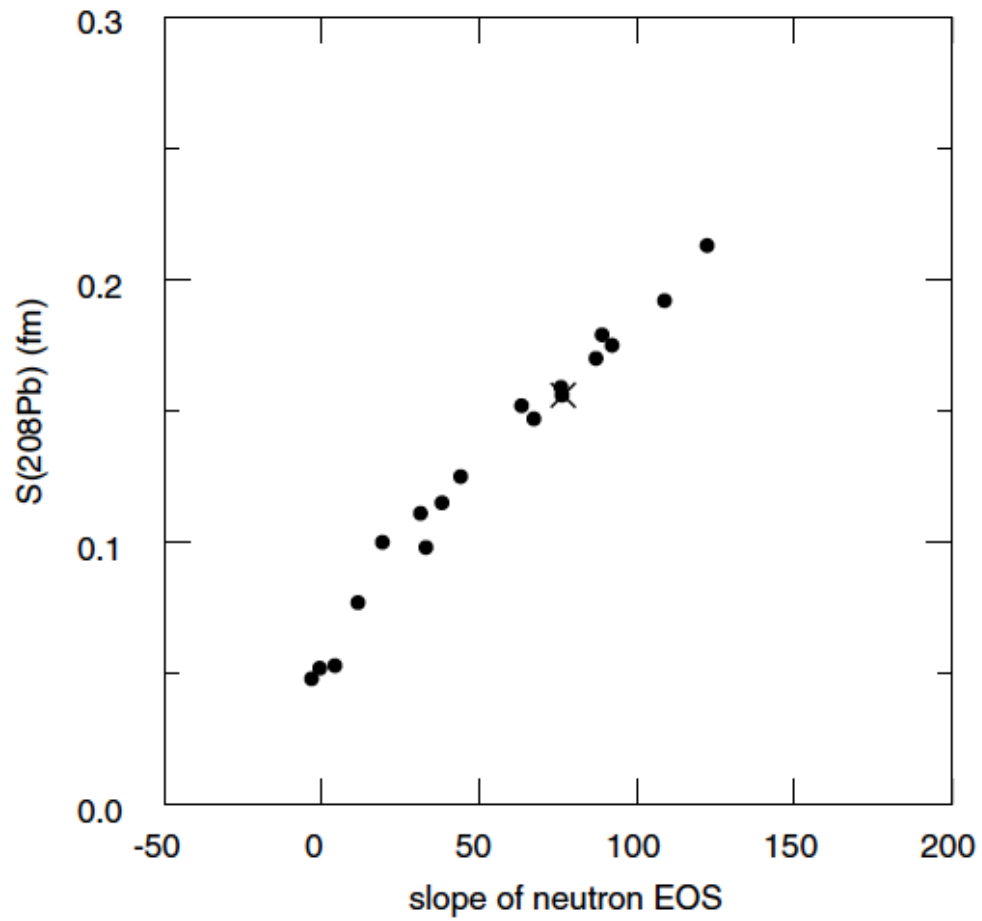
Figure 2.3: From B.A. Brown[8], the neutron skin thickness, here denoted as S, as a function of slope L of neutron equation of state for various Skyrme models.
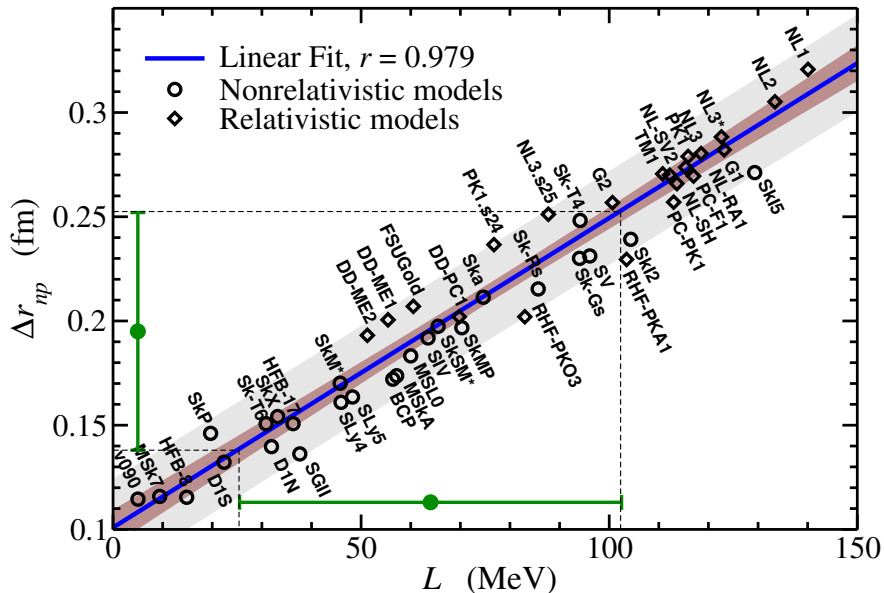
Figure 2.4: From Roca-Maza et. al.[13], a plot highlighting the linear correlation between the ^{208}Pb neutron skin thickness and slope of the symmetry energy L, with points for the predicted values from mean field and Skyrme models. The green points show the neutron skin R_{np} (here presented as Δr_{np}) and L for an asymmetry of 715 ppm with 3% error.

densities allowed for other types of baryonic matter. From measurements of this skin, we can pin down acceptable symmetry slopes L.

These models agree on the relationship between L and skin thickness, the predicted values have a range that can be narrowed with measurements of this skin. Viñas, Centelles, Roca-Maza and Warda[13] show in their work that this correlation is not coincidental, but can be exactly calculated, with a linear relationship between the skin and L, as shown in Fig. 2.4. From this result, as well as predictions from models, we know that a skin thickness measurement, such as PREX was designed to make, can access this slope of symmetry energy. An improved understanding of the symmetry slope L allows for more accurate modeling of the structure of other baryonic, neutron rich matter, such as neutron stars.

2.4.3 Neutron Star Structure

Neutron stars, as massive stellar objects, are comprised of baryons (protons, neutrons) and leptons (electrons, muons). The relatively low density surface forms a crust, which behaves similar to terrestrial matter. However, in the core of the neutron star matter may be more exotic, as the protons and electrons decrease their Fermi energy by reverse β decay into neutrons[14]. As the density of neutrons increases, the neutron star becomes a dense, pre-

dominantly neutron volume towards the core. As creating similarly dense, neutron rich matter stably in a laboratory environment would be challenging, methods of analyzing the behavior of the more dense, inner layers of the neutron star rely on indirect calculations.

The symmetry energy slope L, as introduced in Sec. 2.4.1, can be used to constrain the behavior of neutron stars. As the core of a neutron star is dense and dominated by neutrons, the symmetry energy is a large component of the total energy density per nucleon ε. As the neutron star is a complex balance of a massive ensemble and quantum forces, the behavior of a neutron star can be approached via studies of the relation between pressure and energy density, given by

$$P = \rho^2 \frac{\partial \varepsilon}{\partial \rho} \tag{2.29}$$

where the pressure P is defined by the density of matter ρ and energy ε of the neutron star. This pressure, arising from Pauli exclusion, opposes the attractive gravitational force associated with the massive ensemble, with the balance of the two defining the radius and mass of the star[15]. For a neutron star in β decay equilibrium at saturation density ρ_0, this can simplify to[16]

$$P(\rho_0) \approx \frac{\rho_0}{3}L + 0.048\rho_0 \left(\frac{S_0}{30}\right)^3 \left(S_0 - \frac{4}{3}L\right) \tag{2.30}$$

The radius depends on this slope L by[16]

$$R \approx \frac{C(M, \rho_0)}{2} L^{0.25} \tag{2.31}$$

for a constant $C(M, \rho_0)$, a constant describing the predicted neutron star mass at saturation density found from numerical fits to many models[17]. Plotted for a neutron star with a mass of 1.4 solar masses (1.4M⊙), Fig. 2.5 shows the correlation between the neutron skin thickness and the neutron star size, for their shared dependence on L for a collection of models. The neutron star's mass also can be related to the pressure defined in Eq. 2.29[18]. The neutron star is in hydrostatic equilibrium, which, according to general relativity, is given by

$$\frac{dp(r)}{dr} = \frac{G}{c^2} \frac{[p(r) + \rho(r)c^2][M(r) + 4\pi r^3 p(r)/c^2]}{r(r - 2GM(r)/c^2)}, \frac{dM(r)}{dr} = 4\pi^2 \rho(r) \tag{2.32}$$

stating that for gravitational constant G, the maximum neutron star mass is limited by the pressure P, density ρ, both of which are limited by the symmetry slope L. The limits on the
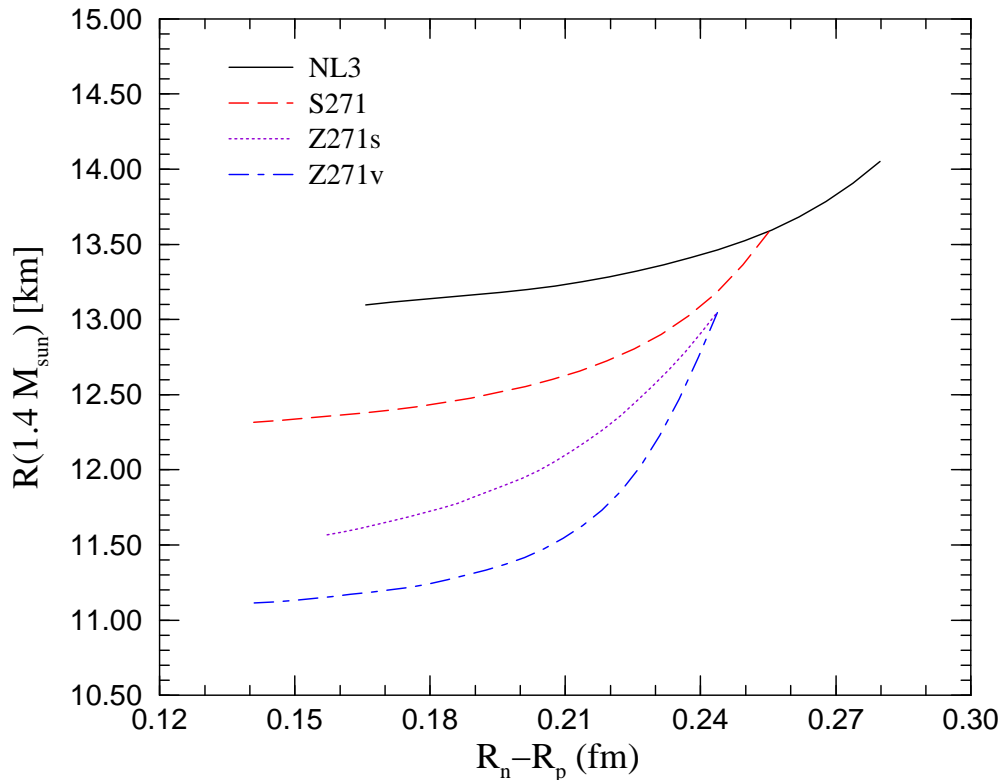
Figure 2.5: From Horowitz and Piekarewicz[19], curves for the relation between radius of a $1.4 M_\odot$ neutron star and the neutron skin thickness for various Skyrme models. Each model describes a different range of possible neutron star radii, based on neutron skin thicknesses allowed by each model.

mass and radius of a neutron star constrain the possible behavior of matter in the core of the neutron star. This leads to the possibility of more exotic behavior, such as modeled by Lattimer and Prakash for lighter, less dense stars[18][17].

The pressure-energy density relation, in combination with measurements of the mass and radii of neutron stars, provide constraints on models. The relation between radius and mass given by the symmetry-energy dependent pressure-energy density relation has been calculated for various models in an attempt to predict the range of sizes and masses of neutron stars, as shown in Fig. 2.6. Recently, measurements of heavier neutron stars have recently ruled out softer equations of state (with symmetry energy weakly dependent on density) based on the parameters of stars like J0348+0432[20] and J1614-2230[21]. These star are both $\approx 2 M_\odot$ objects, with masses calculated based on their rotations both axially and within the binary they rotate within, and require a larger energy cost associated with nucleon asymmetries, resulting in a more uniform density.
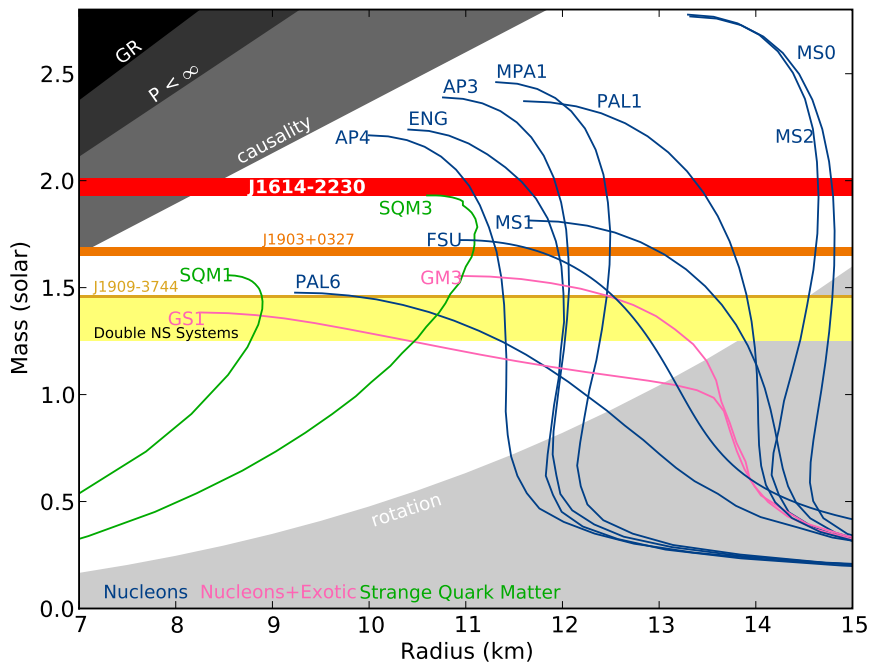
Figure 2.6: From Demorest et. al.[21], curves for the relation between mass and radius for a neutron star for various models. Recent measurements have ruled out models that do not allow $2M_\odot$ neutron stars.

2.4.4 Urca Cooling

Information from the ^{208}Pb radius can also provide insight into cooling processes for neutron stars. The density of the neutron star also relates to the rate of cooling. One method by which energy is removed from the neutron star is by emitted neutrinos[22], a process known as Urca cooling. As a neutron star is a dense material with a large neutron excess, the neutrons in the star will β decay via

$$n \to p + e^- + \bar{\nu}_e \tag{2.33}$$

Additionally, the free electrons will flavor change from electrons to muons via

$$e^- \to \mu^- + \nu^\mu + \bar{\nu}_e \tag{2.34}$$

Of the byproducts of these processes, the proton, electron, and muon will not leave the neutron star, given their interaction lengths in dense matter, but the neutrinos (with a longer interaction length) will escape and remove some energy from the system. These neutrino-emitting processes continue until the neutron star reaches an equilibrium state, such that

$$\mu_n - \mu_p = \mu_e = \mu_\mu \tag{2.35}$$

for the neutron, proton, electron and muon chemical potentials μ. These chemical potential $\mu_x = \frac{dF}{dN_x}$ represent the change in free energy F associated with changing the number of particles N to N±1. This statement implies that the free energy of the entire ensemble is at a minimum, with any additional proton and electron produced by β decay or muon from flavor change increasing the energy of the system. This cooling shows a direct impact of the symmetry energy, as the changing from neutron to proton will decrease the nucleon asymmetry and therefore the symmetry energy in the system.

Another dependence on the behavior of the nucleon asymmetry is the dependence on proton fraction $x = \frac{Z}{A}$ for the Z protons and A nucleons in the neutron star. To conserve momentum in the neutron star, the direct Urca process requires a high proton fraction[23]. The alternative cooling method is the modified Urca process, requiring a second nucleon to facilitate, with the decay as

$$(n, p) + n \to (n, p) + p + e^- + \bar{\nu}_e \tag{2.36}$$
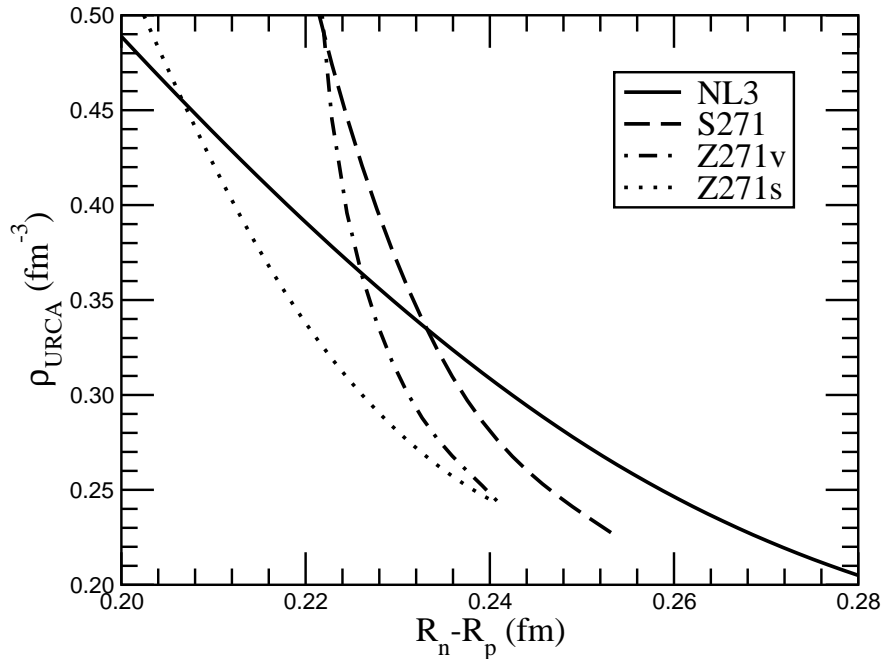
Figure 2.7: From Horowitz and Piekarewicz[22], the density direct Urca cooling occurs at as a function of neutron skin thickness for various mean-field models.

As the requirement for a second nucleon decreases the likelihood of the interaction, the energy removed from a neutron star via Urca cooling increases with larger proton fractions. The proton fraction in β-decay equilibrium will be dependent on the symmetry energy and the proton Fermi energy. This balance is equivalent to the condition[23]

$$\hbar c \left(3\pi^2 \rho_p\right)^{1/3} = 4S\left(\rho\right)\left(\frac{\rho_n - \rho_p}{\rho_n + \rho_p}\right) \tag{2.37}$$

where the total number of protons is limited by symmetry energy S associated with adding protons to the volume relative to the Fermi momentum required for a generated proton. As such, any improved understanding of the symmetry energy of dense matter will add constraints to models of Urca cooling. In Fig 2.7 for the mean field model NL3, and modifications S271 (fixing the symmetry curvature K at 271 MeV), Z271s and Z271v (the S271 model with fixed contributions from two added terms), Horowitz and Piekarewicz made calculation for the likelihood of Urca cooling based on symmetry energy effects. As shown, there is a direct, though model dependent, connection between neutron skin and ρ_{Urca}, the density with a proton fraction large enough to allow direct Urca cooling. Defining the neutron skin thickness will allow additional constraints to be placed on models for neutrino, or two nucleon-density (NNρ), interactions such as those found in Urca cooling.

23

2.5 PREX Design Goals

A measurement of the parity violating electron scattering asymmetry from the PREX experiment will contribute to all of the applications listed in Sec. 2.4. The asymmetry is predicted to be on the order of 10^{-7}. Based on ^{208}Pb skin thickness predictions of the mean field and Skyrme models, the design goal of the PREX experiment is a 1% error on the neutron r.m.s. radius $\sqrt{\langle r_n^2 \rangle}$[7]. A $\pm 1\%$ error in neutron skin thickness requires the measurement of the asymmetry accurate to $\pm 3\%$, with a design goal of $\pm 2\%$ systematic error[24].

CHAPTER 3

EXPERIMENTAL OVERVIEW

The PREX experiment, measuring the scattering asymmetry for longitudinally polarized electrons from a ^{208}Pb nucleus, ran at Thomas Jefferson National Laboratory (JLab) from March through June, 2010. Jefferson Lab's Continuous Electron Beam Accelerator Facility (CEBAF) provides an 85-90% polarized beam of up to 6 GeV electrons, with a current of up to 190 μA. The injector uses a strained gallium-arsenide crystal, designed to provide the 85-90% polarization and allows for the helicity flipping of the generated electrons at a rate of 120 Hz. These electrons are accelerated by the linear accelerator to our desired energy of 1 GeV before entering experimental Hall A, a cartoon of which is shown in Fig. 3.1. Electrons pass through the experimental hall, scattering from our ^{208}Pb target. The electrons scattering at the selected 5.5° angle pass through the high resolution spectrometer, transporting the elastically scattered electrons to the detector package. This detector package can be used to measure the position of the electrons entering the hall, correlated with the scattering parameters at the target, and the total flux of electrons in each helicity state scattering from our target, which we can use to calculate the helicity-correlated scattering asymmetry. Additionally, Hall A features a number of position, current, and polarization monitors to precisely determine the state of the beam before the electrons scatter from our ^{208}Pb target. The settings for beam energy and scattering angle for the PREX experiment are listed in Table 3.1.

25

E	1.0605 GeV
Current	50 μA / 70 μA
Central Angle θ	5.5°
Beam Polarization	88.2%
Helicity Flip Rate	120 Hz
Target Thickness	≈ 0.50 mm
Momentum Resolution	0.0011 GeV
Angular Acceptance	30 mrad. (horiz.)
	60 mrad. (vert.)
Angular Resolution	0.5 mrad. (horiz.)
	1.0 mrad. (vert.)

Table 3.1: List of beam & experiment parameters.
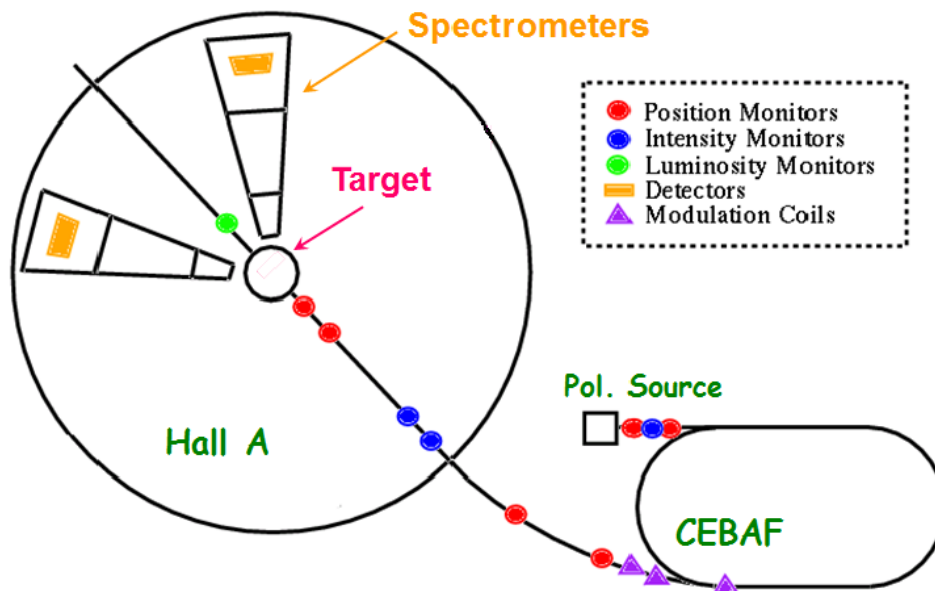
Figure 3.1: Cartoon of the layout of Hall A, the Jefferson Laboratory experimental hall in which the PREX experiment ran showing the beam monitors, polarimetry, spectrometers and detector package relative to the target in the hall.

3.1 Injector at Jefferson Lab

3.1.1 The Polarized Electron Source

The electron beam at Jefferson Lab is generated at the injector. The electrons are ejected from a strained gallium-arsenide (GaAs) crystal when struck with circularly polarized light. The ejected electron's spin orientation is dependent on the polarization of the incident photons, such that the beam helicity is defined by the seed laser's polarization. In order to provide independently controlled beams to the experimental halls, each hall has a separate laser set-up in the injector, shown in Fig. 3.2. Each hall's separate laser system is driven at 499 MHz so that, in combination with a beam chopper upstream of each hall, the beam for each hall is generated and delivered independently of the settings for other experimental halls [25]. The Hall A set-up uses a seed laser that is directed into an optical amplifier, which controls the intensity of the laser. The laser later passes through an attenuator, comprised of a linear polarizer and a half-wave plate. Photons are passed through a linear polarizer so as to be able to become circularly polarized by the Pockel cell located downstream of the half-wave plate. A Pockel cell is effectively a voltage-controlled birefringent retardation plate[26]. The voltage applied, approximately ± 2.8 kV[25], to the Pockel cell determines the outgoing circular polarization of the photons and, by extension, the electron beam helicity. As such, the Pockel cell is controlled by the helicity generator, which is designed to supply voltage that causes a $\pm \lambda/4$ retardation in the photon polarization at our desired flip rate. The half-wave plate, insertable remotely, alters the polarization of the photons by 90°, which reverses the direction of circular polarization and therefore the polarization of the generated electrons.

The outgoing photons from the Pockel cell are 99.9% circularly polarized. As polarizations are added in quadrature, it means there is a 1-2% linear polarization of the beam[25]. The linearly polarized component stems from the birefringence of apparatus elements upstream of the Pockel cell (such as vacuum windows). The linear component of the polarization, with orientation determined by the Pockel cell, will interact differently with all downstream components, creating a polarization-induced transport asymmetry (PITA) in the number of photons with each polarization. From these birefringent elements, we can parametrize the phase shift after the Pockel cell for left (δ_L) and right (δ_R) circular polarization by

27
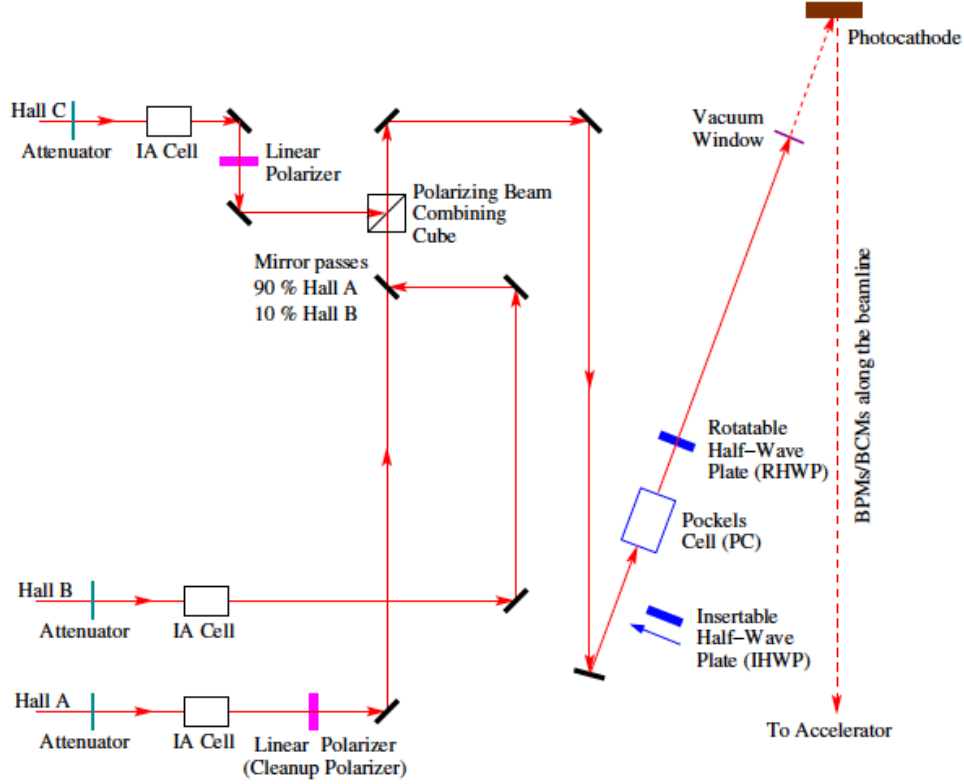
Figure 3.2: Schematic of the injector. Reproduced from R. Silwal[27].

$$\delta_L = + \left(\frac{\pi}{2} + \alpha\right) - \Delta; \ \delta_R = - \left(\frac{\pi}{2} + \alpha\right) - \Delta \tag{3.1}$$

for symmetric phase offset α and asymmetric offset Δ. The quantum efficiency of the strained GaAs crystal depends on the sign of the circular polarization, so an asymmetric correction produces an asymmetry in the number of electrons ejected between helicity states, which will create an asymmetry in our measurement not associated with the weak scattering PREX was designed to measure. To compensate for this, JLab uses a PITA feedback system, which measures the beam intensity in the experimental hall (using monitors described in Sec. 3.8) and calculates the asymmetry in intensity between helicity states over a 40 second period. The feedback system then changes the voltage sent to the Pockel cell in each state to minimize the asymmetry in intensity between left- and right-helicity electrons.

The significance of using a strained GaAs photocathode is that the strain separates the energy levels of the valence electrons[28]. In GaAs the valence band has a degenerate $p_{3/2}$ energy level. In an unstrained crystal, the band gap between the degenerate levels is small enough that a circularly polarized photon will promote an electron in either band to the

28
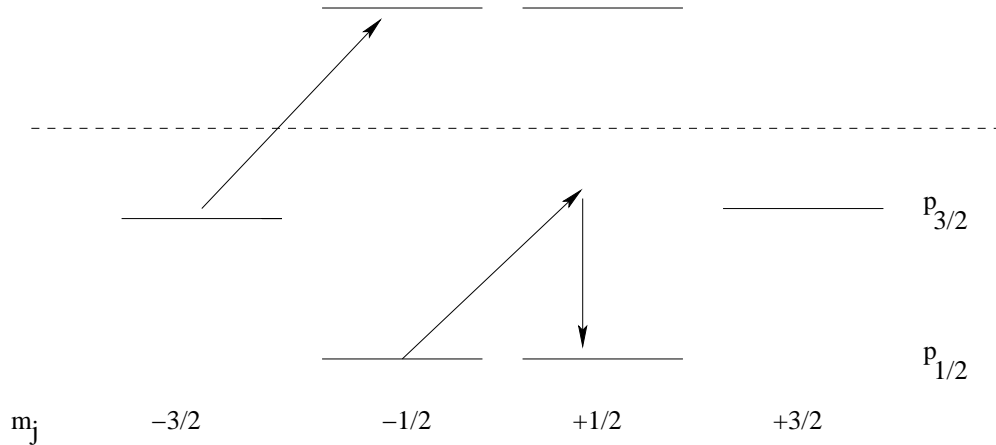
Figure 3.3: Diagram of band structure for strained GaAs. Photons do not possess the energy to promote the $p_{1/2}$ valence electrons to the conduction band, preferentially ejecting electrons with spin $-\frac{1}{2}$, promoted from the $p_{3/2}$ valence state.

conduction band, resulting in equal probability that the electron ejected from the GaAs is in either spin state. By straining the crystal, the levels split to non-degenerate $p_{3/2}$ and $p_{1/2}$ bands. This spacing between energy levels allows tuning the photon source to promote the $p_{3/2}$ level electrons more frequently than the $p_{1/2}$ level, resulting in a polarized beam, as diagrammed in Fig. 3.3. It is the usage of the strained GaAs that allows the polarization, and therefore enforces the stringent requirements on photon polarization.

3.1.2 Helicity Controls

The electrons ejected from the GaAs crystal are polarized, with the polarization correlated to the laser's polarization. The photon polarization is switched between left- and right-circular polarization at a rate called the helicity flip rate, set to 120 Hz for PREX. Each $8.\bar{3}$ millisecond period, referred to as an 'event', has electrons with the longitudinal polarization (and will have the same helicity entering the experimental hall), with these time periods called helicity windows. Each helicity window is produced in sequence with a window of opposite helicity, allowing us to form pairs of events with left- and right-helicity electrons for which we can then calculate a scattering asymmetry. For PREX, we elected to run using four window multiplets, such that electrons were generated in pairs of pairs, of the form left-right-right-left (LRRL) or right-left-left-right (RLLR). This flipping was handled by setting Pockel cell voltages, as shown in Fig. 3.4 for a single four-event multiplet. Each multiplet includes a 100 μs delay between states to allow the Pockel cell to settle, allowing
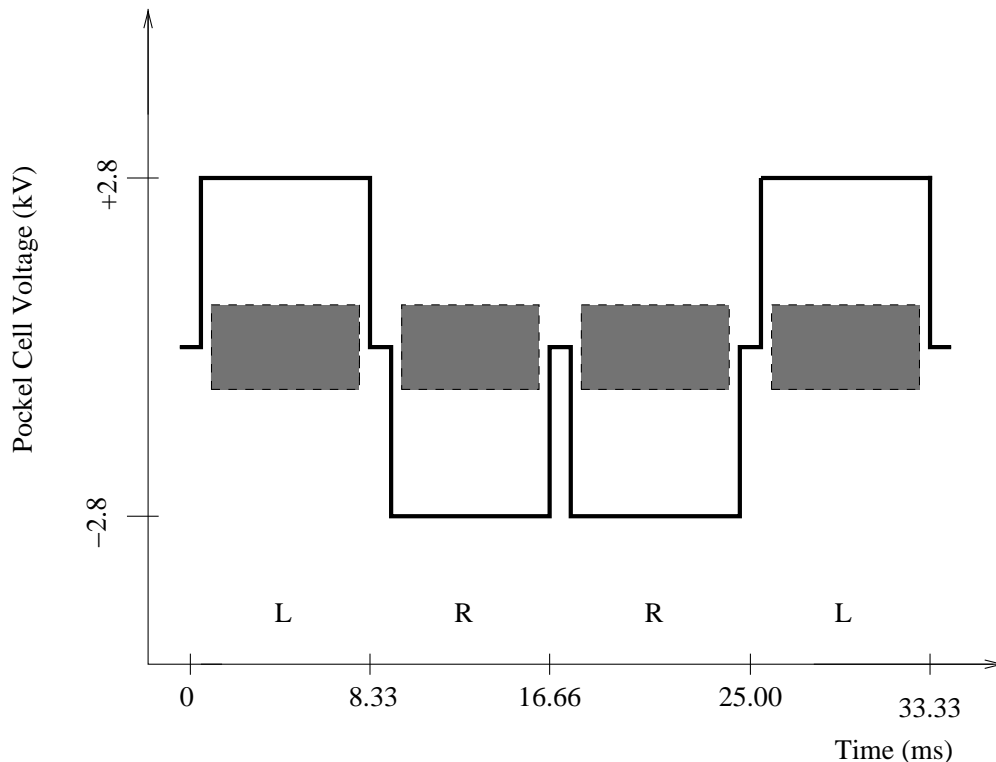
Figure 3.4: Cartoon of a four event multiplet (quartet). The Pockel cell voltage controls the initial electron helicity, resulting in left(L) or right (R) handed electrons entering the hall. Data was stored during the time marked by the dashed lines, selecting an appropriate delay before collecting data.

the polarization of the electrons in a given window to stabilize. To exclude this 100 μs delay, the data acquisition equipment recorded the middle $8.2\bar{3}$ ms of a window (tuned to minimize dead time in the apparatus but not measure any 'ringing' effects associated with the Pockel cell changing voltages).

These multiplets were generated pseudorandomly, with the ordering of multiplets determined by a sufficiently long, randomly generated sequence. This allows us to reconstruct the exact pair structure if needed while still disordered enough to minimize systematic effects associated with having a strict sequence of helicity windows. In order to prevent biasing from the signals sent by the injector, the helicity signal is generated by a circuit independent of the overall injector electronics. Also, the helicity as reported to the halls was stored in a buffer then sent after an eight window delay; while the correct helicities were matched to the relevant event, the helicity of the event is recorded concurrently with the signals from electrons generated 66 ms later, removing any correlation.

The electron will propagate through a number of magnets downstream of the injector,

30
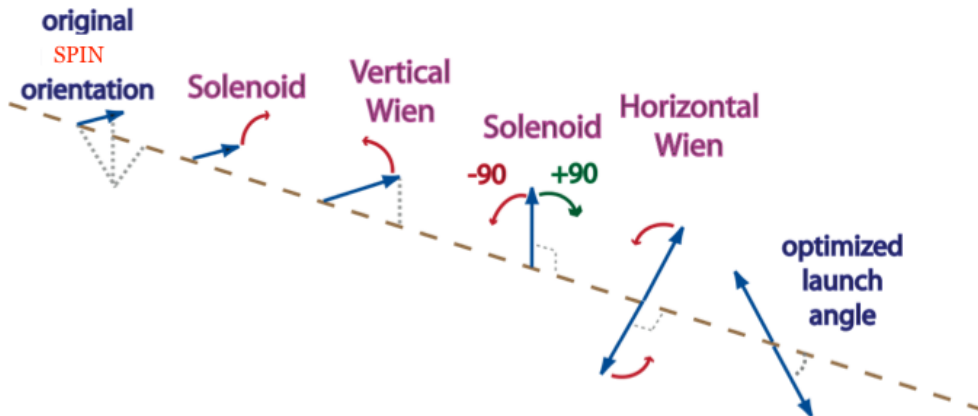
Figure 3.5: Wien filter methodology. Magnetic fields precess spin, with additional magnets added for PREX to provide a second slow reversal method for the spin. Reproduced from R. Michaels[29].

which will precess the spin of the electron. As such, the spin of the electron leaving the injector will need to be oriented such that the spin and momentum are aligned entering the hall. To do this, the electrons pass through a double Wien filter and have the orientation of their spin altered to account for this precession. This filter is comprised of crossed magnetic and electric fields. The applied magnetic fields precess the spin into the desired orientation before reaching the accelerator, as shown in Fig. 3.5, with the electric field tuned to maintain the electron's direction of travel.

Added to the Wien filter for PREX was a third magnet. This additional magnet is designed to precess the spin 90° away from vertical (before the horizontal Wien sets the final outgoing orientation). This changes the helicity of the electrons by a factor of ± 1, which we use in combination with the factor of ± 1 from the half-wave plate to test for any systematic effects associated with either helicity control. By independently inserting a half-wave plate or changing the applied voltage to the double Wien filter, collectively known as slow reversals, we are able to check if either of these devices cause a measurable effect on the asymmetry measurement. The analysis of the effects of the combined half-wave plate/Wien settings is discussed in detail in Sec. 5.4.

3.2 The Accelerator, CEBAF

After exiting the injector, polarized electrons are accelerated in the linear accelerator (LINAC) of the Continuous Electron Beam Accelerator Facility (CEBAF), as shown in Fig. 3.6. The

31

LINAC is a racetrack design, consisting of two linear regions and a pair of recirculating arcs. The two linear regions each contain twenty cryomodules, with each cryomodule containing 160 superconducting radio frequency (rf) cavities. Each cavity is run at 1497 MHz (the frequency required to accelerate electrons generated by the three of the 499 MHz-driven seed lasers in the injector independently) with accelerating gradient of 5 MV/m[30], such that an electron passing through all 20 cryomodules in a LINAC will accelerate 0.6 GeV. Each rf cavity is phase locked with a master clock, ensuring that the electrons gain the most energy possible from the accelerating gradient when traveling between rf cavities. This master clock, set by the injector, is a 30Hz pulse that allows for synchronizing of equipment between halls. The choice of superconducting rf cavities allows for a well-controlled electron beam, with 2.5×10^{-5} rms relative energy spread and $\approx 80 \mu m$ rms beam size in the transverse direction[30].

Similar to the feedback control to the Pockel cell that ensures the beam intensity is stable (as discussed in Sec. 3.1), the accelerator has a feedback system to ensure the energy of the beam is stable. Any drifts in beam energy, measured by the monitors described in Sec. 3.8.3, are corrected for using cavities near the exit of the accelerator. These cavities are sent an analog signal which alters their accelerating gradients, thereby changing the energy of the electrons exiting the injector. By changing these signals in response to drifts in beam energy in the monitors, we can maintain the energy of the beam at a level stable enough for a precise measurement of our asymmetry.

The recirculating arcs use five different tracks, each with a magnetic field tuned to bend electrons with a given number of passes through the accelerator 180°. The arcs were designed so as to minimize the physical position between electron bunches, optimizing the acceleration for electrons regardless of number of passes. The five recirculation tracks allow for acceleration of electrons up to 6 GeV, with currents of up to 190 μA. This magnetic field does cause a precession in the spin, as mentioned in Sec. 3.1.2. However, since tuning the beam to ensure the electrons pass through the recirculating arcs requires knowing the beam energy and magnetic field precisely, we can calculate the precession of the spin of an electron in the field of the recirculating arc. Given a known precession in the accelerator and the desired final spin entering the hall, the correction is performed in the Wien filter settings to account for the precession in the ARC. Once the electrons have reached the desired beam energy, they are split off into the relevant experimental hall.
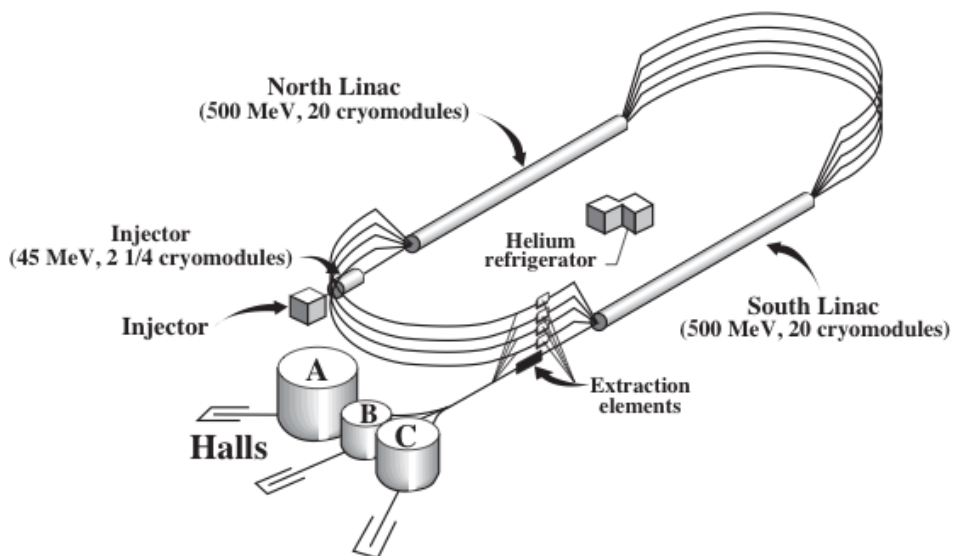
Figure 3.6: Schematic of the Jefferson Lab accelerator site. Electrons generated in the injector recirculate throught the racetrack design accelerator before being diverted into the experimental halls. Reproduced from Alcorn et. al.[31]

3.3   Hall A

The PREX experiment ran in Hall A. As shown in Fig. 3.1, electrons that enter Hall A pass through a pair of polarimeters, measuring the polarization of the electrons via both Compton scattering and (only during polarization measurements) Møller scattering. The electrons also pass through a number of position, energy, and current monitors, accumulating data on the parameters of the beam to account for fluctuations in the beam. The beam electrons reach the target ladder, contained within a vacuum chamber in the center of Hall A.

The electrons that do not scatter from the target continue along the beam line until they reach the beam dump. In order to selectively measure electrons scattering elastically with four-momentum transfer Q^2 desired, we use the high resolution spectrometers. These spectrometers are tuned to transport electrons with the desired parameters into the detector hut, where they are measured by the detector array. The data from the detectors, as well as from the position monitors, spectrometer settings, and polarimeter data are recorded for use during the analysis.

3.4   Target Ladder

In the center of Hall A the target ladder sits inside the vacuum-sealed target chamber, containing all of the targets used in each experiment. The ladder itself is removable in order to install the collection of targets necessary for each experiment. The target ladder is positioned vertically by a stepper motor, with the position recorded for each run by the position encoder signal. Also recorded are the conditions of the target chamber, most importantly the vacuum pressure and target chamber temperature (nominally held around 1μTorr and 20K, respectively). The target is selected with a graphical user interface (GUI), with each target's name and stepper motor position coded into it. The ordering of targets is as shown in Table 3.2, with each target presented with its elemental composition and thickness.

The standard target ladder contains a beryllium oxide (BeO) target, a tantalum target, and a number of carbon targets with different thicknesses. The BeO target emits light when struck with the electron beam. This light can be seen via a camera installed in the target chamber, allowing operators to visually ensure that the electron beam is aligned with a target in the target ladder. The carbon and tantalum targets have high melting points and well known cross sections, making them useful for tests as well as used in the Q^2 measurements. A water cell target (used only during commissioning, removed before high-current production running) was used in analyzing the optics, with data taken on this target serving as an important calibration for determining Q^2, as described in Sec. 5.10. Also in the ladder was a thin lead target which was used at low currents as another foil for optics tests, providing a sample target to measure how electrons will scatter from ^{208}Pb. The last target in the ladder, the Carbon Hole target, is a carbon target with a hole in the center, providing a signature that allows checks for alignment of the target based on where the reconstruction of electron tracks to the target shows no electrons scattered.

The other targets installed for this experiment included the optics target and the ^{208}Pb production targets. The optics target consisted of five carbon foil targets spaced in 7.5 cm increments along the path of the beam. The path of the scattering electron from these foils was calculated based on measurements from our spectrometers (as discussed in Sec. 3.5) in order to check the analysis of the optics was correct. The production targets were three 0.5 mm thick 99% isotopically pure ^{208}Pb foils. Given the energy deposited by the beam would melt an unprotected lead target, the target mounting was designed to minimize the risk of
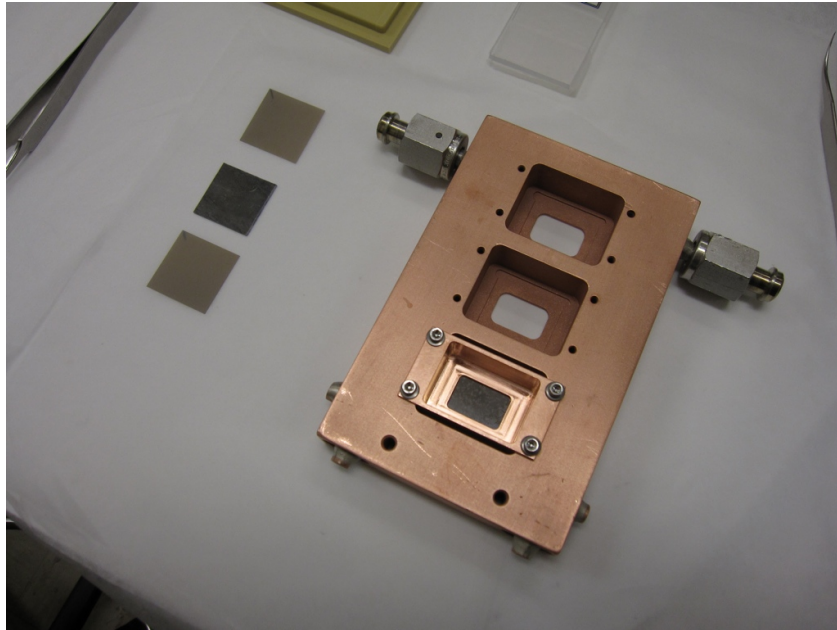
Figure 3.7: Photograph, by Robert Michaels, from a test assembly of the lead-diamond sandwich target. At left, the ^{208}Pb foil, with the ^{12}C diamond foils above and below. At right, the copper frame, with valves to connect to the cryogenic helium source. Installed on the lowest opening in the ladder is a PbD sandwich target, with the ^{208}Pb foil in between the ^{12}C diamond foils.

melting. In addition to rastering the beam (as discussed in Sec. 3.4.1), the ^{208}Pb foils were each placed in thermal contact with two, approximately 0.15 mm thick, diamond foils, shown with the foil in Fig. 3.7. The thicknesses of these targets were measured by Dave Meekins, and listed in Tables 3.3 and 3.4 in terms of centimeters and grams/centimeter^2 (proportional to the number of nuclei per unit area). Additionally, these lead-diamond sandwich targets, the PbD targets, were mounted in a copper frame. The frame itself had a pipe through which cryogenic helium was pumped in order to keep the frame, and by extension the target, cooled. To improve thermal conductivity, vacuum grease was applied to the ^{208}Pb foil to improve conductivity to the ^{12}C foil and a layer of silver paste was applied to the copper to improve conductivity between the PbD target and the frame[32]. The targets were pressed to the frame by a copper plug, also with a brushing of silver paste.

Target Name	Material	Thickness (g/cm^2)
Optics Target (Foils at 0, $\pm$7.5, $\pm$15)	C	0.042$\pm$0.0001 (ea.)
Pb Diamond #1	^{208}Pb and ^{12}C	See Tab. 3.4
Pb Diamond #2	^{208}Pb and ^{12}C	-
Pb Diamond #3	^{208}Pb and ^{12}C	-
BeO Viewer	BeO	0.149$\pm$0.001
Tantalum	Ta	0.12237$\pm$0.000341
Thin Lead	Pb	0.5524$\pm$0.00080
Thick Carbon	C	0.4422$\pm$0.00049
Thin Carbon	C	0.026867$\pm$0.000057
Super Thin Carbon	C	0.008991$\pm$0.000047
Carbon Hole	C	0.08388$\pm$0.00012

Table 3.2: A list of targets, with thicknesses.

Target	Front ^{12}C (cm.)	Back ^{12}C (cm.)	^{208}Pb (cm)
PbD #1	0.0135	0.0146	0.051
PbD #2	0.0128	0.0132	0.05136
PbD #3	0.0216	0.0210	0.0494

Table 3.3: A table of the thickness, in cm., for the ^{208}Pb foil and the ^{12}C foils up- and downstream of the ^{208}Pb foil, measured before the experiment.

Target	^{12}C Thickness (g/cm^2)	^{208}Pb (g/cm^2)
PbD #1	0.0983	0.5743
PbD #2	0.0909	0.5824
PbD #3	0.1492	0.5605

Table 3.4: A table of the thickness in g/cm^2 for the foils, for the combined front and back ^{12}C foils and the ^{208}Pb foil. The dimension g/cm^2 is proportional to the probability of interaction with the incident electrons.

3.4.1 Beam Rastering

Each high energy electron deposited a significant amount of energy into a ^{208}Pb target, which led to the deterioration of the ^{208}Pb foil. This deterioration was mitigated by moving the beam spot over the face of the target, spreading the energy (and heat) over a larger area and allowing the diamond foils to conduct thermal energy away. To move the beam spot over the face of the target, a set of raster magnets were placed in the beam line. The raster magnets, designed to generate orthogonal magnetic fields in the x- and y-directions, can run between 17-25 kHz to smear the electron beam into a 4 mm×4 mm rectangle (as measured by the BPMs) over the face of our target.

While the raster magnets were initially run unsynchronized to the timing of the injector and accelerator, early data showed that the electron beam was not sampling a uniform amount of target thickness in each helicity window in a left-right helicity pair (discussed in detail in Sec. 5.8.2). As a result, after the detector signals are corrected for correlations between the detector signals and beam position and energy as discussed in Sec. 3.8.4, data from the independent detectors in the right and left spectrometer arms showed a correlation. This correlation, shown in Fig. 3.8, arose from the electrons scattering from different target thicknesses in each helicity window of a pair. This additional common mode noise created a correlation in the responses of each separate detector arm. This indicated that after running for high luminosity the ^{208}Pb foil was developing worsening deformations with thickness on the order of 10%.

To ensure the electrons sample the same amount of target thickness in each helicity window, the controlling signals to the raster magnets were changed such that the beam spot traced the same pattern. The frequency difference between the raster magnets was tested for multiples of 120 Hz, as having the frequency difference set to a multiple of 120 Hz resulted in the the raster smearing the beam spot uniformly over the same area, with the end of the helicity window coinciding with the end of the raster pattern. While the raster was run at a 240 Hz difference (with the two raster magnets having frequencies of 25.19995 kHz and 24.95995 kHz) there was some indication from the data running with the frequency difference set to a larger multiple of 120 Hz would produce a better signal. As shown in Fig. 3.9 for the first data set after changing the raster settings, data taken with the modified raster settings did not show the correlation between independent detector arms. By removing the common mode noise associated with non-uniform target sampling, we were able to get the
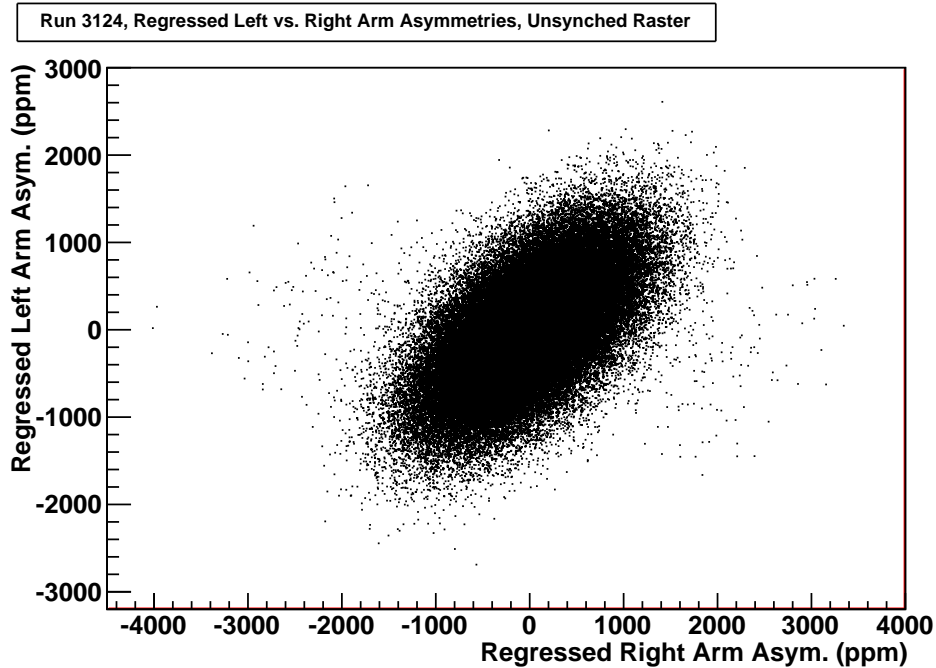
Figure 3.8: Plot of the regression-corrected asymmetries for the left and right spectrometer arms in data run 3124, with the raster unsynchronized. After removal of correlations calculated for position and energy, the signals between arms still show some correlation.

full statistics from averaging over each arm.

To synchronize the magnets to the master pulse signal (MPS) that defines the helicity time structure, the PREX experiment used Agilent frequency generators. Instead of relying on the internal reference time of the Agilent box, the synchronized raster set up had the 10 MHz external time-based reference from the MPS as an input for the first Agilent box, with the Agilent box's frequency set at 25.19995 kHz. The 10 MHz clock from the first Agilent was then used as an external reference for the second Agilent, set to 24.95995 kHz. The 10 MHz output from the first Agilent box was then used as the external reference for the second Agilent box, and as a result the rastered electron beam traced the same pattern in every helicity window, and therefore sampled the same thickness of ^{208}Pb. These signals were checked on the scope and compared to the 30 Hz Pockel cell time structure and found to be in time with each other. Any mismatched settings appeared on the oscilloscope as a slow drift of the Agilent with respect to the 30 Hz signal from the MPS. A schematic of this is shown in Fig. 3.10.

Run 3453, Regressed Left vs. Right Arm Asymmetries, Synched Raster
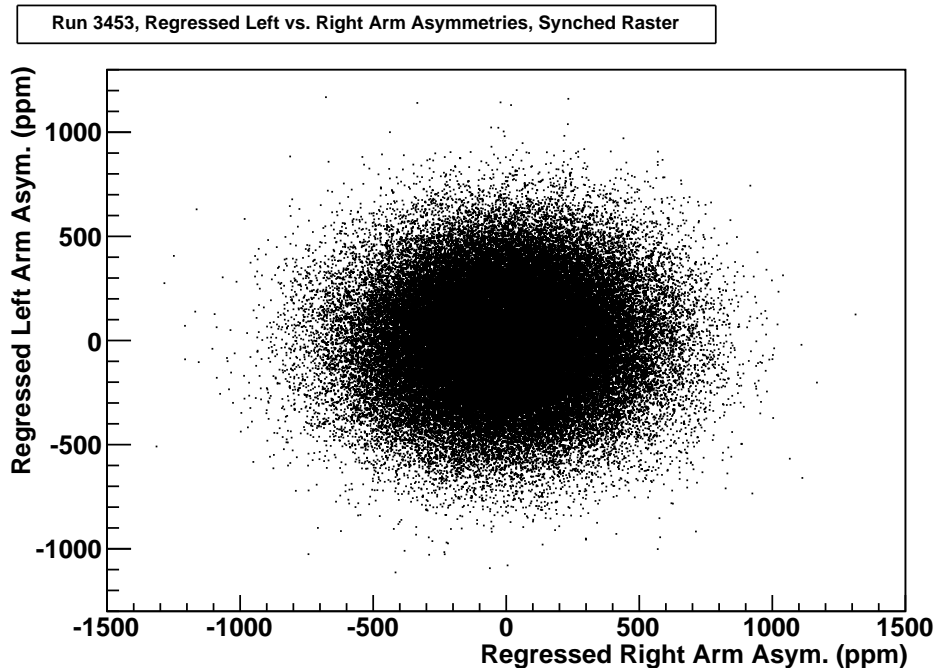
Figure 3.9: Plot of the regression-corrected asymmetries for the left and right spectrometer arms in data run 3543, with the raster controls synchronized. Using the same correction scheme as the data from Fig. 3.8, synchronizing the raster removes the correlation between the two independent detectors.

3.5   High Resolution Spectrometers

Scattering experiments such as PREX require some mechanism by which we can isolate and measure our desired flux of particles scattering from the target. In the case of PREX, this requires extracting the elastically scattering electrons from the total flux of scattering electrons. Given, in the case of PREX, that our ^{208}Pb target nuclei have a mass of ≈ 200 GeV/c^2, a 1 GeV electron scattering elastically from a ^{208}Pb target will result in negligible energy loss from scattering recoil. Therefore, the correlation between scattering angle and energy is negligible, resulting in the electrons scattering elastically from the target at 5.5° away from the beam line having 1 GeV of energy, matching the incident electron energy.

In order to selectively measure elastically scattering particles we rely on Hall A's high resolution spectrometers (HRS). The two identical HRS in Hall A are QQDQ spectrometers, consisting of two superconducting quadrupole magnets, a superconducting 45° vertical dipole, and a third quadrupole magnet, all cooled with a combination of LN$_2$ and liquid helium prepared in the Hall A Cryogenics Distribution System[31]. The HRS are shown by the schematic diagram in Fig. 3.11. The benefits of a QQDQ spectrometer is that we

From Accelerator

10MHz external
time based reference

Scope

30Hz MPS signal

10MHz

Agilent 33220a

25.19995 kHz

Agilent 33250a

24.95995 kHz

To Raster
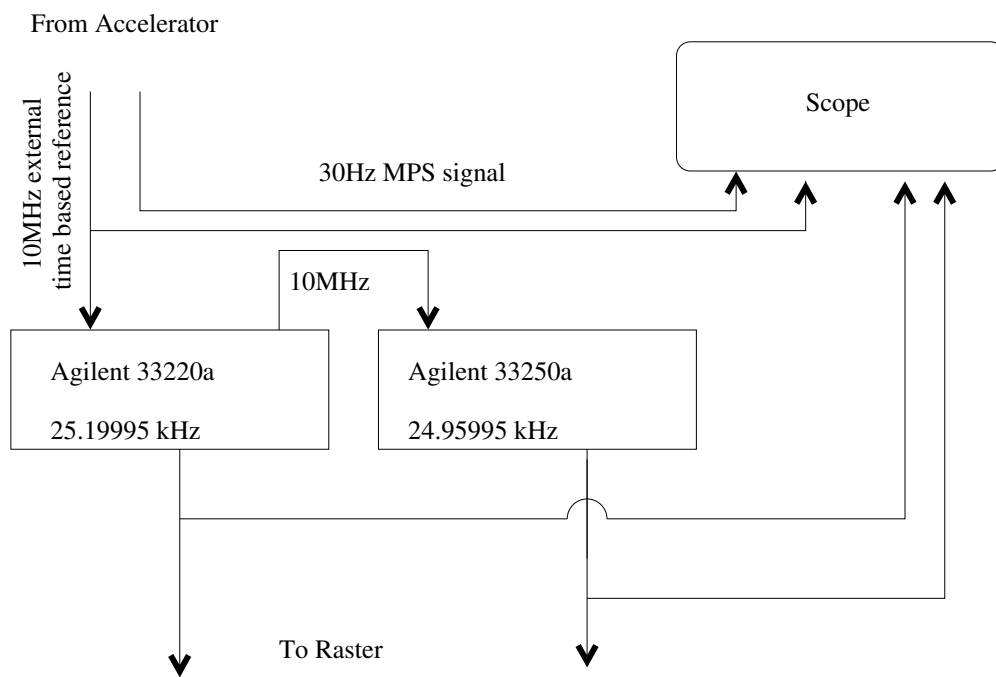
Figure 3.10: Schematic of the Agilent rain. The 10 MHz external time-based reference, used as a reference for the 30 Hz MPS signal to the Pockel cell, is sent from the injector to the first Agilent box, whose 10 MHz clock is used as a reference for the second. The 10 MHz external reference, the 30 Hz signal setting the helicity, and the output from the Agilents are connected to a scope to ensure timing. Adapted from a schematic by R. Silwal.

can use the quadrupoles and dipoles to control the transport of electrons based on the position and velocity (dependent on the scattering angle and energy) to produce a new set of "transported" coordinates at the exit. For the Hall A spectrometer magnets, the spatial orientation of the electrons leaving the HRS are correlated directly with the energy and scattering angle, allowing the detector package (discussed in Sec. 3.6) to measure the number of electrons scattering from the target in terms of their scattering parameters. Additionally, the field integral of the electrons passing through the magnetic field in the dipole separates the electrons by their momentum.

To perform these transformations, the first quadrupole, Q1, in each spectrometer is used to focus the scattering particles in the vertical plane x (associated with dispersion). The second (Q2) and third (Q3) focus in the transverse direction y. The dipole (D1), situated between Q2 and Q3, bends the scattered electrons vertically towards the detector hut, with the HRS designed to transport particles with momenta as low as 0.8 GeV and up to 4.0 GeV at a momentum resolution of $\frac{\delta p}{p} = 10^{-4}$. The momentum resolution of the HRS represents a compromise between measurement accuracy and the cost of the magnets[31]. The hardware resolution also benefitted from the choice of vertical bend instead of horizontal bend, as a vertical bend spectrometer decouples first order effects from target length. The resolution of the magnets by themselves is $\frac{\delta p}{p} = 10^{-3}$, stemming from field integral being dependent on particle energy. Therefore, the angle and position the electrons leave the HRS are dependent on the electron's energy. In the case of PREX, this 10^{-3} resolution alone can separate the elastically scattering electrons, at 1 GeV, from the first inelastic peak of ^{208}Pb, where the first inelastic peak has an energy loss of 2.4 MeV. The fields of each magnet are measured constantly, with the dipole field recorded from both NMR field probes and Hall probes placed inside the magnets, and the quadrupoles measured exclusively with a Hall probe. In addition, as the Hall probes alone brings up concerns of long-term stability and reproducibility of settings, the current sent to each magnet is also recorded to be used in calibration as well as a secondary check of the magnet status.

Each spectrometer is mounted on a carriage, shown in Fig. 3.12 in context of the experimental hall, which provides the ability to select a central angle between 12°-130° in the right arm and 12°-150° in the left. The angular bite in the lab frame is designed to be ±30 mrad horizontally and ±60 mrad vertically, with resolutions 0.5 and 1.0 mrad respectively[31]. By having two identical spectrometers, the HRS can be positioned so as to make simultaneous measurements of different angles θ with respect to the target. In front of the acceptance-
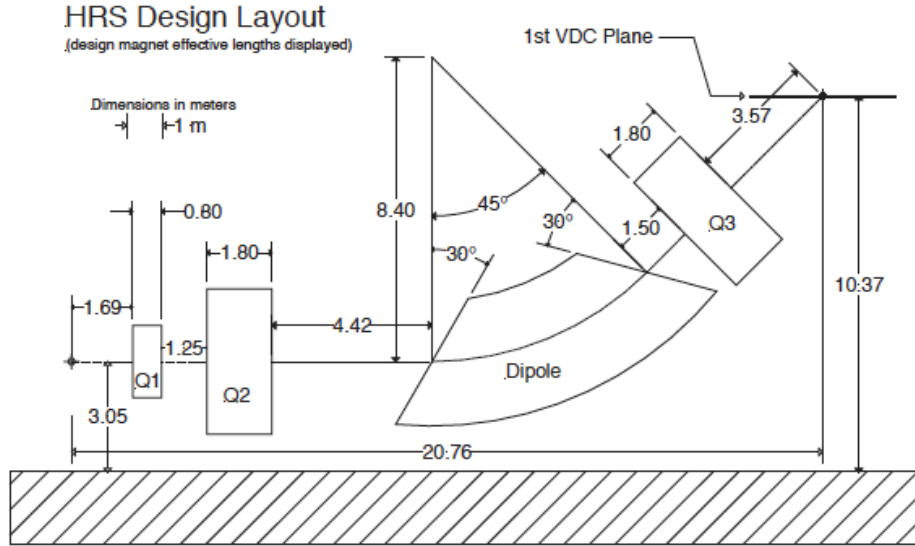
Figure 3.11: Schematic of the HRS. The schematic shows the relative placement of the elements of the HRS. From the left-most point measured as the end of the target, this shows the length of the electron path between the target and the first element of the detector package, the first VDC plane. Reproduced from Alcorn et. al.[31].

defining collimators are a pair of insertable tungsten sieves with holes (of varying diameters) drilled in a grid pattern. By comparing the position and angle our analysis reconstructs for the electron passing through the sieve against the measured position of the holes in the sieve the electrons passed through, we can calibrate the reconstruction of the scattered particle tracks and ensure that we understand how particles propagate from the target to the detectors.

For the kinematic settings of the PREX experiment, the accepted solid angle was defined by a pair of 80 mm thick tungsten collimators designed and installed for this experiment, as shown in Fig. 3.13, located 1.1 m downstream of the target. Collimation was done by installing the 80 mm thick tungsten collimators at the opening of Q1 in each arm. These collimators selected electrons between 4° and 7° symmetrically to ensure the central angle for each arm was identical (within 0.1 mm). These collimators, in addition to defining our acceptance, have an asymmetric pair of holes cut in them (one high, one low) to measure the transverse asymmetry and thus dubbed 'A_T' holes. These holes are filled with beryllium in order to decrease the energy of the electrons that pass through it. The energy loss from electrons passing through beryllium affects transport through the HRS, with the resulting 'A_T' electrons appearing at a smaller energy and scattering angle compared to the elasti-

42
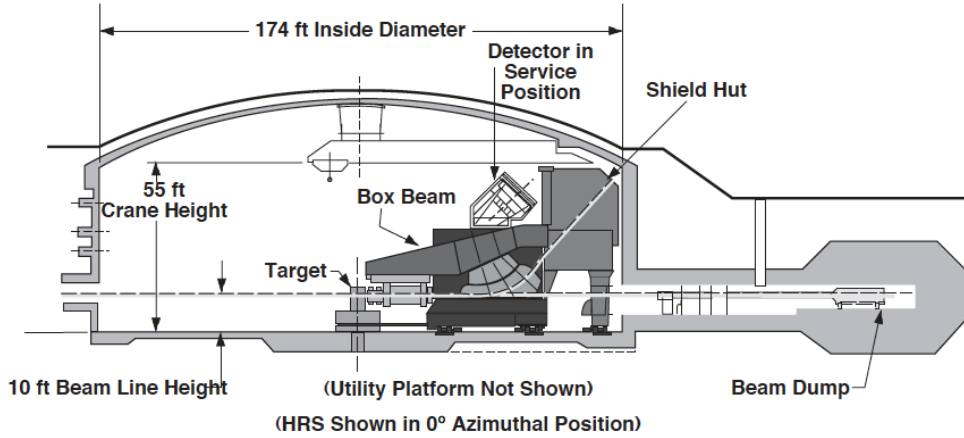
Figure 3.12: Drawing of the HRS in the context of Hall A, to scale with the rest of the hall and the beam dump. Reproduced from Alcorn et. al.[31]

cally scattering electrons. These electrons are measured in order to identify the size of the transverse asymmetry, with electrons passing through these openings scattering differently between the two arms, thereby measuring the scattering flux ϕ (about the beam line, relative to θ which measures angle away from it) and testing the azimuthal scattering symmetry.

The electrons that pass through the HRS exit the third quadrupole Q3 organized spatially in the focal plane. The focal plane, as simulated in Fig. 3.14 and plotted for a JLab data run in Fig. 3.15, is defined to propagate normal to the electron's direction of motion. Electrons in the focal plane are distributed with the energy and angle scattering from the target correlated with the x and y positions at the exit of the HRS. The energy is associated with the dispersive direction x while the scattering angle is correlated to the transverse direction, y. Given the electrons are scattering elastically from a heavy target, as previously stated, there is negligible energy loss from recoil. This has the added benefit, as the scattering recoil energy depends on scattering angle θ, that for targets with masses on the order of our beam energy there is a correlation between energy and θ for a given four-momentum transfer Q^2. As the recoil is negligible, the energy and angle are independent and therefore the spread of angle and energy for a given Q^2 is such that the HRS magnet settings can be selected so as to narrow the elastic peak. The resulting tune has the elastic peak, representing the bulk of the particles scattering elastically and propagating through the HRS focused to a point, in this case the origin of Fig. 3.14. The smearing of the elastic peak in x stems from the radiative tail of the electron distribution, where elastically scattering electrons lose small amounts of energy through bremsstrahlung radiation. As a result, the data from electrons scattering
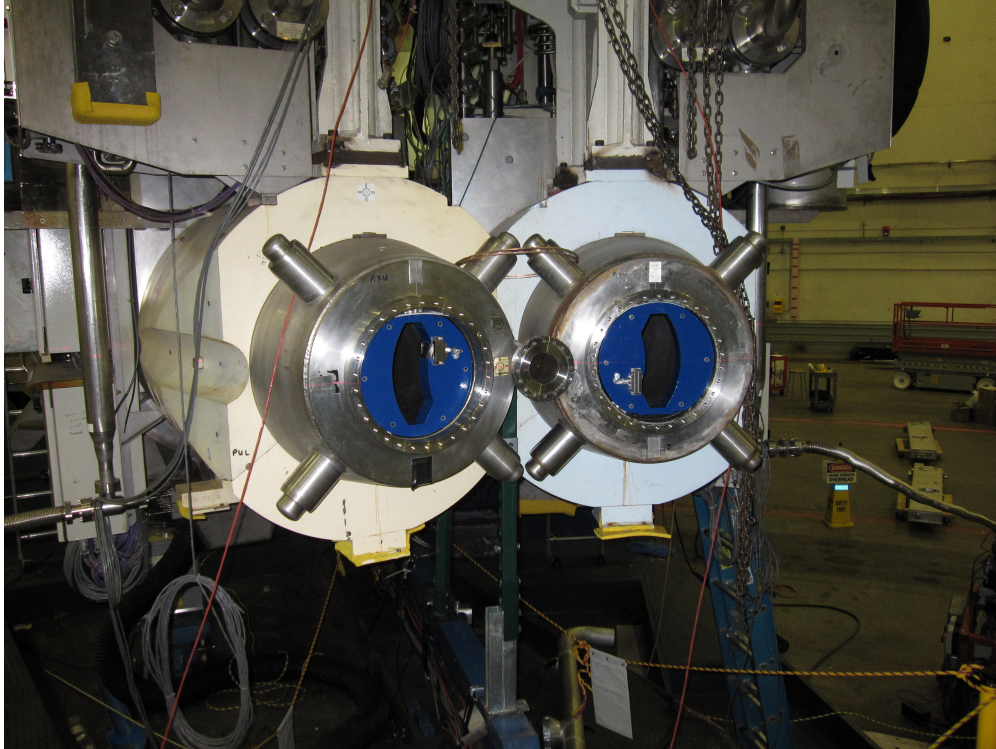
Figure 3.13: Photograph, by Robert Michaels, of the acceptance defining collimators, painted blue, installed on the entrance to Q1 in both arms. The asymmetrically-placed beryllium mountings, near each opening, were placed to measure the magnitude of the transverse scattering asymmetry.
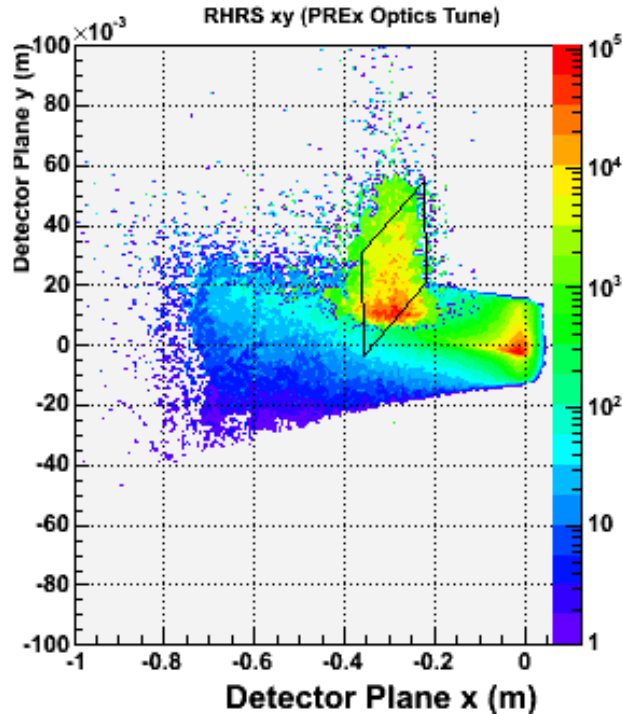
Figure 3.14: Produced by D. McNulty, a simulation of the electron focal plane using the Hall A Monte Carlo (HAMC) simulation package. Axes are defined such that the elastic peak is located at (0,0). The spread of data in x, the energy-dependent dispersive direction, shows the energy loss in electrons that can still propagate to the target. The vertical smearing is symmetric about our central angle, showing a symmetric angular acceptance.

elastically off the thin ^{208}Pb target described in Sec. 3.4, show the elastic peak, with a 10 cm spread in x and 3.5 cm spread in y. The plot is symmetric around our central angle, showing a small spread in angular acceptance. Knowing that the kinematics for PREX are optimized for 1 GeV electrons elastically scattering at $\approx 5.5°$, we can tune the HRS to isolate electrons with those parameters. The secondary peak, centered at (-0.3, 10) in Fig. 3.14, is associated with the electrons passing through the beryllium-blocked A_T holes.

The final component of the HRS is the septum magnet. Designed for the PREX experiment, a septum magnet was installed on the front end of the HRS to propagate electrons scattering at $5.5°$ into the HRS, with minimum design angle of $12.5°$. The design goal of the septum was to bend the electrons scattering at $5.5°$ into the mouth of the HRS, with emphasis on maintaining a hardware resolution capable of distinguishing between the 2.6 MeV first inelastic peak of ^{208}Pb from the elastically scattering electrons[33].

VDC Focal Plane Distribution, Run 6773
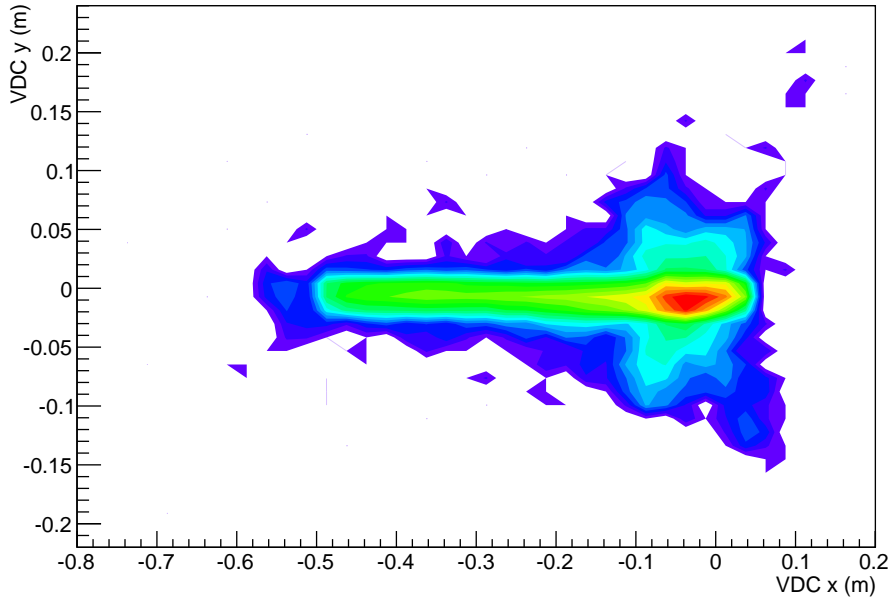
Figure 3.15: The focal plane as measured in hits on the VDC. The VDC's x and y coordinates show the focal plane as a peak, with a smearing along the dispersive (x) direction.

3.6   Detector Package

The magnetic fields from the spectrometer magnets channel the electrons directly into the detector hut, with the spatial x and y of the hut correlated to the energy and scattering angle of the electron at the target. The contents of the hut are protected by a set of 450 tonne concrete-lead doors, shielding the contained detectors from the ambient radiation in the experimental hall during running, in combination with the line-of-sight blocking pair of concrete blocks located on top of spectrometer quadrupoles Q1 and Q2. This shield protects the detector package and data acquisition (DAQ) electronics, installed on a movable frame inside the detector hut. The movable frame allows for modifying the contained detector package depending on the experimental needs.

The standard detector package, as shown in Fig. 3.16, includes triggering, in order to identify the particle, and tracking, used to provide information on the electron's energy, position and angle after scattering. The triggering system for the DAQ is designed to register a signal when a particle passes through it, with the signal used to trigger the DAQ to record an event from the rest of the detector package. The triggers, required for low current measurements such as alignment checks and Q^2 measurements, are signals from the Cerenkov
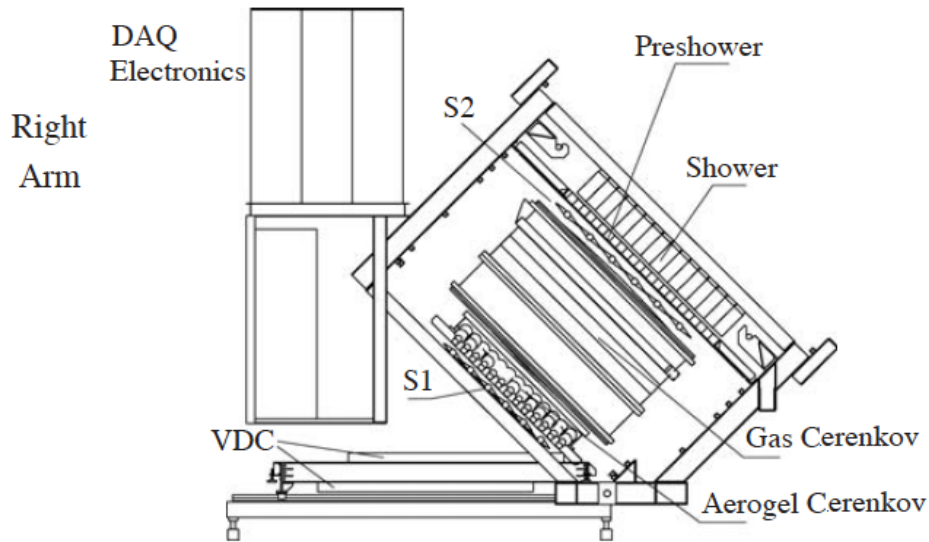
Figure 3.16: Reproduced from Alcorn et. al.[31], a schematic of the detector hut, showing the VDC in the bottom left and the scintillator S1 downstream.

detectors and a lead shower counter, of which we primarily the triggering scintillator plane (S1) upstream of the detectors. The scintillator planes are comprised of six paddles made of 5 mm BC408 plastic scintillator and a pair of Burle 8578 PMTs. In addition, a second scintillator, 'S0', using the same plastic but two XP2312 PMTs was placed on top of the vertical drift chamber, and was used in initial alignment checking.

The detector package's particle tracking detectors are designed to measure the position and direction the electrons propagate as they enter the detector package. The tracking is done by the vertical drift chambers (VDCs) in each arm. The VDCs (which were used to produce Fig. 3.14) consist of two wire chambers, separated vertically by 0.335 m, the lower of the two being positioned near the exit to focusing quadrupole Q3. In each VDC, the gas, an equal mixture, by volume, of 99.9% pure argon and 99.0% pure ethane gases, flows through adjacent cells, with each cell isolated by a gas window. Across the VDC, a vertical electric field is applied provided by high voltage windows, held at -4 kV, on top and bottom of the chamber. A sensing wire, held at +5.0 V, is strung along the length of the chamber, through the center of the chamber, parallel to the cathodes. Electrons passing through the gas chamber will ionize the gas, and the electric field will induce a current flow away from the cathodes and towards the wire. The wire in the chamber will sense the ionized electrons and return a signal.

47
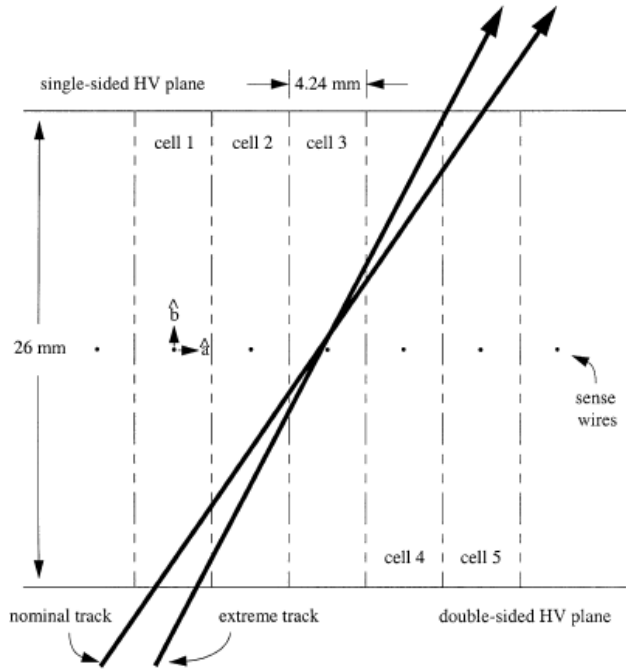
Figure 3.17: Cartoon of a single vertical drift chamber from the side. Electrons passing through each gas chamber induce charge flow, measured by the sensing wire. Arrows represent the nominal 45° and most extreme, 52°, tracks. Reproduced from Fissum et. al.[34].
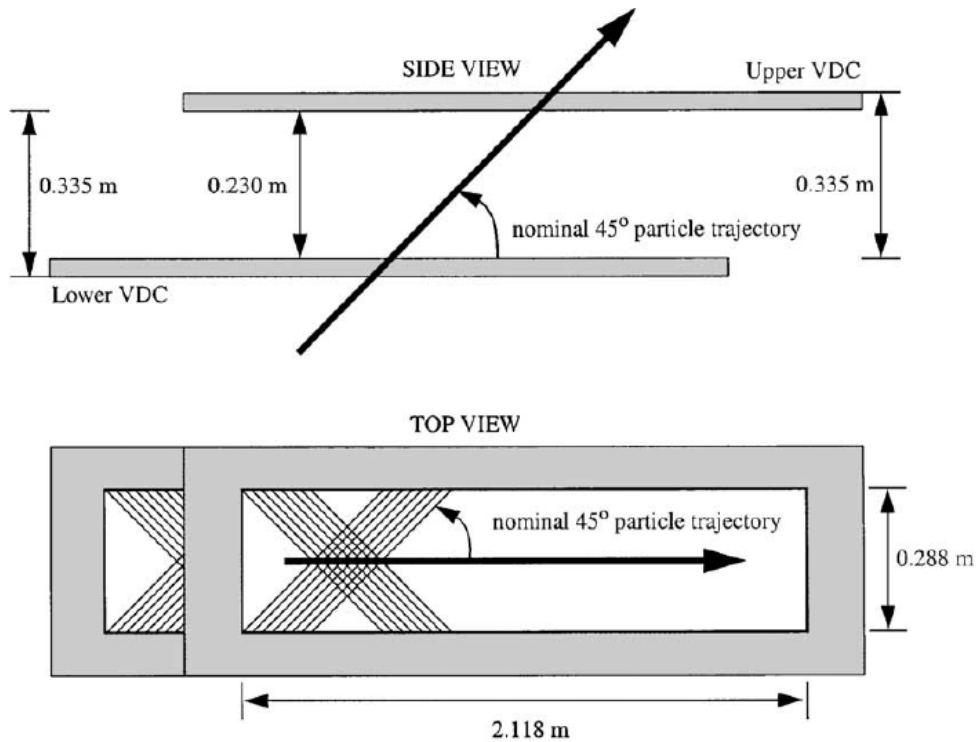
Figure 3.18: A sketch of the vertical drift chambers from side and top views. The solid black arrow represents nominal particle track. Reproduced from Fissum et. al.[34].

These chambers are placed side-by-side, the length of the VDC. The orientation of these chambers is such that an electron will pass through multiple chambers, as shown in Fig. 3.17, with each chamber reporting an separate signal. The VDC design is such that we can analyze the position and time differences in each signal (with a time resolution of 4.5ns leading to a position resolution of 225μm)[34], to reconstruct how the electron moves in the gas regions. Each VDC includes two sets of these planes, oriented orthogonally along u and v (which can be transformed into x-y coordinates), providing information about the transit in two directions. Additionally, entire VDC consists of two of these paired layers, as shown in Fig. 3.18, allowing us to measure both the location and motion of the electrons through these chamber as well as after the propagation between the two chambers. This allows for reconstruction of the track with increased accuracy, showing the direction of motion as the electron passes through the detector hut and into our PREX detectors. Knowing the HRS, as described in Sec. 3.5, are designed to transform the scattering energy and angle at the target into spatial x and y at the exit of the HRS, a tracking measurement of the position and momentum entering the detector hut provides insight into how it scattered from the target, which can be further used for measurements of the Q^2 of electrons scattering from the ^{208}Pb nucleus.

Suspended over the VDCs were the detectors designed for the PREX experiment, discussed in detail in Chapter 4, used to measure electron flux during high current running. Each detector consisted of a quartz block aligned with the elastic peak of the transported electrons, and a photomultiplier tube which gathered the generated Cerenkov photons and produced the measured signal. Each arm contained two of these detectors, stacked vertically and aligned such that both quartz blocks were aligned with the elastic peak. For low beam currents, such as runs using the VDC, these detectors were connected directly to the data acquisition to measure the signal for individual electron events. To ensure the detector was centered on the elastic peak, data was collected comparing the electrons in the VDC as a function of position, with and without requiring a response in the PREX detectors. In Figs. 3.19 and 3.20, the VDC signal is superimposed on the VDC signal correlated with any detector signal. Fig. 3.20 is the transverse direction results, with the agreement showing the PREX detector is centered with respect to transported angle. Fig. 3.19 shows that the PREX detectors are positioned to register a signal for electrons passing though a 14 cm range in the dispersive direction as measured by the VDC. This region is the peak signal, which we can (by comparison with Fig. 3.14) claim is the elastic peak, thereby showing the

Dispersive Spectrum

Rarm, 6722

lower Q cut

Events/2mm

Detector plane x (m) at z=0.90 m
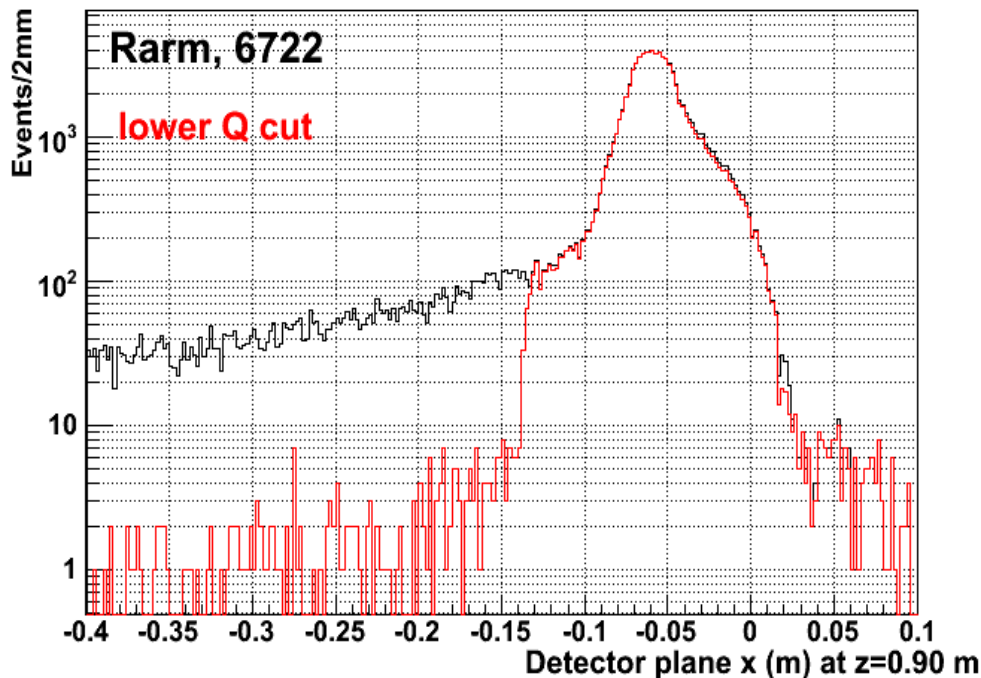
Figure 3.19: Data from electrons transported to the VDC as a function of the transported energy coordinate x. The black line shows the data in the VDC, while the red line shows the same data with the imposed requirement that the PREX detector measured a non-zero signal. The overlay of the lines shows the PREX detector is centered on the elastic peak in x but does not measure the radiative tail. Plot produced by D. McNulty.

PREX detectors are positioned to measure the electrons scattering elastically from the target and no electrons in the radiative tail. In the case of high current events, these detectors were used to integrate the signal of the flux of electrons for a single window. As such, the detectors were filtered through an RC box, composed of a resistor and capactitor, in order to improve signal quality before being passed to an analog-to-digital converter (ADC). The integrating ADC reports the photon flux at the photomultiplier face over the course of a helicity window, giving a signal proportional the number of electrons passing through the quartz.

3.7 Data Acquisition

In order to analyze the signals from the detector in the context of the experiment, the data acquisition systems (DAQ) in Hall A correlate the measurements from beam monitors upstream of the target and detectors to each helicity window, with two different data systems
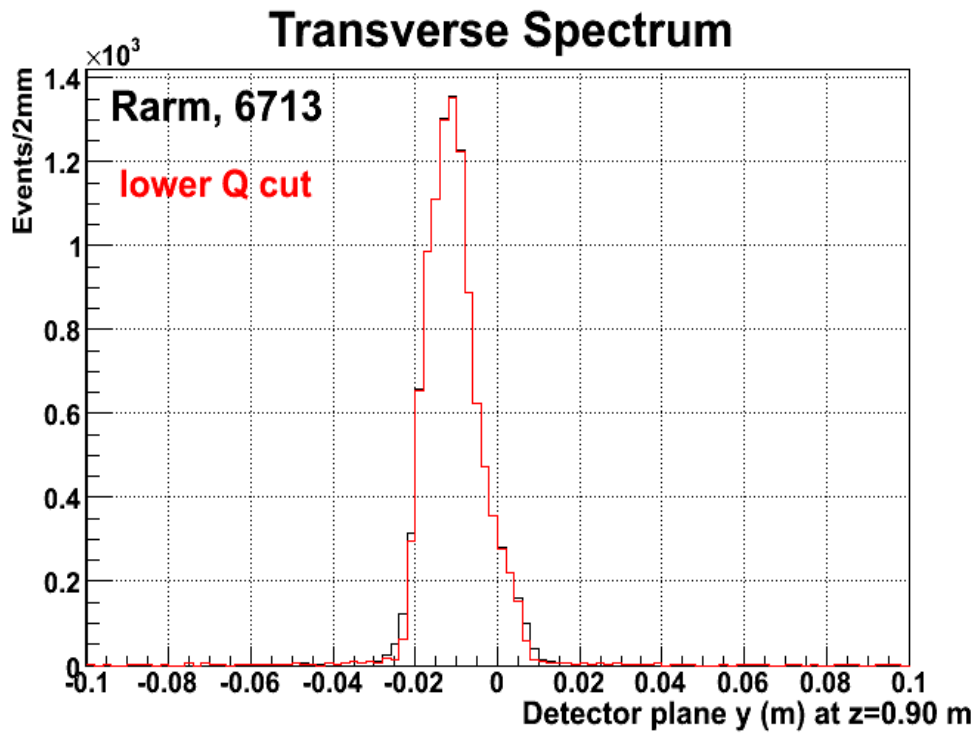
Figure 3.20: Data from electrons transported to the VDC as a function of the transported scattering angle coordinate y. The black line shows the data in the VDC, while the red line shows the same data with the imposed requirement that the PREX detector measured a non-zero signal. The overlay of the lines shows the PREX detector is centered on the elastic peak in y. Plot produced by D. McNulty.

each handling different sorts of measurements. The data stream organizes data based on the timing of events, collecting all data necessary both for the intended measurement and the reconstruction of the particle track. By correlating the measured detector signals to data on beam parameters, such as current, position, and energy, we can account for any response in the detectors associated with beam parameter fluctuations (as described in Sec. 5.6.1).

For low current runs, PREX collected data using the 'spectrometer DAQ'. This DAQ, run for each spectrometer arm separately, has each event triggered by the response of a set of defined scintillators in the detector hut described in Sec. 3.6. This separates each electron into an independent event. Having data on individual electrons allows for reconstruction of separate tracks, which is important for measuring the four-momentum transfer Q^2 and detector responses. However, it is not designed to measure a large flux of electrons, with certain components (such as the vertical drift chambers described in Sec. 3.6) unable to run without the risk of damage.

As the PREX result is expected to be on the order of 10^{-7}, we require a large sample of electrons. In order to measure the required electrons efficiently, it is desirable to measure bunches of electrons instead of individual particles. A second DAQ system, named the 'parity DAQ', is coded such that it measures the signals in both spectrometer arms and integrates over each window of left- or right-handed electrons. At the cost of being unable to measure the tracks of individual electrons, the parity DAQ allows us to measure high rates of electrons, which translates to an increased number of weakly scattering electrons per window and thereby increasing the asymmetry in detector signals between helicity states.

The detectors, described in Chapter 4, are designed to generate a signal proportional to the number of electrons that enter them. The signal from each electron, as well as the signals in all beam monitors, is accumulated during the helicity window in an integrating analog-to-digital converter (ADC). These integrated signals, the sum of the detector responses per individual electron over the helicity window, were recorded in the data stream, allowing measurements of approximately 3.5 million electrons per $8.\bar{3}$ second window.

3.8 Beam Monitors

In order to ensure the beam has the same intensity between helicity windows, and that the electrons will scatter from the target with the design-specified Q^2, the Hall A apparatus includes monitors that measure the beam upstream of the target. The importance of the

beam monitors stems from the fact that the data collected by our detectors is dependent on the number of electrons that reach the detectors. For the signal $d_\pm$ associated with windows of positive and negative electron helicity, the asymmetry measured by the detectors is the difference in the signal measured between the helicity states normalized to the total signal between the states

$$A = \frac{d_+ - d_-}{d_+ + d_-} = \frac{\delta d}{2d} \tag{3.2}$$

This signal measures the fractional difference in signal between helicity states, similar to the ratio of weak and charged form factors discussed in Sec. 2.3. However, this equation does not include any calibration for the incident beam parameters, which fluctuate and therefore affect the number of scattered electrons that reach the detector. As the number of electrons that scatter from the target will be proportional to the number of electrons that reach the target, there needs to be a calibration for the data based on the beam intensity for each helicity window, such that each calibrated detector signal D needs to be normalized by the current of the beam incident on the target I. Expanding the pair asymmetry for the normalized detector signal, to first order,

$$A = \frac{\Delta D}{2D} - \frac{\Delta I}{2I} \tag{3.3}$$

for event-event differences in detector signal ΔD and intensity ΔI, assuming the signals and current measured between events are stable (this will be treated with full formalism in Sec. 5.1).

This is not a complete description of the asymmetry, as the measured asymmetry depends on the beam energy E and the scattering angle θ (which is defined by the position of the beam spot relative to the fixed location of the acceptance-defining collimator downstream discussed in Sec. 3.5). As such, our asymmetry measurement needs to be calibrated to account for fluctuations in the beam. Following the approach devised for the HAPPEX experiments[25], we calibrate by modulating the beam parameters and measuring the position monitor responses and detector responses. We can amend Eq. 3.3 to include these beam fluctuations as

$$A = \frac{\Delta D}{2D} - \frac{\Delta I}{2I} - \sum_j \alpha_j \chi_j \tag{3.4}$$
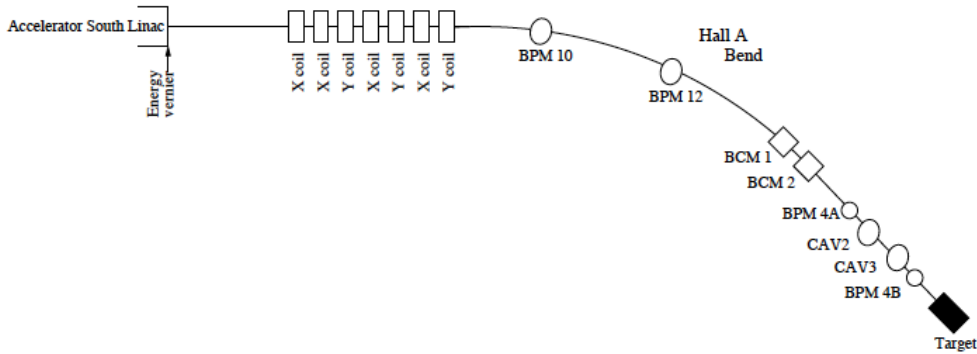
Figure 3.21: Drawing of the beamline between the accelerator and target. Shows the relative locations of the position (BPM) and current (BCM) monitors. Reproduced from Kaufman[35].

with the change in asymmetry dependent on the signal from the j-th BPM χ_j. The coefficient α_j is calculated from the correlation between the detector and j-th BPM $\frac{\partial D}{\partial \chi_j}$. Therefore, applying these beam corrections requires measuring the correlation between detector and BPM signals. As such, correcting for asymmetries stemming from differences in beam intensity, energy, and position between windows requires measuring these parameters. The Hall A monitor system consists of a number of position and current monitors, defining the location of the beam and it's intensity, ordered as in Fig. 3.21.

3.8.1 Position

The position of the beam as it hits the target affects the scattering angle. The electrons travel along z, with x and y oriented parallel and normal to the floor of the experimental hall, respectively. To measure the beam position, we use a set of beam position monitors (BPMs). These BPMs are each comprised of four strip-line antennae. These antennae are oriented at $\pm u$ and $\pm v$, where u and v are 45° rotated from x and y about z in the coordinates of the hall. The induced current in each wire, proportional to the distance between the beam and the wire, is recorded for each event to the data stream. The position is then calculated as an asymmetry for these wire signals, providing a current-independent result for the position. The wires primarily used in the position analysis were BPM4a and BPM4b, located 7.524m and 1.286m upstream of the target respectively. By having the x and y positions at two points before the target, we can determine the position and angle of the beam at the target. These monitors were calibrated using independent wire scanners, known as superharps, in

54

order to measure the position relative to Hall A coordinates.

For low current runs, the wires are inaccurate as the current induces a small signal that is hard to separate from background signals. As such, the low current tracking runs need different hardware. For runs below 1μA, the beam position was measured by a pair of cavity monitors. While unable to run at high currents these can be run to much lower currents, which was important for Q^2 measurements run at 50 nA. The cavity monitors were cross-calibrated at 9.5μA and 1μA. Below this, the cavities were calibrated using a detector signal, comparing the drop in PMT signal to the drop in beam current for currents below 1μA. These were calibrated to less than 0.2 mm for all currents based on the stripline-cavity correlation at 1μA.

3.8.2   Beam Intensity

The beam current monitor (BCM) package includes three monitors: a pair of rf cavities (BCM1 and BCM3) and an Unser monitor (BCM5), all located 25m upstream of the target. The rf cavities BCM1 and BCM3 are high-Q waveguides tuned to the accelerator's frequency. As these are tuned to the frequency of the beam as given by the injector for all the halls, the cavity records a voltage proportional to the current during each helicity window. Since the rf cavities are nonlinear at lower currents (below 5 μA), an independent, linear current monitor is required in order to calibrate for the dark current reported by each rf cavity.

The Unser monitor, BCM5, is a parametric current transformer, which is calibrated using a known current through a wire and can then measure an absolute signal. The Unser is useful as a calibration for the other monitors but is too unstable (with significant drifts in average signal occurring on the order of minutes) to be used as an accurate measure of current during long runs. As such, the BCM5 data was used to calibrate the rf cavities, BCM1 and BCM3, with respect to the dark current signals. Using the Unser monitor to measure the dark current for the rf cavities requires measuring the signal from all BCMs as the beam current increases and fit the data between the Unser and the rf cavities, as discussed in Sec. 5.3.

As we are trying to measure the scattering of electrons and compare signals between helicity states, it is important to have the overall beam current stay the same between windows. To ensure the integrated charge is uniform between windows, the PREX experiment used the Hall A charge feedback monitor, which measures the current for each negative and positive helicity window for uniformity. The current feedback monitor then calculates any changes to the Pockel cell necessary to improve the uniformity of the signal, returning a

voltage difference that minimizes the asymmetry in beam intensity between windows[26] as discussed in Sec. 3.1.

3.8.3 Energy

The beam energy is measured using the Arc method, which measures the position of the electron beam as its path is bent by magnets when entering Hall A. As the change in the path of the electrons depends on the field integral, and therefore the energy, there will be a position difference in this arc relative to the energy of the electron entering the hall. The momentum of the beam in terms of angle is given by

$$p = 0.3 \frac{GeV}{Tm} \int \frac{B \cdot d\ell}{\theta} \tag{3.5}$$

for momentum p, field strength B, length ℓ and bending angle θ. As a result, the measured deflection is proportional to the momentum of the electron. This measurement is made by both recording the voltage sent to the magnet as well as by a position measurement in the bending direction from BPM12x, the designated energy BPM, which reports the energy as a horizontal position. The energy of the beam is also controlled by a fast feedback system, with data sampled from the measured beam in the hall used as the parameter to be corrected. The correction is applied by rf cavities, described in Sec. 3.2, in the linear accelerator. These cavities accept an analog signal that modifies the gradient of the cavity, changing the acceleration of the electron in the cavity (and thereby changing the energy of the electron entering the hall). The cavities used in this correction, the 'energy vernier', are immediately before the beam chopper that controls which hall receives which bunches of electrons[36].

3.8.4 Beam Modulation

With measurements of these beam parameters, we can calculate the corrections needed for Eq. 3.4. There were two separate methods applied to measure the slopes α_j, the calculations of which are described in Sec. 5.6, each of which relies on different methods of measuring the BPM and detector signals. One method, regression, calculates α_j from measurements of the beam's natural fluctuations and detector responses. As the beam corrections are required to correct for a measurable effect on detector signals, the behavior of the beam during standard data collection can be used to calculate these slopes. The description of how the slopes are calculated from the natural beam fluctuations is given in Sec. 5.6.2.

56

The other method, dithering, involves deliberately altering the beam position and energy and measuring the response to that motion in the BPMs and detectors. The modulation in beam energy is performed by the energy vernier in the south LINAC, using the same set of rf cavities that control the fast feedback as described in Sec. 3.8.3. The modulations in beam position are performed by seven air-core corrector coils (four oriented to modulate the beam position in x and three to modulate the y position). These coils are oriented such that a set of four coils can measure changes in x, y, as well as θ_x and θ_y. The angles θ_x and θ_y refer to the change $\frac{dx}{dz}$ and $\frac{dy}{dz}$, or the change in the x and y variables as the electrons travel towards the target. The additional three coils allow for checks to see if there is some dependence on specific coils. All coils were controlled remotely to move the beam every nine minutes, with position changes based on the voltage applied to the coils for 5 seconds each. The nominal coil settings move the beam between 0.3 and 0.5 μm, while the energy vernier changes the beam energy by up to 300 keV (corresponding to a change in position of 0.75 mm at the energy BPM). Using these coils, we can calibrate our corrections to the detector signal based on these changes in position and beam energy. The process of modulating of all of the coils, referred to as dither cycle, was performed once every 9.6 minutes during asymmetry measurements, with each cycle lasting 90 seconds (including a five second window before and after the beam modulation to turn off the feedback controls). The analysis of the modulations is summarized in Sec. 5.6.1.

3.9 Polarimetry

Since PREX is measuring the scattering of longitudinally polarized electrons off nuclei, we need to have accurate data on the polarization of the beam. The polarization of the beam P describes the fraction of electrons in a helicity window of the desired helicity relative to the total number of electrons. The polarization is defined in terms of the number of electrons in positive and negative helicity states (N^+ and N^- respectively) in a given helicity window, such that $N^+_{L,R}$ is the number of electrons with positive helicity in a window with left- or right- helicity. We can, for $N^+_{L,R}$ and $N^-_{L,R}$ write the beam polarization for a left or right helicity window $P_{L,R}$ as

$$P_{L,R} = \frac{N^+_{L,R} - N^-_{L,R}}{N^+_{L,R} + N^-_{L,R}} \tag{3.6}$$

Assuming that the beam intensity is the same between helicity windows, and that the

magnitude of the beam polarization is constant, given by $|P_L| = |P_R|$, we can rewrite Eq. 3.6 to describe the number of electrons of a given helicity measured in a window $N^{\pm}_{L,R}$ in terms of the total number of electrons $N^0 = N^+ + N^-$ and beam polarization $P_{L,R}$ like

$$N^{\pm}_{L,R} = \frac{N^0}{2} \left(1 \pm P_{L,R}\right) \tag{3.7}$$

To extract information on the beam polarization, we need to use a polarimeter, which consists of a target with helicity-dependent interactions and a detector to measure the interactions. The cross-section can be expressed as

$$\sigma^{\pm} = \sigma^0 \left(1 \pm A\right) \tag{3.8}$$

where the helicity dependent cross section $\sigma^{\pm}$ is related to a helicity independent component σ^0 and the analyzing power A, correlated to the theoretical asymmetry. A polarimeter will measure a signal $S_{L,R}$ from the interaction with the beam, where $S_{L,R}$ is the signal measured during the left- and right-helicity windows. We can express the measured polarimeter signal $S_{L,R}$ as a function of the probability of scattering, $\sigma^{\pm}$ and the flux of electrons with the given helicity $N^{\pm}_{L,R}$ associated with the cross section

$$S_{L,R} = \sigma^+ N^+_{L,R} + + \sigma^- N^-_{L,R} \tag{3.9}$$

such that the response of the detector depends on the number of electrons in a given state N and the probability that the electrons will scatter off the target into the detector σ. We can take the asymmetry between these polarimeter responses to find A_{exp}, which simplifies via substitution to just the product of the analyzing power and polarization, allowing us to extract the beam polarization from a measurement of the polarimeter measurements and analyzing power.

$$A_{exp} = \frac{S_L - S_R}{S_L + S_R} = AP \tag{3.10}$$

To measure the beam polarization, the PREX experiment used two polarimeters, a Compton polarimeter and a Møller polarimeter. The Compton polarimeter and Møller polarimeter, both located inside Hall A, were upgraded in anticipation of this experiment in order to improve the accuracy of the polarization results.

3.9.1   Compton Polarimeter

The Compton polarimeter measures the electron polarization from the helicity dependence of electron-photon scattering. As the photons will scatter at a rate relative to the beam polarization, we can measure the photons scattering between electron helicity states to quantify the electron polarization. As such, the Compton polarimeter consists of a laser table, to create the stable, intense beam of photons, and a photon detector, to measure the resulting scattered photons. As the cross section for the scattering of a polarized electron and polarized photon depends on the polarization of the particles, the integrated scattering rate contains information on the polarization of the beam, as given by [37]

$$A_{meas.}^{P} = \frac{N^+ + N^-}{N^+ + N^-} = P_e P_\gamma A_C \qquad (3.11)$$

for electron and photon polarizations P_e and P_γ. This requires measuring spin-dependent Compton asymmetry A_C, in terms of cross sections for the photon and electron polarizations parallel ($\sigma_{\Rightarrow}^{\rightarrow}$) or anti-parallel ($\sigma_{\Rightarrow}^{\leftarrow}$)spins, given by

$$A_C = \frac{\sigma_{\Rightarrow}^{\rightarrow} - \sigma_{\Rightarrow}^{\leftarrow}}{\sigma_{\Rightarrow}^{\rightarrow} + \sigma_{\Rightarrow}^{\leftarrow}} \qquad (3.12)$$

The Compton polarimeter measures the asymmetry in photons scattered relative to the photon polarization and electron helicity. The Compton cross section is small, with analyzing power $\sqrt{\langle A_C^2 \rangle} = 6.4\%$ [37]. Having a low analyzing power resulting in requiring a large number of possible interactions in order to measure a significant scattering asymmetry. As we are using a fixed beam intensity, we can increase the number of scattering electrons by increasing the number of target photons.

The Compton polarimeter itself is comprised of three elements; the magnetic chicane, the laser table, and the detectors. The Compton polarimeter is not on the main beam line (allowing for beam usage while the polarimeter is non-functional), installed in a chicane parallel to the main beam line. To use the Compton polarimeter, two pairs of magnetic dipoles are activated to change the path of the electrons. The first pair of dipoles bend the path of the electrons through the chicane to the laser table, and the second pair bends the electrons that do not interact with the photons back to the main beam line. The Compton chicane has three position monitors along it, used to ensure beam position stability as well as assist in the tuning the chicane magnet settings.
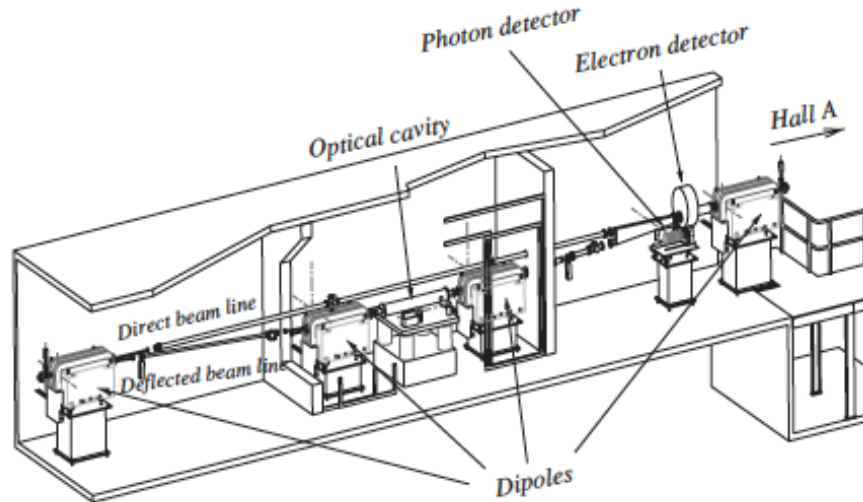
Figure 3.22: Schematic of the Compton polarimeter. Electrons are deflected downward, away from the direct path, by a pair of dipoles when the Compton polarimeter is in use. The electrons pass through the optical cavity and then are deflected back to the beamline by a second pair of dipoles. Reproduced from Alcorn et. al.[31]

The laser table features the laser, the optics required for a clean, polarized photon beam, and an optical cavity to accumulate photons in the path of the electron beam. In preparation for the PREX experiment, the laser was upgraded to a green 532 nm beam using a PPLN crystal, increasing the scattering cross section and therefore the precision. The polarization is changed to circularly polarized using a quarter wave plate, with the plate able to rotate in order to generate both left- and right-handed photons. Then, to increase the intensity of photons interacting with the electrons, the beam is directed into a Fabry-Pérot cavity. The Fabry-Pérot cavity is a pair of mirrors, aligned and spaced such that the photons from our seed laser will reflect between the mirrors and constructively interfere. By accumulating photons in the cavity, the power of the laser increases by a factor of 7300 in the cavity relative to the power of the beam alone[31]. The photons scattering from electrons in the beam are measured in an electromagnetic calorimeter, whose signal is used to calculate the asymmetry between scattering states.

3.9.2   Møller Polarimeter

Downstream of the Compton polarimeter is the Møller polarimeter. The Møller polarimeter uses superconducting magnets to polarize the electrons of an iron foil. As beam electrons pass through the foils, they scatter off the target electrons, with the scattering rate dependent

on the beam helicity and the spin orientation of the electrons in the iron foil. By measuring the electrons in each helicity state, we can measure an asymmetry equal to

$$A_{exp}^{Mol} = \sum_{i=X,Y,Z} A_i^{Mol} P_i^e P_i^{targ} \tag{3.13}$$

with index i defining the projection of the polarization onto the beam (with $\hat{p} = \hat{z}$) and Møller analyzing power A_i^{Mol} dependent on center of mass scattering angle θ_{CM}

$$A_Z^{Mol} = -\frac{\sin^2 \theta_{CM} \left(7 + \cos^2 \theta_{CM}\right)}{\left(3 + \cos^2 \theta_{CM}\right)^2}. \tag{3.14}$$

The transverse asymmetries are given by

$$A_X^{Mol} = \frac{\sin^4 \theta_{CM}}{\left(3 + \cos^2 \theta_{CM}\right)} = -A_Y^{Mol} \tag{3.15}$$

The maximum of A_Z^{Mol} is at $\theta_{CM} = 90°$ with $A_Z^{Mol} = \frac{7}{9}$. For the same angle, $A_X^{Mol} = -A_Y^{Mol} = \frac{A_Z^{Mol}}{7} = \frac{1}{9}$.

The polarized target is a ferromagnetic foil in a magnetic field, which will align the spins of the free electrons in the foil. The maximum polarization for the ferromagnetic foils is $P_i^{targ} = 0.076$ along the axis of the foil. The foil itself was oriented at $\pm 20°$, as having the two angles symmetric around the beam axis allowed for the cancelling of transverse effects. As the dominant source of error in the Møller measurement comes from target polarization, the magnet was upgraded to a 3T field to minimize the systematic error from polarization, resulting in a 0.25% error contribution[38].

As shown in Fig. 3.23, the electrons pass through three quadrupoles (for focusing) and a dipole (to separate scattered electrons). Electrons interact with the foils (as described in Eq. 3.13) and scatter into one of the calorimeters. These calorimeter signals measure the number of electrons scattering from each of the helicity states, then calculates the asymmetry from that. These measurements cannot be made during data collection, as the presence of high fields affects the beam parameters and that the Møller polarimeter can only be run with electron beam currents less than 9μA. Because the process is invasive, the Møller polarimeter took nine measurements during specifically designated runs scheduled weekly during the experiment.
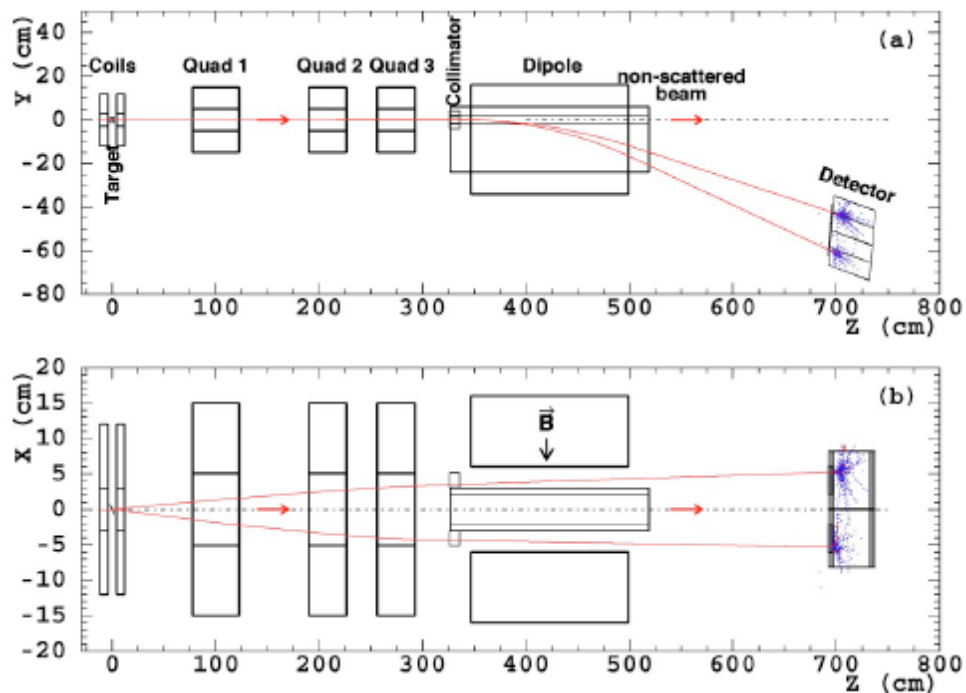
Figure 3.23: Side and top-down schematic diagrams for the Hall A Møller polarimeter. Reproduced from Aniol. et. al.[25]

CHAPTER 4

DETECTOR DESIGN AND CONSTRUCTION

The experimental demands for PREX require a detector that collects data related to the scattering asymmetry between left- and right-handed electrons elastically scattering from a ^{208}Pb target. As described in Sec. 3.5, electrons that reach the detector hut are oriented spatially in coordinates correlated with energy E and scattering angle θ. Focal plane electrons, having elastically scattered with energy of 1 GeV and scattering at approximately 5.5°, are constrained to a narrow area in the detector hut by the spectrometer magnet settings, resulting in the elastic peak spanning a 10 cm×3.5 cm area relative to the momentum of the electron. To measure the flux of desired electrons, the PREX detector must produce a signal response from the entire elastic peak, as measured in the focal plane of the detector hut.

We also recognize that weakly scattering electrons represent a small fraction of the electrons reaching the detector hut. As alluded to in Sec. 3.7, we need to be able to measure the number of electrons in each scattering window precisely enough to discern the change in signal associated with weak scattering electrons between helicity states. For an experiment like PREX, expecting a total scattering rate on the order of 1 GHz, this gives us requirements on our detector designs; maximizing signal per electron and mitigating the possibility of radiation from 1 GHz of electrons damaging the detector.

Work was performed at the University of Massachusetts-Amherst and Smith College to design and fabricate detectors that achieved these goals in preparation for the experiment. Early tests of these detectors used a single quartz block to generate Cerenkov photons, with a light guide designed to funnel these photons towards the light-measuring photomultipler tube. The quartz block is a pure Cerenkov-emitting material, emitting no scintillation light. Therefore, photons are generated only while the electron passes through the quartz. By
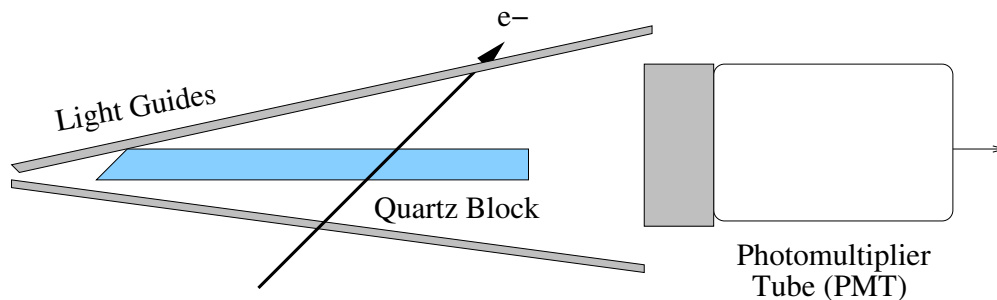
Figure 4.1: Cartoon of the PREX detector (not shown to scale). A quartz block is aligned with the elastic peak in the focal plane. Cerenkov photons are funneled towards a photomultiplier tube by an aluminum light guide. The light guide consists of plates above, below and beside (not shown) the quartz, as well as a cylindrical mirror in front of the PMT.

measuring the flux of photons with a photomultiplier tube (PMT) we have a measurement of photons correlated with the electron's helicity window, with the number of photons at the PMT in an optimized detector directly proportional to the number of electrons passing through the quartz. Following the finalized settings for HRS magnets and elastic peak size, the PREX detectors were designed with a quartz block featuring a face of 14 cm×3.5 cm, spanning the 10 cm×3.5 cm elastic peak with the quartz held at 45° relative to the focal plane. The thickness of the quartz blocks was, through simulation and testing using our cosmic ray detection apparatus (described in Sec. 4.3), determined to produce the best results for a range of thicknesses between 6 mm and 10 mm in the up- and downstream detector pairs located in each spectrometer arm's detector hut. The detector was designed to be constructed entirely of aluminum.

Tests following the PREX experiment were performed using cosmic ray muons, necessitating the construction of a cosmic ray detection apparatus. After completing the cosmic ray test set-up, tests were performed in order to investigate our understanding of the behavior of the detectors with respect to the expected signal per incident muon, as well as to compare with similar results from Jefferson Lab. These detectors were also tested later at the MAMI microtron at the Johannes Gutenberg Universität in Mainz, Germany, along with prototypes of similar detector geometries for possible use in future parity measurements.

4.1 Overview of Cerenkov Detectors

In order to measure high electron rates, the detector design used quartz blocks to generate the Cerenkov radiation from electrons traveling through the quartz. Cerenkov light is generated

by charged particles with velocity greater than the speed of light in the medium. As the electron are moving near the speed of light in vacuum, they enter the quartz (index of refraction n=1.455) at a speed greater than the speed of light in that medium and produce Cerenkov photons. The number of photons produced in terms of electron energy E passing through a medium with thickness dx depends only on the Cerenkov photon scattering angle θ_c and of the constituent particle charge Z of each element in the material, given by[39]

$$\frac{d^2N}{dEdx} = \frac{\alpha Z^2}{\hbar c} \sin^2 \theta_c = 370 Z^2 \sin^2 \theta_c \frac{1}{eV\ cm} \tag{4.1}$$

for Cerenkov scattering angle given by (for electron velocity v)

$$\cos \theta_c = \frac{1}{n\frac{v}{c}} = \frac{1}{n\beta} \tag{4.2}$$

The Cerenkov light the electrons emit is on the order of a few eV, which can be measured by our 2 inch Hamamatsu R7723Q photomultiplier tubes (PMTs). These PMTs absorb photons at the photocathode, producing electrons by the photoelectric effect that, at each of the 8 dynode stages produce additional electrons. These electrons are all absorbed by the anode, producing a signal linearly proportional to the number of photons absorbed. The R7723Q PMTs were selected for their sensitivies, with the specially ordered quartz windows accepting a range of photons with wavelengths between 200 and 600 nm, peaking around 420 nm. The probability of a photon of a given wavelength ejecting an electron from the cathode is called the quantum efficiency. The quantum efficiencies for various PMT materials (listed as 'photocathode radiant sensitivity') is shown in Fig. 4.2, with the quantum efficiency for our PMTs highlighted in red. Having a PMT sensitive to photons with shorter wavelengths is important to a quartz Cerenkov detector, as the number of photons generated N(λ) goes like $\frac{1}{\lambda}$. In order to precisely measure the number of electrons passing through the quartz, it is important to maximize the number of photons measured per electron, so it is important to have our PMTs sensitive to these lower wavelength photons.

The number of photons generated per incident electron follows a Poisson distribution, with the mean dependent on the amount of quartz material the electron passes through. As such, the expected number of photons measured can be quantified by a Gaussian width in the signal associated with the number of photons per incident electron. If properly designed, the total flux of photons at the PMT and the number of electrons incident on the quartz are linearly proportional. The gains of these PMTs, quantifying the increase in signal between
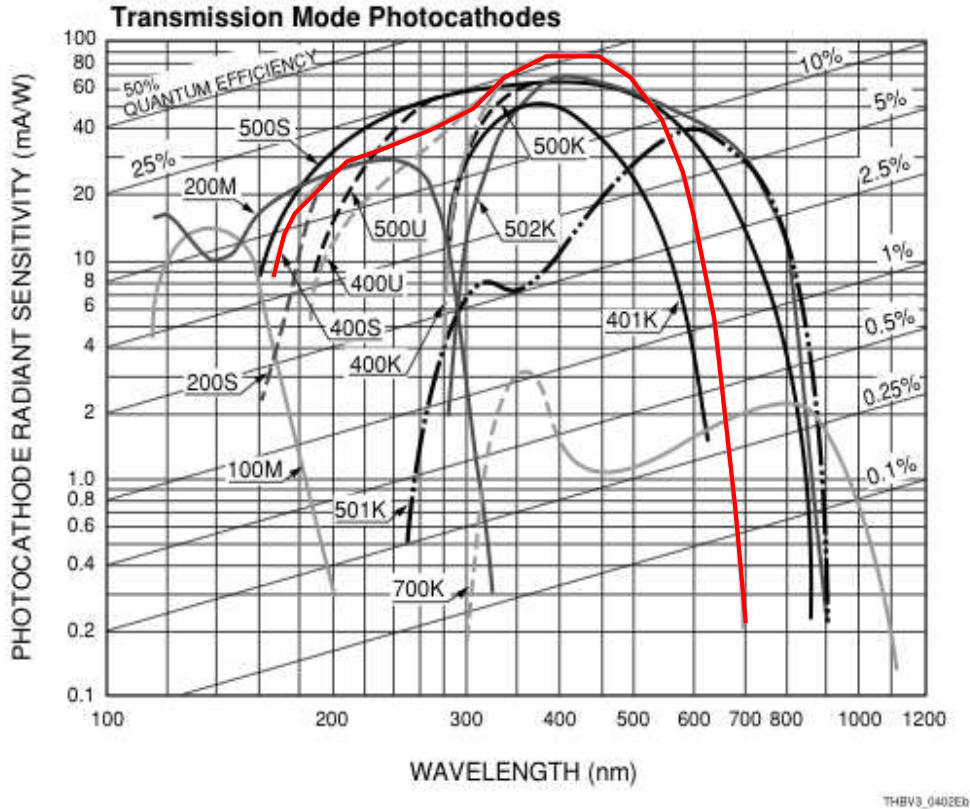
Figure 4.2: From the Hamamatsu PMT handbook[40], a plot of photocathode transmissions as a function of wavelength for various PMT window materials. The quantum efficiency of the PMTs used follows the 400S transmission curve, highlighted in red for clarity.

the cathode and anode of the PMT, are listed in Table 4.1.

In order to maximize the number of Cerenkov photons reaching the photomultiplier tube, the quartz blocks were designed to optimize the number of generated photons propagating towards the PMT. To do this, the blocks were designed to capitalize on the energy of the electrons and quartz properties. Cerenkov photons, for electrons with velocity ν, are emitted at an angle θ_c relative to the electron's velocity with θ_c given by Eq. 4.2 which equals, for 1 GeV electrons with $1 - \beta = 10^{-8}$, 46.58° relative to the electron's direction of motion. Using the same index of refraction, Snell's Law states the total internal reflection angle is 43.42°. This means that there is a range of angles in which the photons created in the quartz will be trapped via total internal reflection, as cartooned in Fig. 4.3. The quartz block is designed such that electrons entering at 45° will generate radiation that will internally reflect off of the top and bottom faces of the quartz. In order to allow photons to escape the quartz, the face near the PMT is oriented normal to the PMT - as such, photons will be incident to that

Detector	PMT	Gain (V)
#1	ZK5555	6.04×10^5
#2	ZK4033	4.31×10^5
A_T Right	ZK4035	5.59×10^5
#3	ZK5401	7.36×10^5
#4	ZK5369	8.78×10^5
A_T Left	ZK5366	4.11×10^5

Table 4.1: A table of the gains for each PMT at -2000V, listed by associated detector.
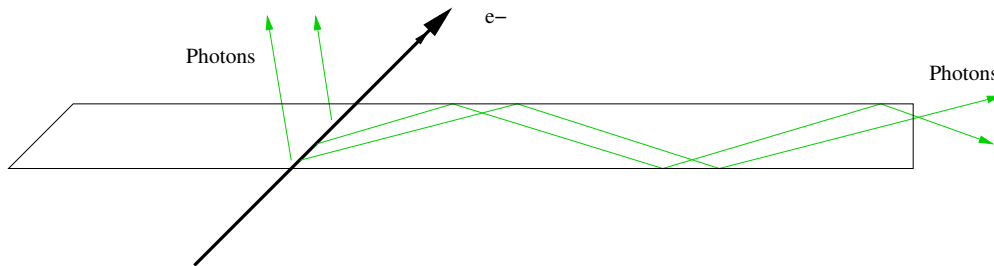
Figure 4.3: Cartoon of an electron passing through a PREX-style quartz block. The electron (solid black arrow) emits photons at 46.6° relative to it's direction of motion. Half of the photons (green arrows) propagate through the quartz via total internal reflection, while the backscattering photons escape.

face with an angle less than the total internal reflection angle and will thus escape. On the far face, in order to prevent the photons that reflect away from the PMT from escaping, the quartz has a 45° bevel with a mirror attached. The photons can escape from the 45° bevel, but will reflect off of the mirror. In order to minimize effects associated with transitions between materials, the mirror is affixed with optical grease. By placing the mirror, the photons are reflected back into the quartz at the angle they exited, maintaining the desired total internal reflection effect that encourages forward propagation.

The area of the quartz is designed to span the elastic peak in the focal plane from the HRS. As all electrons in the quartz will generate Cerenkov photons, having the quartz span this peak allows us to use the PMT response as a measurement of the electrons scattering elasticall from our target. The thickness of the quartz is selected to balance concerns about statistics and additional processes. The number of Cerenkov photons is proportional to the amount of material the electron passes through, so increasing the thickness of the quartz means there's less sensitivity to statistical fluctuations in the number of photons generated. The maximum thickness of the quartz is limited by the Landau tail of the distribution. When an electron passes through the quartz material, the probability of the incident electron ionizing
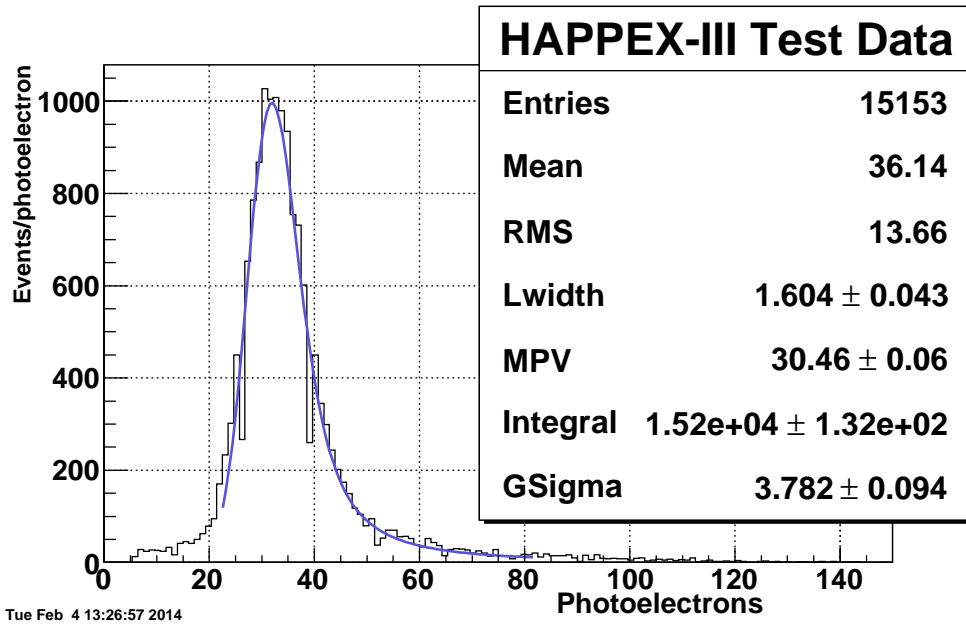
Figure 4.4: Sample fit to a quartz detector design. The fit used is a convolution of a Gaussian, describing the resolution for single electron events, and a Landau function, fitting the additional signal from secondary particles.

an electron in the quartz material, such as δ rays, increases. These secondary electrons also emit Cerenkov radiation measured by our PMTs. The sum of photons from the incident and secondary electrons produce signals described by the tail of a Landau function, increasing the width of the signal associated with a single incident electron. The optimized quartz thickness will minimize the width of the Landau tail, minimizing the width of the signal for a single electron, while maximizing the signal produced per electron.

A sample fit to the data taken using a quartz Cerenkov detector is shown in Fig. 4.4. This function is the convolution of a Gaussian and a Landau function. The Gaussian fit models the generation of photons by a single electron incident on the quartz, which will have some Poisson fluctuations (listed in Fig. 4.4 as 'GSigma') around some average (the 'MPV', or most probable value). The convoluted Landau function fits the events outside of this Gaussian, in the tail of the Landau, where the parameter 'LWidth' describes the width of the Landau function (quantifying the contribution of the Landau to the total fit).

In order to maximize the yield of generated photons reaching the PMT, the quartz is surrounded with an aluminum light guide. This light guide is designed to reflect the photons that do not propagate via total internal reflection within the quartz towards the PMT, attempting to collect some fraction of those photons. Additionally, this light guide

68

will reflect photons that leave the quartz face close to the PMT but would travel such as to miss the PMT face. Adapted from the concept of a light focusing Winston cone, the light guides surrounding the quartz are arranged with trapezoidal mirrors forming a channel that widens near the PMT. Recognizing that all photons have some component of their momentum directed towards the PMT, any photon reflecting off the angled mirror will increase the fraction of momentum along the cone and towards the PMT, improving the yield compared to a flat mirror. However, with reflectivities below unity, a detector design for PREX should minimize the number of reflections from the mirror ('bounces') a photon makes before reaching the PMT.

4.2 Error Contribution for Detected Photons

As alluded to in Sec. 4.1, an optimized detector will maximize the average signal per electron $\bar{x}$ while minimizing the width of the Gaussian-Landau convolution σ_x. The ratio of $\bar{x}$ and RMS σ_x of a data, $\frac{\sigma_x}{\bar{x}}$, defines the resolution of the detector. This resolution describes the precision at which one can determine the number of incident electrons for a given PMT signal.

The resolution of the PMT response to a single electron is important for the PREX experiment. At a flux of ≈ 1 GHz, one cannot determine the signal from individual electrons. However, attempting to measure the number of weakly-scattering electrons from the flux of all electrons requires a detector that can precisely distinguish between small differences in incident electron flux. For a smaller resolution, the signal per electron is more precise, such that the sum of the signal for all incident electrons is narrower, resulting in a more defined relation between the number of electrons and PMT signal. The error on the asymmetry A associated with the resolution of the detector is given by

$$\delta A = \sqrt{\frac{1 + \sigma_x^2/\bar{x}^2}{N}}, \tag{4.3}$$

dependent on the square of the resolution. The N in Eq. 4.3 is the sum of the electrons incident on the quartz over a helicity pair, reflecting the total number of electrons contributing to the signals. As such, minimizing the error increases the accuracy of the asymmetry measurement, asymptotically approaching the statistical error of $\frac{1}{\sqrt{N}}$. This reinforces the importance of minimizing the tail associated with secondary particles, as these will increase σ_x, increasing the resolution of the detector.
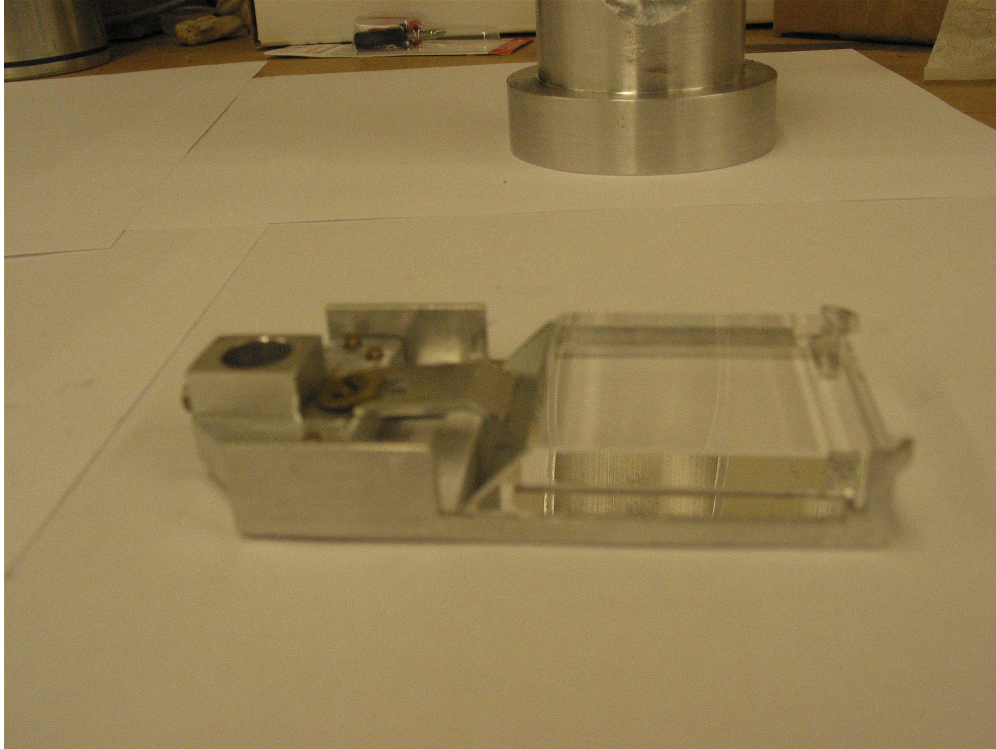
Figure 4.5: From Piotr Decowski, a photograph of an early PREX detector design.

4.3   Early Designs

Early detector designs utilized a small quartz block, with a face 4 cm×5 cm and a thickness of 0.5 cm. These blocks each have at the 45° bevel in order to reflect photons towards the PMT. Our test quartz was assembled from a pair of blocks, such that the beveled faces formed a single plane, with the two blocks attached using a silicone grease. As the number of photons would decrease ≈ 3% transitioning between the air and the quartz, a layer of silicone grease minimizes this loss by filling the air gap between the quartz blocks, therefore optically functioning as a single block. A small mirror was affixed to the beveled face, also with silicone grease, to maximize the reflection at the bevel. This quartz assembly rested on a tray consisting of two indented bars connected to a solid support block and clamped in place via pressure on the mirror, as shown in Fig. 4.5.

The support was then attached to a pipe, 2 inches in diameter, using a post attached to both the pipe and detector stand. This design allowed for a small conical mirror connected to the post, to reflect photons that do not reflect internally, as well as a cylindrical mirror spanning the distance between the conical mirror and the PMT, to direct all photons that would otherwise hit the non-reflective support. The PMT was then inserted into the pipe,

λ (nm)	Aluminum	ALZAK	MIRO-4
365	81%	67%	32%
405	82%	80%	75%
436	74%	55%	90%

Table 4.2: A table of the reflectivity measured for the visible mercury lamp excitation lines for aluminum, ALZAK and MIRO-4 samples.

with the PMT face located 10.2 cm from the nearest face of the quartz. The entire device is then enclosed in a light-tight cover that was then taped in place with electrical tape to prevent stray, ambient light from entering the detector.

Tests on this design focused in finding an ideal material and geometry for the mirror and PMT placement. As mentioned in Sec. 4.1, all reflectors have some probability that a photon will be absorbed (instead of reflected) by the material, decreasing the number of photons reaching the PMT. These tests considered three reflector materials, based on each's listed reflectivity and availability; Anolux-coated aluminum, ALZAK, and MIRO4. The aluminum mirror had a lower reflectivity than the ALZAK, but ALZAK had a cut-off for photons with wavelengths below 300 nm.

The reflectivities of the reflector mirror materials were measured with a mercury lamp and a light meter, as seen in Fig. 4.6. The mirror sample was placed on a 30.5 cm pivot, one end centered under the diffraction grating in front of the mercury lamp. The light meter was supported on a second stand, tied by a 20.5 cm string to the mirror base. We measure the unreflected flux of light with the mirror removed, then insert the mirror. Measurments of the light intensity after reflection at different angles allows us to quantify the mirror reflectivity, as well as average over angles to find the approximate reflection for a given photon energy. The results of this measurement, shown in Table 4.2, informed our decision to use the Anolux-coated aluminum mirrors, with the best overall reflectivity for the visible lines of the mercury lamp.

Also affecting the signal measured was the spacing between the PMT and quartz faces. If the spacing was too small, any superelastic electron, which pass through the detector plane closer to the PMT mimicking electrons with energy above the beam energy, could hit the PMT. Electrons passing through the quartz-windowed PMT create large signals independent of the quartz block and possibly damage to the PMT electronics. Conversely, if the spacing is too large, it will take more bounces for photons to reach the PMT, decreasing our signal. This spacing was tested with a mix of simulations and bench tests, eventually settling on a
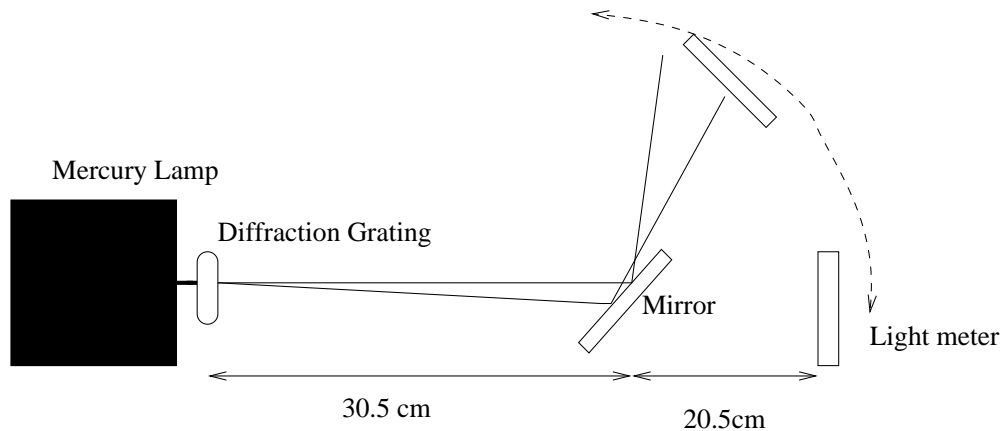
Figure 4.6: Schematic diagram for the reflectivity tests. Light from the lamp is separated by wavelength in the diffraction grating before reflecting off of the test mirror material. Rays continue to separate, allowing us to position our light meter so as to only measure reflected light from each wavelength individually, to compare with the unreflected flux at the same distance from the grating.

spacing of 8 cm.

The detector was tested measuring cosmic rays using a black-box set up at Smith College. In these tests, we fixed the detector in place using an optical filter clamp gripping the tube supporting the PMT. The alignment was rudimentarily checked to be 45° relative to the table such that atmospheric cosmic rays passed through the quartz at the same 45° angle we expected electrons to travel during the experiment. To ensure the signal from the PMT is associated with an energetic muon, we used a pair of scintillators spaced approximately 50 cm apart. One scintillator was hung above the detector, and a second was placed below four 5 cm Pb blocks, with the scintillators' active regions aligned with the quartz. By having the Pb blocks between the scintillators, we ensure that any muon reaching the lower scintillator has some minimum energy (in this case, approximately 300 MeV).

In parallel with these tests, simulations were coded to match the test detector design. The simulations, using the GEANT4 libraries written by CERN to accurately model particle physics processes, simulated a variety of particles and energies passing through the 5 cm×4 cm quartz face at a 45° angle. The simulation used reflectivity numbers similar to the tests run at Smith, but with a calibration to lower the reflectivity to agree with signal size measured in early tests. These tests approximate the reflectivity as 60% for photons with wavelengths below 200 nm, 70% between 200 and 300 nm, and 75% above that. The quantum efficiency of the PMT was added to the simulation, initially hardcoded at 20% in early tests.
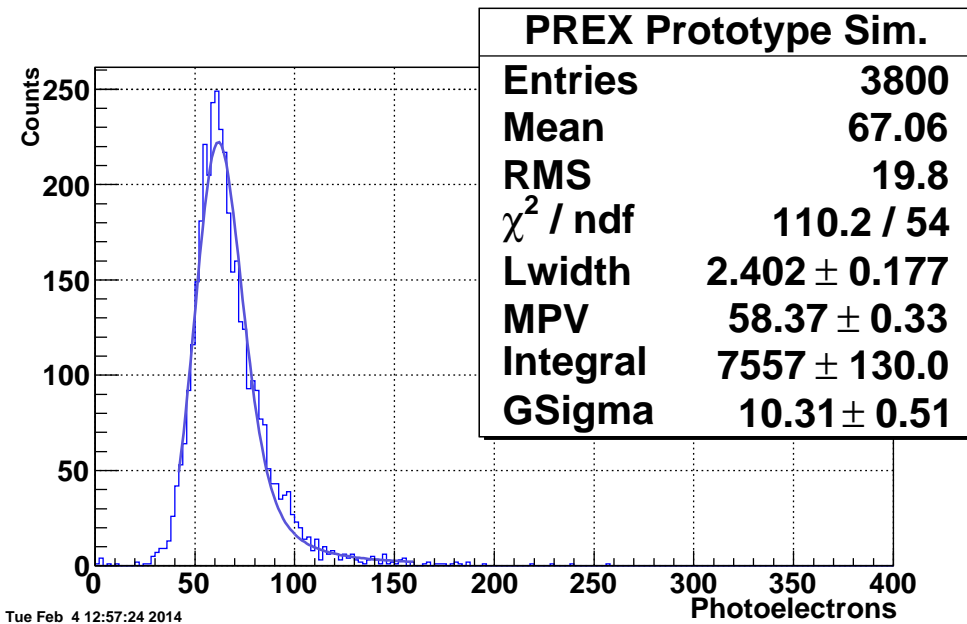
Figure 4.7: Simulation results for the original PREX detector design.

This was later updated to reflect the design specifications of a quartz-windowed PMT, as shown in Fig. 4.2, with peak value of 28% near 420nm. The refractive index of the quartz, defining the Cerenkov photon scattering angle and total internal reflection angle, is coded in terms of photon energy, using data from M. Gericke's study of quartz properties[41], by

$$n(E) = 1.455 - \frac{0.0058}{eV}E + \frac{0.0033}{eV^2}E^2 \tag{4.4}$$

Similarly, the absorption length A for photons in the quartz reported by Gericke follows the form

$$A(E) = e^{4.325 + \frac{1.191E}{eV} - \frac{0.213E^2}{eV^2}} \tag{4.5}$$

These simulations, for the given design, produced a fit with the most probable value (MPV) of the number of photoelectrons to be 58.3 photoelectrons per event with 29% data resolution (Fig. 4.7). This design was then brought to and installed during a commissioning phase for HAPPEX-III, another parity experiment that ran in late 2009. This test used the HAPPEX-III beam, with electron energy 1.204 GeV and on a tantalum target, at an HRS angle set at 14°. On PMT ZK4035, we saw 30.5 channel signals per event, with a resolution of 35%, shown in Fig. 4.8 (previously shown in Sec. 4.1 as a example of the Gaussian-Landau convolution). While the resolution and predicted number of photoelectrons are not

73

HAPPEX-III Test Data	
Entries	15153
Mean	36.14
RMS	13.66
Lwidth	1.604 ± 0.043
MPV	30.46 ± 0.06
Integral	$1.52e+04 \pm 1.32e+02$
GSigma	3.782 ± 0.094

Tue Feb 4 13:26:57 2014
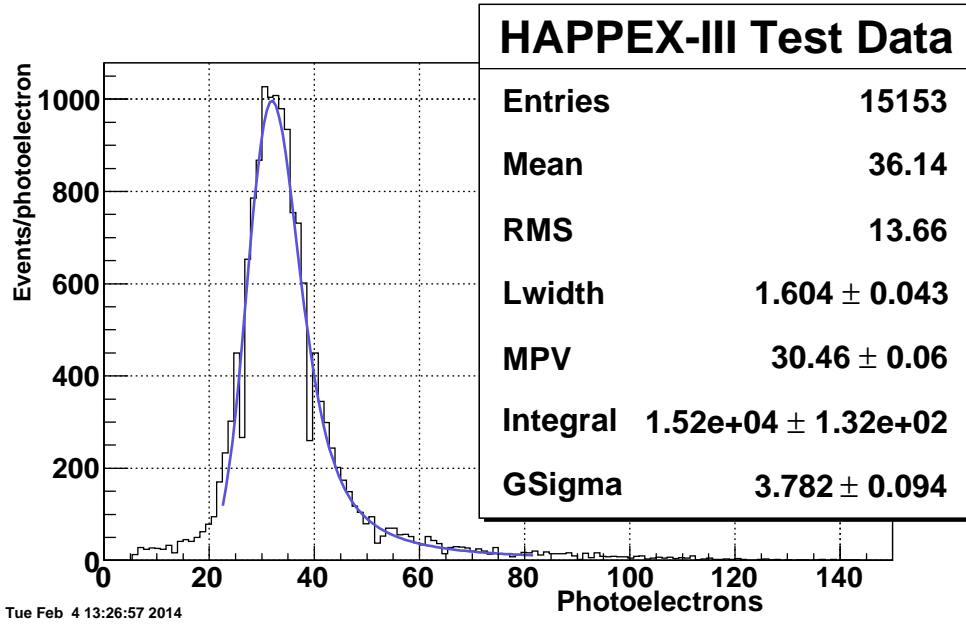
Figure 4.8: Test run results for the original PREX detector design, measured at JLab.

in agreement with simulations, these results marked both an increase from earlier tests and an acceptable signal for the given beam size. As a result, we proceeded with an understanding of the detector function as well as approximate material parameters.

4.4 PREX Detector Simulations

Following this in-situ detector test, simulations performed at Jefferson Lab relating to the electron transport between the target and detector hut found the elastic peak to measure 10 cm by 3.5 cm normal to the VDC face, as described in Sec. 3.5, much larger than the face of the quartz used in early designs. The detector was initially designed to fit the 2 in. PMT face at the mouth of the light guide and wide enough to enclose the quartz block, which allows for a modest 5° angle in the mirror. To design a similar cone for the 14 cm by 3.5 cm quartz block design, the angle of the cone would be 0.2°, an angle found from simulations too shallow to focus the Cerenkov photons towards the PMT. In order to accommodate a longer quartz block and still have the mirrors angled, we adapted the concept of the Winston cone into a trapezoidal design, as each mirror in the trapezoid can be oriented at different angles. Having the freedom to have each mirror angled differently allows us to angle the side mirrors shallowly enough to accomodate the width of the quartz while steeply angling the mirrors above and below the quartz to focus light towards the PMT.

74

Thickness (mm)	MPV (PEs)	Fit Res. PEs	Data Resolution
6	28.6	30.4	30.3%
7	33.2	35.2	30.5%
8	37.88	41.8	29.9%
9	42.6	49.05	29.6%
10	47.0	53.4	30.7%

Table 4.3: Simulation results for the PREX detector design, varying quartz thickness.

Models were tested varying the quartz's position relative to the PMT face, quartz thickness and mirror angles. The PMT-quartz face distance allowed the optimizing of the signal, balancing concerns of super elastic electrons and solid angle. Superelastic electrons which, by scattering and transmission through the HRS, appear more energetic than the elastically scattering electrons would generate sharp signals by generating Cerenkov photons in the PMT's quartz window, so minimizing this effect became a question of maximizing spacing. However, if the PMT was too far away, it increases the number of bounces required for a photon to reach the PMT, leading to more photons being absorbed by the mirrors and not reaching the PMTs. These were studied using a mix of simulation and bench testing.

The final design used trapezoidal mirrors as a light guide and a 14 cm×3.5 cm face. Simulations were run for a variety of parameters, using the freedom allowed by the new mirror and support design. Tests run varying the vertical position of the quartz relative to the PMT showed a preference for having a quartz 0.6 cm below the center of the PMT, taking advantage of the steeper angle in the upper mirror relative to the lower mirror. Simulations were also run varying the quartz thickness; as a 14 cm×3.5 cm active region required custom-ordered quartz, we could optimize our quartz thickness with respect to detector response. Simulations were run for thicknesses between 6 mm and 10 mm, with results in Table 4.3, reporting the central value of the fitted Gaussian (MPV), the predicted number of photoelectrons from the fit and the resolution of the full data set, both described in Sec 4.2.

The detectors were designed in pairs, with a 1 cm 'thick' quartz detector placed upstream of a 0.6 cm 'thin' quartz detector, which allows for redundant measurements for each arm of the detector. These designs produced a 28 PE and 48 PE per event in the simulations made before construction with resolution less than 20%.

4.5 PREX Detector Construction

With a finalized set of designs for the quartz, photomultiplier tube and light guide, it was necessary to design an architecture to support these elements. The designed architecture needed to support the detectors rigidly, in alignment with each other and with the elastic peak, as well as minimize material in front of any quartz block. The design also needed to be somewhat modular, as it was considered that we may need to remove or swap individual detectors. Lastly, the early design phases assumed that the PREX detector stand would include a set of gas electron multipliers (GEMs), to be used for particle tracking during high-current data collection. These GEMs consisted of a rectangular gas chamber, and a set of electronics that extended from two of the chamber's sides. While the GEMs were not successfully utilized during the PREX run, the detector stand was designed to support the GEMs, as well as provide a method by which we could rotate the GEMs relative to each other.

The detector frame was assembled from January to March 2010 between the University of Massachusetts-Amherst and Smith College, as shown in Fig. 4.9. Each detector assembly was designed to be supported from a single, 30 cm×10 cm aluminum plate. By having each detector supported by a single plate, it simplified transport and switching of individual detectors on the stand. A 2" diameter hole was drilled through the center of a plate, matching the diameter of the PMT face, and a circular plate was installed on one side. To securely install the PMT, it was inserted into a PVC pipe that sockets into the opening in the plate shown in Fig. 4.9. For light-tightness, the entire assembly was sealed with electrical tape including the PMT-pipe interface and the various screws securing all assembly elements.

On the opposite face of the supporting plate, the quartz was supported by a pair of aluminum runners, allowing for the quartz to be supported above the light guide with minimal aluminum placed in the path of incoming electrons. For stability, the quartz was held in by u-channel clamps, serving as a lightweight solution that puts minimal material in front of the quartz. To support the runners while still minimizing the amount of material blocking the elastic peak, a long, L-shaped piece was attached to the aluminum support plate and to the runners. Between the runners and clamps, there is little material in front of the quartz, minimizing the pre-showering that would interfere with the Cerenkov photon signal expected. The placement of this rod simplifies alignment of the quartz and PMT.

The light guide was screwed into holes on the plate, with the guide tapering from the 2"
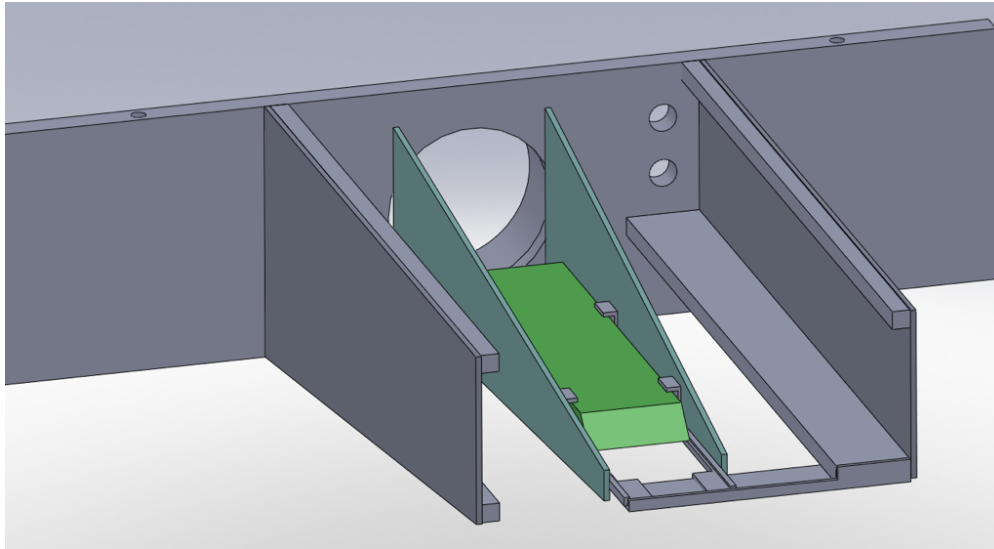
Figure 4.9: Design drawing of the detector apparatus, designed to hold the quartz and PMT. The hole in the center of the plate allows for photons to reach the PMT (not shown). The quartz rests on rails, facing the PMT, surrounded by mirrors on the side, as well as top and bottom (not shown).

opening, past the quartz, down to the spacing of the supporting angle brackets. The side and upper mirrors were a single piece of Anolux-UVS aluminum bent into shape, while the mirror below the quartz was attached separately, allowing us to assemble the light guide without having to enclose the L-shaped support bar. These mirrors had flanges which could be screwed into matching holes on the plate, ensuring the light guide is properly oriented to maximize the reflected photon yield. Additionally, a pair of LEDs were clipped to the quartz support rods, nearest to the PMT, in order to be used in in-situ test of the PMT. These required two holes for BNC feedthroughs, providing power to the LEDs without affecting the light-tightness.

Also attached to the aluminum plate were three square rods which, with the bar connecting the quartz support to the plate, supported two thin aluminum sheets. These sheets, oriented parallel to the quartz, accomplished three goals: to stabilize the quartz support, to shield the mirrors and quartz from damage, and to serve as a frame for the light-tight components. The entire frame was made light-tight by a layer of kapton foil, attached with black electric tape to follow the side walls and encompass all detector components.

These aluminum plates are attached to the supporting structure. In order to measure the same flux, the detectors were oriented so their quartz were both in the beam line, which required the frame design to be long enough to support the two detectors offset vertically
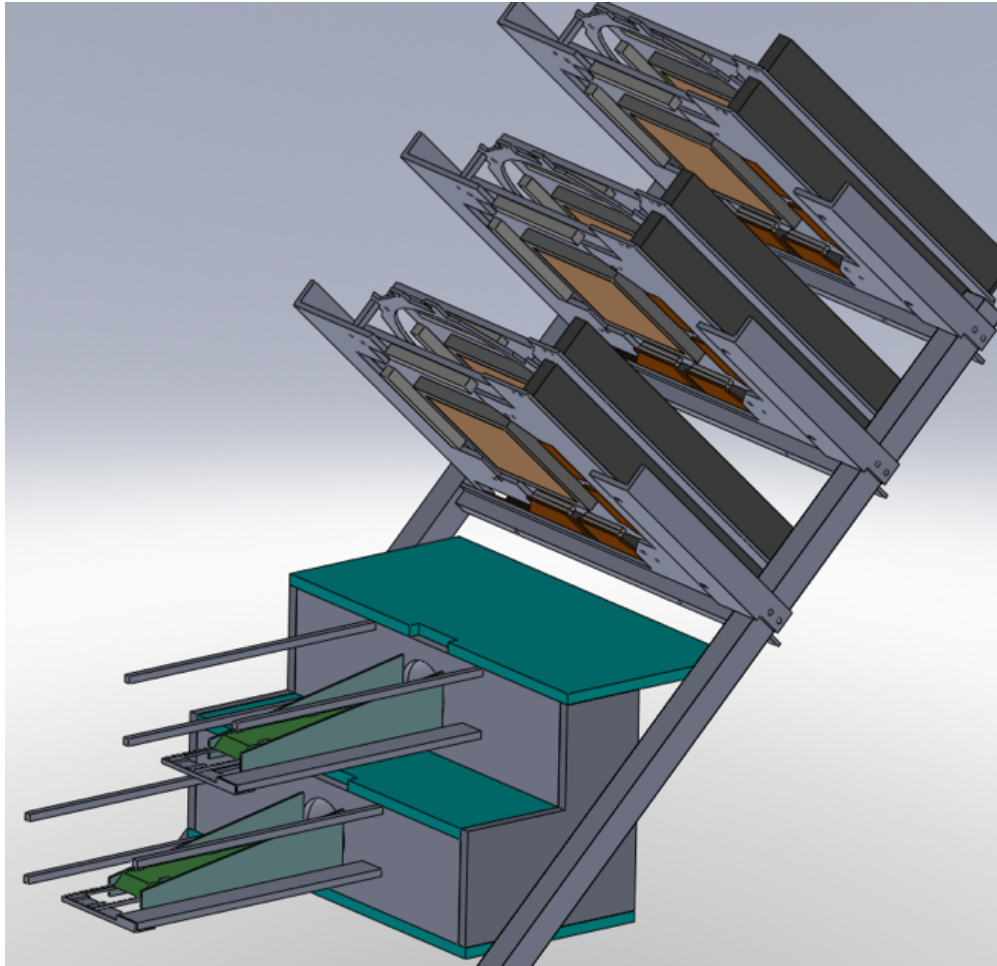
Figure 4.10: The design for the detector stand. The quartz blocks are attached to the frame, with the rods supporting the GEMs held by bars along the same 45° line based on the direction of motion for electrons through the detector hut.

and horizontally. The frame was designed with two levels, connected to the same baseplate by two aluminum plates which both detectors screwed into, as well as two spanning plates for stability. This also allowed bars to run at 45° relative to vertical from the box which we could mount the GEMs on. The complete design is shown in Fig. 4.10, as well as in the design for the detector hut (described in Sec. 3.6) in Fig. 4.11. In the lab, these detectors were supported over the VDCs, minimizing the distance between the tracking from the VDC and the quartz faces, such that the elastic peak, as measured in the VDC, did not propagate a long distance between the top of the VDC and the PREX detectors.

As the face of the quartz was designed to exactly fit the elastic peak, the placement of the detector became important. In order to efficiently align the detectors with the elastic peak, as described in Sec. 3.6, the entire detector stand was mounted on a pair of movable

78
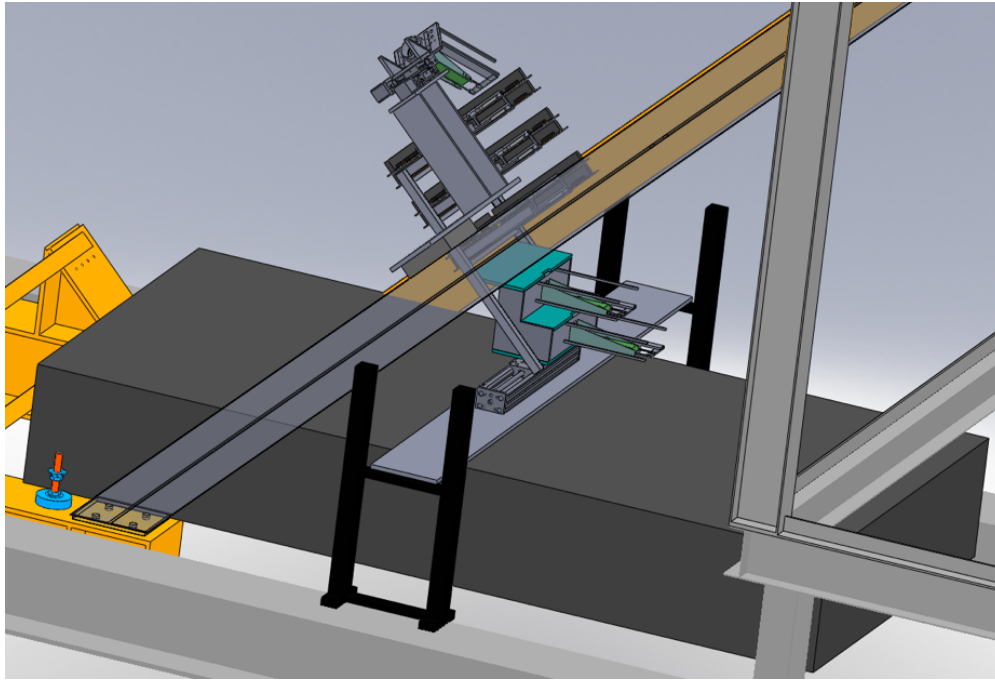
Figure 4.11: Showing the detector stand in context of the detector hut at JLab. The entire apparatus rested above the VDC, supported by a plate held on either side.

stages. These Velmex VX-model motorized stages, attached to the frame of the detector hut, could be controlled remotely. The ideal location of the detector stand was found by measuring the profile of the elastic peak in the VDC with and without cuts on the data for a quartz signal. With the final alignment shown in Figs. 3.19 and 3.20, the stages were used to test various locations in order to maximize the alignment between the elastic peak and our quartz blocks.

During the installation phase of the PREX experiment, low current runs were taken with the detector installed in the hut in order to quantify the expected signal per incident electron of the final design. These runs were performed to benchmark the final, assembled detectors relative to the expectations from the simulations. The results, as shown in Fig. 4.12 through 4.15, show the thin detectors, #1 and #3, expect 12 PEs per incoming electron and the thick detectors, #2 and #4, expect 23 PEs. These signals were sufficiently large, per electron, to produce an acceptable integrated signal per helicity window. Analysis of the integrated data is described in Ch. 5.
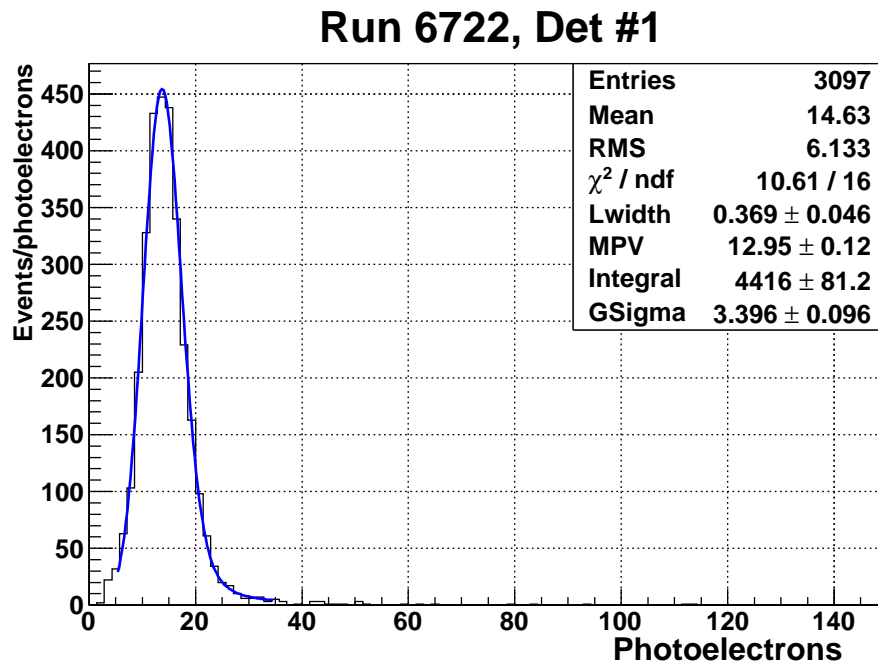
Figure 4.12: ADC spectra for run 6722, Det.#1. Data converted from ADC channels to photoelectrons.
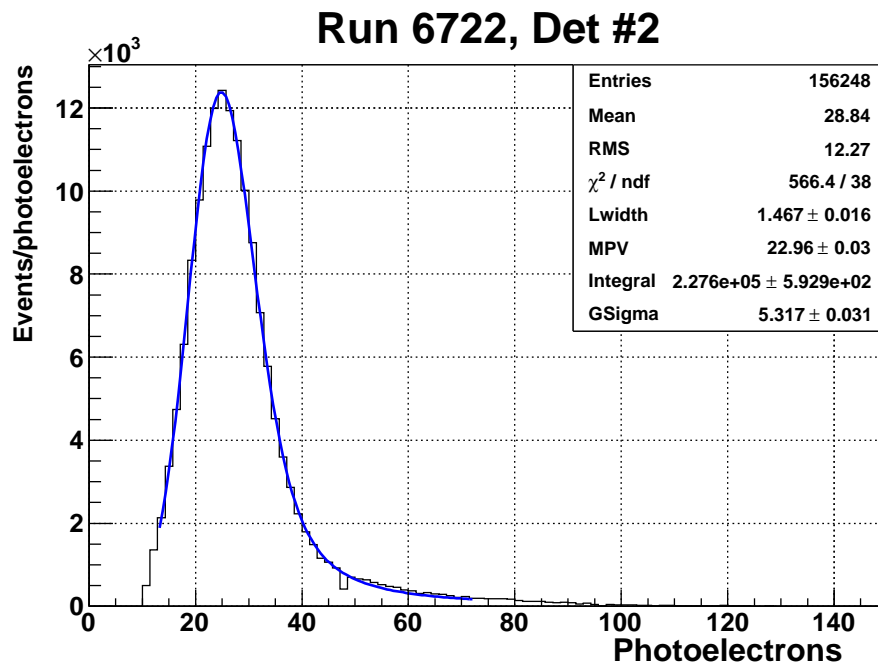
Figure 4.13: ADC spectra for run 6722, Det.#2.
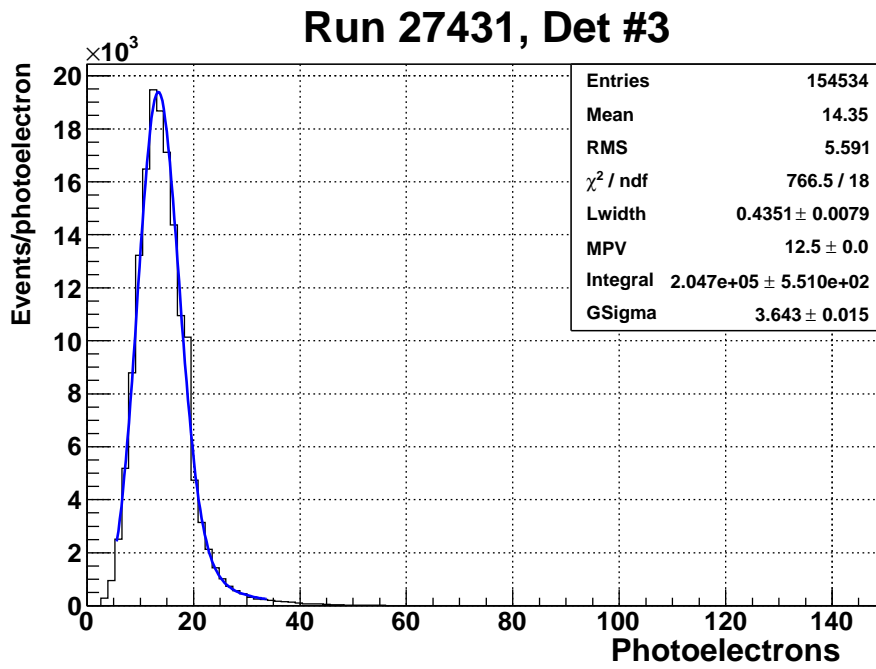
Figure 4.14: ADC spectra for run 27431, Det.#3.
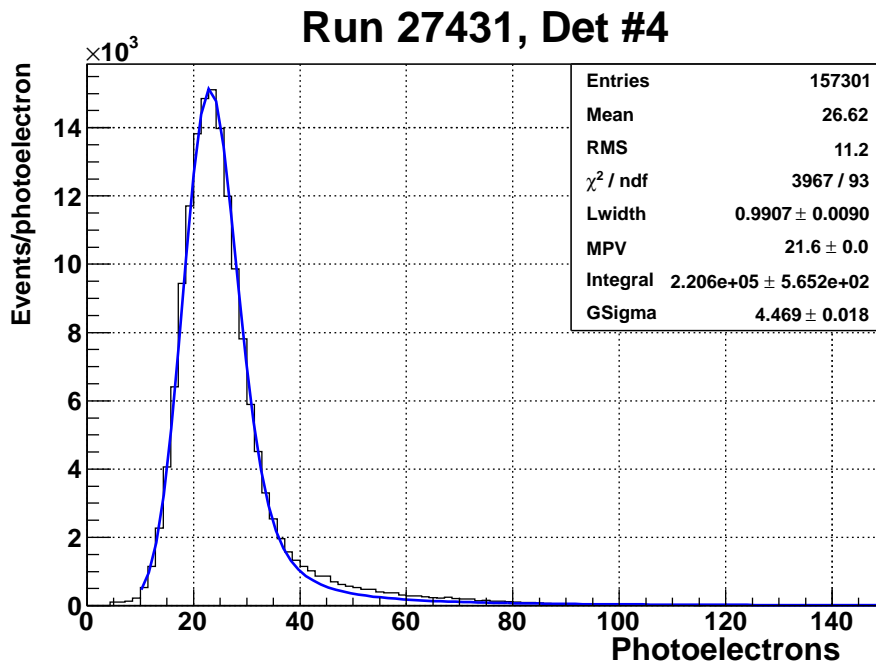
Figure 4.15: ADC spectra for run 27431, Det.#4.

4.6   Final Design Tests

Following the experiment, we tested the design again to ensure our measurements in-situ were in agreement with expectations as well as reproducible. Results for tests using cosmic muons, shown for the thin right-arm detector Det #1 and both thick detectors #2 and #4 in Figs. 4.16 through 4.18, agree on the resolution of the fits, but disagree on the predicted number of photoelectrons. For this measurement, a cosmic ray test set-up was built at the University of Massachusetts-Amherst. Given the space available to the PREX detector group at University of Massachusetts-Amherst was located on the 4th floor of a 16 floor building, the apparatus was designed to be able to pivot and measure the cosmic ray flux from angles away from vertical. Tilting the entire apparatus allows us to fix the required geometric orientation of elements without requiring ourselves to measure the flux of cosmic rays passing through 12 floors of building material.

In addition to the construction of a detector stand, the UMass-Amherst cosmic ray detector required the wiring and design of a data acquisition system. This system, identical to the Smith College cosmic stand described in Sec. 4.3, would be required to identify the presence of a cosmic ray traveling at $\approx 45°$ relative to the quartz face and to record the signal measured by the detector in response to the cosmic ray. An additional function for the UMass-Amherst cosmic ray test apparatus involved making periodic measurements of the detector signal when not triggered by the scintillators, making a distinctly tagged measurement of the dark current associated with the PMT and electronics in use.

4.6.1   Stand for Cosmic Ray Measurements

The design for a stand was based on the Smith College test set-up (see Sec. 4.3), consisting of a pair of scintillators, sensitive to charged particles, with active regions aligned with the quartz, with the quartz oriented at 45° relative to the scintillators. This design, from the same argument in Sec. 4.3 will measure photons generated at angles such that the photons are trapped in the quartz by total internal reflection. The second design requirement is that the scintillators are oriented such that the PMTs were not vertically aligned, minimizing the likelihood that the scintillators produce coincident signals without a cosmic ray in the detector. To minimize the material used, we favored aligning the scintillators anti-parallel, leaving only the active regions aligned.

A major concern for the design was the Pb blocks, used to ensure the cosmic rays had
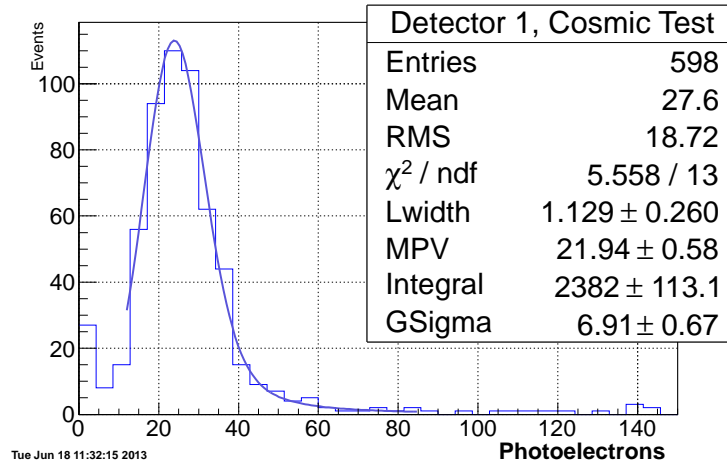
Figure 4.16: Detector #1 signal for cosmic muon test run at UMass-Amherst. The signal has been converted from channels to photoelectrons at the cathode. The signal is fit to a convolution of a Gaussian and Landau function.
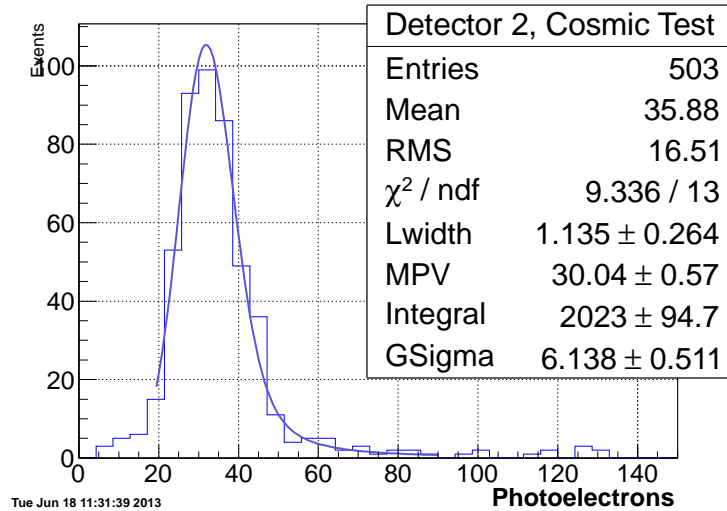
Figure 4.17: Cosmic test signal for detector #2, also converted into photoelectrons.

Detector 4, Cosmic Test	
Entries	501
Mean	39.42
RMS	19.47
χ^2 / ndf	12.39 / 13
Lwidth	1.282 ± 0.308
MPV	33.33 ± 0.62
Integral	1921 ± 94.0
GSigma	6.64 ± 0.66

Tue Jun 18 11:30:05 2013
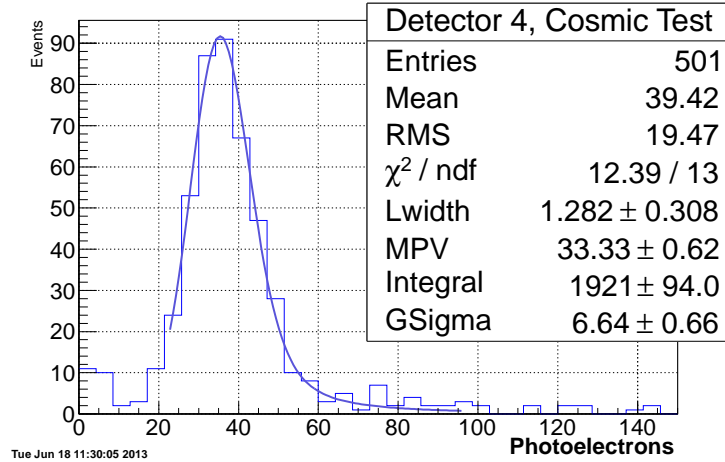
Figure 4.18: Cosmic test signal for detector #4, also converted into photoelectrons.

an energy of at least 300 MeV. The blocks available, needed to cover the entire scintillator active region while still being 20 cm thick, weighed 44 kg, loaded above a fragile scintillator in a way that we could tilt towards the window. To protect the scintillator and allow the entire stand to tilt, the blocks rest on a $\frac{1}{2}$" thick aluminum plate above the scintillator, with a $\frac{1}{2}$" backstop to prevent sliding once the detector is tilted, protecting the scintillators and detector in the case of catastrophic mechanical failure. Lastly, the 45° support for the detector was fabricated to fix the angle between the scintillators and detector as well as maintain said angle when the entire apparatus tilts.

The entire assembly, with diagram shown in Fig. 4.19, is constructed from aluminum, for cost and machining simplicity, with most elements resting on the aluminum plate. The scintillator, as shown in Fig. 4.20, were installed on pairs of runners, with a thin angle bracket holding the scintillator in place and a thick, square rod supporting the weight. The thicknesses and spacings for all parts were chosen such that the active region of the scintillator was held between these runners and level with the base of the test stand for the scintillator's PMT resting on the test stand. To prevent the conical extrusion between the scintillator's active region and PMT from interfering with the alignment, a recession was cut into the bars to accommodate this feature. The detector, as shown in Fig. 4.21 is supported by an angle bracket spanning two hollow square rods. These rods are supported by two solid rods, such that the hollow rods are held at 45° to the base of the stand. For extra stability, the unfixed end of the hollow bars rests against an angle bracket, spaced to again ensure 45°. Lastly, the entire apparatus is lifted by two thick threaded stainless steel rods able to

84

support the 45 kg of lead in addition to the other construction materials.

4.6.2   Cosmic Ray Detector Data Acquisition

The data acquisition system (DAQ), with a schematic shown in Fig. 4.22, accepts the scintillator and detector signals, writing the detector signals out to the controlling computer. The NIM crate contains a discriminator and logic module to process the scintillator signals into a gate signal, as well as a Canberra Model 3002D high voltage power supply for the scintillators, set to -1750 V, and a Bertran Associates Model 315 power supply for the detector PMT, set to -2000 V. The CAMAC crate, responsible for recording the detector signal and passing it to the controlling computer, has a computer-crate interface module and a CAEN C1205 integrating ADC.

To create the signal that triggers the DAQ to read data, the scintillator signals were processed to make a single gate pulse. The signals from each scintillator were separately connected to the EG&G ORTEC 935 QUAD-CFD discriminator module. This module checked for the input scintillator signal to be above a given threshold and, if found, produced a constant -1V signal. These signals were combine in an EG&G CO4010 logic module, programmed to output a -1V square signal when the two inputted signals complete the logic demanded by the module, in this case passing the inputs through an AND gate, identifying times where both scintillators measure a particle. The signal output from the AND gate is called our scintillator trigger, produced in response to the scintillators both measuring a healthy signal. This scintillator trigger is sent to the CAEN C1205 integrating ADC and the WIENER CC-USB CAMAC controller module in the Computer Automated Measurement and Control (CAMAC) crate. In response to this scintillator trigger, the ADC records the signal measured in the serial bus of the CAMAC crate and the controller records that a scintillator trigger was sent. The computer running the DAQ, connected to the CAMAC controller module, queries the crate every 30 seconds, and if a signal was recorded writes the resulting signal to a file for analysis.

If no event is recorded, the DAQ records an event measuring the dark current, referred to as a USB trigger (to distinguish from an event triggered by a scintillator coincidence). This command is sent by the CAMAC crate to a separate CO4010 module, set up with the logic OR in combination with the scintillator trigger. By having the pulse identifying the scintillator trigger and USB trigger come from the same logic module, we ensure that the triggering pulses have the same length (40 μs, the minimum allowed by the CO4010),
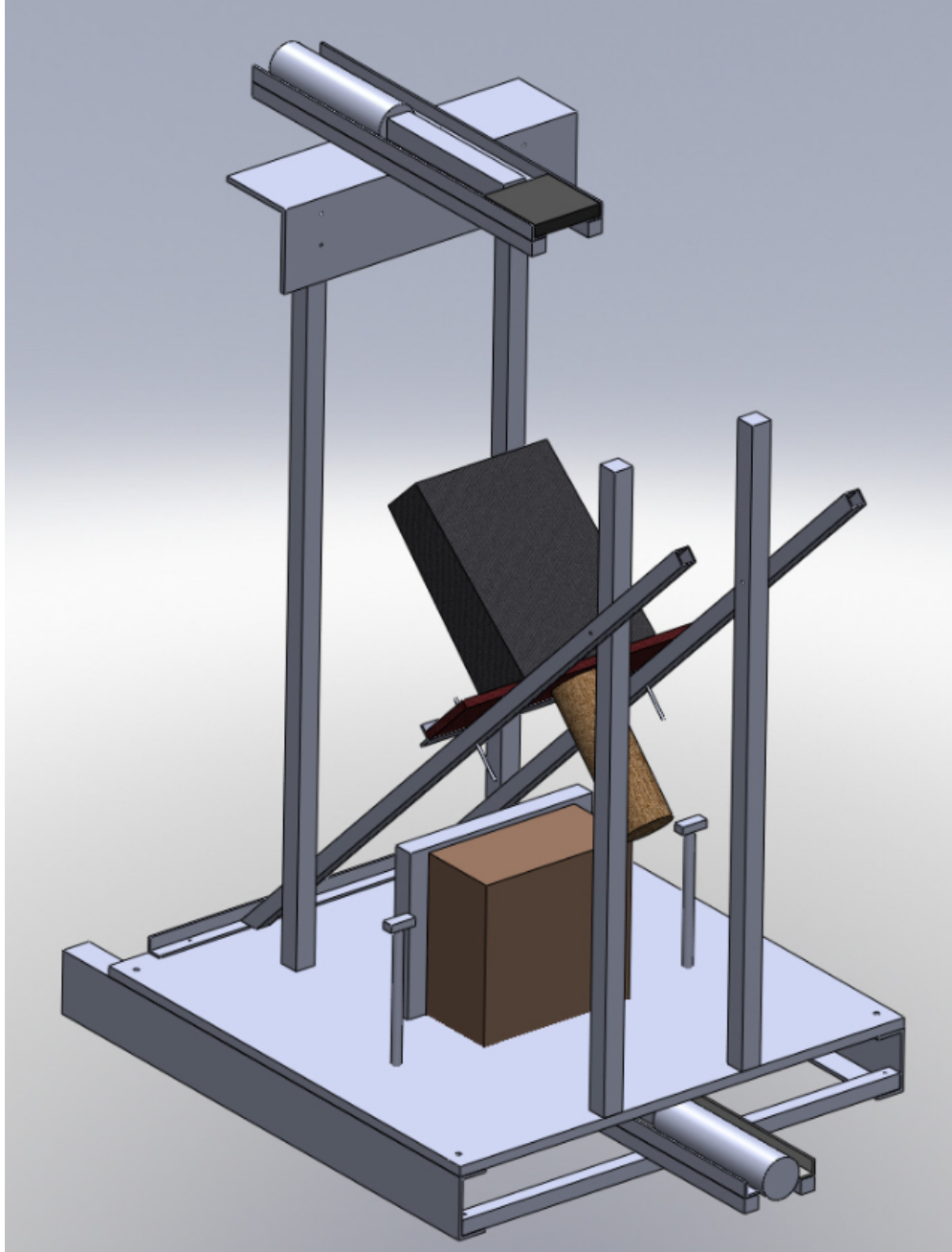
Figure 4.19: Stand design for the cosmic tests run at UMass-Amherst. Cosmic rays pass through the active region of the upper scintillator then through the quartz. The four 5 cm thick lead bricks, used to reject low energy rays, rest on a $\frac{1}{2}$" thick aluminum plate, which is suspended above the second scintillator used for the gate signal.
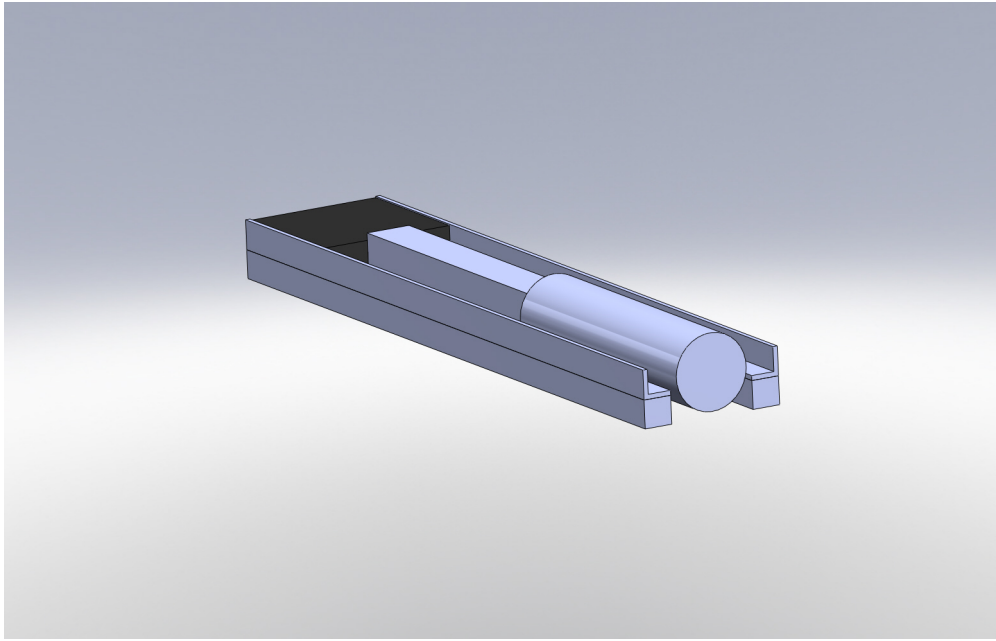
Figure 4.20: The scintillator support. A pair of angle brackets and square bars to support the scintillator level with the apparatus.
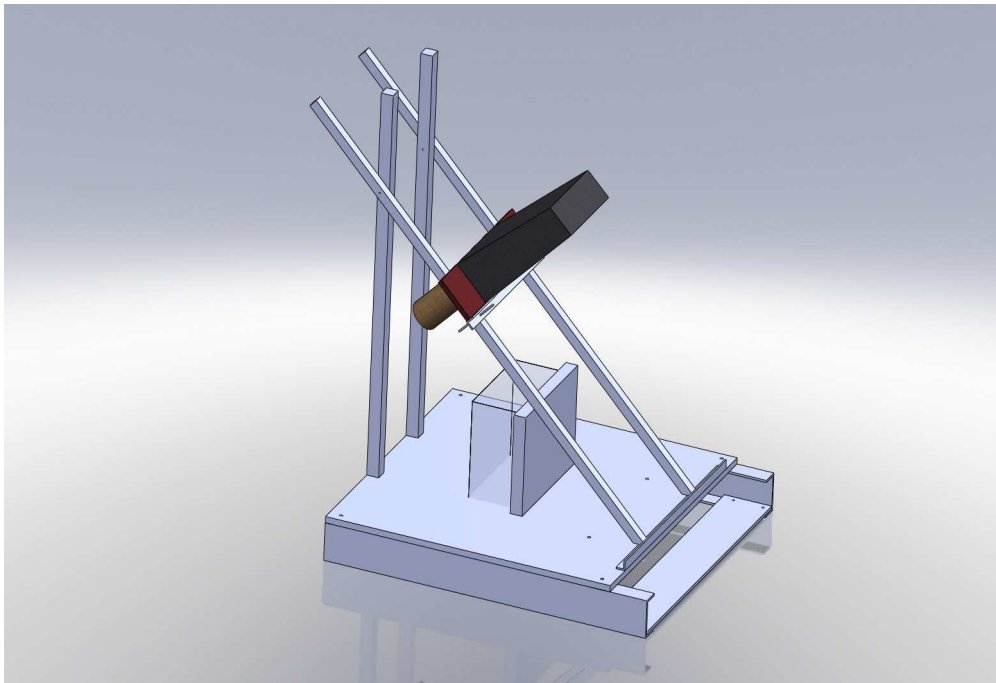
Figure 4.21: Detector support. The detector rests on an angle bracket, spanning two bars. The stand is designed so that the bars (and therefore detectors) are held at 45° relative to the solid base.
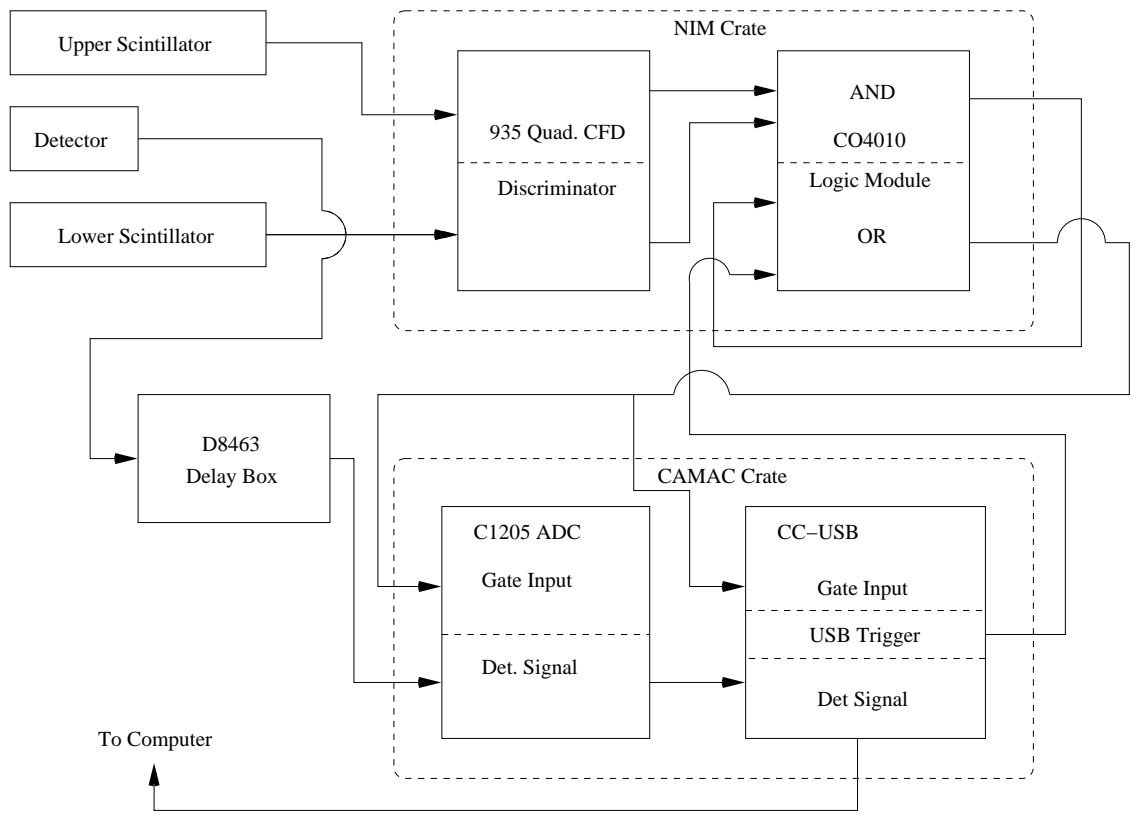
Figure 4.22: Schematic of the DAQ wiring. The scintillator signals go to the NIM crate, where they are processed with a pulse from the CC-USB CAMAC controller into a single gate pulse. This gate pulse is passed to the CAMAC crate in order to send a coincidence detector signal to the computer for analysis.

resulting in the integration time, and therefore dark current, for all events to be equal regardless of the trigger source. By triggering this measurement from the computer, we can identify these events with a separate tag in our data stream, marking them as distinct from events with cosmic rays passing through our detector.

The processing of the scintillator signal takes a measurable amount of time, such that the cosmic ray has already passed through the detector before the gate from the CO4010 can be sent to the CAMAC crate. To ensure the detector signal arrives at the integrating ADC in time with the gate signal, the signal from the PMT is delayed using a EG&G Model D8463 delay box. This delay box is wired such that each switch on the front of the delay box adds a specified delay between the input and output signals, allowing us to modify the timing that the detector signal takes to reach the ADC. These delays are added by adding resistors to the circuit, increasing the amount of time the current takes flowing between the input and output of the box. Starting from increments of 0.5ns, we can delay the signal up to a total of 254ns by using all resistors. Our signal required an approximately 130 ns delay to align with the trigger from the scintillators, with the detector signal registering in the center of the gate signal when compared on an oscilloscope. The detector signal was then connected to a CAEN C1205 model ADC module in the CAMAC crate, with the C1205 chosen for is high sensitivity of 21 fC/channel. The trigger from the logic module is connected to the CC-USB controller module and C1205 ADC, causing the converted detector signal to be recorded in the controller, where it is stored until reading by the computer controller.

Using this stand, this apparatus was used to test the results for cosmic muons passing through detectors 1, 2, and 4; detector 3 was omitted from cosmic ray tests as it was disassembled after the PREX run for comparison testing against the Smith College cosmics stand and never fully reassembled. The first tests done were to optimize the angle of the apparatus relative to the vertical, performed by changing the angle in increments of five degrees for 24 hour runs. It was found that the event rate increased from approximately 1 event every 40 minutes at 0° to a peak of 1 event every 20 minutes at 20°, before the event rate dropped off again.

With the DAQ, stand and alignment finalized, each detector was tested for 500 non-pedestal events, with the event number chosen to balance concerns about signal size and run time. The determination of non-pedestal was made based on a running fit of 50 USB-triggered events, rejecting all events that fall within 3σ of the continuously updated pedestal mean. The DAQ outputs the signal in terms of channels, which is dependent on the elec-

tronics used. The appropriate calibration for the detectors is photoelectrons at the cathode for a single event, which describes the signal yield per individual lepton. The conversion between channels and cathode photoelectrons (PEs) is the product of the sensitivity of the ADC, in fC/channel, the gain of the PMT, and the charge of the electron. The gain for the CAEN C1205 is 21 fC/channel, while the gains at -2000V are listed in Table 4.1.

The PE calibrated data sets were then fit to a convolution of a Landau function and Gaussian function, identical to the fit described in Sec. 4.1. This fit extracts the mean number, or most probable value (MPV), for the number of photons reaching the PMT, and as well as its statistical variance σ for the Gaussian (GSigma). Applying this fit to the cosmic test runs, we found results shown in Figs. 4.16, 4.17, and 4.18.

From the data measured, the two thick quartz detectors (#2 and #4) have a fit resolution, defined by

$$\text{Res.} = \frac{\sigma_G}{MPV} \tag{4.6}$$

of Res.$_{D2} = 20.4 \pm 1.7\%$ and Res.$_{D4} = 19.9 \pm 2.0\%$, showing the two thick quartz detectors function similar to each other. Detector #1, the untouched thin quartz detector, showed a resolution of 31.5%. In addition, these results compare similarly to the results from early in the PREX run where the detector signals were measured. While the absolute scale of the measurements disagrees, the resolutions of detector #1 was measured as 26.4%, detector #2 23.1% and #4 20.6%. This suggests that, from considerations of the resolution for our fits, the behavior of the detectors is consistent between measurement apparatuses.

4.7 Detector Tests at the MAMI Microtron

PREX detector #4 was brought to the accelerator at the Johannes Gutenberg Universität in Mainz, Germany for additional testing using an electron beam. The Mainz accelerator, MAMI, creates electrons through stimulation of strained GaAsP, which are then diverted into a linear accelerator, accelerating the electrons to 3.5 MeV. These electrons then pass through three sequential race track microtrons[42]. Fig. 4.23 shows both a schematic for a racetrack microtron as well as a diagram showing the location of these microtrons at the MAMI site. In each microtron, there is a single leg which contains the accelerating components, creating accelerating gradients of 20 MeV/m[42]. Electrons that pass through this leg enter one of the recirculating end caps. These end caps are designed to, for electron
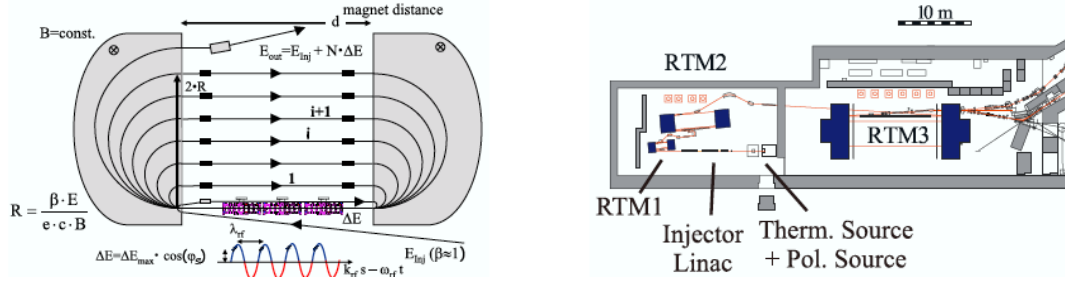
Figure 4.23: Reproduced from Jankowiak[42]. Left: Schematic of a racetrack microtron, demonstrating the recirculating magnets. Right: Diagram of the MAMI accelerator, with the injector and three racetrack microtrons. The detector was placed after the third microtron (RTM3).

energies associated with an integral number of passes through the accelerating leg, bend the electrons into return pipes and then back into the accelerating leg. This allows the MAMI accelerator to create electrons of up to 850 MeV using one set of accelerating components in each of the microtrons.

Running with the quartz at 45° to the MAMI beam line, the signal from the detector was measured for the beam at a grid of 15 points, with five points spanning the 14 cm quartz length, each with three points scanned perpendicular to the beam. These positions were on axis of the quartz (center), as well as 0.8 cm(off center) and 1.3 cm (edge) from the center of the quartz. We assume the signal will be symmetric about the central axis of the quartz, and as such only measured the off-center and edge points in one direction. For these scans, we found a most probable value peaks nearest the quartz, around 24 photoelectrons, before dropping to a 19 photoelectrons over the length of the quartz. Additionally, the data predicted by our Gaussian fit matches this result, supporting our claim of the fit's accuracy in predictions. The data also showed the resolution of the signal, independent of fit, at around 25%. These results are plotted as a function of distance from the nearest point in the quartz to the PMT in Figs. 4.24, 4.25, and 4.26.

The measurement of approximately 20 photoelectrons per incident electron is similar to the results measured using an electron beam at Jefferson Lab (producing an MPV of 23 photoelectrons). This suggests that our previous measurements were correct for accelerator electrons passing through our detectors and reproducible outside of Hall A. The negative trend in photoelectrons measured, as shown in the results based on MPV and fit resolution, is a function of the detector construction. As the electron passes through points closer to the PMT, the face of the 2 in. PMT covers a larger solid angle of Cerenkov photons leaving from
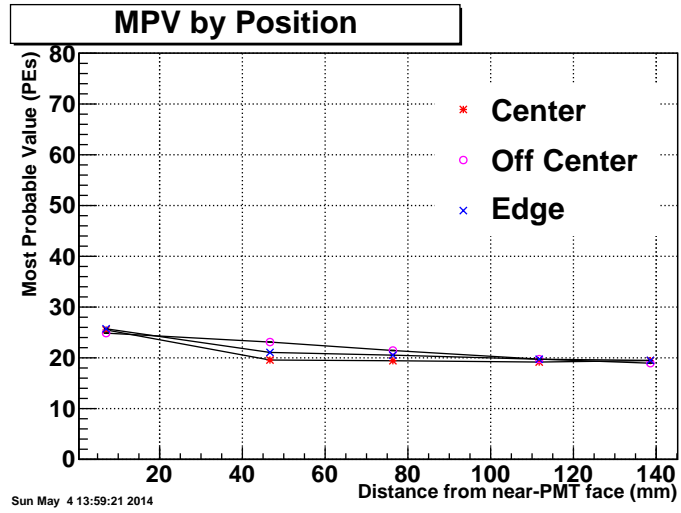
Figure 4.24: Most probable values of PEs, as fitted to the data from the test at Mainz on PREX detector #4. The positions are measured relative to the face nearest the quartz, with the different colors for the center (blue), off center (red) and edge (purple) scans.
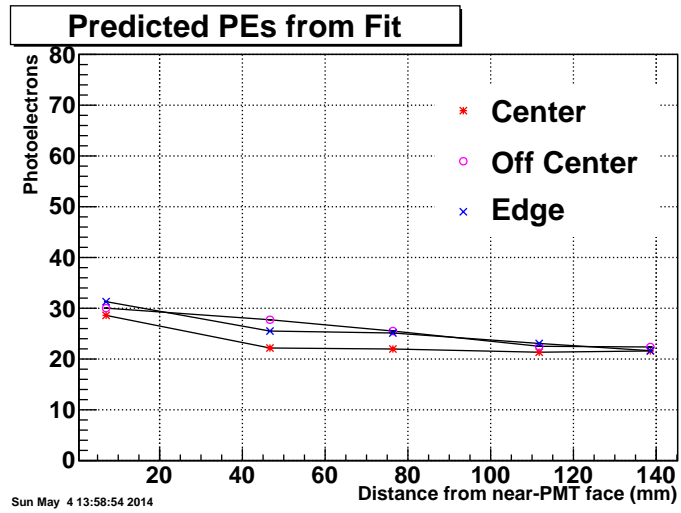
Figure 4.25: The calculated photoelectrons based on the resolution of the fit, as taken at Mainz.
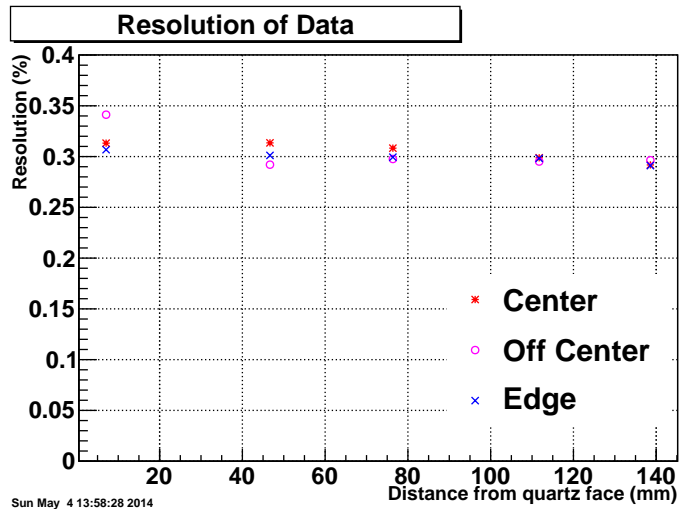
Resolution of Data

Figure 4.26: Data for the resolution $\left(\frac{RMS}{Mean}\right)$ for the position scan of the PREX detector taken at Mainz.

the PMT face, maximizing the number of photons that travel directly from the quartz to the PMT. Additionally, the electron passing through the quartz closer to the PMT reduces the number of bounces a photon must make to reach the PMT, reducing the likelihood the photon is absorbed by the reflectors in our light guide.

Additional runs taken at Mainz checked alternate configurations for Cerenkov photon measurements in order to improve yields in future experiments. From those results, we see a preference towards moving the quartz closer to the PMT, as shown in Fig. 4.27, comparing yields for the nominal quartz-PMT distance, 5.9 cm, to yields from a distance of 3.5 cm. This change increases the yield from around 20 PEs to 50 PEs, similar to the 280% increase in solid angle measured between 3.5 cm and 5.9 cm. This dependence on solid angle can be capitalized on in future detector designs.

4.8 Detectors Possibilities for Future Experiments

Given the opportunity to test alternate detector configurations using the electron beam at Mainz, a pair of detectors were assembled at University of Massachusetts-Amherst to test quartz material properties in preparation for future parity violating electron scattering experiments at Jefferson Lab. These other designs tested geometries that did not require any sort of light guide, attempting to maximize the signal for a design with only the quartz, the PMT, and a supporting frame. The goal of the UMass test group was to determine the quartz orientation that maximizes the signal leaving the face of the quartz in the direction

93

MPV by Position
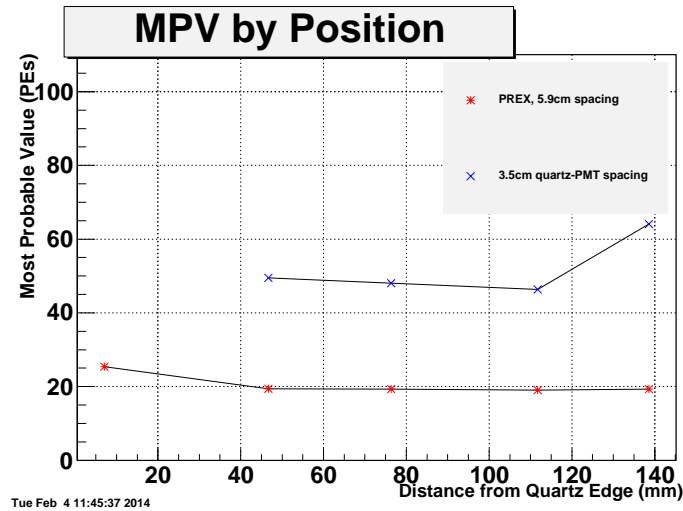
Figure 4.27: Data for MPV recorded in the center scan of the PREX detector taken at Mainz, comparing the PREX scan (red) to a scan with the quartz moved forward 1.4 cm (blue).

of the PMT.

The first design tested was the direct analogue to the PREX detector. The quartz was placed 2.5 cm from the face of the PMT, with the centers of the quartz and PMT aligned. Following the quartz support design in the PREX detector, the quartz is supported using small clamps attached to thin angle-bracket running along the quartz. These thin angle brackets are attached to a thicker angle bracket, used to support the weight of the quartz and additional material used for light-tightness. Unlike the CAD design, shown in Fig. 4.28, a decision on-site flipped the orientation of the support such that the supporting runners were upstream of the quartz. The runners were attached to an angle bracket, in turn attached to a supporting plate. The supporting plate reflects early design choice for a detector where each detector design possibility was supported by a single plate, allowing us to change between designs by swapping support plates. While a number of alternate designs did not perform adequately in preliminary simulations, the choice of the plate remained in the design.

The photomultiplier tube support was modeled directly after the PREX design, featuring a PVC pipe lathed so as to match the shape of the PMT, improving the light tightness and stability. This PVC pipe is then inset on a support plate. Unlike the PREX design, where the PVC pipe fed through the plate to improve light tightness around the PMT, designs requiring the quartz and PMT as close as possible forced the design choice of having the pipe only feed into a metal tube used to mate the PVC and the support plate. Without the
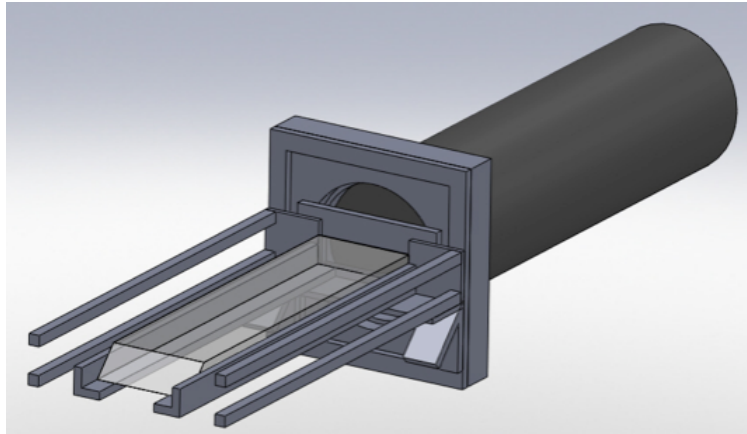
Figure 4.28: CAD drawing of the flat MOLLER detector design.

PVC pipe feeding through the entire plate, the design allowed for an inset on the opposite face that were used to support 3 mm thick long-pass optical filters.

A second design branched away from the PREX design by changing the orientation of the quartz. This design, referred to as the 'angled quartz' orientation, requires the small beveled face of the PREX quartz be parallel with the face of the PMT. As shown in Fig. 4.29, the quartz is supported at a 45° angle in this alignment, using an identical clamp/runner system. The supporting angle bracket could not be moved out of the way of the quartz in this design, blocking some of the material. In this design, the angle bracket connecting the supporting runners to the plate is instead connected to a pair of fabricated 45° blocks to enforce that angle relative to the PMT, with the support plate put in contact with the PMT support (identical with the flat quartz design's PMT support).

In this design, the quartz is oriented with the large face normal to the beam. Given that the total internal reflection and Cerenkov angles are 43° and 46° respectively, a photon generated by an electron traveling normal to the quartz face will be trapped by total internal reflection until it reaches the beveled face positioned 3.0 cm from the PMT, a half centimeter further than the flat design spacing. The difference in spacing between the flat and angled designed stems from the usage of the same PMT support/base plate design, where the additional components required to support the quartz at an angle add material and therefore space between the quartz face and PMT. This design relies heavily on the polish and quality of the quartz and the orientation of the quartz relative to the beam: any chips or cracks in the quartz will allow total internal reflection electrons to escape, while having a 3° difference in the total internal reflection angle and Cerenkov scattering angle means that for any angle
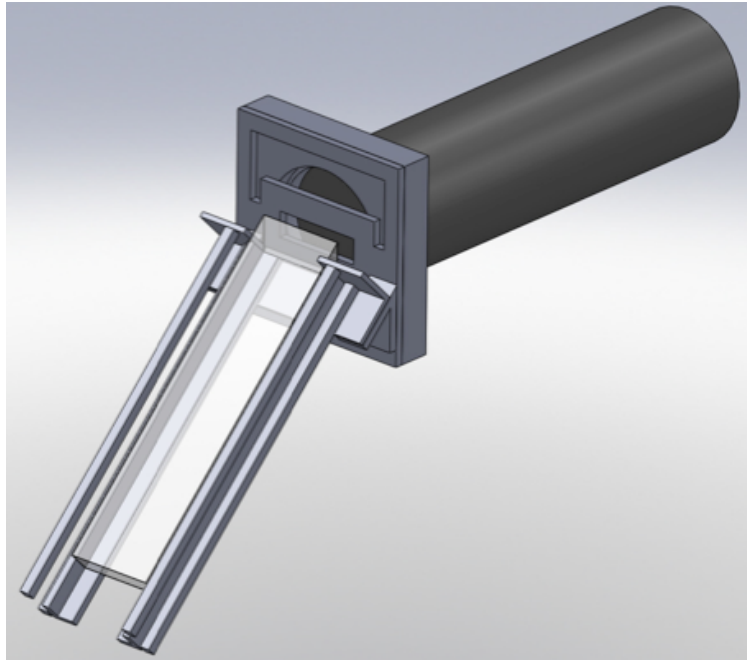
Figure 4.29: CAD drawing of the MOLLER detector design using an angled quartz.

beyond that all photons will not reflect internally and escape, yielding a dramatically reduced signal. The benefit of such a design is that 100% of the photons will reflect internally, instead of the 50% for the PREX design, improving the yields for any single electron.

Simulations on these detectors showed a 31 photoelectron MPV for the flat design and 44 PEs for the angled design, which showed a preference towards the angled design. However, cosmic tests, performed at UMass, found 15 PEs for the flat design but only 6 PEs for the angled case. This is a function of the angular dependence for total internal reflection allowing a 1.5 degree variation from the design-intended 45° angle. The stand is oriented to hold the quartz at 45° relative to the trigger scintillators. However, the spacing and size of the scintillator active region allows a 5° acceptance, meaning a number of measured signals were outside the angular range that produces electrons scattering by total internal reflection. As a result, this effect could be responsible for measured signals with low numbers of photons.

As previously stated, data was collected at Mainz for these two detector geometries. Like the PREX data, results were collected for a 5×3 grid scanning along the length of the quartz. When comparing the general form of the results for the center of the quartz in each scan, shown in Fig. 4.30, all seem to have similar tails and peak-Gaussian structure, but the position of the signal above pedestal differs. The PREX, flat, and angled design MPVs
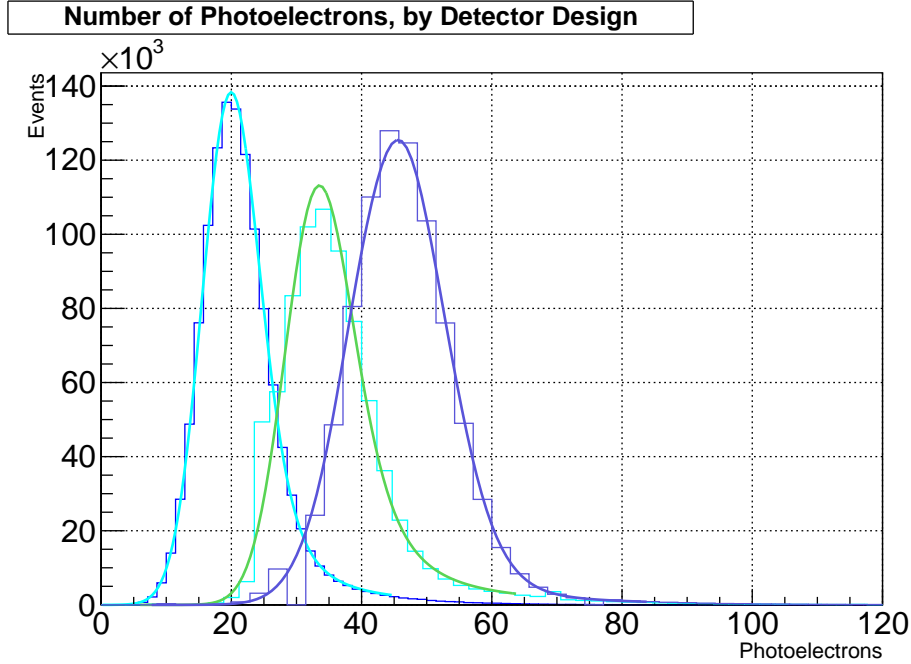
Figure 4.30: Fits for the PREX (light blue, 19 PEs), flat design prototype (green, 32 PEs) and angled prototype (purple, 44 PEs) runs on the center of the quartz.

are 19, 32, and 44 photoelectrons, respectively. The difference between the flat design's 32 PE peak and the PREX design's 19 PE peak is a combination of the geometric gains in solid angle (approximately a 500% increase in solid angle measured), a portion of the PMT blocked by other support materials, the lack of mirrors in the flat design (which can be a loss of up to 50% from simulations), as well as other possible factors that should be explored in the designs for the MOLLER detectors. The difference between the angle design and the flat design, 44 vs. 32 PEs, points to a large gain from total internal reflection, given the comparable blocking support structures and solid angles associated with quartz-PMT distances.

The positional scan for the angled design also shows features that do not appear in the PREX design. Comparing the MPV from the angled quartz scan, in Fig. 4.31, the number of photoelectrons measured is independent of the distance between the beam spot and quartz face, where the PREX scan shows the MPV drop off as a function of position. In addition, the angled design showed a resolution of sub-20%, a previously unreached milestone. as shown by the results for $\frac{RMS}{Mean}$ plotted in Fig. 4.32. With a signal that does not depend on the location of the incident electrons on the quartz face and a cleaner signal than other designs, the angled design allows for flexibility in the size of the quartz. While further

97

MPV by Position
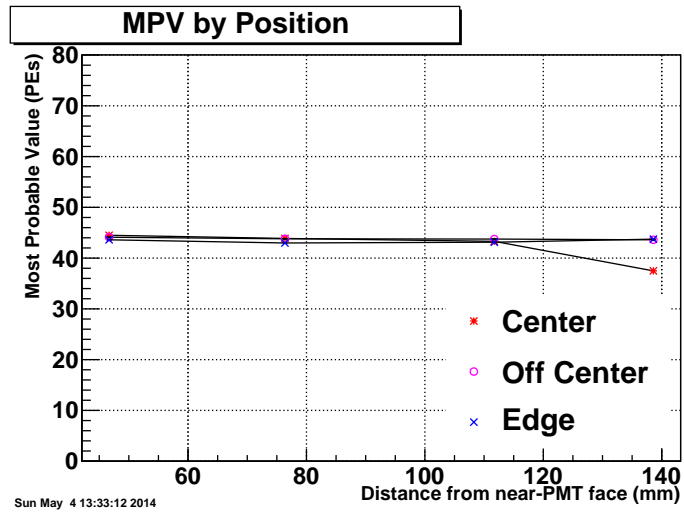
Figure 4.31: Plot of the MPV for the fits at each point in the angled quartz scan as a function of position.

designs are dependent on frame design and experimental concern, and as such are outside the scope of this dissertation, we argue that the angled quartz result, as well as the increased yield associated with moving the quartz closer to the PMT, provides an obvious avenue to investigate towards improvements in yields beyond the PREX result for future experiments.
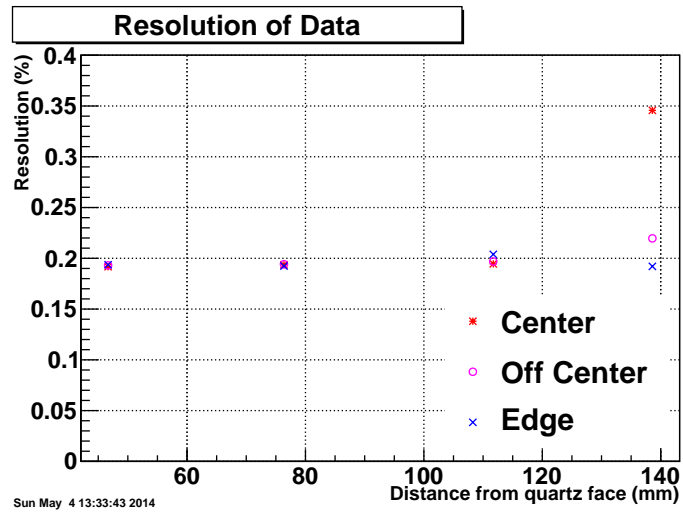
Figure 4.32: Position dependence of the resolution, $\left(\frac{RMS}{Mean}\right)$, for the angled detector design, for each point in the scan.

CHAPTER 5

DATA ANALYSIS

The PREX experiment measured electrons from a 50 μA-70 μA beam scattering from a ^{208}Pb target. Data from the apparatus is collected in sets called 'runs', with an individual 50 minute run collecting approximately 360,000 events. An event, as defined in Sec. 3.1.2, represents the integrated signal from each beam monitor and detector over an 8.2$\bar{3}$ ms range of a helicity window. The data from the PREX experiment consists of 295 runs, 232 of which had both arms operational, 44 with only the left HRS functioning, and 19 with the right arm only. These runs were then grouped into 'slugs'. Each of the slugs collects runs made for a given half-wave plate and double Wien filter setting (with these helicity-control apparatuses described in Sec. 3.1.2), such that all runs in a slug contain the same sign. The full data set for the PREX run was divided into 23 slugs, with the accepted slugs numbered 16 to 40, with exceptions for slugs 21 (for poorly monitored beam parameters) and 27 (when the electron beam was not running).

The analysis of the PREX data calculates the scattering asymmetry of weakly scattering electrons from a ^{208}Pb target from the raw data, in a procedure diagrammed in Fig. 5.1. The raw data from the detectors used in the analysis is the signal from the detector PMT, described in Chapter 4 as integrated over the event by the parity DAQ described in Sec. 3.7. Taking the difference a left- and right-handed helicity window can produce a detector asymmetry, but this does not account for any behavior of the beam. The detector signal is first normalized to the beam intensity, as the detector signal is linearly related to the number of electrons scattering from the target. Then, given the fluctuations through the injector, accelerator, and Hall A equipment, the state of the electron beam upstream of the target may be unacceptable for a parity-quality measurement. To ensure that the asymmetry comes from acceptable beam conditions, we have designed selection criteria to ensure that the elec-

tron beam's parameters and fluctuations are uniform for all accepted events, as discussed in Sec. 5.2. In addition, the pedestals, associated with the dark current for all of the electronics, need to be measured and corrected for the detectors and BCMs, so as to not affect our asymmetry calculations. With cuts, pedestal calibration, and intensity normalization, we have the 'raw asymmetry' associated with our detector signals.

After the application of selection cuts, the asymmetry must be calibrated for the fluctuation of beam parameters. As discussed in Sec. 3.8, in addition to normalization to the current, to correct for the fluctuations in scattering associated with the changes in beam position and energy, the PREX analysis calculates the correlation between the positions and energy, as measured by the beam position monitors (BPM), and the detector signals. The two approaches, either using the stochastic beam fluctuations (regression) or the dithering coils described in Sec. 3.8.4, calculates a 'slope' relating the BPM signals to a correction to the detector. After applying these slopes, we have the regression and dither-corrected asymmetries.

Lastly, to calculate the asymmetry associated strictly with electrons scattering weakly from the ^{208}Pb target (the 'physics' asymmetry), the PREX experiment quantified the systematic contributions to our measurement, described in Sec 5.8. These corrections to the asymmetry include corrections for the carbon foils in the PREX target (with the foils described in Sec. 3.4), the beam polarization, the correction associated with having a finite spread of angles accepted, and for any contamination of transverse polarization reaching our detector. Lastly, we applied the other corrections to our experiment, such as pole tip scattering, electrons rescattering in the HRS, and transverse polarization (all defined and addressed in Sec 5.8).

Independently, data from the spectrometer DAQ was analyzed in order to extract the four-momentum transfer Q^2. While the high resolution spectrometers and collimators were positioned to accept electrons scattering at 5.5°, a measurement of the scattering was taken to define the exact angle at which the electrons were scattering from the target into the HRS. This Q^2 depends on the acceptance of our collimator, which also must be defined in order to calculate what angles of electrons are reaching the spectrometer.

The analysis used ROOT, an object-oriented analysis structure provided by CERN. Hall A's parity group wrote libraries to build on this structure, the Parity ANalyzer (PAN) package, adding libraries specifically to handle the data structure recorded in the Hall A spectrometers. The data stream from the DAQ is interpreted by the PAN libraries to sort
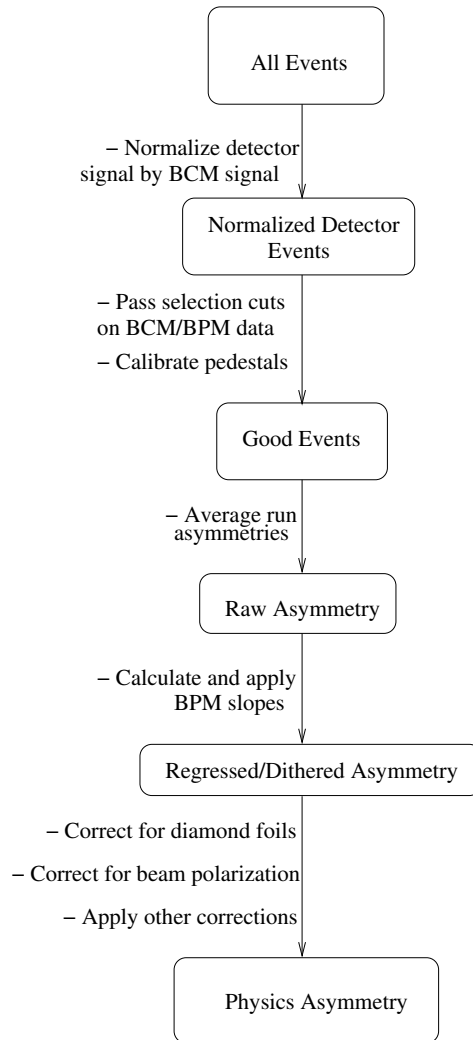
Figure 5.1: A flow chart of the method used in extracting the physics asymmetry from the raw detector data.

the data for each monitor (or monitor combination, as desired) into a separate array, or 'branch', of the ROOT file. All the branches of a given 'tree' in the ROOT file are indexed by the associated event, allowing for data to be finessed based on criteria from other monitors. This feature allows correlation of detector signals into the asymmetry we aim to measure, as described in Sec. 5.1, as well as interpreting these asymmetries in terms of beam parameters, which allows us to improve upon the selection cuts described in Sec. 5.2. This analysis work is performed on the individual ROOT files associated with each run, with the file for each slug created using the run's ROOT files.

In addition to the raw data branch, analyzing and ordering each event separately, this analysis package produces a pair and multiplet tree. As events are generated in the pseudorandom groups of four events, generating electrons with left (L) and right (R) handed helicities in groupings of LRRL and RLLR (as described in Sec. 3.1.2), we can form events in pairs and quartets. These left-right pairs and quartets group events together, comprised of equal numbers of left and right helicity windows. Having these groups allows us to calculate average signals between events as well as the asymmetries and differences in signals between left- and right-handed helicity windows.

5.1 Asymmetry

For all of the approximately 360,000 helicity windows in a run, we record the signals from the position and current monitors as well as the detectors. To measure the scattering asymmetry between electron helicities we compare the number of electrons that scatter in both helicity states into our detectors which, by design of our detectors in Chapter 4, is linearly proportional to the integrated signal from the photomultiplier tube. As described in Sec. 3.1, each helicity window is paired with a nearly in time window of opposite helicity to form a pair of events. As described in detail in Sec. 3.8, the asymmetry of the detector signal is then the difference in detector signal normalized by their sum,

$$A_{Det} = \frac{D_L - D_R}{D_L + D_R} \tag{5.1}$$

for signal D during the windows for left and right handed electrons, similar to the definition of the theoretical asymmetry for the left- and right-handed electron cross sections given in Eq. 2.19. This returns a result that we can compare against other signals, given that the asymmetry removes dependence on overall signal size. While Eq. 5.1 shows uses a single left-

right pair, we can also construct a four event multiplet from two sequential pairs by summing the left- and right-handed electron windows from each pair separately before calculating the asymmetry, as shown in Fig. 3.4. Measuring the multiplet asymmetry allows better normalization, as combining two pairs reduces the fluctuations by increasing the number of electrons measured in the asymmetry while also reducing the 60 Hz noise associated with the electronics.

This asymmetry assumes that the detector is measuring the flux from otherwise identical helicity windows. As the current in the beam fluctuates between events, the asymmetry needs to account for this. This is done by normalizing each detector signal by the beam current measured during that event separately and then calculating the asymmetry from the normalized detector signals. For beam currents I_L and I_R associated with detector signals D_L and D_R, this becomes what we called the normalized raw asymmetry.

$$A_{Raw} = \frac{\frac{D_L}{I_L} - \frac{D_R}{I_R}}{\frac{D_L}{I_L} + \frac{D_R}{I_R}} \tag{5.2}$$

However, calibration for beam intensity does not correct for instabilities in the beam current. As such, we make selection cuts on the data to ensure that the pairs used to calculate our measured asymmetry reflect optimal running conditions.

5.2 Cuts

Selection cuts were designed to remove events with unacceptable beam parameters from our data stream. As these cuts only look at data associated with the current monitors and position monitors upstream of the target and the data stream itself, they are independent of the detector signals and are therefore not designed to remove data based on helicity correlations. Each of these cuts is defined in terms of a cut criteria and a number of events called an "extent cut". The extent cut identifies a range of events around a single event failing the cut as having unacceptable beam conditions for removal as well. Each cut has an independently defined range of events in the extent, reflecting that certain cuts (low beam intensity, poor beam stability) identify poor beam parameters that can affect nearby events while other cuts (such as DAQ performance) correct for more isolated errors. The analysis package included a standard list of cuts in PAN, which was later expanded on by this experiment.

These cuts criteria are checked during the interpretation of the raw data in producing a run's associated ROOT file. Each event is recorded as passing the conditions for each cut separately and if it is within the extent cut of an event that failed each condition. These cuts are also combined into a single variable, "ok_cut", which records if a given event falls within the range of any cut. The ROOT file associated with a slug, required for the dithering analysis of the data described in Sec. 5.6.1, includes only data passing the ok_cut, requiring that the criteria of each cut are completely understood before completion of the analysis.

The PAN package includes a list of nine cuts pre-programmed. These cuts were written over the course of previous parity measurements and reflect an understanding of the minimal set of cuts to ensure parity quality signal. This includes cuts on the current monitor signal (Low_beam, Beam_burp), the data stream (Evt_seq, Pair_seq, Startup, Adcx_DAC_burp, Scaler_bad, Adcx_Bad), and on the position monitors (Mon_Saturate, Pos_burp_E). Designed during the PREX analysis were cuts on the fluctuations over a two second period, setting a threshold on the RMS of data in these windows to remove shorter beam instabilities. Cuts on the RMS of the data were added for the current monitor (Beam_burp_RMS), the individual position monitors (Pos_Sat_RMS), and the stability of BPM12 (DDiff_RMS). The list of these cuts is presented in Table 5.1.

Separately, there existed a by-hand cut on event number. This list of events, limited to selecting a single range of events in a run, exists to account for external factors that would not show up in the data but had an impact on the detector signal. This was mainly used to account for situations where the HRS magnets, which are downstream of the target and are not recorded in the parity events, were non-functional. These cuts were defined during the experiment so as to be accurate reflections of the running conditions, and used only to reflect data where there were explicit, mechanical explanations for a missing signals or those of unacceptable quality.

5.2.1 Current Monitor Cuts

The current monitor signal supplies information on the beam intensity. This signal is relative number of electrons incident on the target, and therefore proportional to the number of electrons scattering from the target. The data analysis framework for PREX makes two kinds of cuts on the current monitors; ensuring the beam is present in the hall, and to ensure it is stable in the hall.

To the first point, the Low_beam cut compares the current monitor signal, BCM3, against

Cut	Description
Low_beam	Ensures electron beam is on
Beam_burp	Checks BCM stable from event-event difference
Beam_burp_RMS	Checks BCM stable over 2 second period
Evt_Seq	Checks if events recorded in order
Pair_Seq	Checks if helicities for each evt. pair
Startup	Removes first event
Scaler_bad	Ensures scalers working as expected
Adcx_dac_burp	Checks for DAC baseline glitches
Adcx_bad	Checks if monitor signals recorded correctly
Mon_Saturate	Checks if BPM wire signal over threshold
Pos_Sat_RMS	Checks if BPM12 wires saturate in 2 sec. period
Pos_burp_E	Checks if BPM12x signal stable from event-event diff.
DDiff_RMS	Checks if BPM12 and BCM3 measure the same current.

Table 5.1: List of cuts.

a threshold. As the BCM reports a signal proportional to the intensity of the electron beam upstream of the target, we can set a threshold to ensure that the beam is on, reaching the experimental hall, and with an intensity around 50 μA (or 70μA for slugs running at that beam intensity). The threshold for Low_beam was set as approximately 75% of of the average current across the slug, removing all the data where the current is below that threshold (as shown in Fig 5.2). These thresholds were consistent between similar run settings and only changed under explicit changes to the beam, such as increased current or after a long beam down-time so as to mitigate any biasing that may come from overzealous modifications to the threshold.

The extent cut for the Low_beam was 40 events before and 5000 after. This extent removes the 40 events before the cut condition was failed, designed to remove events during the drop in signal, as well as the 5000 events after the beam rose above 75% signal, accounting for events with the beam current rising up to the requested current. The 5000 events, while long, is not a concern for removing large blocks of data, as the combination of threshold level and extent cut does not remove the entire ramp process, leaving events that are still ramping yet produce relatively stable asymmetry signals. Longer extent cuts were tested for the Low_beam cut, though these were found to be invasive by removing data that was consistent with other acceptable events.

In addition to ensuring the overall BCM signal size, we need to ensure that the beam intensity is stable between events in a left-right helicity pair. While small fluctuations were
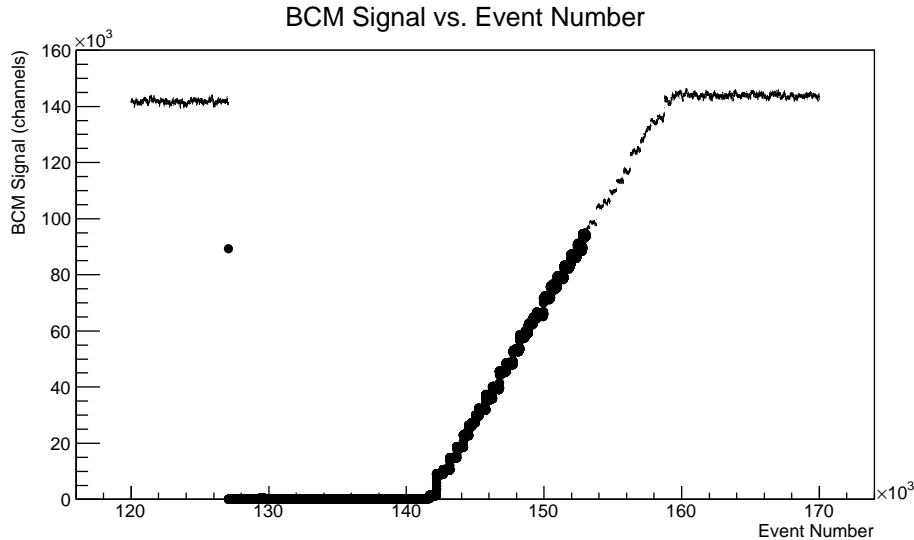
Figure 5.2: The current measured by BCM3 against event number for a subset of parity run 4698. Darker points are events that fall below threshold.

acceptable, any large, abrupt change in the beam intensity is indicative of some unacceptable beam instability. To account for this, we use the Beam_burp cut which functions by comparing the difference in sequential current monitor signals against a threshold value. The threshold is defined so as to accept a normal fluctuation in data while removing events associated with a large fluctuation, as shown in Fig. 5.3. To calibrate the threshold on this cut, for an arbitrarily selected sample of runs in a slug, the event-event difference in BCM signal was plotted. The threshold of the Beam_burp cut is then defined as a factor of five larger than the largest RMS recorded in event-event signal differences for the sample of runs examined, approximating a 5σ cut on the worst value of σ recorded for event-event current monitor differences. The extent for this cut is 40 events before and after the burp event, accounting for any transient instability in the beam before and after the events triggering the Beam_burp cut. Longer extent cuts were tested, though no gains in accuracy were seen by removing more events.

However, we found the BCM signal would undergo periods of instability which would not trigger the burp cut. These instabilities were significant, though transient enough that changing the threshold on the burp cut would remove a large number of otherwise accepted events. To account for this, a Beam_Burp_RMS cut was designed specifically for the PREX data. To perform this cut, each BCM signal is recorded in a 240-row array. The difference in beam signal is then compared to the RMS of this array. If the difference is greater than

107
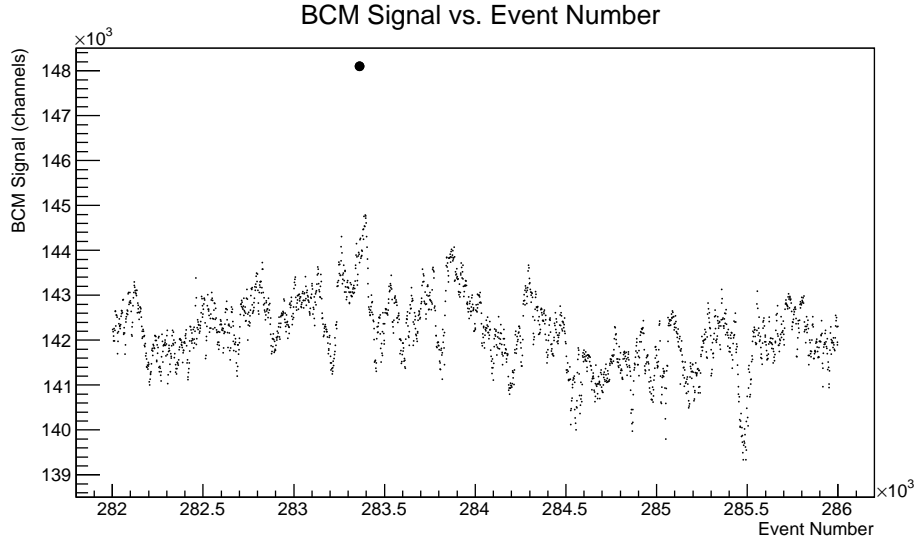
Figure 5.3: Sample of a beam burp cut. The plot shows the BCM3 signal as a function of event number. The circle near event 283500 is a discrete jump between BCM signals, failing the beam burp cut.

7 times that RMS, the event, as well as the preceding and following 40 events, are removed. The factor of 7 makes this a conservative cut, as this cut is based on a small subset of the data and should therefore account for the existence of excursions in the signal. This cut is redundant with the burp cut in most cases, though it does not handle the beam ramping well and is not designed to check the first 240 events of any run (as the RMS for an unfilled array could reject otherwise accepted data), but does remove small but discrete jumps in current that the Beam_burp cut misses.

5.2.2   Data Stream Cuts

There are also a number of cuts based on the data stream. This ensures that code processing the raw data stream correctly orders and interprets the events recorded during a run. To ensure the ordering is correct, the data uses the Evt_seq and Pair_seq cuts. These cuts compare the event (or pair number) helicity to the expected helicity from extracted from the pseudorandom sequence (as defined in Sec. 3.1.2. If a single event has the incorrect helicity or the pair has the same helicity, it implies that the event is improperly ordered, and should be removed to prevent that event from being compared to events that occurred chronologically out of sequence with it. These cuts use an extent cut of 25 events before and after, assuming that the event ordering will sort itself after 25 events.

108
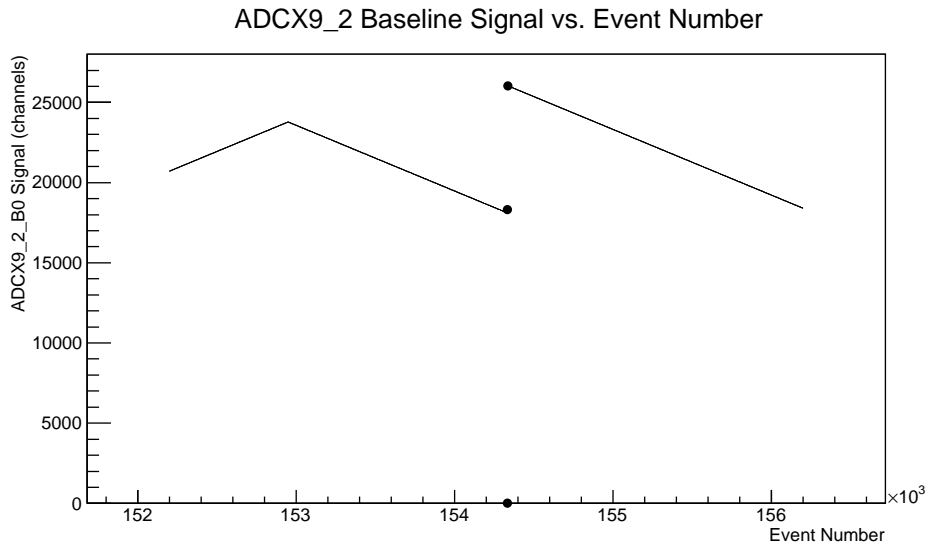
Figure 5.4: Sample of the ADCX burp cut. Plot of the baseline of ADCX9's second channel, showing a discrete jump in the baseline signal. The circles show points that fail this cut.

The Startup cut reflects that certain registers may have incorrect or non-physical values stored on resumption of running (especially after power cycling). This cut removes these events, so as to ensure the data stream is recording real, measured signals from the reporting devices. In order to account for unphysical behavior from the digital-to-analog converters (DAC), the Adcx_DAC_burp cut checks the behavior of these devices. The DACs were found during a previous experiment to experience glitches, reporting abnormal, meaningless signals. These glitches, as shown in Fig. 5.4, appear as abrupt, discontinuous changes in the changing baseline reported from the analog-to-digital converter (ADC). This cut on the reported baseline ensures that the DAC is functioning normally during running so as to remove these non-physical events by checking the change in the baseline between any two events is within threshold for any DAC baseline, with the threshold defined in terms of event-event differences (measured identically to the process used in tuning the beam burp cut).

In addition, there is a cut that checks if a scaler, a value assigned to scale a signal to match similar signals, has been recorded correctly, and removing events where this is not the case. This ensures that the scaling that is designed to occur with each event is done uniformly. These scalers are checked by having an expected value for the measured scaler number, set as proportional to the device's clock. The predicted and measured value are then compared to see if they agree within 10%, and if that is not the case the event is

109
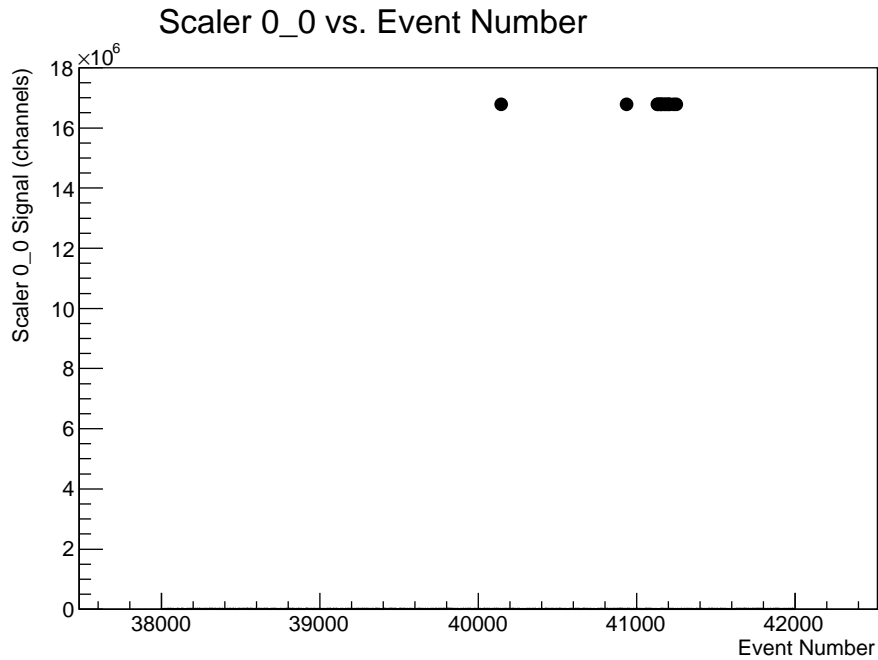
Figure 5.5: Sample of a scaler bad cut. The events around 18M channels fail the cut.

rejected. This expected value has an upper limit defined as the integration time of the DAQ multiplied by 10, or approximately 14,000 channels.

A cut was restored to the PREX data analysis to correct a problem that arose from comparing results between computers used in the analysis. The UMass analysis and a parallel Jefferson Lab analysis, using the same list of cuts, produced inconsistent results with respect to the number of accepted events. This was found to be related to how the machines parsed data from events that were incorrectly recorded in the data stream. While normal events received headers correlating the results to the type of monitor, occasional events were labeled as 'type 7', an otherwise unused type, and recorded event signals of hexadecimal value 'FFFFFF'. The Adcx_Bad cut checks to ensure that every event is associated with an existing monitor type, removing erroneously recorded events. This has no extent cut, so as to remove only the failing event. This cut was designed to preempt other cuts, such that these bad monitor signals did not trigger other cuts.

5.2.3 Position Monitor Cuts

The list of cuts also includes a pair of cuts on the position monitor signals. As the asymmetry measured in each event is dependent on the energy and scattering angle, drifts in the position
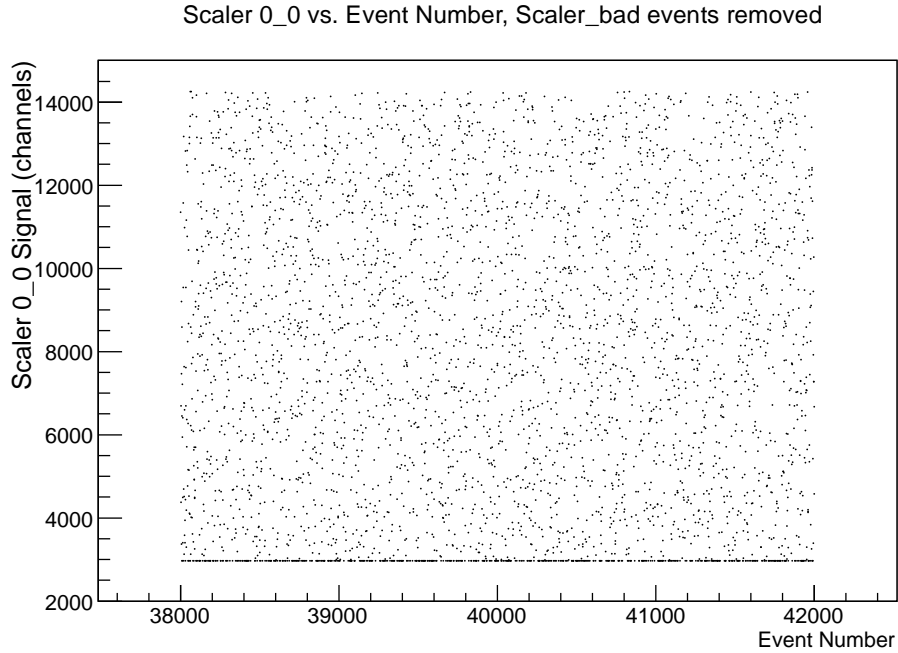
Figure 5.6: Plot of the accepted events across the range shown in Fig. 5.5. Shows stable behavior.

at which the electron scatters, as well as it's energy, need to be recorded to ensure we can later calibrate for these changes. The position monitors, while measuring the position well for certain combinations of signal and gain, occasionally would have a wire measure a signal above the maximum signal it could record. In these cases the wire would saturate, returning this maximum signal. When the wire saturated, the data stream would not show the small stochastic drifts needed to calculate beam corrections (described in Sec. 3.8.4), resulting in an incorrectly calibrated asymmetry. To account for this, the Mon_Saturate cut compares the signal on each BPM wire to the threshold where it cuts off ($\approx$500,000 channels), and removes the 30 events before and after that event, so as to remove the saturated event and events associated with the monitor signal saturating.

However, the monitor saturation cut was deemed incomplete, as there were still events that saturated on the energy monitor BPM12x. These would, similar to the outliers in the signal, complicate accurate corrections for beam parameters. To try to isolate these events, we recognized that there was little drift in the signal when the wire was saturating. From this, using a method similar to the Beam_burp_RMS cut, a new cut was added to measured the RMS of the BPM wire signals. Unlike previous cuts described, this Pos_Sat_RMS cut checks that the RMS of the signal is above a given threshold, because the saturated events

111
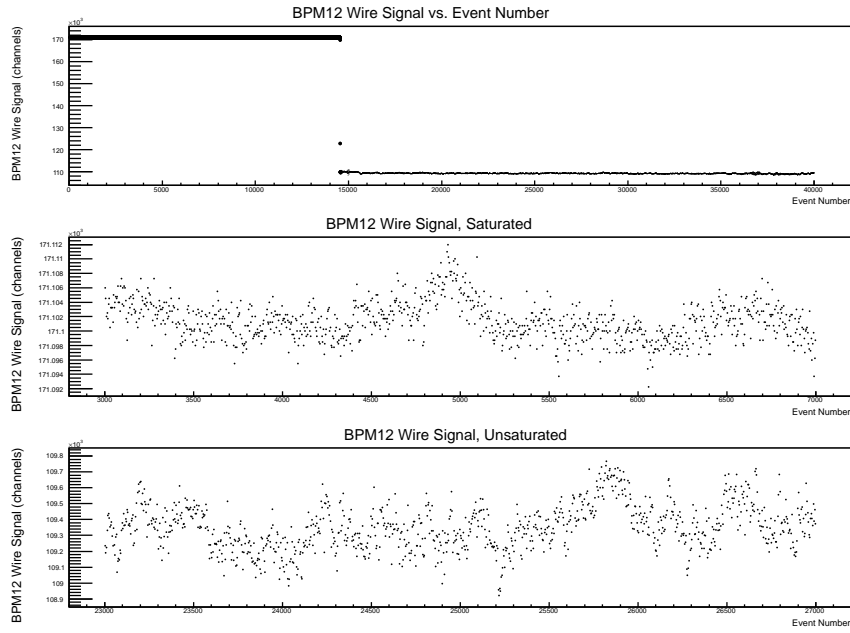
Figure 5.7: Sample of a BPM12 saturation cut. This plot shows the current measured in a single wire of BPM12 (in this case, the positive x wire) as a function of event number. The upper plot shows a 40000 event sample, containing signals from saturated (darker points) and unsaturated (lighter points) wires. The middle and bottom plots show 3000 event samples for the saturated (middle) and unsaturated (bottom) regions.

do not demonstrate the same stochastic drift (unlike other events where the concern was outliers), as seen in Fig. 5.7. In the upper plot of Fig. 5.7, there are two distinct sections: where the wire is saturating ($\approx$170k channels) and where the wire is not ($\approx$110k channels). The center plot shows the fluctuation in the saturating BPM12x events, where the recorded signal only spans a range of 20 channels in a 3000 event period. By comparison, the bottom plot shows, for a similar length of time, the unsaturated BPM12x signals range span a range of approximately 1000 channels. We designed the cut with a threshold such that the 20 channel range is rejected, based on the variance of the monitor signal over a set time frame, while the 1000 channel range is accepted for this example; other runs show different ranges, but similar behavior, requiring a different threshold on the fluctuation in BPM12x signals.

To decide on a threshold, we examined the pair difference in the monitor signal in regions we could identify as having saturated. The RMS was found for these regions, then the largest was taken as the σ for that slug. The threshold is then set at 10σ, an exceptionally conservative limit reflecting concerns that a cut on a minimum allowable RMS would be invasive to data without BPM saturation. This cut checks a buffer of 60 events, which are
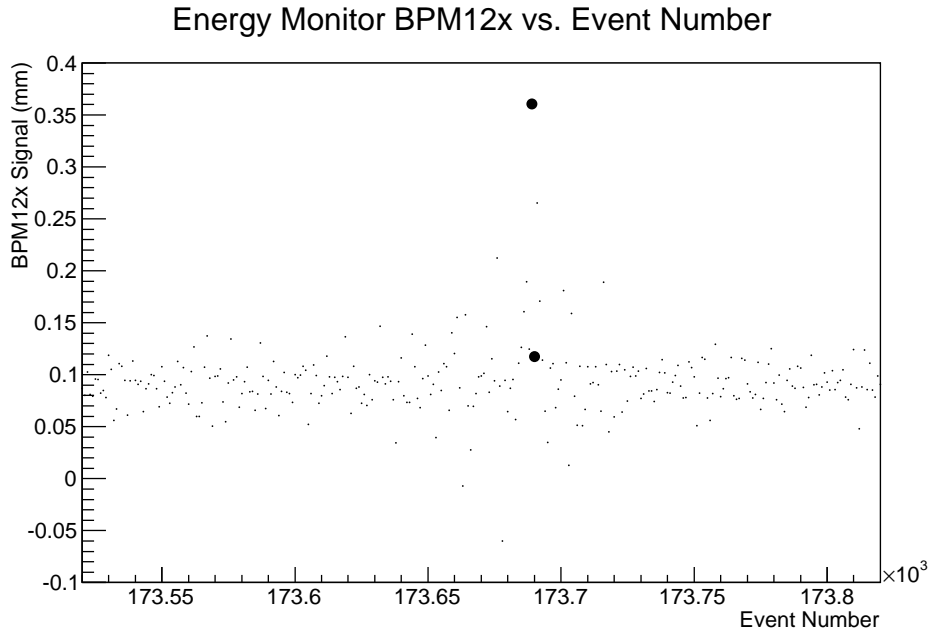
Figure 5.8: Sample of a Pos_burp_E cut. This plot shows the energy measured, with the circle showing an event-event difference above the threshold.

all removed in the case an event fails this cut. There is an additional 40 events removed after saturation, with this upper threshold selected for symmetry with other burp cuts.

In addition to a check on the saturation of the BPMs, there were cuts on the stability of the beam energy as measured by BPM12x. The events in any pair should have similar energy. To ensure this, similar to the Beam_burp, the Pos_burp_E cut checks to ensure the change in energy between events is below a designated threshold. In this case, the threshold was defined based on the event-event differences in the beam energy, as recorded by the energy monitor BPM12x. The threshold is defined as 5σ for the largest RMS measured in the sample of runs checked for each slug. This ensures small fluctuations in energy. The extent cut for the Pos_burp_E cut was also optimized, finding a balance between removing too many events and ensuring beam stability. The results showed the best extent cut removed 100 events before and 1000 events after the failing event.

As an additional test on beam quality for the data analysis for PREX, we wanted a cut that checked if the energy monitor BPM12 was functioning correctly compared to other signals. We utilized the fact that the signals from each of the BPM12 wires could be summed together, effectively recording the beam current near BPM12. We compared the asymmetry in both BCM3 and the asymmetry in the sum of the BPM12 wire signals between helicity

113
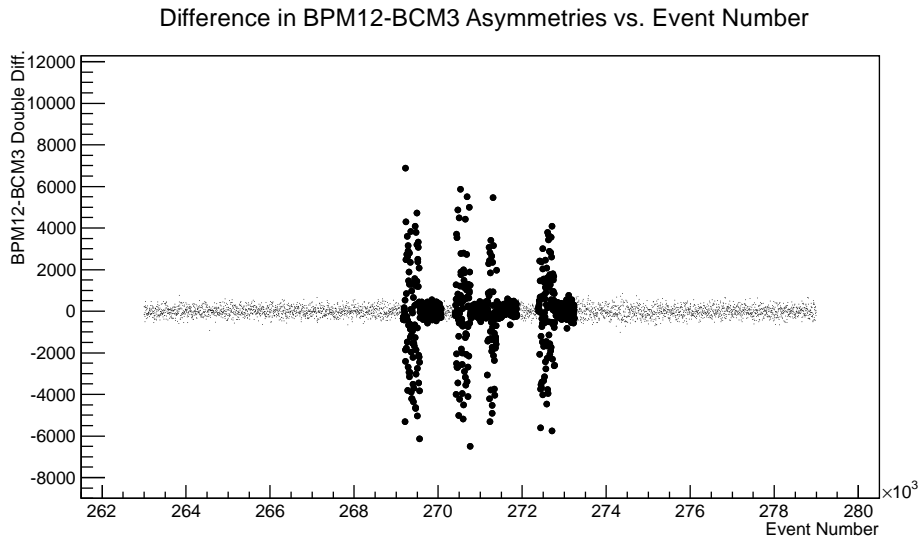
Figure 5.9: Sample of a double difference cut. This plot shows the difference between the charge asymmetry measured on BPM12 and as measured on BCM3. The circles represent events where the RMS of the previous 240 events is found to be above the threshold set for the cut.

windows, then took the difference between those values. This was called the 'double difference' as it measured the differences in intensity measured in two helicity windows measured by two different monitors. Since the BPM12 wire sum and BCM3 are both measuring a beam current, the changes in the reported intensities should be similar, and therefore any excursions in the double difference must be associated with an inaccurate measurement from one of the monitors.

By defining a threshold on the expected stability between these differences, we can make a selection cut ensuring that the BPM12 signal and BCM3 signals are reporting the same beam fluctuations. To do this, the designed DDiff_RMS cut, identically to the Beam_burp_RMS cut, records the differences in these signals in a 240 event buffer. For each event, the analysis code compares the RMS of this buffer to a threshold. This threshold was set by comparing the double difference RMS of a sample of runs, then taking the threshold as 5σ for the largest measured σ. This cut removed 120 events before and after the RMS went over the threshold, as this filters the latter half of the events in the buffer, as well as the following 120 events so as to isolate these position excursions.

Multiplet Asymmetry, Run 4698
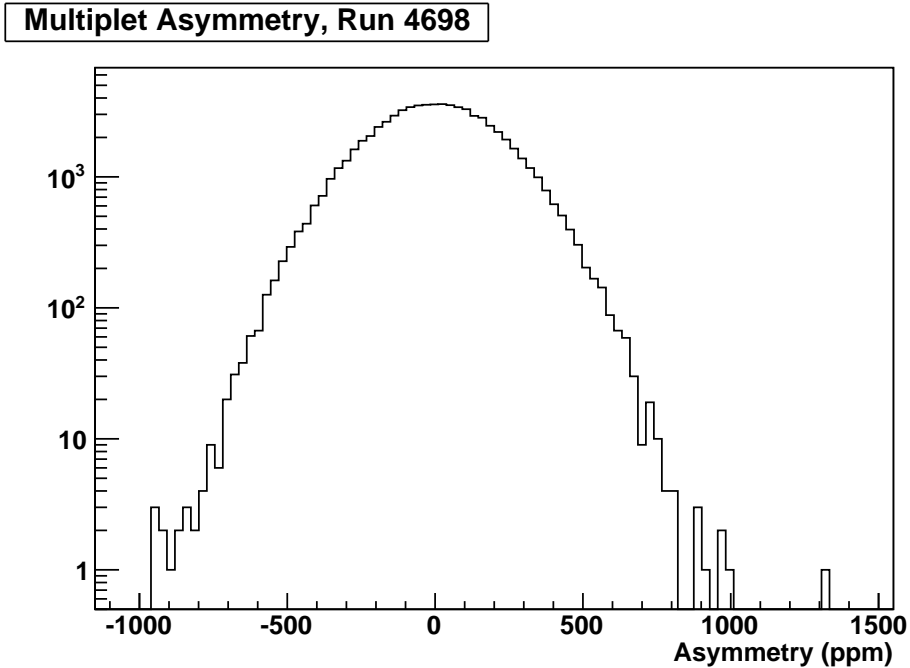
Figure 5.10: Sample single-run asymmetry result, from data run 4698, on a logarithmic scale with all cuts applied.

5.2.4 Data After Selection Cuts

With these cuts, the resulting asymmetry is approximately Gaussian on the run-level, as shown in Fig. 5.10. The number of events cut are presented in Appendix A for events cut by the Low_beam cut, then by events that fail any other cut. Over 92% of the events with the beam on (defined as passing the low beam cut) pass all other cuts, indicating that the beam is very stable and our extent cuts are not so invasive as to remove a substantial number of acceptable events. The event sequence, monitor saturate, and startup cuts remove no events, suggesting the DAQ is fairly stable and the monitors, in general, do not saturate. The Adcx_Bad cut only removed two events after reintroduction, implying the ADC glitch this corrects is not a pervasive problem, indicating why the problem escaped notice. The Mon_saturate cut effectively became redundant with the implementation of the position monitor RMS cut, and required setting a threshold that was not too aggressive for any monitor, indicating why no events were removed.

The most events removed by a single cut were for the Pos_burp_E cut, with slightly over 1M events. The threshold was set at a value larger than a factor of five above the variance in any given run for each slug, suggesting the beam energy is prone to dramatic changes

between events rather than an aggressively set threshold. Of the added cuts, the double difference cut agrees with this argument about beam energy, removing 160k events (with overlap in the Pos_burp_E cut). The Pos_Sat_RMS cut removed 100k events, implying that the monitor is saturating at a level below other beam monitors, and with a non-negligible frequency. The beam burp RMS cut was created to be redundant with the standard burp cut, with the beam burp cut designed to remove instabilities rather than larger transient signals. With identical extent cuts, fewer events failed the beam burp RMS cut than the event-event threshold cut, suggesting the beam is more prone to single event jumps than long lasted instabilities in beam intensity.

5.3 Pedestal Calibration

Another important step in the processing of the data is pedestal calibration. The BCM cavities and the detector PMTs each return a dark current signal associated with the equipment being on. This dark current, or 'pedestal', is not associated with the physics to be measured but needs to be accounted for as it produces a measurable effect on our measured asymmetries. A signal $S_{L,R}$ from a left- or right-helicity window is the sum of the helicity-dependent measurement of the scattered electrons by our detector $S_{L,R}^{phys}$ and the helicity-independent pedestal associated with our detector S^{ped}. For these signals $S_{L,R}$ the (unnormalized) asymmetry is

$$A = \frac{S_L - S_R}{S_L + S_R} = \frac{S_L^{phys} - S_R^{phys}}{S_L^{phys} + S_R^{phys} + 2S^{ped}} \tag{5.3}$$

For a non-zero pedestal, the resulting asymmetry will depend in part of the size of the pedestal, which supplies a contribution not associated with the helicity-dependent scattering cross section. Including the BCM signals to normalize the detector signal introduces additional terms associated with the BCM pedestals, further affecting our results.

The parity analyzer accepts a list of user-defined pedestals values, in channels, that it subtracts from the values in the data stream when writing the analyzed data file. To use this pedestal correction feature, we must accurately measure the pedestals associated with each monitor.

These calibrations cannot be performed by measuring the signal with no beam in the hall; the BCM pedestals depend on the total signal. As a result, the predicted dark current in the BCM, when fit against other signals that do vary linearly with beam current, differs from the

116

Current Monitor Signals During Beam Ramp, Run 4687

Pedestal = 202.4 +- 31.4 channels

BCM3 Signal (channels)

BCM5 Signal (channels)
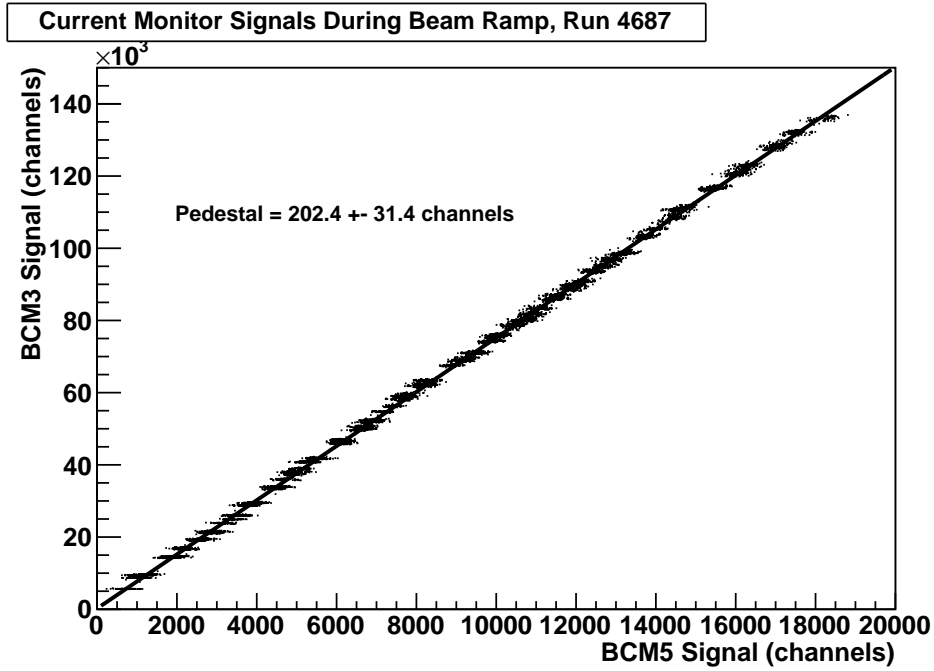
Figure 5.11: Fit of BCM3 vs. Unser for pedestal run 4687, showing a 202 channel pedestal for our 140,000 channel BCM3 signal.

signal reported by the BCM when the beam is off. To calibrate the BCM pedestals we use the Unser, described in Sec. 3.8.2. The Unser is a cavity monitor designed to be accurate to low currents, and therefore will accurately fit the BCM dark current as a function of beam current, but drifts on the scale of minutes. Using data where the beam current ramps up and down, we compare the current measured by the cavity monitors BCM1 and BCM3 and the average signal from each electron detector to the beam intensity measured by the Unser monitor BCM5. By fitting the Unser response to the cavity response above zero current, we can extrapolate the cavity response to no beam and use that as the pedestal. Shown in Fig. 5.11, a sample run fitting the normalizing current monitor BCM3 against the Unser monitor BCM5 predicts a negligibly small pedestal offset of 50 channels for slugs 37-40 (compared to a signal of 540 channels average for the beam-off data points).

The trouble with this approach alone is that it relies on the Unser, which drifts on the timescale of the beam current ramping from 0 to 50 μA. To ensure the results are not dominated by these drifts, we can compare the calibrated signals for high current running by comparing the normalized asymmetry against the beam asymmetry and checking that the results are uncorrelated. If the normalized asymmetry is correlated with a beam asymmetry, it suggests there is some additional factor (i.e. some uncorrected pedestal) correlated between

117
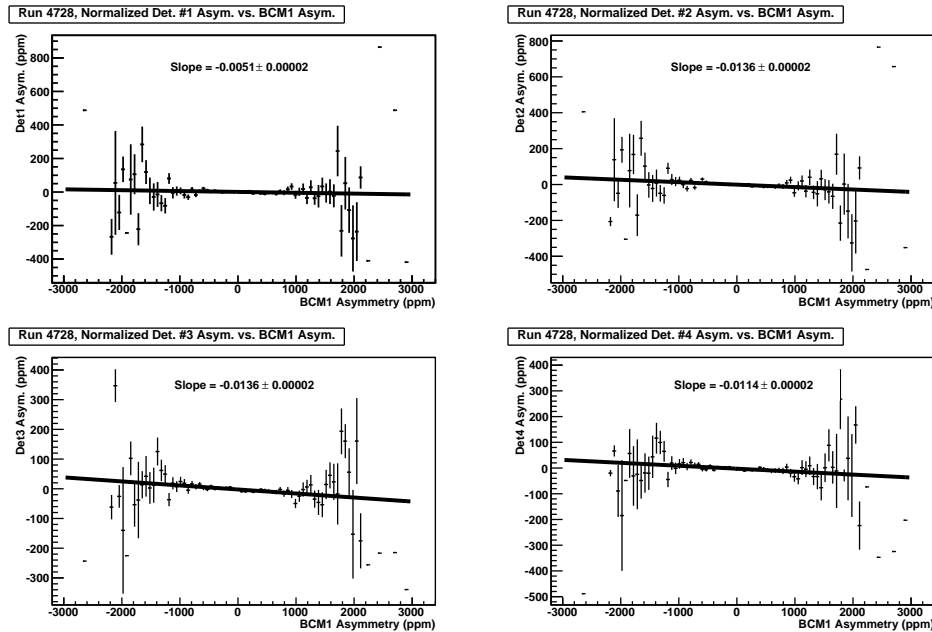
Figure 5.12: Fit of normalized detector asymmetry against charge asymmetry for run 4728, using pedestals from run 4687.

the two signals. Fig. 5.12 shows a plot of the correlation between the current monitor BCM1 and each detector for run 4728. Each detector shows small correlations for this run, the largest being 1.7%, deemed acceptable before the corrections for other beam parameters. As the beam is normalized against BCM3, it is important to use a separate BCM, in this case BCM1, to remove correlations associated with the measurements on BCM3.

The pedestals change only after changes to the apparatus, such as after the beam being off for days or the settings changed between 50 and 70 μA. Using pedestals calibrated after experimental changes, we apply these pedestals to all intervening runs and check the correlations. As shown in Fig. 5.13, these slopes were calculated for each slug, then averaged over to find the correlation for each detector over the span of the experiment. The correlation for these detectors falls below 1.5%. Though not an ideal result, difficulties with fitting pedestals due to drift in the Unser and consistency of the results limit our ability to calibrate further.

5.4   Beam Performance

After selection cuts, the resulting beam parameters should be relatively stable. We judge the beam stability by calculating the difference in signal recorded by the beam monitors between helicity windows, with the expectation that these event-event differences in current, position,
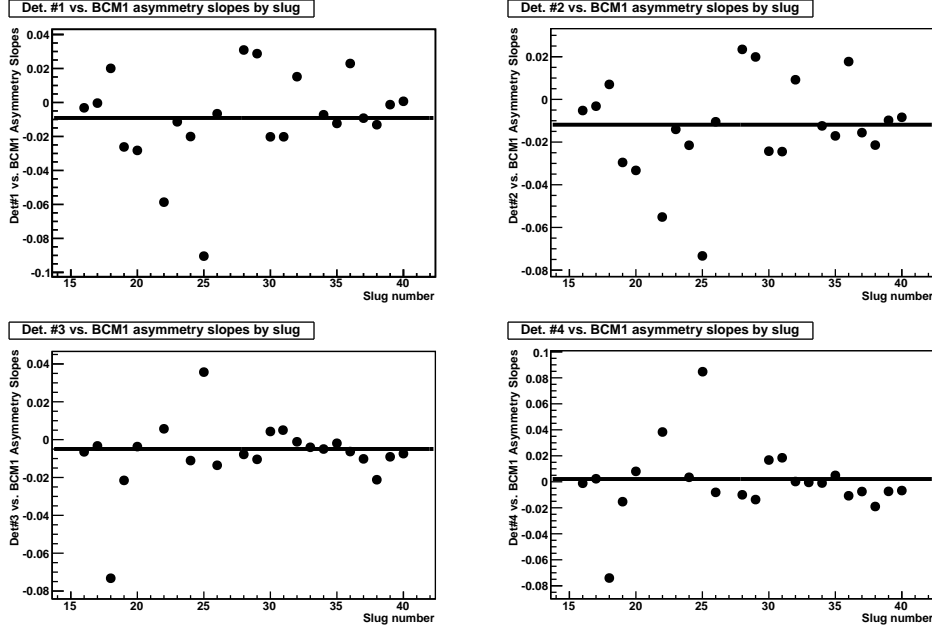
Figure 5.13: Average correlations between detector and BCM1 asymmetries for all data.

and energy should be negligibly small, as discussed in Sec. 3.8. The monitors tested, selected for their use in defining beam corrections (discussed in Sec. 5.6), were the energy monitor BPM12x and position monitors BPM4a and BPM4b. Both position BPMs report an x and y position, allowing a pair of checks on the x and y positions of the beam. It was assumed that each of the spin-flipping mechanisms, described in Sec. 3.1, would induce some measurable effect on these beam parameters as well. As such, the PREX experiment installed the double Wien filter, in addition to the previously present half-wave plate, in order to isolate these effects.

To test for these effects, we sorted each slug by it's half wave plate and Wien state. Then, after applying sign corrections, we look at the difference in monitor signals between helicity windows for all slugs and take the average, expecting this result to agree with zero. In addition, we look at the average helicity-window differences for each Wien/IHWP separately, anticipating that the separate Wien/IHWP setting signals will not necessarily be in agreement with zero.

In the terminology of the experiment, inserting the half-wave plate (IHWP In) and the Wien oriented to spin the electrons left (Wien Left) each contribute a factor of -1 to the measured pair differences (reflecting an interchange between the positive and negative helicity particles between helicity states). The half-wave plate removed (IHWP Out) and Wien Right

119

Slug #	IHWP	Wien	Sign	Slug #	IHWP	Wien	Sign
16	In	Left	+1	30	In	Right	-1
17	Out	Left	-1	31	Out	Right	+1
18	Out	Right	+1	32	Out	Left	-1
19	In	Right	-1	33	In	Left	+1
20	In	Right	-1	34	In	Right	-1
22	Out	Left	-1	35	Out	Right	+1
23	In	Left	+1	36	In	Right	-1
24	Out	Left	-1	37	In	Left	+1
25	Out	Right	+1	38	Out	Left	-1
26	In	Right	-1	39	In	Left	+1
28	In	Right	-1	40	Out	Left	-1
29	Out	Right	+1				

Table 5.2: A table of each slug's Wien and half-wave plate state, as well as combined sign flip.

states each contribute a factor of +1, reflecting no change. The states of the Wien and IHWP are not recorded as part of the data stream for each run, so the sign flips are accounted for in the offline analysis. The device states and overall sign of each slug is given in Table 5.2.

The Wien and IHWP define corrections to the sign of the asymmetry, but do not define the absolute signs of the scattering asymmetry between left- and right-handed electrons. To find this sign, data with an intentionally large asymmetry was measured by the polarimeters in the experimental hall. By measuring a large asymmetry in the Møller polarimeter, whose sign is known correlated to right-left (R-L) electron helicity difference, we can find the definite sign of the PREX asymmetry. As the Møller asymmetry found to be positive for helicity bit true, the PREX L-R asymmetry, as defined by convention, was found to be negative.

With these corrections, we can see the effect in the recorded BPM differences. In Fig. 5.14, using the energy monitor BPM12x as an example, we report the difference in signals from BPM12x for between helicity states, grouped by Wien and IHWP settings but without sign corrections. The differences in beam position for windows with left- and right-handed electrons are between 0.15 and 0.026 μm for each separate IHWP/Wien state, though the precision of these each have them neither agree with each other or zero, as predicted. Fig. 5.15 includes the differences in BPM12x signals for all slugs with the sign corrections given in Table 5.2. With all slugs and sign corrections the difference in position over the course of the experiment averages to 0.001117 $\pm$ 0.004311 μm difference between beam positions for left- and right-handed electrons in the energy monitor BPM12x, agreeing with zero.

120
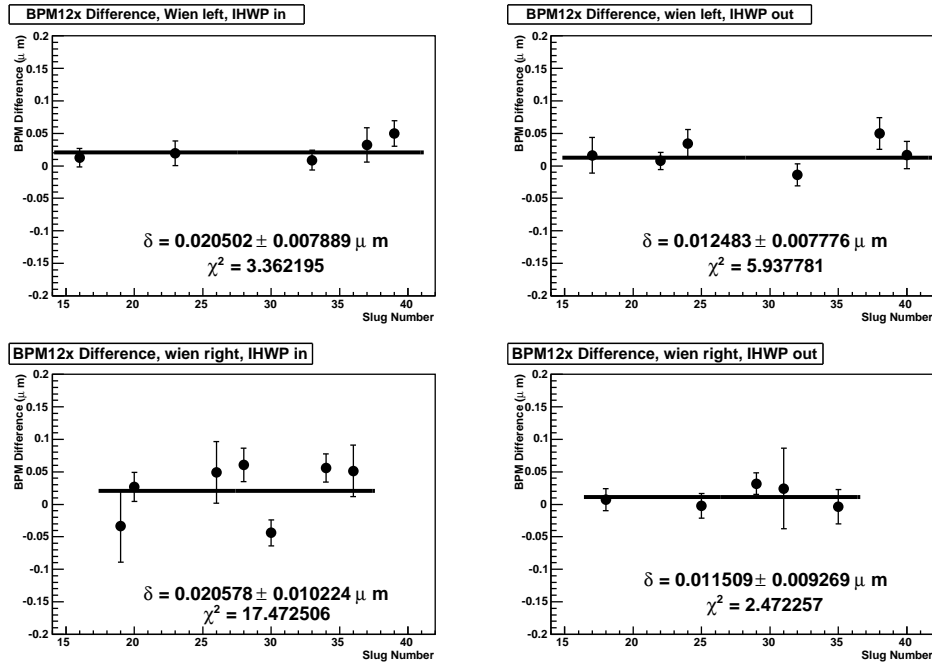
Figure 5.14: Plot of the multiplet difference in BPM 12x as a function of slug number. Each plot contains the slugs sharing a single IHWP and Wien state, without the sign change applied.
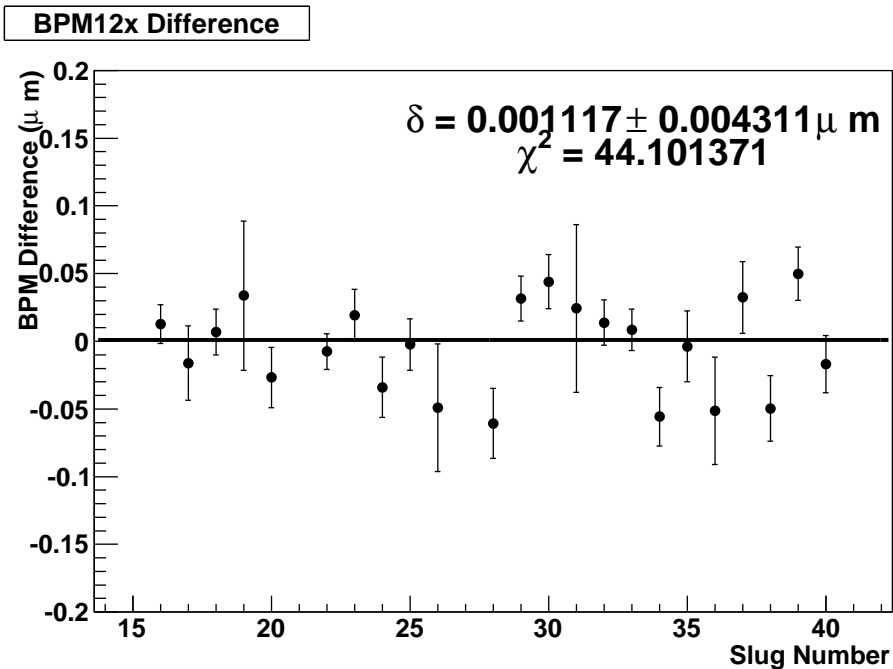
Figure 5.15: Plot of the multiplet difference in BPM 12x as a function of slug number. Each slug has the sign change applied, such that this data is for left-right differences.

BPM	L, In (μm)	L, Out (μm)	R, In (μm)	R, Out (μm)	Avg. (μm)
12x	0.020 ± 0.008	0.012 ± 0.008	0.021 ± 0.010	0.011 ± 0.009	0.002 ± 0.003
4ax	0.022 ± 0.004	0.026 ± 0.005	0.019 ± 0.006	0.020 ± 0.008	0.001 ± 0.004
4ay	0.001 ± 0.004	-0.003 ± 0.005	0.002 ± 0.007	-0.007 ± 0.008	-0.0001 ± 0.003
4bx	0.012 ± 0.004	0.024 ± 0.006	0.029 ± 0.008	0.027 ± 0.010	-0.002 ± 0.003
4by	-0.007 ± 0.005	-0.011 ± 0.006	-0.002 ± 0.008	-0.009 ± 0.009	-0.0001 ± 0.003

Table 5.3: Helicity-correlated beam differences by BPM, separated for Wien left (L) or right (R) and IHWP either in or out. These results presented with the average after sign corrections.

Plots for both the IHWP/Wien separated slugs and sign-corrected averages for the four position BPMs (4ax, 4ay, 4bx, 4by) appear in Appendix B, while the averages are presented in Table 5.3. From this data, we can see that the independent IHWP and Wien helicity controls each contribute some effect to the differences measured in position, which can be accounted for and removed by averaging over the four possible states.

Also tested for stability was the beam intensity. As the current is reported on the order of 200,000 ADC channels, the charge asymmetry between events is compared instead of a straight difference. As shown in Fig. 5.16 and Fig. 5.17, we see that the same dependence in the helicity state (though each separate Wien/IHWP state current average does agree with zero), with the sign-corrected average of 0.0088 ± 0.0798 ppm. This, combined with the BPM averages, shows that over the course of the experiment there was no position or current bias in favor of either helicity state, with the beam quality commensurate with extracting a scattering asymmetry from the detectors.

5.5   Raw Asymmetry

With optimized selection cuts and stable beam parameters, we can calculate the asymmetry measured with only corrections for charge normalization, called the 'raw asymmetry'. This asymmetry is calculated from the charge-normalized detector asymmetry for each run. Each run's asymmetry is composed of three detector asymmetry measurements; the asymmetry from all detectors when both HRS arms are running and, if for any reason data was taken with an arm of the HRS was down, the asymmetry from a single arm of the detector for when only the left (L) or right (R) spectrometer arm is functional. Each slug asymmetry is the average of the asymmetries from each run in that slug. The combined 'raw asymmetry' is the average of all of the slug asymmetries, with sign corrections.
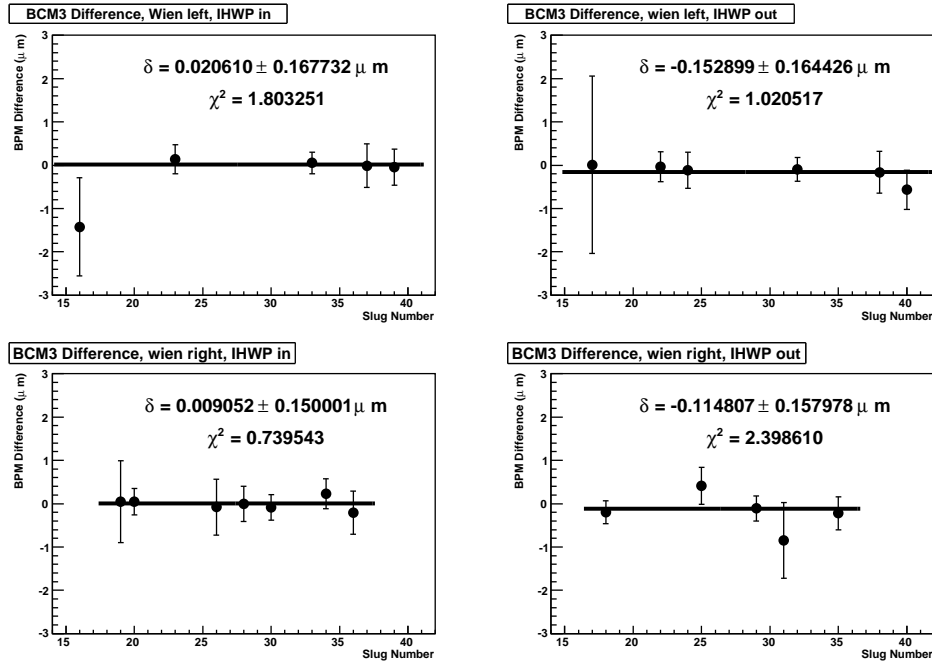
Figure 5.16: Plot of the multiplet charge asymmetry reported from BCM3 as a function of slug number. Each plot contains the slugs sharing a single IHWP and Wien state, without the sign change applied.
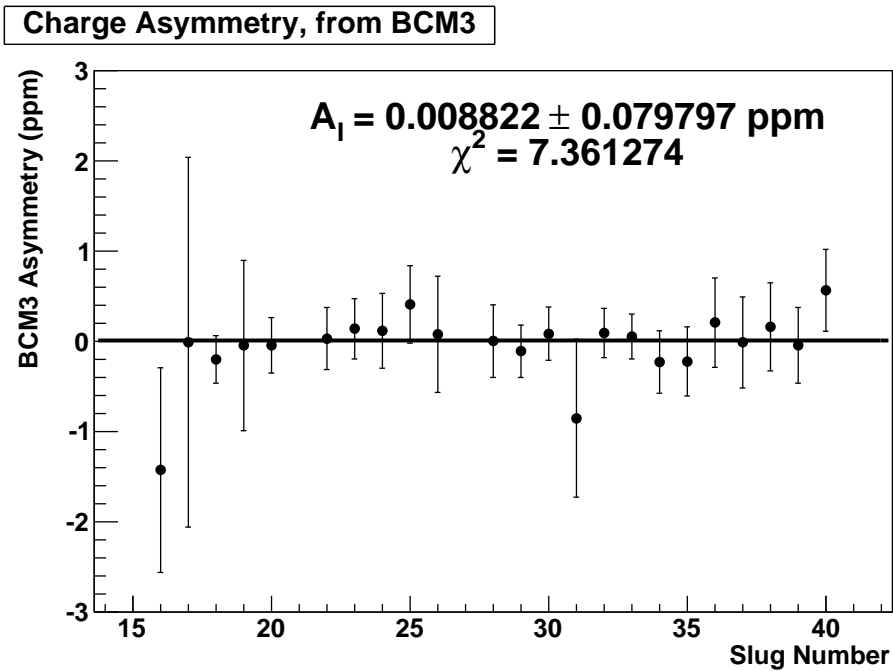
Figure 5.17: Plot of the multiplet charge asymmetry from BCM3 as a function of slug number. Each plot contains the slugs sharing a single IHWP and Wien state, without the sign change applied.

In averaging the slug asymmetries together, each run's asymmetry is weighted by its statistical error σ, given by $\frac{RMS}{\sqrt{N}}$ for N events in a given run. This method biases the average towards runs with a smaller statistical error. Given that the statistical fluctuation decreases with the number of detectors used, weighting by the statistical error correctly weights all single-arm asymmetries as less significant than asymmetries with both HRS arms functional. The asymmetries are averaged, with a contribution from the i-th run, as

$$A = \frac{\sum_i \frac{A_i}{\sigma_i^2}}{\sum_i \frac{1}{\sigma_i^2}} \tag{5.4}$$

with an error defined by

$$\sigma^2 = \frac{1}{\sum_i \frac{1}{\sigma_i^2}} \tag{5.5}$$

Using the asymmetries and errors calculated from each run, the asymmetry from the raw data was found to be $A_{Raw} = -0.5535 \pm 0.0634$ ppm, as shown in Fig. 5.18. This asymmetry, while useful for analysis process, does not reflect the physics asymmetry, as it does not account for the fluctuations in the asymmetry due to shifts in beam position and energy.

5.6   Beam Corrections

After cuts and tests for beam stability, the beam undergoes some stochastic fluctuations. As discussed in Sec. 3.8, changes in the beam position and energy between helicity windows affect the number of electrons measured by the detectors, affecting the asymmetry measured by (as given in Eq. 3.4)

$$A = \frac{\Delta D}{2D} - \frac{\Delta I}{2I} - \sum_j \alpha_j \chi_j \tag{5.6}$$

for signal of the j-th BPM χ correlated to the asymmetry by slope α_j. These effects are referred to as 'false asymmetries', noting that while they contribute to the asymmetry between electrons measured by the detectors they are dependent on experimental procedure, not the weak scattering of electrons. Unlike the current, corrections for the beam position and energy require calculating the correlation between beam position and the asymmetry.
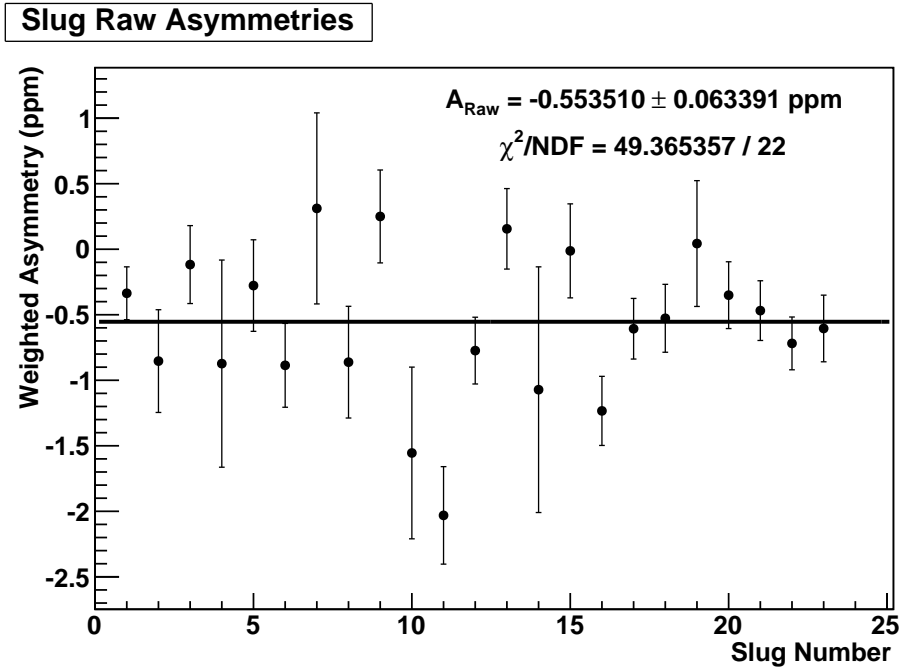
Figure 5.18: Plot of asymmetries for each slug. The plotted line is a fit to these data points, with error. The asymmetry and it's χ^2 are for this fit.

This is found by, using data from either the entire run or deliberate beam modulations, calculating slopes equating a change in beam parameters with a change in the asymmetry.

Changes in the beam energy and position affect the 4-momentum transfer Q^2. As Q^2 depends on energy and scattering angle, changes to the energy of the beam will change Q^2. The position of the beam affects the angle, as the collimator was designed to measure electrons scattering between 4 and 7° from the center of the target. As the position of the beam spot moves, the angle between the electron's initial path and the collimator changes, resulting in the electrons passing through the collimator having a different scattering angle (which propagates through to Q^2 and our asymmetry).

Corrections for the beam energy are complicated by the fact that these are not independent fluctuations. Electrons with different energies propagate differently, so energy fluctuations can be measured on position monitors indistinguishably from other position-altering effects (i.e. magnet changes, accelerator fluctuations). As these all affect Q^2, the affects on the measured asymmetry are convoluted.

Other parity experiments in Jefferson Lab's Hall A needed to make similar corrections, and as such there exists a pair of independent methodologies for calculating beam corrections: regression and dithering. In both of these approaches, the analysis correlates the relationship

between the detector's measured signal and a set of beam parameters. In these analyses, the beam is parametrized by the energy monitor BPM12x and the position monitors BPM4a and BPM4b (each reporting an x and y coordinate) for a total of five parameters. The signal of the beam is then measured against these five parameters, resulting in a set of corrective slopes between the detector and BPM signals. These slopes are calculated for and applied to subsets of data (dependent on the method and data availability). Each of these methods reports a separate final asymmetry, referred to as the dithered or regressed asymmetries.

5.6.1   Dithering

Dithering calibrates the detector response using the beam modulation hardware described in Sec. 3.8.4. Upstream of all of the beam monitors are seven magnetic coils, which alter the direction of the electron beam (with four along the x direction, three along y). By modulating the voltage applied, we can change the position of the electron beam passing through the BPM and at the target. In addition a signal is sent to one of the cryomodules in the linear accelerator to modulate the beam energy. The coils (including the energy modulation as the eighth coil) were activated in sequence every eight minutes, with the entire cycle for all eight coils lasting one minute. The voltage applied to the coils changed sinusoidally, with the DAQ measuring the response in the BPMs and detectors.

By comparing different points in the sinusoid, we are able to calculate the response of the detector D to the current sent to the coil C, $\frac{dD}{dC}$, and of the position monitor M to the coil $\frac{DM}{dC}$, for any combination of coil, detector and BPM. Given that there are more coils than there are monitors, the coils that produced the most well-defined response were used to calculate our slopes.

To extract the slopes, denoted $\frac{dD}{dM}$ equivalent to the α_j in Eq. 5.6, in this scheme we recognize that

$$\frac{dD}{dC} = \left(\frac{dM}{dC}\right)^{-1} \frac{dD}{dM} \tag{5.7}$$

for measured detector-coil and monitor-coil slopes. However, we cannot extract the slopes directly from Eq. 5.7, as these monitors are correlated for a given coil modulation. To extract all the slopes, for the given set of coils and monitors, we construct the following equation for arbitrary detector D.

$$\begin{pmatrix} \frac{dD}{dC_1} \\ \frac{dD}{dC_2} \\ \frac{dD}{dC_3} \\ \frac{dD}{dC_4} \\ \frac{dD}{dC_5} \end{pmatrix} = \begin{pmatrix} \frac{dM_{4ax}}{dC_1} & \frac{dM_{4ax}}{dC_2} & \frac{dM_{4ax}}{dC_3} & \frac{dM_{4ax}}{dC_4} & \frac{dM_{4ax}}{dC_5} \\ \frac{dM_{4ay}}{dC_1} & \frac{dM_{4ay}}{dC_2} & \frac{dM_{4ay}}{dC_3} & \frac{dM_{4ay}}{dC_4} & \frac{dM_{4ay}}{dC_5} \\ \frac{dM_{4bx}}{dC_1} & \frac{dM_{4bx}}{dC_2} & \frac{dM_{4bx}}{dC_3} & \frac{dM_{4bx}}{dC_4} & \frac{dM_{4bx}}{dC_5} \\ \frac{dM_{4by}}{dC_1} & \frac{dM_{4by}}{dC_2} & \frac{dM_{4by}}{dC_3} & \frac{dM_{4by}}{dC_4} & \frac{dM_{4by}}{dC_5} \\ \frac{dM_{12x}}{dC_1} & \frac{dM_{12x}}{dC_2} & \frac{dM_{12x}}{dC_3} & \frac{dM_{12x}}{dC_4} & \frac{dM_{12x}}{dC_5} \end{pmatrix} \begin{pmatrix} \frac{dD}{dM_{4ax}} \\ \frac{dD}{dM_{4ay}} \\ \frac{dD}{dM_{4bx}} \\ \frac{dD}{dM_{4by}} \\ \frac{dD}{dM_{12x}} \end{pmatrix} \tag{5.8}$$

This matrix defines the response to a detector for each monitor as a function of coil behavior and monitor response. For each detector, including the combination detectors, this matrix equation is solved for the slopes. Work by Chun-Min Jen analyzing the dithering results found that an minimum number of dither cycles required to find accurate slopes was 10. The only criteria for acceptable dither cycles was that the events in the cycle must pass all cuts except the energy burp and RMS cuts, as each cycle included intentional modulation of the measured beam energy. The slopes applied to the data were taken from the average of the results from at least 10 acceptable dither cycles, taken from a group of sequential runs in the same slug. As such, the dithering slopes in the code are changed approximately every three runs, and with only one set of slopes applied to each run such that the dither cycles from one run did not apply to the next set if the 10th cycle for a given set of slopes occurred in the middle of a run.

Following this analysis, and using the weighting scheme described in Sec. 5.5, the dithering analysis produced an asymmetry of $A_{Meas.} = -593.6 \pm 50.4$ ppb, as shown in Fig. 5.19 which is a -40.1 ppb correction.

We can again see the effects of including the Wien and IHWP while looking at the resulting asymmetries. Parallel to the discussion of the divided Wien/IHWP results in Sec. 5.6, we can examine the asymmetry results by the helicity control state. In Fig. 5.20 the asymmetries plotted do not have the sign flips applied. The asymmetries shown range in magnitude from 0.686 ppm to 0.492 ppm, indicating that there is an effect on the asymmetry associated with our spin-flipping methodology. By installing the double Wien filter for PREX, we are able to see an effect associated with the IHWP, validating the installation, as well as providing two data sets for each IHWP to average over.

5.6.2 Regression

Regression, the less invasive of the two beam correction approaches, attempts to apply beam corrections based on stochastic beam fluctuations and minimizing the χ^2 of a given fit[43]. The PREX analysis used the matrix inversion analysis code, similar to the dithering

127
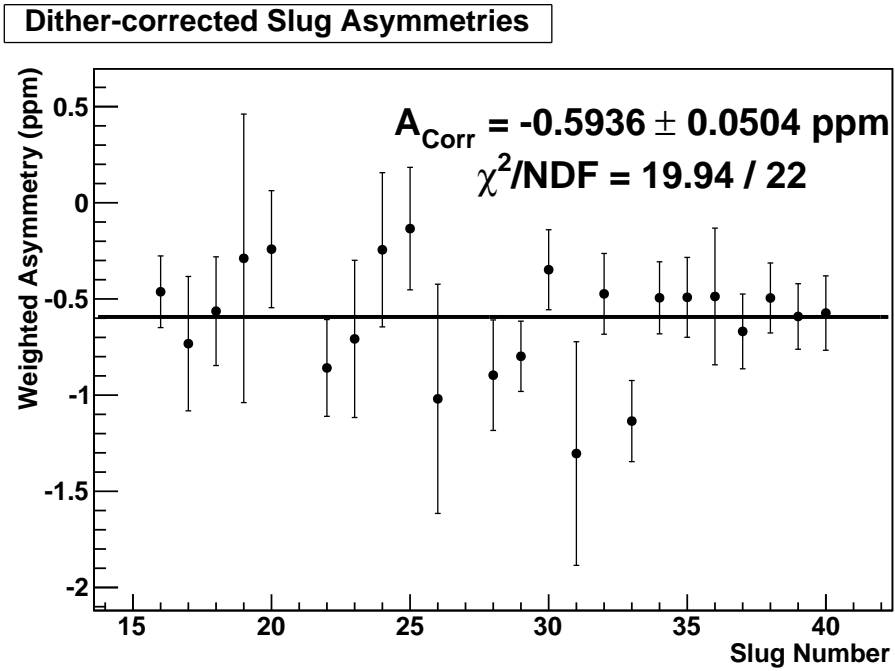
Figure 5.19: Signal-weighted detector asymmetries by slug number. These asymmetries are corrected using slopes generated by the dithering analysis.
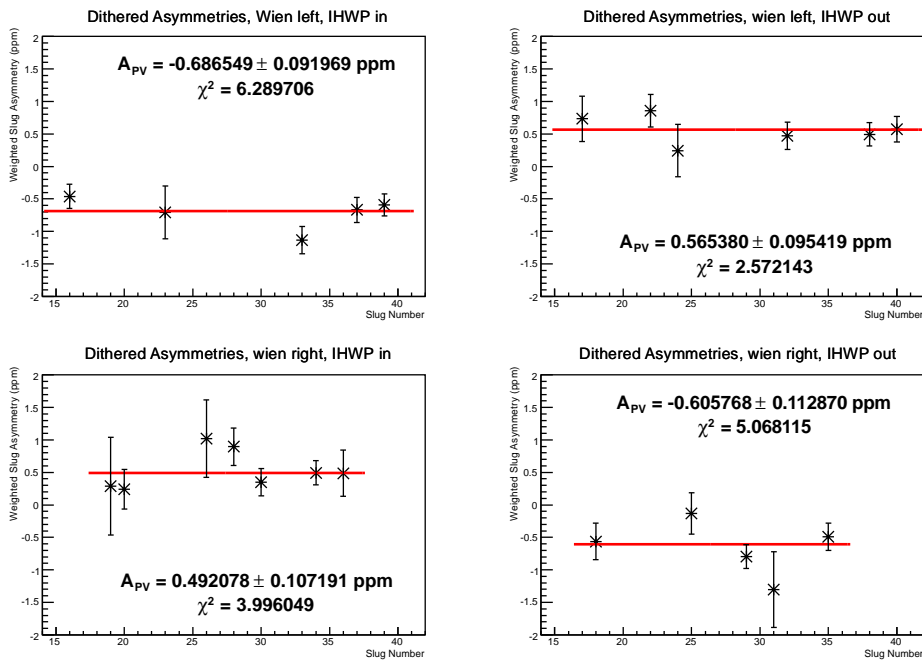
Figure 5.20: Plots of the dithered asymmetries, with slugs grouped by Wien and IHWP state. Note that these asymmetries are presented above without corrections for sign flips.

approach, to approximate the beam-correlated asymmetry dependent on the sum of the slopes and independent variable. For the independent variables being the BPM signals, this equation, the regression is performed by solving the equation

$$y = \sum_{j}^{m} B_j x_j \tag{5.9}$$

for m independent variables (BPMs), each with detector-monitor correlating slope B_j and monitor signal x_j. We can then predict the probability of measuring a value for the signal in the i-th event y_i from this equation. The slope can then be solved by minimizing the χ^2 for the predicted y_i for a given monitor signal $(x_j)_i$.

$$\chi^2 = \sum_{i} \frac{y_i - \sum_{j}^{m} B_j \left(x_j \right)_i}{\sigma_i^2} \tag{5.10}$$

for errors of σ_i, assuming a Gaussian probability[43]. This χ^2 is minimized for the slopes B_j (equivalent to α_j from Eq. 5.6) of all monitors, effectively finding the slopes that give $\frac{\partial \chi^2}{\partial B_j} = 0$.

This events for this analysis are taken from the complete data set, subdividing the runs into 5000 event blocks. The slopes are then found for, and applied to, this subset of the data, minimizing effects caused by drifts in the beam parameters. After applying the regression slopes to the raw asymmetry, the corrected asymmetry was found to be $A_{Reg} = -0.6005 \pm 0.0481$ ppm, as show in Fig 5.21. While the dithering-corrected asymmetry was the one used to extract the final asymmetry value, the regression-corrected asymmetry was used as a check for the dithered results. The regression analysis code was packaged in the analyzer and able to be called to produce the slopes for the BPM and BCM signals measured, making regression a valuable tool when dithering slopes were in early iterations.

5.7   Pull Plots

It is important to test if the dithered asymmetry we produced is accurate. One method of testing this is producing a pull plot. A pull plot calculates the contribution to the average, or 'pull' of each run. For the dithered asymmetries, with all beam parameters accounted for and corrected, the contribution of each run to the average should roughly follow a Gaussian. The pull of an individual data point on the calculated average is calculated for the i-th run

Regression-corrected Slug Asymmetries

A_{Reg} = -0.6005 ± 0.04809 ppm

χ^2/NDF = 28.24 / 22
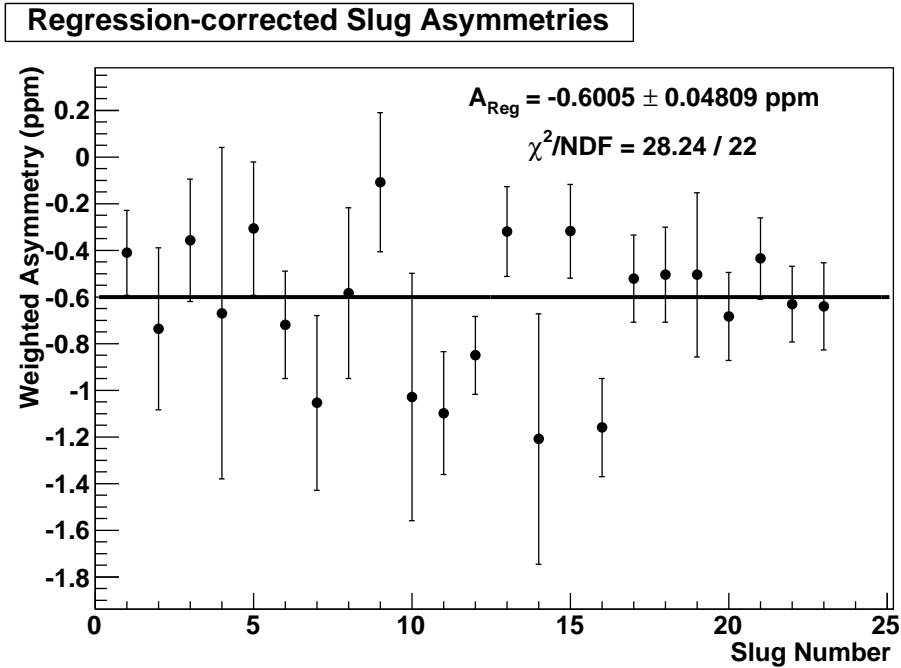
Figure 5.21: Signal-weighted detector asymmetries by slug number. The asymmetries are corrected by slopes generated using the regression analysis.

like

$$P_i = \frac{\langle \bar{A} \rangle - A_i}{\sigma_i} \tag{5.11}$$

This calculates the difference in all run asymmetries from the average, then divides by that error on that data point, quantifying how strongly the run pulls the weighted average of the asymmetry in any direction. By construction, a pull plot should see few points outside of 3σ. A larger than 3σ pull means that the run is an extremely accurate measurement of an asymmetry well removed from our measured average, and as a result having a markedly larger effect on the reported asymmetry. As seen in Fig. 5.22, we show a mean close to zero, and as such there is not a large trend in how the runs are affecting the asymmetry. Also, given that the RMS is approximately equal to 1 (suggesting that 65% of the run means fall within 1σ of the mean). This plot indicates that there are no $3\sigma+$ outliers, the contributions of each run are Gaussian, centered around our mean of approximately zero.

130
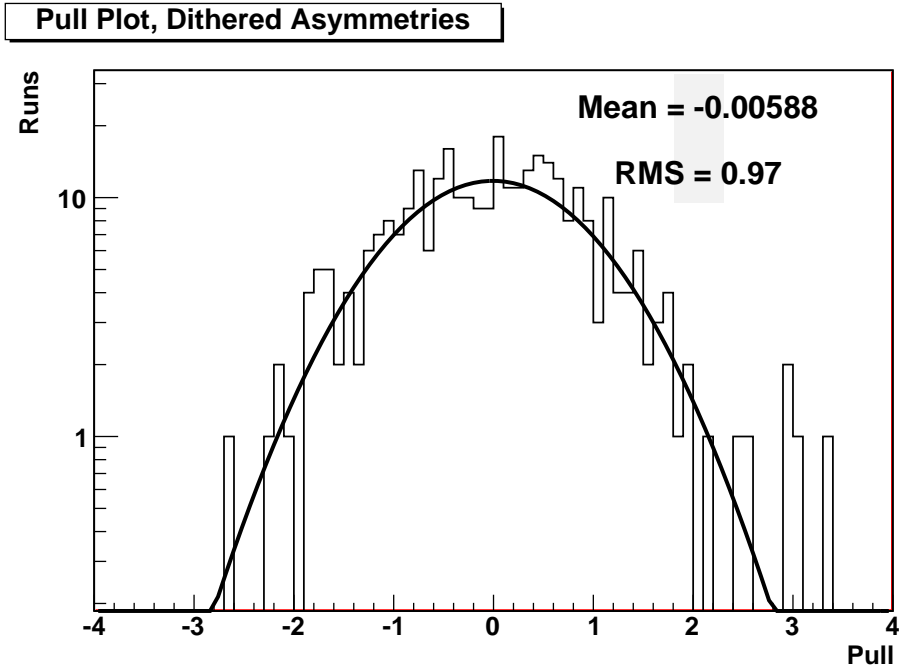
Figure 5.22: Pull plot of the dithered run asymmetry results, with entries defined by Eq. 5.11.

5.8   Applying Corrections to the PREX Asymmetry

After finalizing the dithered asymmetry and having an understanding of our track reconstruction and Q^2, our result needs to be corrected for a number of systematic effects. These effects refer to the elements of experimental approach that must be accounted for. Corrections applied to the dithered asymmetry produce the physics asymmetry, associated with the scattering process of electrons scattering off of ^{208}Pb nuclei. A list of the included systematic errors and the magnitude of the correction is listed in Table 5.4.

5.8.1   Polarization

The equation for the scattering of electrons weakly from a nucleus is defined for an electron with explicit helicity. While the electron injector at Jefferson Lab, described in Sec. 3.1, can control the helicity of the beam, the beam has a maximum polarization of 90%. Therefore, for 90% of the beam polarized (and therefore scattering) as expected, 10% of the electrons in the beam are in a different polarization state. These other electrons still have the appropriate energy and some value of helicity, but will not exhibit the same weak-scattering behavior as the bulk of the electrons in the helicity window. To account for the effects of polarization, we scale the measured asymmetry and statistical error by the measured polarization,

131

Error	Absolute (ppm.)	Relative(%)
Polarization	0.0071	1.1%
Det. Linearity	0.0071	1.1%
BCM Linearity	0.0007	0.1%
Rescattering	0.0001	0.0%
Transverse Pol.	0.0012	0.2%
Q^2	0.0028	0.4%
Target Thickness	0.0006	0.1%
A_C	0.0025	0.4%
Inelastics	0.0000	0.0%
Beam	0.0072	1.1%

Table 5.4: A table listing the systematic errors in the PREX results.

approximating the increase in helicity-dependent signal difference will increase linearly with an increase in the beam polarization. For polarization P and measured dithered asymmetry $A_{meas.}$ (with the distinction of $A_{meas.}$ coming from our detectors with the goal of measuring the physics asymmetry $A_{phys.}$), this gives the scaled asymmetry result as

$$A_{pol.} = \frac{A_{meas.}}{P} \tag{5.12}$$

The polarization P is the weighted average of the polarization measurements from the Møller and Compton polarimeters, described in Sec. 3.9. The Compton polarimeter measured a polarization of $P_C = 88.20 \pm 0.12(\text{stat.}) \pm 1.04(\text{sys.})\%$, while the Møller polarimeter measured a polarization of $P_M = 90.32 \pm 0.07(\text{stat.}) \pm 1.12(\text{sys.})\%$. This yields an average beam polarization of $P = 89.2 \pm 1.0\%$. Propagating the polarimeter error and the asymmetry's statistical error through this equation, this contributes a ± 0.0071 ppm error on our measurement.

5.8.2 Carbon Foils

As described in Sec. 3.4, concerns about thermal damage to the target led to the ^{208}Pb foil target being sandwiched between two diamond foils, composed of ^{12}C atoms. However, when the electrons scatter from the target, the detector is unable to differentiate between electrons scattering off the ^{208}Pb target or the surrounding ^{12}C diamond foils. As a result, the dithered asymmetry was calculated for the helicity-correlated differences for electrons scattering from either a ^{12}C or ^{208}Pb nucleus. The likelihood an electron will scatter from either of the nuclei is given by the contamination ratio D. The contamination ratio D is defined in terms of the

Target	Front ^{12}C (cm.)	Back ^{12}C (cm.)	^{208}Pb (cm)
PbD #1	0.0135	0.0146	0.051
PbD #2	0.0128	0.0132	0.05136
PbD #3	0.0216	0.0210	0.0494

Table 5.5: A table of the thicknesses, in cm., of the ^{12}C and ^{208}Pb foils before the experiment.

Target	^{12}C Thickness (g/cm^2)	^{208}Pb (g/cm^2)
PbD #1	0.0983	0.5743
PbD #2	0.0909	0.5824
PbD #3	0.1492	0.5605

Table 5.6: A table of the thickness in g/cm^2 for the foils.

relative number of nuclei in the target, from the thickness in g/cm^2 defining the weight per unit area, and the cross sections, defining the ratio in terms of how often the electron will scatter from a nucleus and how many of that nuclei there are to scatter off. The thickness of the foils was measured for the ^{12}C and ^{208}Pb by Dave Meekins before being installed in the target ladder, as listed in Tables 5.5 and 5.6, previously listed in Sec. 3.4. Therefore, for our dithered asymmetry, after corrections for beam polarization, $A_{pol.}$ the contribution of the scattering asymmetry from each target is given by

$$A_{pol.} = (1 - D) A_{Pb} + D A_C \qquad (5.13)$$

The final, ^{208}Pb result requires we subtract the carbon contamination from the measured result, by accounting for both the diamond's asymmetry and the ratio of ^{12}C to ^{208}Pb D, we can solve Eq. 5.13 for A_{Pb} as

$$A_{Pb} = (1 + D) A_{pol.} - D A_C \qquad (5.14)$$

For the ^{12}C asymmetry, we used the theoretical asymmetry calculated for the nucleus, as

$$A_C = \frac{G_F Q^2}{2\sqrt{2}} \frac{\sin \theta_W{}^2}{2\pi\alpha} \qquad (5.15)$$

which gives an average value of 817 ppb.

However, data early in the experiment showed worrisome correlation between detectors in different arms of the experiment. The utility of having two separate arms of the detector is that they measure different electron fluxes, resulting in different signals. With a correlation between detector signals between detector huts, as shown in Fig. 5.23, without any correlation

133
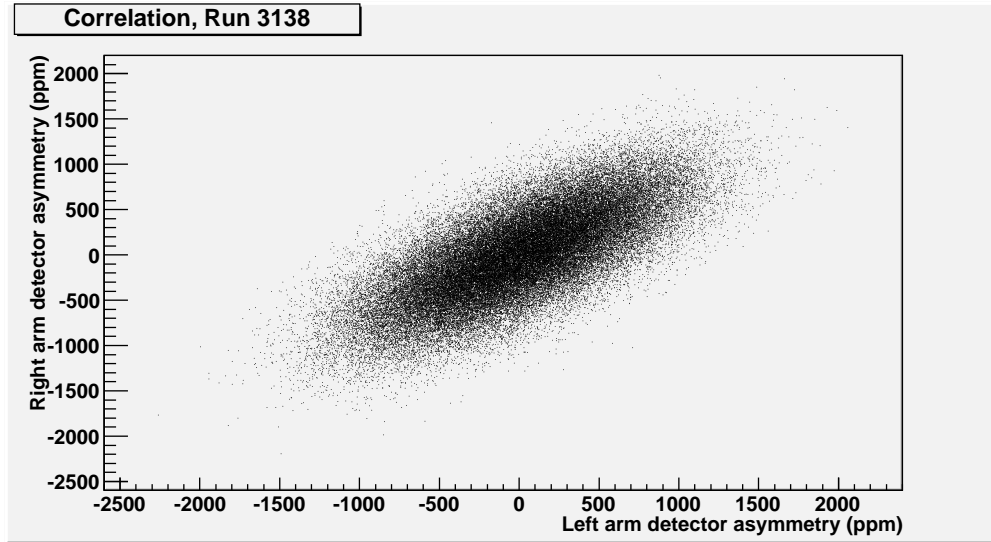
Figure 5.23: A plot of the regressed asymmetry measured in the left arm detectors against the right arm detector asymmetry. As regression calibrates for the position and current monitors, the pronounced correlation shown is unlikely a feature of beam parameters. Information from track reconstruction, as shown in Fig. 5.24, shows the correlation comes from target non-uniformities.

to the BPM and BCM signals, the data indicates that the correlation must be associated with an effect in the target chamber. Plots of the reconstructed electron tracks (shown in Fig. 5.24) show the electrons were not scattering uniformly from the ^{208}Pb target. The non-uniform scattering from the target shown in Fig. 5.24 appeared gradually, indicating that the target degraded to that point and therefore was being altered by the intensity of electrons incident on it. As this damage affects the ^{208}Pb foil but not the ^{12}C diamond foil, we know there is a correlation between the amount of beam time for a given target and the contamination ratio D. To calibrate the effect of the target melting, measurements were taken of the ratio of events scattering from the ^{12}C and ^{208}Pb, as defined by the ratios of form factors of the full nucleus, electric charge, and number of nucleons.

$$\frac{yield(C)}{yield(Pb)} \propto \frac{FF(C)^2}{FF(Pb)^2} \frac{Z_C^2}{Z_{Pb}^2} \frac{t_C}{t_{Pb}} \tag{5.16}$$

This defines the expected ratio of electrons scattering from the ^{12}C and ^{208}Pb in terms of the form factors, the number of protons, and the thickness of the ^{12}C foil t_C and ^{208}Pb foil t_{Pb}. Knowing that ^{208}Pb has $Z = 82$ and ^{12}C has $Z = 6$, the the ratio of yields requires defining the target thickness and form factors. Performed by Kiadtisak Saenboonruang and Robert Michaels, measurements of the form factors at different Q^2 values were taken, resulting in a

134
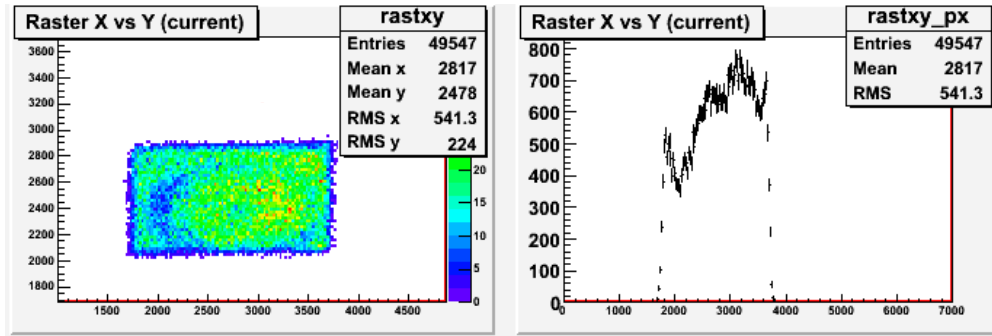
Figure 5.24: The raster check taken during the alignment procedure for the first target. The left contour plot shows the relative frequency of an electron reaching the VDC relative to the raster current, effectively the x-y position on the target face. The lighter regions have fewer electrons reaching the target, implying there is less lead material at that position. The right plot shows the scattering rate relative to horizontal position, with the dip correlating to the lighter spot at left.

ratio of 0.01863. Note that these different Q^2 are a reflection of the fact that for the same scattering angle correlates to a different Q^2 for the given material.

The calibration was performed using low-current data from the raster check, a reconstruction of the x-y point of scattering from the target in a low-current run, made during the process to resume high current running. These runs recorded the position of the electrons as they entered the detector hut and at the target (via track reconstruction described in Sec. 5.10.2). As the scattering is dependent on the amount of lead, these alignment checks can serve as a history for the target thickness, as shown for our second target, using the first run, 27160, and the last run, 27698, in checks for alignment.

The analysis, as done by Kiadtisak Saenboonruang, subdivides the 4 mm×4 mm covered by the rastered beam into a grid of points. To perform this correction, we used the data from when the beam alignment was tested plotting the electrons entering our detector as a function of x and y position on the target face, as shown in Fig. 5.25 and Fig. 5.25 for an unmelted and melted ^{208}Pb foil, respectively. Using the alignment check for the installation of the target, Fig. 5.25, before any high-current beam is sent to the target, we assume that the thickness is uniform, measuring a baseline thickness for each grid point relative to the upper left corner of the raster scan (shown as grid location 'A1' in Fig. 5.25). The upper left corner is selected for the normalization, as that grid point is presumed to change the least, given the decay shown in Fig. 5.26. Then, for each alignment check, it finds the number of events in the grid, then takes the ratio of events in each grid block against the upper left
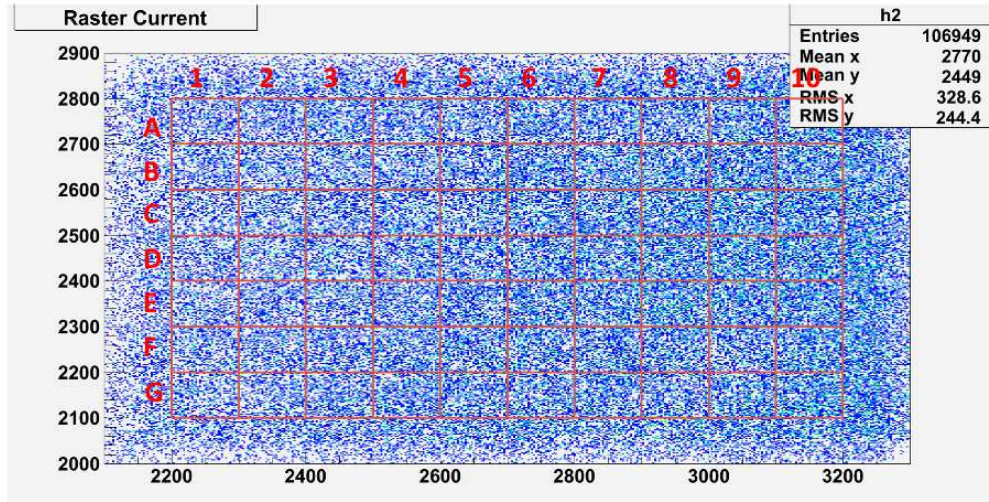
Figure 5.25: The raster check taken during the alignment procedure for the first installation of the second target. The signal is relatively uniform. Reproduced from internal analysis document by Kiadsitak Saenboonruang.
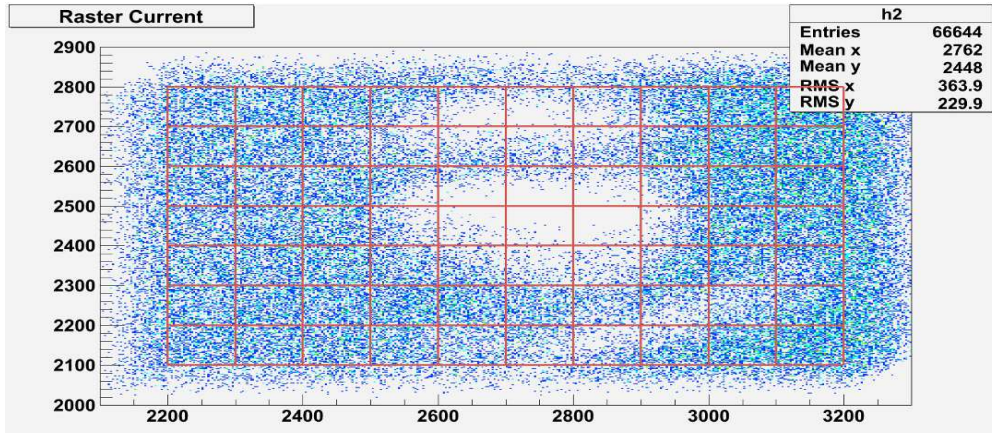
Figure 5.26: The alignment check for a late run on the second target. The signal is still uniform on the edges, but the center of the signal has lost events. Originally presented by Kiadsitak Saenboonruang.

corner's accepted events. As the number of events is proportional to beam current, time and the thickness, by normalizing the left hand corner we can discuss this ratio of events as proportional to the ratio of thicknesses. Then, to calculate a weighted thickness t for the target, we weight the thickness at each grid point t_i by the number of events recorded in the installation run $\#_i$.

$$t = \frac{\sum_i t_i \#_i}{\sum_i \#_i} \tag{5.17}$$

By weighting against the bin's events from the uniform target run, the contribution to the average thickness of each bin is weighted by the fraction of the events that would scatter into the target from that x-y bin for a uniform target. This calibrates the effects of the change in thickness to the expected number of events. These ratios were compiled and correlated to the parity data measurements, with the carbon/lead ratio for each run interpolated from thickness calculations made as part of the beam alignment checks. Using this interpolation, we were able to find ratios for each run (averaging 6.7%), which we can use with Eq. 5.14 to correct for the carbon contamination. This effect resulted in a 9.8 ppm correction to the physics asymmetry, with associated error of ±2.5 ppm.

5.8.3 Finite Acceptance

From the collimation and HRS described, the data measured is selected to be for a specific Q^2. However, the experimental design accepts data over the range of Q^2 defined by the collimator, where each angle has a different Q^2 and therefore a different cross section. As such, this data requires a correction for the fact that the measured flux is over some average Q^2.

To define a correction for this data, we use the Hall A Monte Carlo, designed to simulate the transport of electrons from the target to the detector hut, to measure the expected flux from the scattering. With this Monte Carlo, we can identify the acceptance function, as shown in Fig. 5.27, that defines the probability an electron reaches the detector in terms of angle (and therefore in terms of Q^2). With this information, we can identify the correction between the average asymmetry for the measured and expected Q^2 and make a correction based on that. From these simulations, the average asymmetry was found to be 707.8 ppb. This asymmetry is compared to the expected asymmetry for the average Q^2 (from Eq. 5.23), found to be 716.2 ppb. The ratio of asymmetries between our simulation for the
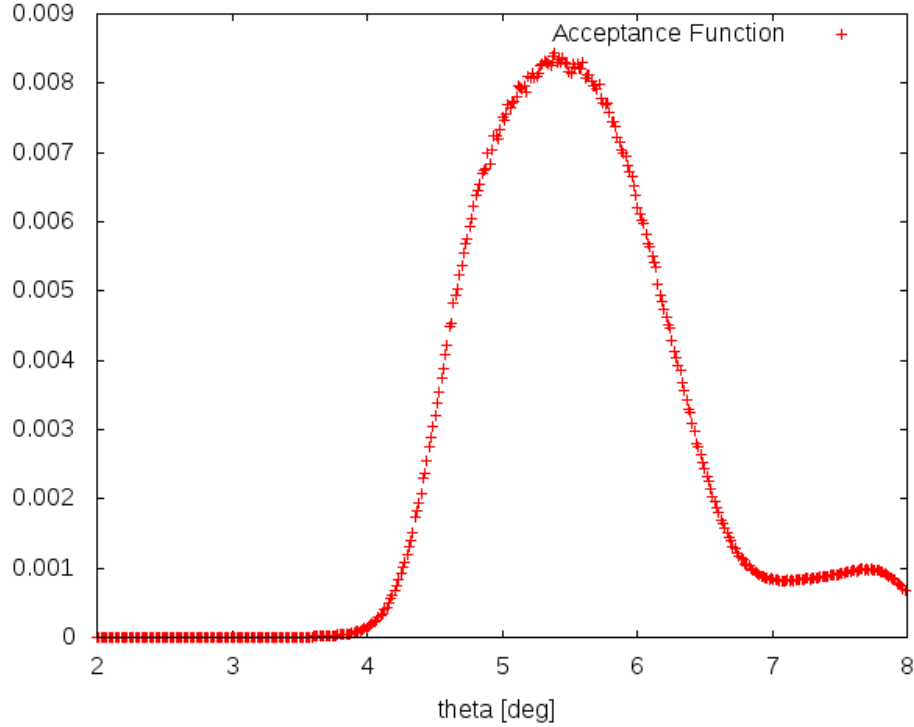
Figure 5.27: By Seamus Riordan, a plot of our acceptance function. This function defines the probability that an electron reaches the detector hut in terms of its scattering angle θ.

full acceptance and for our expected Q^2 from the acceptance proscribes a -1.2% correction to the measured asymmetry, decreasing the asymmetry based on the expectation from the measured Q^2.

5.8.4 Rescattering

Another concern relating to scattered electrons involves the rescattering of inelastically scattered electrons. Electrons that scatter inelastically from the target will be directed away from our detectors in the HRS, as described in Sec. 3.5. However, electrons scatter from the material of the magnets and be redirected in such a way as to propagate into our detector. The number of electrons that rescatter into our detector, the rescattering background B, can be written as

$$B = \int_{E_{thr}}^{E_{max}} P_{rs}(E)R(E)dE \tag{5.18}$$

for energy range between the threshold E_{thr} and maximum E_{max} energies over the energy-weighted rescattering probability $P_{rs}(E)$ and rate R (enumerating the flux of electrons in

the HRS). The rescattering probability is given by

$$P_{rs}(E) = RP\frac{E_{max} - E}{E_{max}} \tag{5.19}$$

and rate R is defined by the ratio of the elastic and inelastic cross sections

$$R(E) = \frac{\frac{d\sigma^2}{d\Omega dE}}{\frac{d\sigma}{d\Omega}} \tag{5.20}$$

To determine the rescattering probability RP in Eq. 5.19, we increased the central momentum of the HRS, defining the energy of the electrons that will reach our detector, and measured the average signal in our detector. By increasing the central momentum of the HRS, the elastically scattering electrons that would otherwise reach the detectors instead are bent out of the acceptance and into the frame of the dipole magnet. In doing so, we can use the elastically scattering electrons to test the behavior of electrons that pass into the dipole magnet frame. By measuring the fraction of electrons that reach the detector for a given percent increase in accepted momentum (for example, 5%), we can calculate the probability with which, during normal running conditions, an electron with the same percent decrease in energy (i.e. 5% below our 1 GeV elastics) that would also enter the detector.

Measurements were made during the PREX experiment in order to find the rescattering rate for electrons scattered during this experiment, the results of which are in Fig. 5.28. Because of a short in the right arm HRS on installation any right arm changes to the spectrometer magnets would require a 30 minute wait, so the rescattering test was run only on the left HRS. An initial measurement was made, representing $\frac{\delta p}{p} = 0$ at our production settings of approximately 10,000 channels. The dipole magnet, which defines the energy of electrons entering the detector, was changed to allow electrons with increasing energy to enter the hut, representing particles in the dipole that could rescatter, providing information on the relative contribution of different energy electrons to the flux of electrons measured. This information was combined with the expected asymmetries based on the Monte Carlo to find the correction to the asymmetry from the rescattered electrons, as produced by Seamus Riordan in Fig. 5.29. From work by Chun-Min Jen, the correction for rescattering was found to be ± 0.0001 ppm.
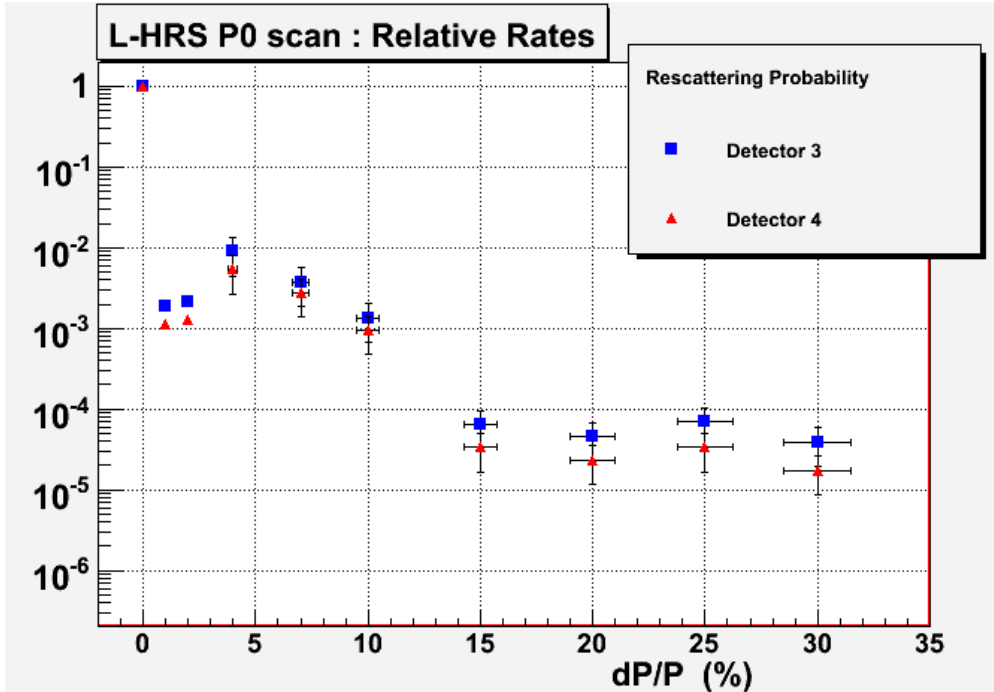
Figure 5.28: Summary of the rescattering measurements. The x-axis shows the percent change in central momentum accepted into the spectrometer, while data shows the signal size relative to the production momentum of E=1.0605 GeV.

5.8.5 Detector Linearity

The PREX detectors, as described in Chapter 4, are designed such that we assume that the signal measured in the PMT is proportional to the flux of electrons through the quartz. However, at certain voltages the PMT produces a nonlinear response, resulting in a disproportionate increase in signal relative to an increase in photons measured. This is a significant issue for a parity experiment, we expect the helicity dependence of weak scattering to affect the number of electrons in a window (and therefore the number of Cerenkov photons in the quartz). For a difference in electron flux at the detector, it is important to have the response uniform per electron, otherwise we would see a false asymmetry stemming from the nonlinear change in signal associated with the PMT. For a nonlinear PMT with nonlinearity β, the signal measured by $N^{L,R}$ photons in a left or right helicity window is given by

$$N_{meas.}^{L,R} = N^{L,R}\left(1 + \beta N^{L,R}\right) \tag{5.21}$$

A combination of bench tests and in-situ tests were performed on the photomultiplier tubes in order to ensure linearity by finding an operational voltage that is linear for our
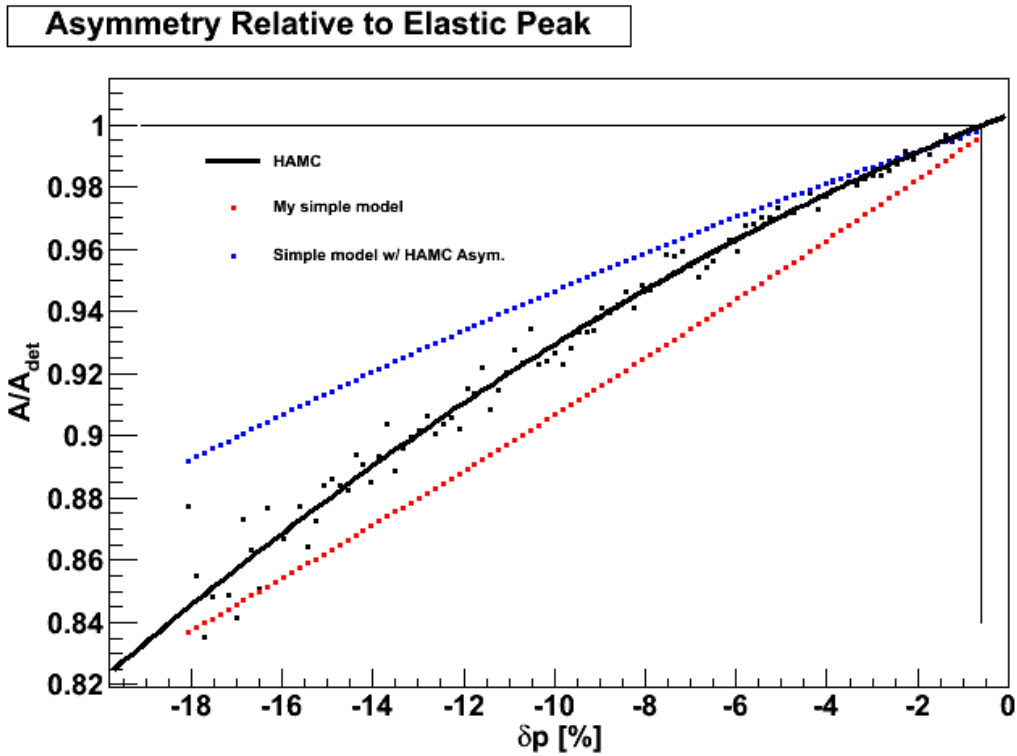
Figure 5.29: From Seamus Riordan, the results for a Monte Carlo simulation for asymmetry measured based on central momentum. The black line represents the results directly from the Monte Carlo. The red line represents the theoretical dependence for the asymmetry from the proposal, while the blue dotted line uses the Monte Carlo asymmetry combined with the proposal.

given signal size.

The bench tests used a black-box designed by Luis Mercado for the HAPPEX-III experiment. The black box uses the parity DAQ (with no beam in the experimental hall) to measure the response of a PMT to the change in signal from a pulsed LED above some flat baseline. Each PMT was installed in the black box, facing a pair of LED light sources which functioned as a baseline LED and a pulsed LED. The baseline LED was sent a uniform signal, producing a constant light flux measured by the PMT. The second LED was sent a voltage by a pulse generator, with the frequency of the pulse set at our helicity frequency. From these two LEDs, we have a flat signal shared between helicity windows, and a pulse that occurs in alternating windows, and using the parity DAQ we can measure the difference in signal size between events. We can then modify the settings for a filter wheel in front of the baseline LED (with 0%, 20%, 40%, 60%, 80% and 100% filters) to change the size of the base signal size while keeping the pulser unchanged. With the unchanged pulser (producing the same number of photons), a linear LED should report the same difference in signal size between the pulsed and unpulsed windows for all of the filter wheel settings. Similar to the black box tests, the in-situ tests used the LEDs installed on the quartz support rods, with the pulser and low voltage to power these LEDs and create a baseline and pulsed signal. The only difference between the in-situ tests and the bench tests is the filter wheel; the in-situ test did not have the wheel, so generating the baseline involved changing the LED voltage applied.

In each test, a linear PMT will have the signal difference between the pulsed and unpulsed signals should be independent of the filter used. A nonlinear measurement will still have a second order term, the β term in Eq. 5.21, and will appear as the signal measured as dependent on the baseline. Each PMT was tested for linearity over a range of 800-950V in order to find a range with a nonlinearity of less than 2%. In order to minimize systematic effects associated with the behavior of the PMT such as thermal stability, each test involved a pseudorandom cycling through filter settings[44]. The asymmetry, using the nonlinear signal size from Eq. 5.21, goes like

$$A_{NL} = A_{true} \left(1 + \beta \frac{N^+ + N^-}{2} \right) \tag{5.22}$$

for pulsed window N^+ and unpulsed window N^-. Fig. 5.30 shows a sample run, with the pulser on and baseline cycling, which appear as pairs of lines. The lower line in this figure

142
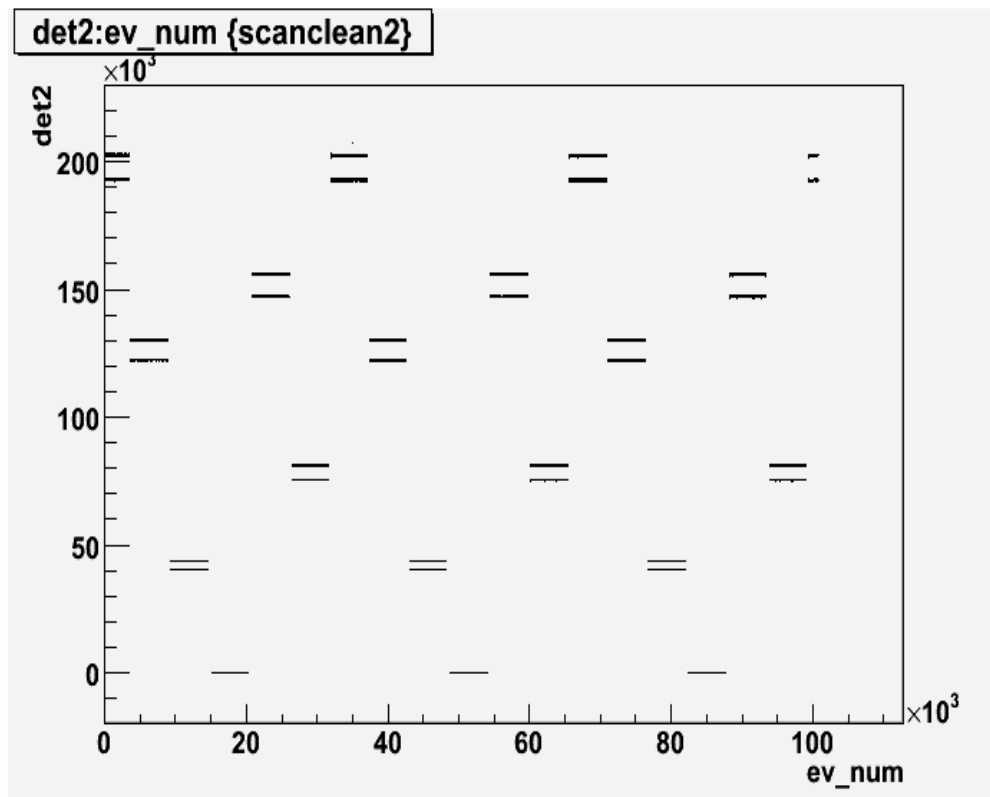
Figure 5.30: A sample plot of the PMT bench tests for detector 2 PMT.

is the baseline, and the upper line the pulsed signal. We can calculate the average difference between events for each baseline to be the signal from the pulser only, with the expectation that this number is fairly constant. Figs. 5.31 and 5.32 are plots of these differences in terms of the baselines for two different runs. Fig. 5.31 is linear, as the differences between pulsed and unpulsed signal are uncorrelated with the baseline, where Fig. 5.32 is nonlinear.

The data was sorted based on filter wheel position, with an example shown in Fig. 5.30. The difference can be sorted based on baseline signal and fit to a straight line to approximate the correlation between signal difference and baseline, with a preference towards having a weak correlation between these variables. Examples of these correlations are shown in Figures 5.31 and 5.32.

Measuring the nonlinear asymmetry A_{NL} in terms of the average signal allows us to extract the nonlinearity β. The effects for the nonlinearity were minimal at 150,000 channels, and as such the PMT HVs were modified throughout the experiment to maintain that signal size. A sample of these HV is listed in Table 5.7, representing a finalized set for the $50\mu A$ running.

143
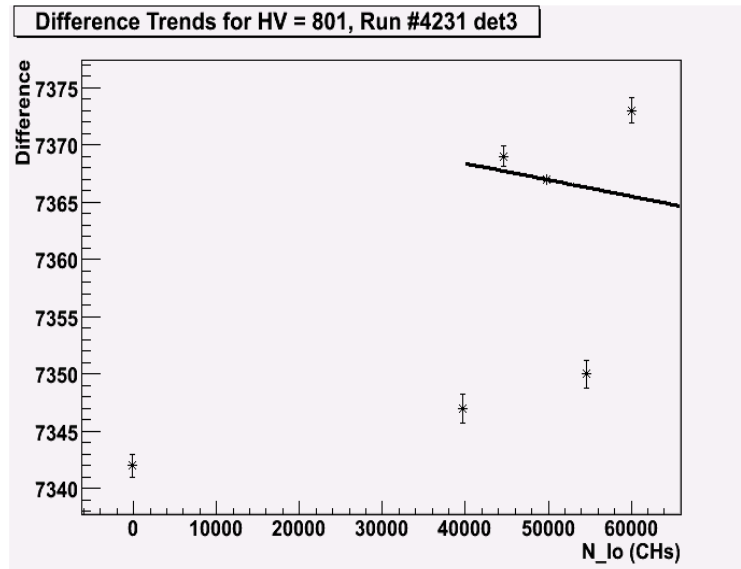
Figure 5.31: Detector 3 signal from run 4231, with PMT voltage set to -801V. The difference in signal for the pulser on and off, plotted against the signal size for pulse-off windows N_lo. This result shows a linear response to increased signal in our detector, as the difference in current between the pulsed and unpulsed detector windows does not depend on the total signal size.
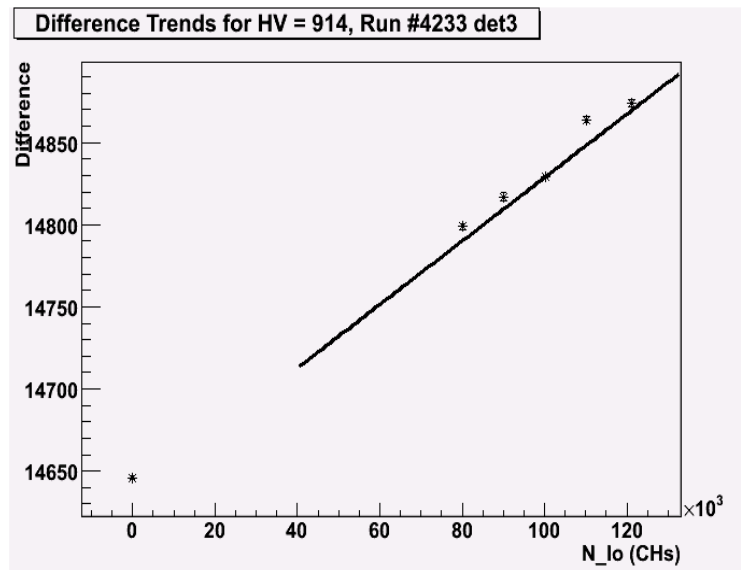
Figure 5.32: Detector 3 data for run 4233, with PMT voltage set to -914V. Shows stronger correlation than run 4231. In contrast with Fig. 5.31, the increase in signal associated with the pulser (with a fixed voltage, and therefore consistent number of photons) increases with the baseline. This shows the detector signal depends on the total signal size at -914V, showing the detector has a nonlinear response at this voltage.

144

Detector	PMT	HV (V)
#1	ZK5555	-675
#2	ZK4033	-725
A_T Right	ZK4035	-1000
#3	ZK5401	-900
#4	ZK5369	-622
A_T Left	ZK5366	-695

Table 5.7: A table of final HV settings for 50 μA running for 150,000 channel signals.

From these analyses, we found nonlinearity to be 1%. This uncertainty on the detector signal propagates through our analysis as a 7.6 ppb systematic uncertainty.

5.8.6 BCM Linearity

Given that the asymmetry is normalized to beam current, the PREX analysis is sensitive to any nonlinearity in the beam current monitors. The PREX BCM linearity correction was chosen to agree with the studies performed in the experiment previous to it, HAPPEX-III. For the HAPPEX-III analysis, the BCM asymmetry was compared with the difference in asymmetries between BCM1 and BCM2[27]. Similar to the argument for the DDiff_RMS cut, in Sec. 5.2, the double difference in the asymmetry between two beam monitors compares the precision at which the monitors measure the beam relative to each other. For two linear BCMs, the change in difference in signals between helicity windows should be roughly equivalent between BCMs. Therefore, there should be no correlation between the intensity asymmetry for a single BCM and the double difference. While the HAPPEX experiment found a -0.012% correlation between BCM1 and the double difference[27]. However, in light of the fact that no dedicated study on this effect was performed on the run level (meaning we are sensitive to any effects that may change the linearity of the BCMs), the HAPPEX-III experiment applied a larger correction on the order of 2.0%. As a result, for the PREX analysis the BCM linearity correction was conservatively set at 1.5%. This translates to a 1.5 ppb uncertainty.

5.8.7 Error on Q^2

Following Kiadtisak's analysis of the four momentum transfer for the PREX experiment (discussed in detail in Sec. 5.10), the uncertainty on the measurement of Q^2 was 1%. To identify the error in the asymmetry measurement to ascribe to this, Seamus Riordan used

HAMC to calculate a dependence of the asymmetry on Q^2. Following his analysis, the asymmetry measured for a pure lead target is given by

$$A = -0.0303 + 134.6Q^2 - 6142Q^4 + 29700Q^6 \qquad (5.23)$$

From this fit, the derivative of A with respect to Q^2 results in a 0.5% error for a 1% error on Q^2.

5.8.8   Poletip Scattering

Another correction to our asymmetry comes from poletip scattering. Similar to the arguments on rescattering in Sec. 5.8.4, electrons can scatter off of the iron in the mouth of the spectrometer and back into the acceptance. However, as the field from the dipole magnet polarizes the electrons in the iron, the effect of electrons scattering from the mouth of the dipole is dependent on the helicity of the scattering electron, producing a helicity-correlated effect. To account for this, we adapted the method used to make a similar calculation in the HAPPEX experiment. This approach uses Monte Carlo simulations to approximate the frequency of electrons scattering from the iron into the acceptance, and then the calculates the helicity-dependent asymmetry of such scattering.

The Monte Carlo is designed to calculate the electrons as they propagate from the beam line, off the target, then through the magnets. In order to use the simulation, we added additional 'apertures', or target volumes, matching the shape of the dipole apertures while being 0.3 mm wider. The decision to use 0.3 mm wider apertures is that the energy loss per unit length for 1.0605 GeV through iron is 0.3%, which would be out of our acceptance. By comparing the number of electrons measured that pass through the poletips relative to the dipole opening, we find the ratio of events to be 1.1×10^{-4}.

To calculate the analyzing power of the dipole frame, we needed the relative angle between polarizations for the iron and beam electrons and the polarization of the material. Following the analysis performed for HAPPEX comparing the fringe field directions to the beamline, the angle was accepted to be $\cos(\phi) = 0.2$. The simulations demonstrated that the electrons were scattering from the stainless steel upper lip of the frame. Calculating the polarization was done by defining the stainless steel polarization in terms of the iron's maximum polarizability (7%) and the ratio of the magnetic susceptibilities. For 0.4T, iron has a susceptibility on the order of 6000, while the stainless steel has a polarizability of 0.003,

giving a ratio of 5×10^{-7} between material polarizations[45].

Lastly, we needed to calculate the analyzing power of the poletip scattering. The dominant component of this analyzing power is for scattering where the spins of the electrons in the foil and beam are aligned, as given by

$$A_{zz} = -\sin^2(\theta_{CM}) \frac{7 + \cos^2(\theta_{CM})}{(3 + \cos^2(\theta_{CM}))^2} \tag{5.24}$$

and weighted by cross section

$$\frac{d\sigma}{d\Omega} = \left[R_0 \sqrt{\frac{m}{2E}} \frac{4 - \sin^2(\theta_{CM})}{\sin^2(\theta_{CM})} \right]^2 \tag{5.25}$$

These depend on center of mass scattering angle θ_{CM}, classical electron radius $R_0 = 2.818fm$, as well as electron mass and energy. While these need to be integrated over to find the full contribution of this poletip scattering, we realize that the electrons that scatter from the iron will pass through some quantity of iron. By the same reasoning by which we selected the dipole frame to accept electrons that lose no more than 0.3% of their energy, the path length the electrons would pass through for any scatter less than 6° would transit over enough iron to lose 0.3% of it's energy. Therefore, we need only integrate $A_{zz} \times \frac{d\sigma}{d\Omega}$ from 6-180°, giving a result 0.036.

Combining the frequency at which the electrons scatter from the poletips, the fraction of electrons in the dipole frame that are polarized, and the rate by which the electrons scatter to generate this asymmetry, the total effect is $(1.1 \times 10^{-4}) \times 0.2 \times (0.07 \times 5 \times 10^{-7}) \times 0.036 = 3.96 \times 10^{-13}$. This asymmetry, 0.396 ppb, is a small concern relative to the asymmetry, order 10^{-7}.

5.8.9 Transverse Polarization

Another concerning factor was the transverse polarization of the beam. Given the component of the spin normal to the motion of the beam, there will be a different scattering asymmetry associated with this interaction between transverse-spin electrons and the nucleus. This effect is a combination of the fraction of spin normal to the beam relative to the fraction of the spin oriented with the beam motion, and the size of the transverse asymmetry.

To find the transverse component in our asymmetry, we need to measure the transverse polarization (as this will define the contribution of transverse scattering to overall scattering). To do this, we examine data from a "spin dance", which measures the polarization of the
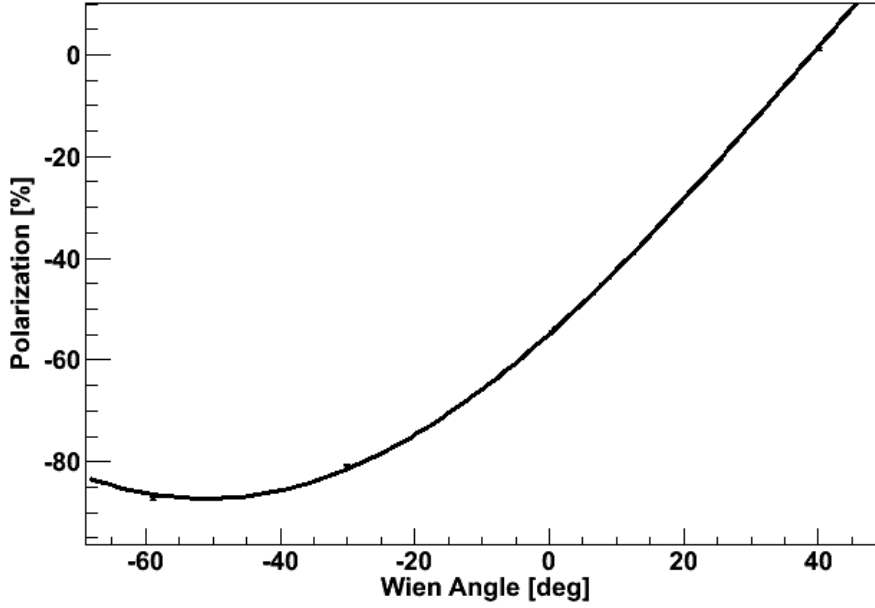
Figure 5.33: From Seamus Riordan, a fit of beam polarization entering the hall as a function of the Wien angle setting for -60°, -35°, 0° and 40°.

beam relative to the Wien angle setting. Seamus Riordan's analysis of the four data points, omitting the difficult-to-configure 90° point, suggests the polarization P is described by

$$P = P_0 \sin{(\phi - \phi_0)} \qquad (5.26)$$

with best fit parameters P_0=87.24 and ϕ_0=38.95°, from the fit in Fig. 5.33. This peaks at -51.05°, which is 0.95° from the -52° degrees we ran at, resulting in a suppression of 0.017 degrees for the transverse asymmmetry. Following concerns about calibration drifts as well as controlling the polarization in both x and y, our analysis presumes a 3° transverse contamination.

While the final transverse asymmetry, discussed more in Section 5.9, was found to be $A^T_{Pb} = 0.28 \pm 0.25$ppm for ^{208}Pb, and $A^T_C = -6.49 \pm 0.38$ppm for ^{12}C, this analysis was performed with preliminary transverse asymmetry numbers for ^{208}Pb of 120 ± 190 ppb (producing a negligible difference in results).

The last contribution to the error associated with the transverse asymmetry is the acceptance error e, a factor in how the error asymmetrically enters the detectors based on the acceptance. Analyses from Robert Michaels and Kent Paschke use a worst-case symmetric cancellation factor of 0.1, which presumes that from various settings and previous experience

that a 10% error was the maximum uncanceled factor between the two arms of the experiment. From this 10% factor, we add a factor of two for the different rate between the arms, defining our acceptance error as 0.2 for this transverse asymmetry contribution. With these factors combined, the correction is

$$\delta_{AT} = A_T P_T e = 0.12 ppm * 0.054 * 0.2 = 1.3 ppb \tag{5.27}$$

yielding a 1.3 ppb correction to the asymmetry.

5.9 Transverse Asymmetry

5.9.1 Analysis

In addition to the primary measurement, the PREX experiment took approximately one day of data with the electrons polarized transverse to the beam motion, in order to have data on the size of the transverse asymmetry contaminating the measurement of the longitudinally polarized electrons off ^{208}Pb. These results were collected both for ^{12}C and ^{208}Pb. Because weak interactions uphold time reversal symmetry, the single-photon exchange asymmetry is identically zero and this measurement was therefore a probe of multiple photon exchange, which was deemed a potentially interesting physics measurement in its own right.

To create the transverse polarization, the settings to the Wien filter were modified to have the electrons enter the hall with momentum perpendicular to the propagated spin direction. This maintains the parameters of the created electrons, allowing us to use the same settings used in the rest of the experiment. As this requires specific Wien settings, the sign flips for the transverse asymmetry measurement are performed using only the insertable half-wave plate.

The propagation of electrons is otherwise unaffected by spin, so the equipment and analysis procedures upstream of the target are identical to those described in the previous chapters. As the transverse polarization breaks the azimuthal symmetry for scattering, the combination of the detectors in different arms into a single asymmetry measurement is performed differently in this analysis. The measured asymmetry in each arm will differ by a factor of -1, requiring us to handle each arm as a separate measurement in each run. The absolute sign of the transverse asymmetry was found to be positive in the left arm, so the -1 factor was applied to all right-arm asymmetries. The results for the measured asymmetry came from a weighted average of the left and right arm asymmetries.
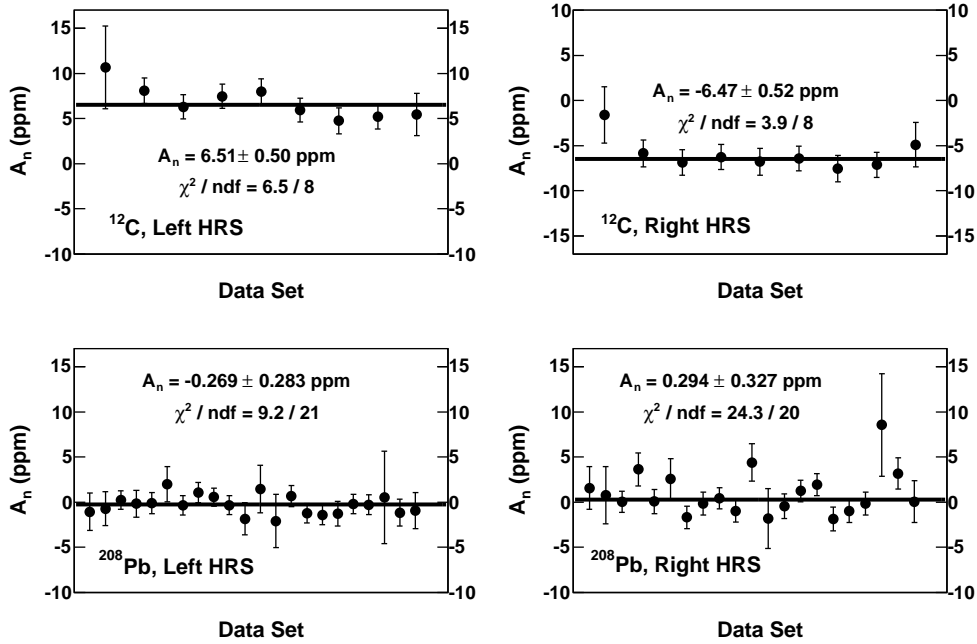
Figure 5.34: Signal-Weighted Transverse Asymmetries by Run Number for all arm-target combinations.

5.9.2 Measured Transverse Asymmetry

These combined results give measured asymmetries of $A_C^m = 5.788 \pm 0.322$ppm and $A_{Pb}^m = 0.221 \pm 0.176$ ppm[46]. With systematic corrections applied, this analysis calculated a ^{12}C transverse asymmetry of $A_C^T = -6.49 \pm 0.36$(stat.)± 0.10(sys.) ppm for $Q_C^2 = 0.009051$ GeV^2. The ^{208}Pb asymmetry was calculated as $A_{Pb}^T = +0.28 \pm 0.21$(stat.) ± 0.14(sys.) ppm from $Q_{Pb}^2 = 0.009082$ GeV^2. This ^{12}C result agrees with theoretical predictions from M. Gorchtein and C. Horowitz[47], while the ^{208}Pb result disagrees with the theoretical result (and in fact agrees with zero). This result, as shown in Fig. 5.35, for ^{208}Pb is the only measured asymmetry disagreeing with models, wher the predictions for ^{12}C, as well as the transverse asymmetries for electrons scattering off ^{1}H and ^{4}He nuclei (measured in other JLab experiments), agree with model predictions. The physical explanation for this zero asymmetry is currently unknown, but is suspected to be related to Coulomb distortions.

5.10 Four-Momentum Transfer

The parity-violating scattering asymmetry, as described in Sec. 2.3, is dependent on the square of the four-momentum transfer, Q^2, between the incident and emitted particles. As
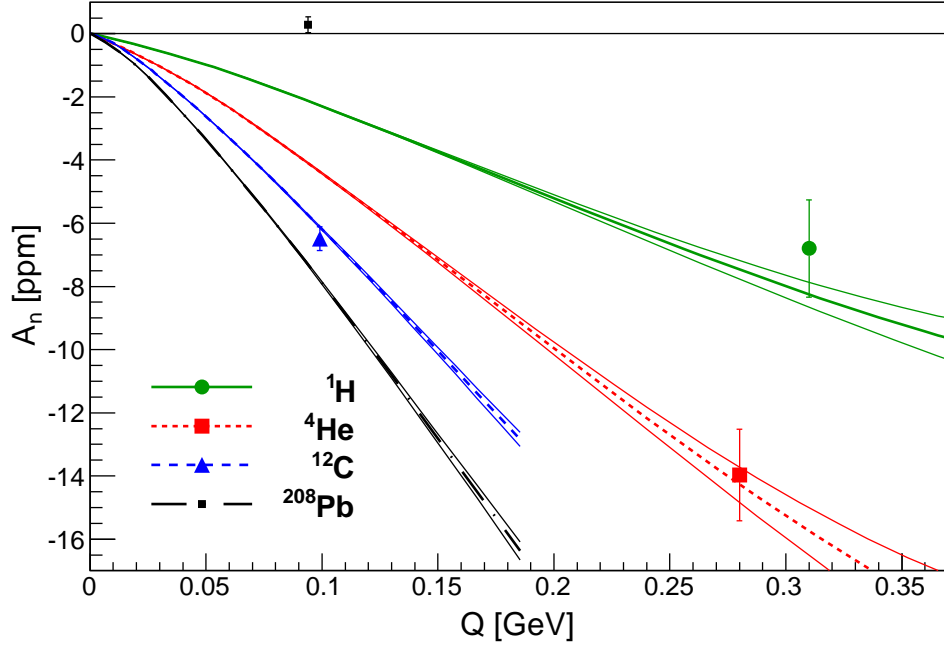
Figure 5.35: From Abrahamyam et. al.[46], the measured transverse asymmetries for ^{1}H, ^{4}He, ^{12}C and ^{208}Pb, shown with predictions. The ^{1}H, ^{4}He, and ^{12}C measured values agree with the model predictions for the transverse asymmetry, while the ^{208}Pb asymmetry does not.

such, any attempts to extract the neutron skin thickness from the asymmetry measurements requires a measurement of Q^2. The four-momentum transfer depends on the initial energy E, final energy E$'$ of the electron, as well as the scattering angle θ, as

$$Q^2 = 2EE'\left(1 - \cos\theta\right) \tag{5.28}$$

The beam energy was measured to the 10^{-3} using the energy measurements on the beam, while the energy of the scattered particles was measured to $\frac{dp}{p} = 5 \times 10^{-4}$ resolution by the high resolution spectrometer. The remaining measurable quantity in Q^2 was the scattering angle. The angle was measured in 31 dedicated low-current runs (15 left-arm Q^2 runs, 16 right-arm runs). The scattering angle θ is comprised of the spectrometer central angle θ_0, which defines the angle between the target and the spectrometer acceptance, and the target angles θ_{tg} and ϕ_{tg}, which define how the electrons scatter relative to the spectrometer angle. This relationship is defined by

$$\theta = \frac{\cos\theta_0 - \phi_{tg}\sin\theta_0}{\sqrt{1 + \theta_{tg}^2 + \phi_{tg}^2}} \tag{5.29}$$

The angle the electrons scattered at was measured using two different methods; the pointing measurement and using spectrometer reconstruction.

5.10.1   Pointing Angle Measurement

The pointing measurement, used as a calibration for the spectrometer reconstruction, measures the differential recoil in scattering energy, defined by

$$E' = \frac{E - E_{loss}}{1 + \frac{2(E - E_{loss})\sin^2\frac{\theta}{2}}{M_t}} - E_{loss} \tag{5.30}$$

This describes the final energy E′ in terms of the initial energy E, energy loss E_{loss}, scattering angle θ and the mass of the scattering target M_t. As the electron will give more energy to a lighter target, the difference between E and E′ will increase for lighter targets. As such, the pointing measurement for PREX involved measuring the energy of electrons scattering from a water target. Since the electrons scatter from both ^{16}O and ^1H, this allows for scattering from two targets using the same beam, minimizing the effects of fluctuating beam parameters and allowing for canceling the E_{loss} by measuring the difference in energy loss between the two targets. A plot of energy loss from electrons scattering from a water target is shown in Fig. 5.36, with peaks marked for the the ^{16}O and ^1H nuclei. With this in mind, the energy difference between the ^{16}O and ^1H peaks in the energy distribution is equal to

$$\Delta E' = E'_O - E'_H = E\left(\frac{1}{1 + \frac{2E\sin^2\frac{\theta}{2}}{M_O}} - \frac{1}{1 + \frac{2E\sin^2\frac{\theta}{2}}{M_H}}\right) + \mathcal{O}\left(E_{loss}\right) \tag{5.31}$$

This measurement is performed using the sieve-slit, selecting events going through only the central hole. By making this selection cut, we ensure that the electrons are scattering at the θ and ϕ angles allowed by the holes in the sieve, which are fixed relative to the target position. This measurement was taken for three HRS settings, which changes the final values of E′ without affecting the scattering angle, probing three different points in the HRS focal plane. These data points were fit for a least squares method for $\chi^2 = (\Delta E'_{calc} - \Delta E'_{meas})^2$ for $\Delta E'_{calc}$ from Eq. 5.30.
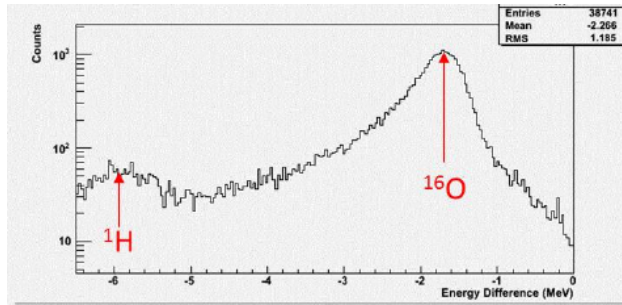
Figure 5.36: From K. Saenboonruang[48], a plot of the energy lost by 1 GeV electrons scattering from a water molecule. The two peaks are associated with the energy loss for an electron scattering from the ^{16}O and ^{1}H nuclei.

This analysis gives a resulting angle of $5.065 \pm 0.020°$ for the left arm and $4.933 \pm 0.020°$ for the right arm.

5.10.2   Spectrometer Reconstruction

The pointing measurement accurately measures the flux from a subset of angles scattering from the target, defining the central angle of the acceptance. In order to measure the average angle from our full acceptance, as needed for PREX, we need to perform a reconstruction of the tracks which the electrons scattered from the target into the detectors. By comparing the physical design of the sieve slits to their locations in the track reconstruction for a number of targets, we can calibrate correlations between hits on the VDC (as described in Sec. 3.6), and the scattering parameters at the target. The use of many scattering targets in this minimize the errors in the reconstruction for all angles. The Q^2 is the calculated for events that pass through the drift chambers and produce a non-pedestal signal, where the weighted average comes from the reconstructed scattering angle and initial/final energies.

From these measurements, the left arm measured electrons with an average $Q_L^2 = 0.009330\,\mathrm{GeV}^2$ (as shown in Fig. 5.37) and the right arm measured $Q_R^2 = 0.008751$ GeV^2. These results are weighted by accounting for left-only, right-only and both arm runs. In doing so, the ratio R then weights the left arm by a factor of $\frac{1}{1+R}$ and the right arm by a factor of $\frac{R}{1+R}$, with R determined by the statistical weights of the runs with the either, or both, HRS arms functioning. By this calculation, the left arm is weighted by 0.5020 and the right by 0.4980. From this weighting, and including the single-arm running data (also by statistical weighting), we find the average $Q^2 = 0.009068$ GeV^2.

153
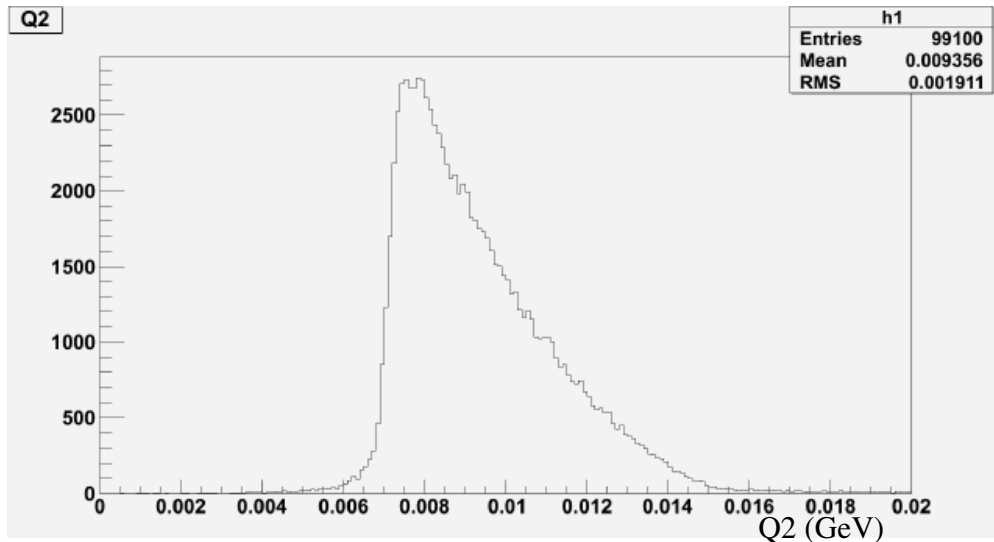
Figure 5.37: From K. Saenboonruang[48], a sample measurement of the four momentum transfer Q^2 for electrons scattering through the left spectrometer.

5.11 Acceptance

The values for Q^2 measured from reconstruction survey the entire acceptance, with the contributions from each angle defined by the acceptance function in Fig. 5.27. However, the reconstruction assumes that the scattering from the target is a single exchange of a γ or Z_0 boson between the electron and a target nucleon, with the four momentum transfer from a single scatter known as Q^2_{vertex}. This assumption neglects factors such as the exchange of multiple bosons or other kinematics, where an electron has a second interaction in the target chamber. If these interactions scatter electrons from their initial scattering angle to an angle within our acceptance, the track reconstruction will correlate the scattering angle at the target based on the position the electron passed through our acceptance-defining collimator. The Q^2 measured, as discussed in Sec. 5.10, is dependent on the angles observed in our track reconstruction. This observed four momentum transfer $Q^2_{obs.}$ differs from Q^2_{vertex} based on the contributions to the measurement from these electrons that scatter multiple times in the chamber.

Multiple scattering, where an electron has two or more interactions within the target chamber, introduces a smearing of our acceptance, where an electron that initially scattered at an angle blocked by the collimator could be redirected in such a way as to enter our acceptance. To account for the multiple scattering, simulations were run using the Hall A Monte Carlo (HAMC) to calculate this smearing. To include this effect, we need to simulate

154

how electrons propagate after the first γ/Z^0 exchange with the target. This propagation is affected by the cross section, defining the scattering angle, multiple scattering, quantifying the probability of a second interaction, and acceptance, defining the range target range of scattering angles, as a function of the initial scattering angle θ. The Monte Carlo produces simulation results for the electrons that propagate to the detector, as well as recording the initial scattering angles. From this information, we can create a map $M(\theta, \theta')$ that describes the probability for an electron scattering into the detector based on its initial scattering angle θ and final angle θ', with θ' given by the reconstruction of the particle track from our detectors.

To find the multiple-scattered acceptance, we calculate the fraction of electrons that are measured in the detector $\alpha'(\theta')$ for a given final angle θ', which reflects how for the reconstructed angle the electrons are measured. This is equal to the simulated number of events that are measured in the detector $N'(\theta')$ at angle θ', normalized by the cross sections for scattering at a given angle, multiplied by the frequency that an electron will multiple scatter from θ to measured angle θ' defined by our map $M(\theta, \theta')$. Therefore, the range of angles accepted by the spectrometer is

$$\alpha'(\theta') = \frac{N'(\theta')}{\int \sigma_{Pb}(\theta) M(\theta, \theta') d\theta} \tag{5.32}$$

For an accurate Monte Carlo, this number of electrons accepted as a function of angle should reproduce the weighted Q^2 measured, following

$$Q^2_{obs.} = \frac{\int 2EE'(1 - \cos(\theta')) \alpha'(\theta') M(\theta, \theta') \sigma(\theta') d\theta'}{\int \alpha'(\theta') M(\theta, \theta') \sigma(\theta') d\theta'} \tag{5.33}$$

With a map that can reproduce the observed Q^2 in terms of initial scattering angles, our acceptance, and our multiple scattering map $M(\theta, \theta')$, we can invert this map to find the probability that an electron observed at θ' was generated at the vertex at angle θ. This inverted map allows for a calculation the contribution to Q^2 in terms of the initial scattering angle θ, then contributing to the number of electrons scattering at that angle $\alpha(\theta)$. From the number of electrons scattering at a given angle θ through our acceptance and into our detectors, we can calculate the four momentum transfer at the scattering vertex Q^2.

Raw Asymmetry	-0.5535 ± 0.06339 ppm
Dithered Asymmetry	-0.5936 ± 0.0504 ppm
Corrections	
Beam polarization	89.2%
Average carbon contamination	6.69 %
Polarization	± 0.0071 ppm
Det. Linearity	±0.0071 ppm
BCM Linearity	±0.0007 ppm
Rescattering	±0.0001 ppm
Transverse Pol.	±0.0012 ppm
Q^2	±0.0028 ppm
Target Thickness	±0.0006 ppm
A_C	±0.0025 ppm
Inelastics	±0.0000 ppm
Beam	± 0.0072 ppm
Carbon/Polarization Corrected Asymmetry	+0.6558 ± 0.0603 ± 0.0130 ppm
After finite acceptance correction	
Physics Asymmetry	+0.6537 ± 0.0603 ± 0.0130 ppm

Table 5.8: A table listing the results. From the normalized 'raw' asymmetry from the detectors, we apply the beam corrections in Sec. 5.6 to produce the dither corrected asymmetry. This asymmetry has corrections for the beam polarization (in Sec. 5.8.1), carbon contamination (from Sec. 5.8.2)/, and other sources in Sec. 5.8 applied to produce the carbon/polarization corrected asymmetry. This asymmetry is lastly corrected for finite acceptance to produce our final physics asymmetry.

5.12   Parity Violating Asymmetry

After applying all corrections and determining the Q^2 of the electrons reaching the detectors, we can quote our physics asymmetry. From the dithering-corrected asymmetry measured by the PREX experiment leads to a parity-violating 'physics asymmetry' of $A_{PV} = 0.6537 \pm 0.0603(\text{stat.}) \pm 0.0130(\text{sys.})$ ppm with $Q^2 = 0.00880 \pm 0.00011$ GeV^2. These errors are a 9.22% and 1.99% error, respectively. The ordering and application of corrections is reiterated in Table 5.8.

5.13   Extraction of R$_n$

With this measurement of the asymmetry, we can extract R$_n$, though not without addressing a number of practical components. Firstly, we must consider the effects of Coulomb distortions. For each proton in a nucleus there is some probability that an electron will scatter elastically. Therefore, for a heavy nucleus with many protons, there exists some probability
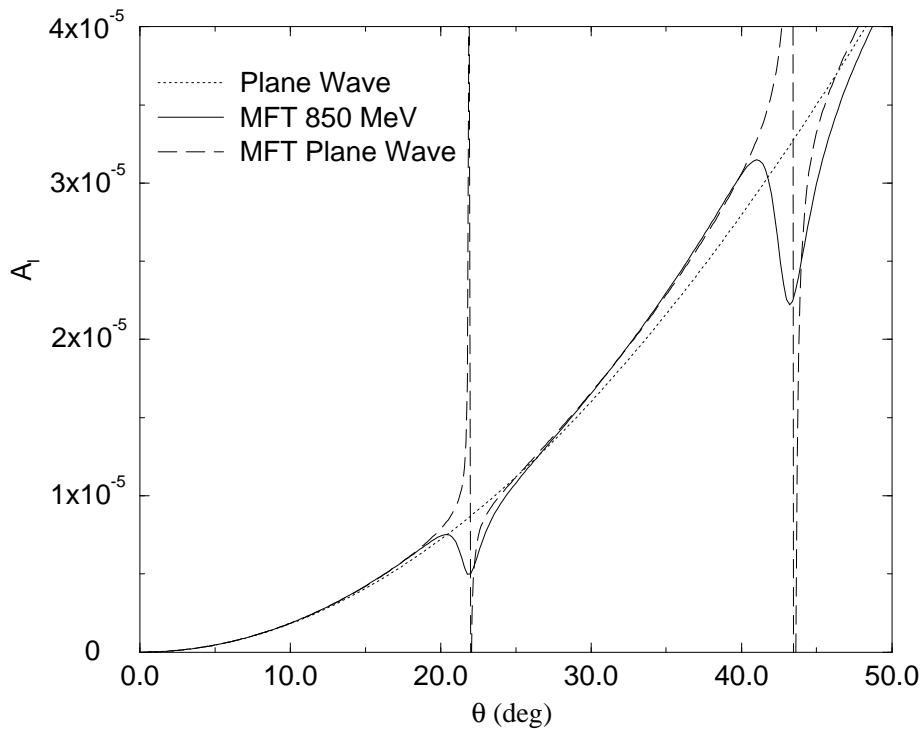
Figure 5.38: From C. Horowitz[49], a plot of scattering angle against asymmetry for a 850 MeV electron in the mean-field theory. This is compared against the plane wave (dashed line), showing diffraction minima, and a plane wave (dotted line), calculated for no neutron skin.

that an electron will scatter from multiple protons elastically, distorting the outgoing wave relative to the initial scattering, with the overall effect on the order of $Z\alpha$. To calculate these distortion of electrons scattering from ^{208}Pb, the electron is decomposed into a partial wave expansion of the Dirac equation, and then the scattering is calculated by summing over the phase shifts to these partial waves[49] to find the expected, undistorted asymmetry. This summation, shown in Fig. 5.38, can be compared to the mean field theory model without Coulomb distortions. As the asymmetry is dependent on the ratio of neutron and proton form factors, the diffraction minima of the form factors will result in a unphysical asymmetry at the proton form factor's diffraction minimum. The inclusion of Coulomb distortions allows for calculating these by removing these infinities from this formulation of the form factor. This Coulomb distortion approach, when compared to a plane wave solution for the proton and neutron radii being equal, show similar behavior away from these minima, as one could expect for a small skin.

Any scattering experiment will measure some spread of angles (however small), which will affect the cross section measured. To account for this, we must consider the acceptance function ϵ, which defines the probability an electron scattering at some angle $d\Omega$ is measured. To do this, the asymmetry is averaged over the cross section and acceptance function for all angles, defining the contribution to the asymmetry from electrons scattering at each angle $\left(\frac{d\sigma}{d\Omega}\right)$ and then reaching our detectors $(\epsilon(\theta))$ like

$$\langle A \rangle = \frac{\int d\theta \sin\theta \epsilon(\theta) \frac{d\sigma}{d\Omega} A_{PV}}{\int d\theta \sin\theta \epsilon(\theta) \frac{d\sigma}{d\Omega}} \tag{5.34}$$

We can then calculate, for a range of models, the predictions for asymmetry as a function of measured charge density and modeled neutron densities, with the final fit giving the neutron skin thickness as $R_n = 0.33^{+0.16}_{-0.18}$ fm[50] for a mean proton radius of 5.45 fm. To test the accuracy of the result, we can calculate the predicted radii from each model. From work by Horowitz et. al.[51], our result was tested against a theoretical asymmetry calculated for electrons scattering from a generalized Wood-Saxon weak charge density

$$\rho_W(r) = \frac{\rho_0}{1 + \exp\frac{r-R}{a}} \tag{5.35}$$

as a function of an average weak charge radius R and parameters ρ_0 and a. From the asymmetry of electrons scattering from the Wood-Saxon potential, we can calculate a weak form factor for different weak charge radii and tune the parameters until the average asymmetry agrees with the PREX result. From the analysis of this model's form factor, we can solve the Helm model exactly to find what the predicted mean neutron radius is, with the result of $R_n = 0.33^{+0.16}_{-0.18}$ fm[51], showing that our extraction of the neutron skin thickness agrees with model predictions for the physics asymmetry from PREX.

158

CHAPTER 6

CONCLUSIONS

The parity violating scattering asymmetry, with all corrections discussed in Sec. 5.8, is reported as $A_{PV} = 0.6537 \pm 0.0603(\text{stat.}) \pm 0.0130(\text{sys.})$ ppm. Using the same Monte Carlo simulation as described in Sec. 5.11, we can use the given acceptance function for the detectors to define the contribution from each scattering angle, allowing for calculation of Coulomb distortions described in Sec. 5.13. The extraction of the neutron skin thickness, primarily performed by C. Horowitz, found the neutron skin thickness to be $R_n - R_p = 0.33^{+0.16}_{-0.18}$ fm, from a mean neutron radius of $R_n = 5.751 \pm 0.175$ (exp.) ± 0.026 (mod) ± 0.005 (strange) fm[51].

6.1 Implications of the PREX Neutron Skin Measurement

The PREX result measures at the 95% confidence level that the r.m.s. neutron radius $\sqrt{\langle r_n^2 \rangle}$ is greater than the proton r.m.s. radius $\sqrt{\langle r_n^2 \rangle}$. As such, this result demonstrates that the predictions from models regarding the existence of a skin are accurate. As discussed in Chapter 2.4, a neutron skin measurement serves as an important constraint on many nuclear models. The PREX result is a measurement of the ^{208}Pb skin with a 3% precision, larger than the design goal of a 1% measurement. From our 3% measurement on the neutron skin, the PREX results for asymmetry do not reject the bulk of possible models, as shown in Fig. 6.1.
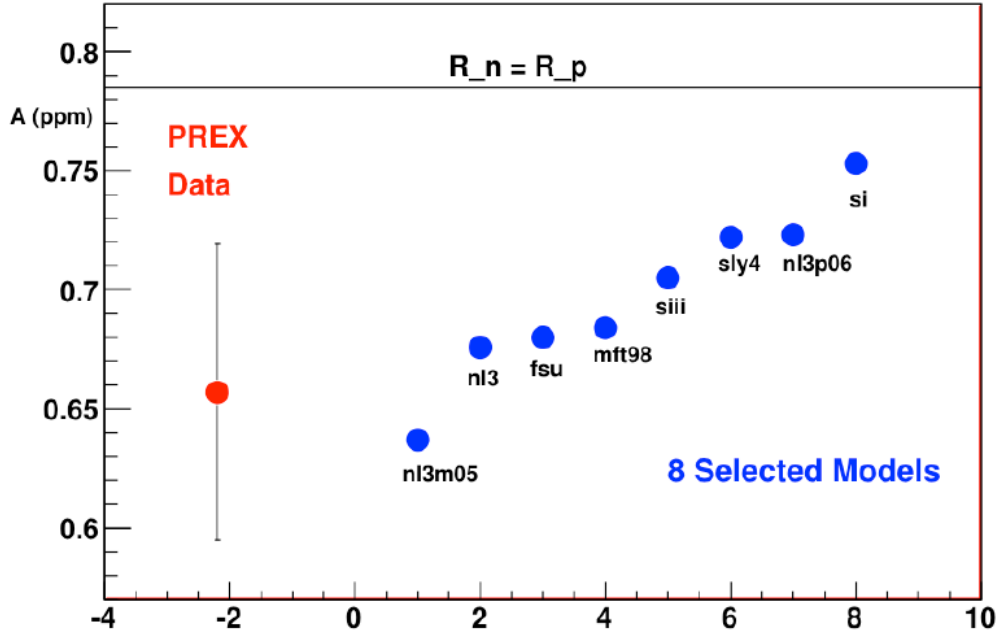
159

Figure 6.1: From R. Michaels[29], a plot of the measured PREX asymmetry against a number of mean field (NL3) and Skyrme models.

6.2 Future Prospects

The future of neutron skin measurements at Jefferson Laboratory is tied to the 3% precision of the PREX result. As the design precision of the measurement, at 1%, would provide stronger constraints on models of neutron-rich matter, a more precise measurement would be able to rule out models and regions of parameter space. Therefore, a second run, PREX-II has been approved at Jefferson Laboratory. The intent of PREX-II is to improve the overall statistical error of the measurement by taking more data, with a focus on preparing for the experimental issues that caused significant loss of beam time for the first run. The significant causes of down time during PREX were two issues: loss of target vacuum, and radiation damage to the magnets. Work is underway to analyze the radiation in the hall in an attempt to better protect the magnet electronics, and the vacuum chamber of the target has had its seal replaced in order to improve the seal at the most susceptible joint.

In parallel to this, a separate proposal has been submitted to the Jefferson Lab advisory committee requesting to measure the parity violating scattering asymmetry from ^{48}Ca[52]. This Calcium Radius Experiment, CREX, selects a nuclei lighter than the ^{208}Pb nucleus which has 20 protons and 28 neutrons. The feature of this atom is that ^{48}Ca is doubly-magic nuclei, minimizing the scattering effects associated with spin while measuring the effects of
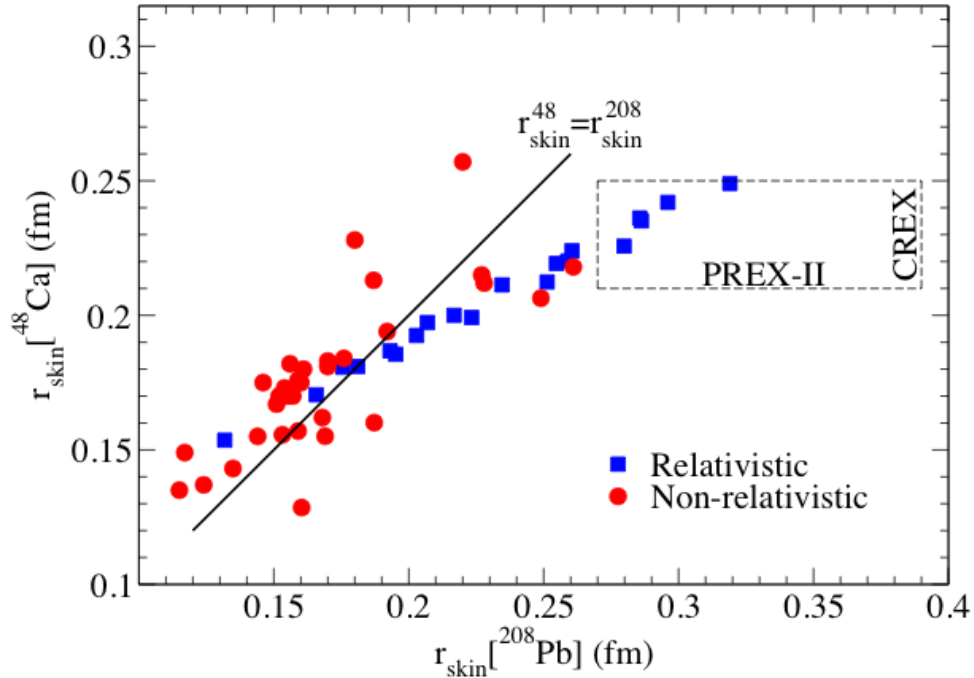
Figure 6.2: From S. Riordan et. al.[52], a plot of the model predictions for the neutron skin thickness of ^{208}Pb and ^{48}Ca from various models. Relativistic and non-relativistic models do not show agreement on which nucleus has a thicker neutron skin.

a neutron skin for another asymmetric nucleus. The addition of CREX measurement of the ^{48}Ca neutron skin thickness to the ensemble of neutron skin thickness measurements addresses points that cannot be analyzed by a ^{208}Pb measurement alone. The predictions for a neutron skin thickness of both atoms, depending on the models used, predict different answers for which nucleus has a larger skin thickness, shown for relativistic and non-relativistic model predictions of the ^{208}Pb and ^{48}Ca skin thicknesses in Fig. 6.2. Constraints on ^{48}Ca, in addition to providing additional insight into the behavior of dense neutron matter, will constrain models of medium-weight nuclei in a way that a PREX-II measurement cannot.

6.3 Concluding Remarks

The PREX measurement successfully measured an asymmetry of $A_{PV} = 0.6537 \pm 0.0603 \text{(stat.)} \pm 0.0130 \text{(sys.)}$ ppm. The systematic error, both in terms of the absolute (± 0.0130ppm) and relative ($\pm$ 1.99%) error represent an achievement in the precision of our measurement. Preparation for the PREX experiment resulted in many innovations in electron scattering measurements. The target for this experiment was a high luminosity ^{208}Pb target, with a

lifetime prolonged by the cooling apparatuses without affecting our ability to measure the scattering from the ^{208}Pb nucleus. Upgrades to both the Møller and Compton polarimeters allowed for polarimetry measurements of a 1 GeV electron beam, a first for Hall A at Jefferson Lab. By improving the raster synchronization with the injector and adding the Wien filter as a helicity control we minimized systematics associated with our injector, producing a parity-quality beam capable of measuring an asymmetry on the order of 10^{-7}. The field settings for the high resolution spectrometers resulted in a compact elastic peak in the focal plane, which was measured by specially designed quartz Cerenkov detectors. Additional tests performed in Mainz, Germany produced data showing the possibility of future detectors having data resolution under 20%, a further improvement on the quartz Cerenkov detectors. These improvements to the polarimetry, beam quality and magnet tuning will contribute to future measurements at Jefferson Lab.

APPENDIX A

EVENTS REMOVED BY CUT

Slug	Total Events	OK Events	Low Beam Cut	Other Cuts
16	1411921	1234605	107539	71845
17	489107	363090	67643	59876
18	800990	676766	106027	18999
19	150610	120975	17304	12555
20	1162555	921976	143477	136247
22	1471881	1223131	148946	101896
23	955682	736399	144111	102484
24	665165	529000	76745	98367
25	1172264	998000	76601	98763
26	199374	185932	8248	5325
28	930008	600940	302380	26897
29	1662058	1429491	176876	57976
30	1127244	1000869	90213	38475
31	153670	125540	25513	2838
32	1569829	1345955	144033	83821
33	1913826	1579435	268685	70700
34	1248295	1063450	132630	56226
35	995483	863765	101132	31900
36	828578	493877	313739	29039
37	1124380	920305	161795	47295
38	1287327	931372	283595	91465
39	1342712	1057739	206068	83250
40	1336434	996491	233753	108286
Total	23999393	19399103	3337053	1434525
%	100%	80.8%	13.9%	5.3%

Table A.1: A table listing the total PREX events, OK events, low-beam events, and other event cuts. The other event cuts are presented as the total number of events that pass low beam but fail at least one other cut.

Slug	B.Burp	E.Seq.	P.Seq.	Start	Mon.Sat.	ADC Burp	Scaler	Pos.B.E.	B.B.RMS	D.Diff.	Pos.Sat.	Adcx Bad
16	342	0	56	0	0	1637	3137	61933	0	4740	0	0
17	47	0	17	0	0	595	594	56578	0	2045	0	0
18	423	0	21	0	0	941	2123	10997	375	4119	0	0
19	121	0	6	0	0	167	231	11826	102	102	0	0
20	2127	0	29	0	0	1408	1868	40071	1148	34494	55102	0
22	1009	0	56	0	0	1595	3638	92700	1422	1475	0	1
23	1447	0	69	0	0	1129	2272	64217	1258	15850	16242	0
24	126	0	28	0	0	810	1593	55579	40	21077	19114	0
25	442	0	41	0	0	1437	1525	94277	204	837	0	0
26	68	0	12	0	0	246	427	4210	20	342	0	0
28	87	0	23	0	0	670	552	25184	21	360	0	0
29	1237	0	41	0	0	1498	2690	47594	1161	3755	0	0
30	1598	0	39	0	0	1049	2722	28406	1386	3275	0	0
31	254	0	18	0	0	79	442	1550	142	353	0	0
32	2269	0	61	0	0	1459	4862	67619	2083	5468	0	0
33	3283	0	63	0	0	1699	2834	53268	3095	6458	0	0
34	577	0	29	0	0	1037	2125	41184	469	6867	3938	0
35	4411	0	18	0	0	991	1779	21194	345	3162	0	0
36	2195	0	29	0	0	788	916	15214	922	7658	1317	0
37	889	0	58	0	0	1274	2000	33662	851	7323	1237	1
38	906	0	12	0	0	1434	2238	49095	1218	21595	14967	0
39	895	0	34	0	0	1648	2949	69003	599	6730	1392	0
40	454	0	35	0	0	1558	1439	98451	566	5783	0	0
Totals	25207	0	795	0	0	25149	44956	1043812	17427	163868	113309	2

Table A.2: A table listing the events removed by cuts other than low beam.

APPENDIX B

BPM PLOTS, BY WIEN/IHWP STATE AND SIGN-CORRECTED

The following are plots for BPM 4ax, 4ay, 4bx, and 4by, separated by Wien/IHWP state, as well as the sign corrected average.
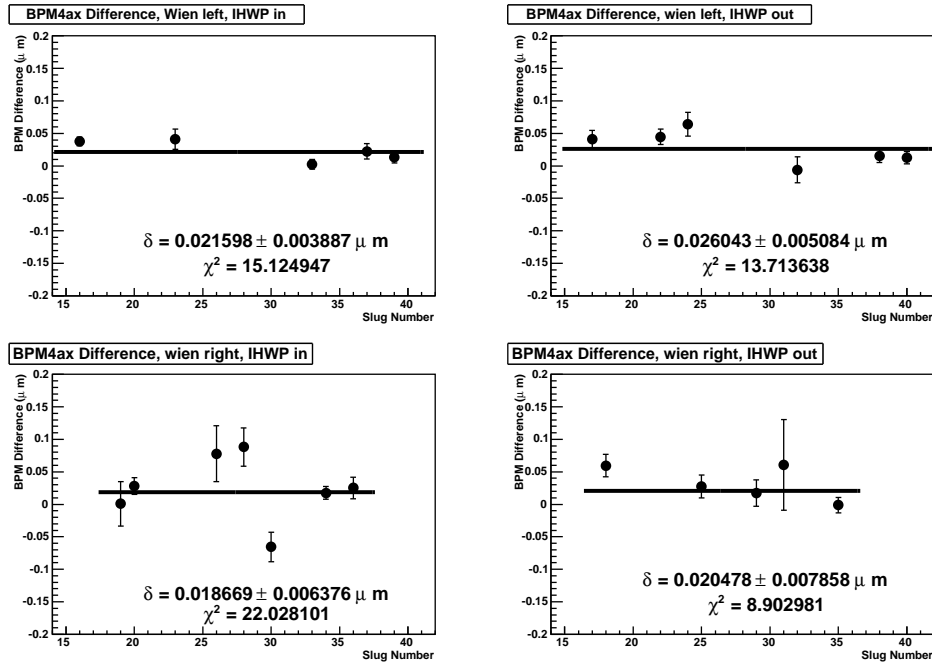
Figure B.1: Plot of the multiplet difference in BPM 4ax as a function of slug number. Each plot contains the slugs sharing a single IHWP and Wien state, without the sign change applied.
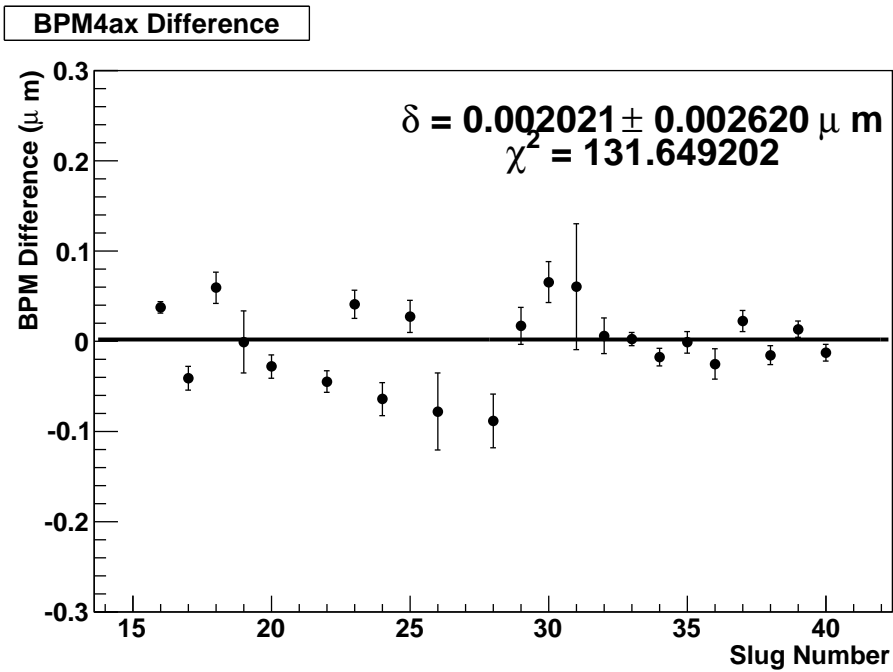

Figure B.2: Plot of the multiplet difference in BPM 4ax as a function of slug number. Each slug has the sign change applied, such that this data is for left-right differences.
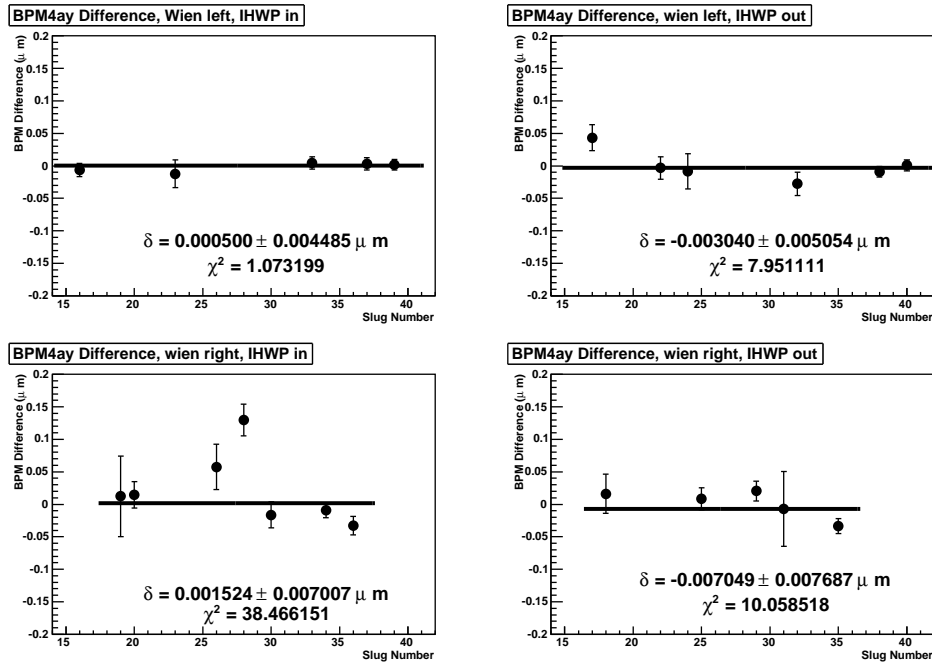
Figure B.3: Plot of the multiplet difference in BPM 4ay as a function of slug number. Each plot contains the slugs sharing a single IHWP and Wien state, without the sign change applied.
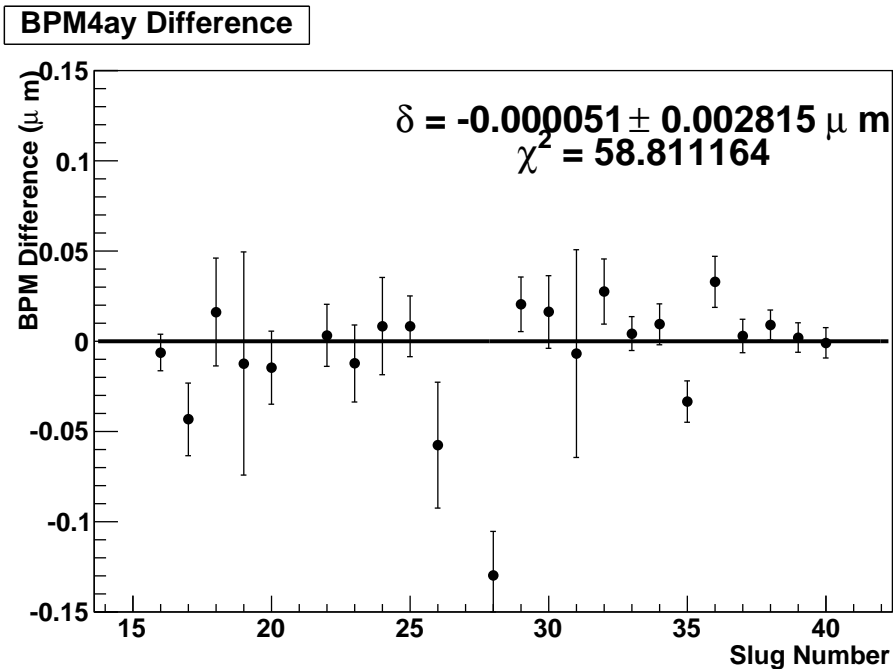

Figure B.4: Plot of the multiplet difference in BPM 4ay as a function of slug number. Each slug has the sign change applied, such that this data is for left-right differences.

Figure B.5: Plot of the multiplet difference in BPM 4bx as a function of slug number. Each plot contains the slugs sharing a single IHWP and Wien state, without the sign change applied.

Figure B.6: Plot of the multiplet difference in BPM 4bx as a function of slug number. Each slug has the sign change applied, such that this data is for left-right differences.
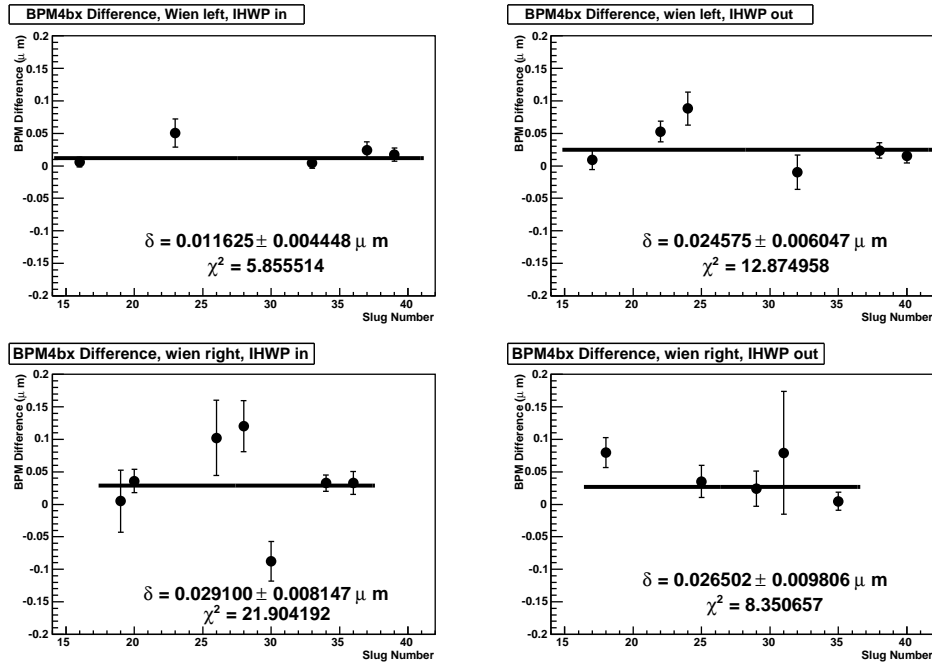
Figure B.7: Plot of the multiplet difference in BPM 4by as a function of slug number. Each plot contains the slugs sharing a single IHWP and Wien state, without the sign change applied.
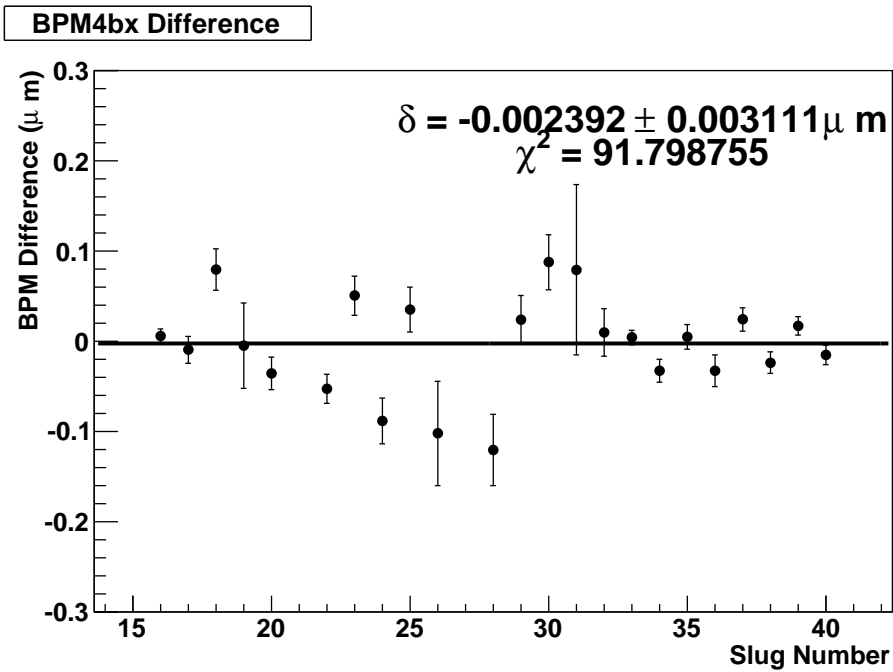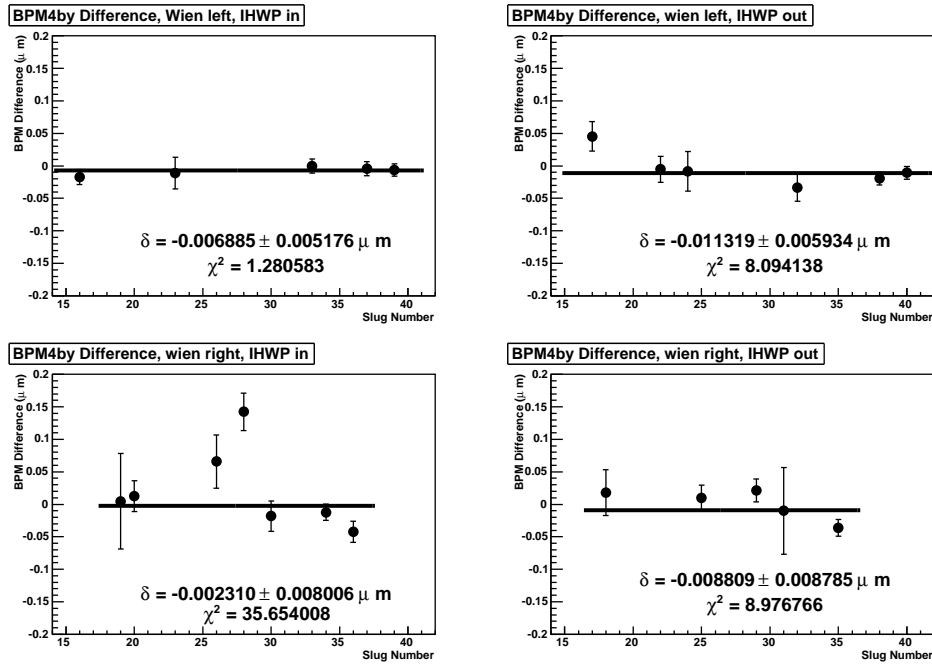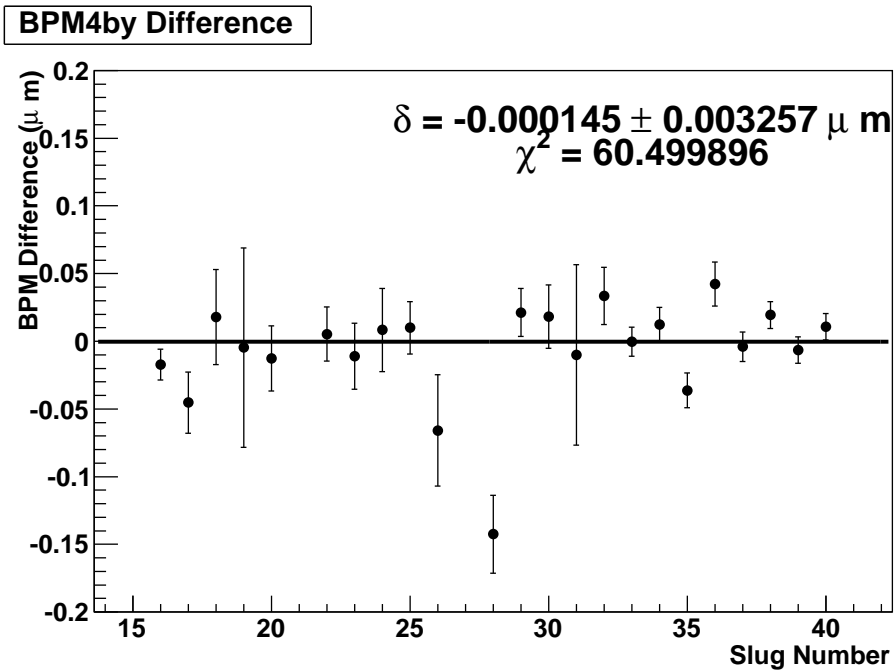

Figure B.8: Plot of the multiplet difference in BPM 4by as a function of slug number. Each slug has the sign change applied, such that this data is for left-right differences.

BIBLIOGRAPHY

[1] J. B. Bellicard et. al., *Scattering of 750-MeV Electrons by Calcium Isotopes*, Phys. Rev. Lett. **19** (1967), 527.

[2] I. Sick et. al., *Shell Structure of the ^{58}Ni Charge Density*, Phys. Rev. Lett. **35** (1975), 910.

[3] B. Frois et. al., *High-Momentum-Transfer Electron Scattering from ^{208}Pb*, Phys. Rev. Lett. **38** (1977), 152.

[4] T.W. Donnelly, J. Dubach, and I. Sick, *Isospin Dependences in Parity-Violating Electron Scattering*, Nucl. Phys. A **503** (1989), 589.

[5] T.D. Lee and C.N. Yang, *Question of Parity Conservation in Weak Interactions*, Phys. Rev. **104** (1956), 254.

[6] C.S. Wu et. al., *Experimental Test of Parity Conservation in Beta Decay*, Phys. Rev. **105** (1957), 1413.

[7] C. J. Horowitz, S. J. Pollock, P. A. Souder, and R. Michaels, *Parity Violating Measurements of Neutron Densities*, Phys. Rev. C **63** (2000), 025501.

[8] B. A. Brown, *Neutron Radii in Nuclei and the Neutron Equation of State*, Phys. Rev. Lett. **85** (2000), 5296.

[9] W. D. Myers and W. J. Swiatecki, *Average Nuclear Properties*, Ann. Phys. **55** (1969), 395.

[10] T.H.R. Skyrme, *The Effective Nuclear Potential*, Nucl. Phys. **9** (1959), 615.

[11] D. Vautherin and D.M. Brink, *Hartree-Fock Calculations with Skyrme's Interaction I. Spherical Nuclei*, Phys. Rev. C **5** (1972), 626.

[12] B.D. Serot and J.D. Walecka, *Recent Progress in Quantum Hadrodynamics*, Int. J. Phys. **E6** (1997), 515.

[13] X. Roca-Maza, M. Centelles, X. Vinas, and M. Warda, *Neutron Skin of ^{208}Pb, Nuclear Symmetry Energy, and the Parity Radius*, Phys. Rev. Lett. **106** (2011), 252501.

[14] C.J. Pethick, A. Akmal, V. R. Pandharipande, and D.G. Ravenhall, *Neutron Star Structure*, 1998.

[15] F. J. Fattoyev and J. Piekarewicz, *Neutron Skins and Neutron Stars*, Phys. Rev. C **86** (2012), 015802.

[16] W.G. Newton, M. Gearheart, J. Hooker, and Bao-An Li, *The Nuclear Symmetry Energy, the Inner Crust, and Global Neutron Star Modeling*, `arxiv.org/abs/1112.2018`, 2011.

[17] J.M. Lattimer and M. Prakash, *Neutron Star Structure and the Equation of State*, Ap. J. **550** (2001), 426.

[18] J. M. Lattimer and M. Prakash, *Neutron Star Observations: Prognosis for Equation of State Constraints*, Phys. Rept. **442** (2006), 109.

[19] C. J. Horowitz and J. Piekarewicz, *The Neutron Radii of Lead and Neutron Stars*, Phys. Rev. C **64** (2001), 062802.

[20] J. Antoniadis et. al., *A Massive Pulsar in a Compact Relativistic Binary*, Science **340** (2013), 6131.

[21] P.B. Demorest et. al., *A Two-Solar-Mass Neutron Star Measured Using shapiro Delay*, Science **467** (2010), 1081.

[22] C. J. Horowitz and J. Piekarewicz, *Constraining URCA Cooling of Neutron Stars from the Neutron Radius of ^{208}Pb*, Phys. Rev. C **66** (2002), 055803.

[23] J.M. Lattimer, C.J. Pethick, M. Prakash, and P. Haensel, *Direct Urca Process in Neutron Stars*, Phys. Rev. Lett. **66** (1991), 2701.

[24] R. Michaels, P.A. Souder, and G.M. Urciuoli et. al., *A Clean Measurement of the Neutron Skin of ^{208}Pb through Parity Violating Electron Scattering*, Jefferson Lab PAC **29** (2005).

[25] K. A. Aniol et. al. [HAPPEX Collaboration], *Parity-Violating Electroweak Asymmetry in e←p Scattering*, Phys. Rev. C **69** (2004), 065501.

[26] K. Paschke, *Controlling Helicity-Correlated Beam Asymmetries in a Polarized Electron Source*, Eur. Phys. J. A **32** (2007), 549.

[27] Rupesh Silwal, *Probing the Strangeness Content of the Proton and Neutron Radius of ^{208}Pb using Parity-Violating Electron Scattering*, Ph.D. thesis, University of Virginia, 2012.

[28] K. Aulenbacher, *Polarized Beams for Electron Accelerators*, European Physical Journal Special Topics **198** (2011), 361.

[29] R. Michaels, *PREX Talks*, `http://hallaweb.jlab.org/parity/prex/prextalks.html`.

[30] C. W. Leeman, D. R. Douglas, and G. A. Krafft, *The Continuous Electron Beam Accelerator Facility: CEBAF at the Jefferson Laboratory*, Annu. Rev. Nucl. Part. Sci. **51** (2001), 413.

[31] Alcorn et. al., *Basic Instrumentation for Hall A at Jefferson Lab*, Nucl. Instr. Methods Phys. Res. A **552** (2004), 294–346.

[32] R. Michaels, *Summary of target assembly.*

[33] John J. Lerose, Paul Brindza, and Robert Michaels, *Summary of Hardware Development Activities*, `hallaweb/jlab.org/parity/prex/pics/PREX_magnet_2008.pdf`, 2008.

[34] K.G. Fissum et. al., *Vertical Drift Chambers for the Hall A High-Resolution Spectrometers at Jefferson Lab*, Nucl. Inst. and Meth. A **474** (2001), 108–131.

[35] Lisa J. Kaufman, *Precision Measurements of the Proton Neutral Weak Form Factors at Q^2 0.1 GeV^2*, Ph.D. thesis, University of Massachusetts-Amherst, 2007.

[36] G. A. Krafft et. al., *Measuring and Controlling Energy Spread in CEBAF*, `arXiv: physics/0009087`, 2000, p. TH205.

[37] J. P. Jorda et. al., *A Fabry-Pérot Cavity for Compton Polarimetry*, Nucl. Inst. and Methods A **413** (1998), 1.

[38] O. Glamazdin, *Møller Polarimeter for PREX (status report)*, `http://hallaweb/jlab.org/equipment/moller/Talks/PREX\_Col\_01\_29\_2011.pdf`, 2011.

[39] Particle Data Group, *Particle Data Group Handbook, sec. 30*, 2013.

[40] Hamamatsu Photonics K.K., *Hamamtsu PMT Handbook, 3rd Edition, Ch. 4.*

[41] M. Gericke, *Excess Noise as a Function of Detector Thickness*, `http://qweak.jlab.org/doc-public/ShowDocument?docid=532`, 2005.

[42] A. Jankowiak, *The Mainz Microtron MAMI - Past and Future*, Eur. Phys. J. A **28** (2006), 149.

[43] B. Moffitt, *Elastic Scattering of Longitudinally Polarized Electrons from ^4He*, Ph.D. thesis, William and Mary, 2007.

[44] Luis Mercado, *Probing Novel Properties of Nucleons and Nuclei via Parity Violating Electron Scattering*, Ph.D. thesis, University of Massachusetts-Amherst, 2012.

[45] National Physical Laboratory, 2.2.6 Magnetic Properties of Materials, *Table of Physical & Chemical Constants 16th Ed.*, 1995.

[46] S. Abrahamyan et. al. [HAPPEX & PREX Collaborations], *New Measurements of the Transverse Beam Asymmetry for Elastic Electron Scattering from Selected Nuclei*, Phys. Rev. Lett. **109** (2012), 192501.

[47] M. Gorchtein and C. J. Horowitz, *Analyzing Power in Elastic Scattering of the Electrons off a Spin-0 Target*, Phys. Rev. C **77** (2008), 044606.

[48] K. Saenboonruang, *Measurement of the Neutron Radius of ^{208}Pb Through Parity Violation in Electron Scattering*, Ph.D. thesis, University of Virginia, 2013.

[49] C. J. Horowitz, *Parity Violating Elastic Electron Scattering and Coulomb Distortions*, Phys. Rev. C **57** (1998), 3430.

[50] S. Abrahamyan et. al. [PREX Collaboration], *Measurement of the Neutron Radius of ^{208}Pb through Parity Violation in Electron Scattering*, Phys. Rev. Lett. **108** (2012), 112502.

[51] C.J. Horowitz et. al., *Weak Charge Form Factor and the Radius of ^{208}Pb through Parity Violation in Electron Scattering*, Phys. Rev. C **85** (2012), 032501.

[52] J. Mammei, D. McNulty, R. Michaels, K. Paschke, S. Riordan, and P.A. Souder et. al., *CREX: Parity Violating Measurement of the Weak Charge Distribution of ^{48}Ca to 0.02 fm Accuracy*, Jefferson Lab PAC **40** (2012).